High-p_T Charged Hadron Suppression in $Au-Au$ Collisions at $\sqrt{s_{NN}} = 200$ GeV

A Dissertation Presented

by

Jiangyong Jia

to

The Graduate School

in Partial Fulfillment of the Requirements

for the Degree of

Doctor of Philosophy

in

Physics

State University of New York
at
Stony Brook

August 2003

Copyright © by
Jiangyong Jia
2003

State University of New York
at Stony Brook

The Graduate School

Jiangyong Jia

We, the dissertation committee for the above candidate for the Doctor of Philosophy degree, hereby recommend acceptance of the dissertation.

Axel Drees (Advisor)
Professor, Department of Astronomy and Physics

Edward Shuryak (Chair)
Professor, Department of Astronomy and Physics

Deane Peterson
Associate Professor, Department of Astronomy and Physics

Yasuyuki Akiba
Senior Scientist, RIKEN Institution

This dissertation is accepted by the Graduate School.

Graduate School

Abstract of the Dissertation

High-p_T Charged Hadron Suppression in $Au - Au$ Collisions at $\sqrt{s_{NN}} = 200$ GeV

by

Jiangyong Jia

Doctor of Philosophy

in

Physics

State University of New York at Stony Brook

2003

The PHENIX experiment at RHIC has measured charged hadron yields at mid-rapidity over a wide range of transverse momentum ($0.5 < p_T < 10$ GeV/c) in $Au - Au$ collisions at $\sqrt{s_{NN}} = 200$ GeV. The data are compared to π^0 measurements from the same experiment. For both charged hadrons and neutral pions, the yields per nucleon-nucleon collision are significantly suppressed in central collisions compared to both peripheral and nucleon-nucleon collisions. The suppression sets in gradually and increases with increasing centrality of the collisions. Above 4–5 GeV/c in p_T, a constant and almost identical suppression of charged hadrons and π^0's is observed. The ratio h/π^0 is ~ 1.6 for all centralities. This value is consistent with the particle composition observed in $p - p$ data at lower $\sqrt{s}$. The p_T spectra are compared to published spectra from $Au - Au$ at $\sqrt{s_{NN}} = 130$ in terms of x_T scaling. Central and peripheral π^0 as well as peripheral charged spectra exhibit the same x_T scaling as observed in $p - p$ data. The charged hadron suppression is also compared with results from $d - Au$ collisions. The

yield per nucleon-nucleon collisions shows a small enhancement, strikingly different from the suppression seen in central $Au - Au$ collisions, and indicates that the suppression in $Au - Au$ collisions is not an initial state effect. The data presented in this work were published in [50, 52, 55, 153].

The measured centrality dependence of suppression of hadron yield, ,suppression of back-to-back correlation and azimuthal anisotropy all imply a strong dependence on the underlying collision geometry. We present a simple model of jet absorption in dense matter which incorporates a realistic nuclear geometry. This model describes quantitatively the observed suppression of the high p_T hadron yield and of the back-to-back angular correlations. The azimuthal anisotropy of high p_T particle production is described qualitatively.

To my mom, my dad and my wife

Contents

Acknowledgements . . . . . **ix**

List of Figures . . . . . **xxvi**

List of Tables . . . . . **xxix**

1 Introduction **1**
1.1 Quark Gluon Plasma and RHIC 1
1.1.1 Collision Geometry for Heavy-Ion Collisions 4
1.2 Hard-scattering as Probe for QGP 8
1.2.1 Hard-scattering in $N-N$ Collisions 8
1.2.2 Hard-scattering as a Probe in Heavy-Ion Collisions . . 10
1.3 High p_T Observables 16
1.3.1 Suppression of High p_T Hadrons 17
1.3.2 Jet Angular Correlation 18
1.3.3 Collision Geometry and High p_T Observable 19
1.4 Organization of the Work 19

2 PHENIX Experiment **21**
2.1 PHENIX Detector 21
2.1.1 Global Detectors 23
2.1.2 The Central Arm Detectors 25
2.2 The Central Arm Detectors 26
2.2.1 The Central Arm Magnet 26
2.2.2 The Drift Chamber 27
2.2.3 The Pad Chambers 29
2.2.4 The Ring Imaging Cerenkov Detectors 31
2.2.5 The Electromagnetic Calorimeters 35
2.2.6 The Time Of Flight 36

3 The Calibration Marathon 38
3.1 The Drift Chamber Calibration 38
3.1.1 v_d and t_0 calibration 42
3.1.2 Slewing and Drift Correction 45
3.1.3 Single Wire Efficiency and Tracking Efficiency 47
3.1.4 Noisy and Inactive Channels 50
3.2 Track Reconstruction 51
3.2.1 DC-PC1 Tracking 51
3.2.2 Momentum Determination and Global Tracking 54
3.2.3 Matching to Outer Detectors 54
3.2.4 Detector Alignment 57
3.3 Momentum Calibration 60
3.3.1 Momentum Resolution 61
3.3.2 Momentum Scale 64

4 Data Analysis 67
4.1 Event Selection and Centrality 67
4.1.1 Minimum Bias Trigger Definition and Efficiency 67
4.1.2 Centrality Definition 69
4.1.3 Glauber Simulation 70
4.1.4 Centrality Selection for the Charged Hadron Analysis . 74
4.2 Tracking and Momentum Measurement of Charged Hadrons . 74
4.3 Background Problem at High p_T 74
4.4 Background Rejection 77
4.4.1 Random Association Background 77
4.4.2 Better Matching Variables 82
4.5 Subtraction of the Irreducible Background 85
4.5.1 Background Sources and Why 87
4.5.2 Separation of Conversion and Decays 92
4.5.3 Conversion Background Subtraction 96
4.5.4 Decay Background Subtraction 102
4.5.5 Systematic Errors on Background Subtraction 112

5 Corrections and Systematic Uncertainties 115
5.1 Geometrical Acceptance and Decay Losses 116
5.2 Matching Cut Efficiency 117
5.3 Reconstruction Efficiency 119
5.4 Momentum Resolution and Scale 120
5.5 Run-by-Run Variation and Acceptance Normalization 122
5.6 Occupancy Dependent Correction 124
5.7 Systematic Uncertainties 125
5.8 Comparison with Identified Charged Hadron Spectra 128

6 Results and Discussion 130
6.1 Inclusive Charged Hadron p_T Spectra 130
6.2 Suppression of High p_T Hadrons 132
6.3 Energy Dependence and x_T Scaling 144
6.4 Model Comparisons 152
6.5 Comparison to Charged Hadron Production in $d-Au$ Collisions 159
6.6 Cronin Effect in $Au-Au$ Collisions ? 161
6.7 Collision Geometry and Jet Absorption 167
6.7.1 The Model 168
6.7.2 Centrality Dependence Compared to Data 171
6.7.3 Discussions 174

7 Summary and Outlook 179

A Charged Hadron Analysis for 130 GeV $Au-Au$ and 200 GeV $d-Au$ Collisions 193
A.1 Charged Hadron Analysis in $Au-Au$ Collisions at $\sqrt{s_{NN}}$ = 130 GeV 194
A.2 Charged Hadron Analysis in $d-Au$ Collisions at $\sqrt{s_{NN}} = 200$ GeV 197
A.2.1 Centrality Selection 198
A.2.2 Matching Cuts and Background 204
A.2.3 Systematic Errors on Inclusive Spectra 204

B Definition of Glauber Variables 206

Acknowledgements

First I would like to express my heartfelt gratitude to my advisor, Professor Axel Drees, and my long-term "mentor", Dr. Federica Messor. From the beginning of my thesis research four years ago, Professor Drees has always been patient and providing crucial advices on directions to follow at critical points during my research. His easy-going personality and humor have made working with him enjoyable. Dr. Messor has been working closely with me for almost 3 years, she helped to build up my programming and analysis skills and to improve my presentation and communication abilities. Her enthusiasm and continuous encouragement have been an important moral support. Their help made the publication of the material presented in this thesis possible.

I would like to thank my colleges at Stony Brook and Brook Haven National Laboratory for their great support. I thank Barbara Jacak, Tom Hemmick, Ralf Averback, Vlad Pantuev, Julia Velkovsky, Stephen Johnson and Momchil Velkovsky for many helps and valuable guidance since I join the group. My gratitude goes to Mike Tannenbaum, Brian Cole and Yasuyuki Akiba and other friends at BNL for countless discussions. My thank goes especially to my co-graduate students, Sean Leckey, Felice Matathias, Sergy Butsyk, Anne Sickles, Jane Burward-Hoy, Anuj Purwar and Columbia University buddies, Chun Zhang, Mickey Chiu, Justin Frantz who have provides numerous technique supports, bug fixes, dinner breaks, and moral ammunition in the many bloody days and frustrating nights.

Last but not least, I would like to acknowledge the careful and timely corrections of my thesis by Ralf Averbeck.

List of Figures

1.1 a) The energy density versus temperature calculated with improved staggered fermions on the lattice [3]. b) Static quark free energy for $N_f = 3$ at temperatures corresponding to T/Tc =0.58, 0.66, 0.74, 0.84, 0.9, 0.94, 0.97, 1.06 and 1.15 (from top to bottom) [5]. $F(r)$ is the free energy, $\sqrt{\sigma}$ is the string tension. Solid line is the $T = 0$ limit. 2

1.2 Space-time picture of a nucleus-nucleus collision. The times and temperatures for different phases are taken from [7]. 3

1.3 Woods-Saxon nuclear density profile for Au. 5

1.4 An illustration of the collision geometry for a non-headon nucleus-nucleus collision. 6

1.5 Schematic representation of a high-p_T reaction factorized into parton distribution functions (f), parton fragmentation functions (D), and a hard-scattering subprocess. 9

1.6 a) The invariant differential cross section for inclusive π^0 production (points) and the results from NLO pQCD calculations using the "KKP" [31](solid line) and "Kretzer" [32] (dashed line) sets of fragmentation functions. b,c) The relative difference between the data and the theory using KKP (b) and Kretzer (c) fragmentation functions with scales of $p_T/2$ (lower curve), p_T, and $2p_T$ (upper curve). This figure is taken from [29]. . . 10

1.7 A Schematic view of k_T broadening before hard-scattering. . 13

1.8 a) Schematic view of the structure function, F_2^A/F_2^D. b) Partial compilation of results for F_2^A/F_2^D (from [41]). Note that below $x \approx 0.01$, the average Q^2 value of the data is smaller than 2 GeV^2. 14

1.9 parton interacting with the nuclear target resolves the transverse area $\sim 1/Q^2$ and, in the target rest frame, the longitudinal distance $\sim 1/(mx)$ [44], where m is the parton mass. 15

2.1 The baseline PHENIX experiment. The left panel shows the PHENIX central arm spectrometers viewed along the beam axis. The right panel shows a side view of the PHENIX muon arm spectrometers. 22

2.2 Layout for PHENIX Experiments in RUN-1 (left panel), RUN-2 (middle panel) and RUN-3 (right panel). 22

2.3 a) CM and MM field lines shown on a cutaway drawing of the PHENIX magnets. The beams travel along the z axis in this figure and collide at $z = 0$. b) z component of the magnetic field, B_z, as a function of, R, the radial distance along the line connecting origin and different z locations at the DC (it is the z component of the magnetic field that bends the track). . . . 28

2.4 a) Layout of the wire position for 4 cells and a blow up drawing of the wire arrangement for a V1 net (the arrangement are similar for other wire nets). b) Top view of a schematic diagram of the stereo wire orientation. 30

2.5 The Pad Chamber system in PHENIX. Several sectors of PC2 and PC3 in the west arm are removed for clarity of the picture. Figure from Ref. [76]. 31

2.6 A cutaway view of the RICH detector [78]. 33

2.7 Schematic r-z view of the RICH and its optics. A typical electron (400 MeV/c) produces Cerenkov photons, which are reflected by the mirror into a ring at the focal plane where they are collected by the PMT array. Hadrons with $\gamma < 35$ do not produce photons in the RICH [79]. 34

2.8 Box plot for RICH PMT hits relative to the track projection point in the RICH, accumulated over many tracks [78]. 35

3.1 a) A typical drift cell with the wire positions. [81] b) The drift lines for six wire planes in an X1 net, different types of wires are marked by arrows. The drift lines are in blue (or dark colored line in black and white). A typical track trajectory is illustrated by the boundary of drift lines to the right. The electrons clouds from the ionization are illustrated by the red dots [82]. (courtesy of Sergy Butsyk). 40

3.2 Drift velocity as function of E/P in the DC working gas mixture. Figure taken from [81]. 41

3.3 A schematic illustration of the drift time measurement for a drift chamber hit. The curve shows the amplified analog signal from a hit. The horizontal dashed line is the charge threshold in the ASD. The difference between leading edge and trailing edge $t_T - t_L$ gives the width of the hit. The short solid vertical line indicate the true drift time, t_a. Thus $t_L - t_a$ is the slewing correction. 41
3.4 The measured BBC start time distribution. 43
3.5 The time distribution for two X planes in the west arm (The third plane in X1, and the second to last plane in X2) from RUN-2 data. Also shown is a fit to the leading and trailing edge of the timing distribution. 44
3.6 The run-by-run variation of t_0 and v_d for the east arm and west arm separately. (a) t_0 versus run number. (b) The t_0 distribution for all runs. (c) v_d versus run number. (d) The v_d distribution for all runs. 45
3.7 a) Channel-by-channel t_0 variation. b) Plane-by-plane v_d variation. 46
3.8 Illustration of three-point method. 46
3.9 a) The residual ΔT distribution for hits with 23 time bins and 47 time bins (1 timebin = $0.822ns$), together with Gauss fits. b) The $\langle \Delta T \rangle$ as function of hit width and a 2 order polynomial fit. This figure is for east arm X1 wires [82]. 47
3.10 The contours of the drift lines for the first (left panel) and the fifth (right panel) X1 plane. The thin contour lines indicate the isochrones. The small dots on the isochrones indicate the normal drift region, where electrons drift along a straight line. The think black lines indicate the typical drift trajectories [82]. 48
3.11 Single hit resolution for the east arm (left) and the west arm (right) in μm. 48
3.12 The width distribution of the DC hits as function of time bins. offline width cut is illustrated by the vertical dashed line. The solid curve (dotted line) are Gaussian (linear) extrapolation of signals to the small width region. 49
3.13 The single wire efficiency calculated by 3-point method from online monitoring. 50
3.14 The DC inactive area shown separately for the east arm (top) and the west arm (bottom), as well as for the north side (right) and the south side(left). 51

3.15 a) A schematic cutaway view of a track in the DC x-y (or r-ϕ) plane. The X1 and X2 hits in the drift chamber are shown as small circles within an outline of the drift chamber. ϕ and α are the feature space variables in the CHT transform (see text). b) A schematic cutaway view of a track in the DC r-z plane. The track polar angle is β. The associated PC1 hit is indicated by the box marker. The track bending angle is δ, which is small, such that the track can be approximated by the straight line linking the PC1 hit and collision vertex measured by the BBC. 52
3.16 Hits in a portion of the drift chamber (left panel) and the corresponding feature space distribution for X1 and X2 wires (right panel) [85]. 53
3.17 PC2 matching variables as function of momentum and charge. From left to right and top to bottom, four panels represents, $mean_z$, $mean_{r\text{-}\phi}$, σ_z and $\sigma_{r\text{-}\phi}$. 56
3.18 Run-by-run variation of the $\sigma_{r\text{-}\phi}$ at 2 GeV/c in momentum (top panel), and the fitting parameters (bottom panel) according to Eq. 3.5. The dashed line at the top panel represents the average. 57
3.19 Centrality dependence of the matching variables as function of p_T. A centrality dependent variation can be seen in $mean_z$ and σ_z, but not in $mean_{r\text{-}\phi}$ and $\sigma_{r\text{-}\phi}$. 57
3.20 $\langle\Delta\alpha\rangle$ as function of ϕ. The marker and the black curve represent the data and the fit, respectively. 59
3.21 A schematic view of the idea for card alignment. The card is indicated by the thick line. The wires with different drift directions are indicated by the open and closed marker. α_1 and α_2 represent the angles corresponding to the drift boundary on each side of the card. 60
3.22 The difference in ϕ between X1 card and X2 card for the east and the west arm. The histogram is the distribution and the line is a fit with two Gaussian functions. 60
3.23 α distribution for tracks passing a 2 σ PC3 z matching cut. . . 62
3.24 α distribution for tracks passing different energy cuts at the EMCal. 63
3.25 m^2 distribution from the TOF in RUN-2.[89] 65
3.26 Momentum dependence of the width (left) and the centroid (right) of m^2 distributions for each identified particle.[90] . . . 65
3.27 The three contributions to the 1σ m^2 width for pions(left) protons(right). Each contribution is shown by a band with different color around the expected m^2 value. [89] 66

3.28 Ratio of measured m^2 centroid to the nominal value for protons and antiprotons as function of momentum before (left) and after (right) a momentum scale correction factor of 1.022 has been applied.[89] 66

4.1 the BBC trigger efficiency as function off z_{vtx} from Ref.[92]. . 68
4.2 $\epsilon^{trigger}_{zdc|bbc}$ as function of run number. The error bars shown are statistical only. (from [93]) 69
4.3 Centrality definition in PHENIX. The left panel shows the ZDC energy vs. BBC charge, together with centralities defined by the clock method. The right panel shows the corresponding track multiplicity for minimum bias events and the four most central centrality classes. 70
4.4 The ZDC vs BBC for different number of participants (left panel) The clock-method to define centrality classes for Monte-Carlo (right panel). Figure from Ref.[97]. 72
4.5 Total geometrical cross section for Glauber calculation with different parameters. Figure from [98]. 73
4.6 Systematic errors on $\langle N_{coll}\rangle$, $\langle T_{AuAu}\rangle$, $\langle N_{part}\rangle$ and $\langle b\rangle$. Figure from [98]. 73
4.7 a) The background origination point in r-z plane. b) The fraction of backgrounds as function of Monte-carlo p_T. 76
4.8 The fractional difference between the generated p_T (p_T^G) and reconstructed p_T (p_T^R) relative to p_T^G. 77
4.9 a) The displacement in r-ϕ, D_ϕ^{PC3}, for both negative and positive tracks in $5 < p_T < 7$ GeV/c. A 3 σ cut on D_z^{PC3} has already been applied to reduce the background. b) The same distribution in z direction, where a 3 σ cut on D_ϕ^{PC3} has been applied. 78
4.10 a) All tracks from DC/PC1 for minimum bias events and tracks that satisfy 2 σ match at PC3. b) Ratio of the two spectra. . . 79
4.11 a) The same as Fig. 4.10a, but including the random association spectra at PC3 (curve with cross markers). b) The random association probability, and random association fraction relative to tracks that satisfy PC3 match. 81
4.12 a) Same as Fig. 4.11a, but also requiring a 2σ match to PC2. b) The random association probability, and random association fraction relative to tracks that satisfy the PC2, PC3 match cut. 82
4.13 Same as Fig. 4.12 for the 0-5% most central collisions. 83

4.14 a) a schematic view of the matching of tracks to PC2 and PC3. b) D_ϕ^{PC2} versus D_ϕ^{PC3} for tracks with reconstructed $p_T > 4$ GeV/c. 84

4.15 The D_ϕ^+ distribution for different z_{DC} ranges for positive (left) and negative (right) particles in $5 < p_T < 7$ GeV/c. 85

4.16 Track density as function of z_{DC} 86

4.17 HIJING [18] simulation of the background level with 2σ matching cut on matching variables as defined in Eq. 4.12. 86

4.18 True p_T distribution of background tracks from conversions (panel a)) and decays (panel b)). 87

4.19 Conversion background vertex distribution in radial direction from simulation. These tracks have a reconstructed $p_T > 5$ GeV/c. 88

4.20 The fractional difference between reconstructed p_T^R and true p_T^G for the secondary particles from K_s^0 (left) and Λ (right). The K_s^0 and Λ are required to have $p_T > 4$ GeV/c. 91

4.21 The matching distribution in D_ϕ^+(left) and D_z^+(right) for difference background sources from simulation. 91

4.22 a) Raw N_{PMT} distribution (solid line) and the estimated random association background (dashed line). b) The probability distribution of N_{PMT} for data after subtracting random background(solid line) and for Monte-Carlo (dashed line). 94

4.23 The $\langle N_{PMT} \rangle$ as function of p_T for $\pi^+ + \pi^-$ from Monte Carlo. 95

4.24 Raw spectra for all tracks (N_A), tracks with RICH hit (N_R) and tracks without RICH hit (N_{NR}) according to Eq. 4.21. 95

4.25 R_e^m as function of reconstructed p_T for different N_{PMT} threshold m for minimum bias data. The definition of R_e^m is given in the figure. 97

4.26 The fitted $R_e = R_e^5$ value for different reconstructed p_T ranges from data. 97

4.27 R_e as function of true p_T from the simulation of single e^+ and e^-. 97

4.28 R_e as function N_{part}. The solid line indicates the average value, and the dashed line indicates the estimated systematic uncertainties. 98

4.29 An illustration of the background subtraction in D_ϕ^+ for tracks with associated RICH PMTs and $6 < p_T < 7$ GeV/c. The subtraction is shown for minimum bias events and separately for positively (left) and negatively (right) charged tracks. Since e^+ and e^- are deflected in opposite directions by the fringe field, they are shifted to positive and negative directions, respectively. The first three distributions represent the raw counts for all tracks with RICH association (solid line), the estimated conversion background based on R_e method (dashed line) and the charged π (dot-dashed line) that were obtained by subtracting the dashed line from the solid line. The thin solid line represents the matching distribution of background electrons from the Monte-Carlo simulation, arbitrarily scaled to match the data. The 2 σ matching window is illustrated by the vertical dashed line. 99
4.30 Background subtraction for N_R tracks. There are very little random associates left at $p_T > 6$ GeV/c. 99
4.31 a) RICH efficiency for charged pions as function of generated p_T. b) R_e and R_π from the MC simulation as function of generated p_T. 101
4.32 Fully corrected charged pion spectra compared to π^0 spectra for three centrality classes. The π^0 data points have been shifted to the right by 0.1 GeV/c for better distinction. 102
4.33 a) Charged kaons and their decay particle p_T distributions. b) The matching distribution for decays in two different reconstructed p_T ranges. 103
4.34 Background level from K_s^0 decay relative to primary $K^\pm$. The left figure shows the reconstructed spectra from HIJING(except for the open square marker, which represents the parent K_s^0 true p_T distribution for daughter particles with reconstructed $p_T > 1$ GeB/c). The right figure shows the K_s^0 feed down contribution relative to the $K^\pm$ yield. 104
4.35 a) Hyperon and anti-hyperon decay contribution compared to primary $p+\bar{p}$ spectra. The HIJING input has been scaled up by a factor 1.64 to match the measured Λ/p ratio (0.9). b) hyperon feed relative to $p + \bar{p}$. 104
4.36 a) Primary $K^+ + K^-$ reconstructed p_T spectra from HIJING with various fits. b) Ratios of different fits to the power-law fit of the HIJING input. c) The K_s^0 background relative to $K^\pm$, $\epsilon_{K_s^0}^{decay}(p_T)$(Eq. 4.30), for different fits. 106

4.37 a) Primary $p + \bar{p}$ reconstructed p_T spectra with various fits. b) The ratios of different fits to the power-law fit of the HIJING input. c) The hyperon background relative to $p + \bar{p}$, $\epsilon^{decay}_{hyperon}(p_T)$(Eq. 4.31), for different fits. 106
4.38 The p_T distribution for tracks without RICH hits (N_{NR}) for minimum bias collisions, the curve is the upper limit of the extrapolation of the signal shape to high p_T. 107
4.39 a) The p_T dependence of R_{NR} form data. b) The p_T dependence of R_{NR} and R_{decay} from simulation. The solid line in both panels is at 0.424, the dashed lines indicate a ± 0.04 variation. 109
4.40 The centrality dependence of $R^{10<p_T<20}_{decay}$. The solid line is at 0.424, the dashed lines indicate a ± 0.03 variation. 109
4.41 Background subtraction in D^+_ϕ for tracks without an associated RICH PMT and with $6 < p_T < 7$ GeV/c. The subtraction is shown for minimum bias events and separately for positively (left) and negatively (right) charged tracks. The first three distributions represent the raw counts for all tracks without a RICH association (solid line), estimated decay background based on the R_{decay} method (dashed line), and signal tracks (dot-dashed line) that were calculated as the difference of the first two distributions. The thin solid line represents the matching distribution of decay background from Monte-Carlo simulation, arbitrarily scaled to match the data. The 2 σ matching windows are illustrated by the vertical dashed lines. 110
4.42 Background subtraction for N_{NR} tracks (Eq. 4.37) in minimum bias events. 110
4.43 a) Signal tracks (closed circles) and remaining background tracks (open circles). b) The fraction of background subtracted (close stars), and remaining background relative to all tracks after subtraction (open stars). 111
4.44 Amount of background estimated as function of p_T for minimum bias collisions. The left figure shows the arbitrarily normalized spectra for the signal (filled squares), e^+e^- from conversion (open squares) and decays (open triangles). The right figure shows the signal to background ratio. Only statistical errors are shown. 112
4.45 a) The signal spectra decomposed into $N_{PMT} \geq 0$ (S_R) and $N_{PMT} < 0$ (S_{NR}). b) The fraction of these two samples relative to the total raw signal yield. 113

5.1 Geometrical acceptance for charged particles in azimuth ϕ as function of p_T. 116

5.2 Averaged correction functions for π^+ and π^-, p and $\bar{p}$, and K^+ and K^-. 117

5.3 The K/π and p/π ratio for central (panel a)) peripheral (panel b)) collisions. 118

5.4 The overall 2σ matching cut efficiency for MC (solid) and data (open). 119

5.5 The ratio of fully corrected spectra for different matching windows for central(left) and peripheral(right) events. 119

5.6 Systematic checks of correction functions. Top panel shows the variations using fits to p_T spectra from minimum bias (middle curve), central (bottom curve) and peripheral (top curve) data as weighting functions. The bottom panel compares corrections obtained by varying the momentum resolution by $\pm 20\%$. . . . 120

5.7 Upper and lower limit on the yield assuming a 0.7% momentum scale error for central (solid marker) and peripheral (open marker) collisions. 121

5.8 Raw spectra for a given run divided by raw spectra for the full data set. a) Ratios of good runs to the full data set. b) Ratios of bad runs to the full data set. 122

5.9 ϕ vs z_{DC} distribution for tracks with $2 < p_T < 3$ GeV/c from good runs (left) and Monte-Carlo simulation (right). 123

5.10 ϕ distributions of the tracks with $2 < p_T < 3$ GeV/c. Several good ϕ ranges used for normalization are indicated by the black bar. a) Tracks at the north side of the DC. b) Tracks at the south side of the DC. MC statistics have been scaled to match the data. 124

5.11 The occupancy dependent efficiency as function of p_T for four centrality classes. 125

5.12 Functions used to correct the charged particle p_T spectra. The upper left panel shows the p_T dependent correction, $c(p_T)$. The upper right panel shows the centrality dependent correction, $c(N_{part})$. Systematic uncertainties are indicated by the dashed lines. The two corrections factorize at $p_T > 1.5$ GeV/c, so that for any centrality the full correction function is given by $c(p_T) \times c(N_{part})$. The accuracy of this factorization is demonstrated in the lower panel. The ratio of the full correction for central collisions (5% most central) to the correction for single particle events varies by less than 3% above 1.5 GeV/c (the error bar is the statistical error from the Monte-Carlo calculation). 127

5.13 The comparison between the sum of the identified charged hadron spectra and unidentified charged hadron spectra from the same experiment for four centrality classes. The errors shown are statistical only. 129

6.1 p_T spectra of charged hadrons for minimum bias collisions along with spectra for 9 centrality classes. The minimum bias spectrum has been multiplied by 5 for visibility. Only statistical errors are shown in the spectra. Most of the p_T dependent systematic errors are independent of centrality and are tabulated in Table. 5.3. 131

6.2 Ratios of centrality selected p_T spectra to the minimum bias spectrum. Ratios for peripheral classes are scaled up for clarity. For the p_T range shown, most of the systematic errors cancel in the ratio. The remaining systematic errors that can change the shape are less than 10% (see Table. 5.4) and are correlated bin-to-bin in p_T. 132

6.3 Centrality dependence of $\langle p_T^{trunc} \rangle$, defined as the average p_T of charged particles with p_T above a threshold p_T^{min} minus the threshold p_T^{min}(see Eq. 6.1). Shown are $\langle p_T^{trunc} \rangle$ values for three p_T^{min} cuts, with $p_T^{min} = 0.5$, 2 and 4.5 GeV/c respectively. Only statistical errors are shown. 133

6.4 Ratio of charged hadron yields per nucleon-nucleon collision between central (0-10%) and peripheral (60-92%) $Au-Au$ collisions. In this ratio, most of the systematic errors cancel. The solid error bars on each data point are statistical. The error bar on the left hand side of the figure is the overall scale error relative to 0.5, which is the quadrature sum of (i) the uncertainty of $\langle N_{coll} \rangle$ (see Table. 4.1.4) and (ii) the uncertainty on the occupancy correction ($\delta_{occupancy}$). The shaded error band on each data point is the p_T dependent systematic error from $\delta_{R_e \oplus R_{decay}}$ and centrality dependent feed down correction ($\delta_{feeddown}$) as given in Table. 5.4. 134

6.5 a) PHENIX π^0 spectrum from $p-p$ collisions at $\sqrt{s} = 200$ GeV together with the power-law fit Eq. 6.3. b) Ratio of the data to the fit together with the systematic error band. 135

6.6 a) ISR data from Ref. [27]. π,K,p are summed to give the h/π ratio. b) h/π ratio as function of momentum found in quark and gluon jets in DELPHI [63]. c) Ratio of PHENIX π^0 data and UA1 [110] charged data to the PHENIX power-law fit. The fit to the UA1/power-law ratio is used to correct the power law to represent the charged hadron reference for 200 GeV. d) Same as c), but using the PHENIX data. 136

6.7 a) PHENIX charged hadron data compared with UA1 [110] and neutral pions from PHENIX [29] scaled by 1.581. Also shown is the $N-N$ reference and its systematic uncertainty. b) Ratio of the data to the reference. The lines indicates the systematic uncertainty on the reference distribution. 138

6.8 R_{AA} for $(h^+ + h^-)/2$ and π^0 as function of p_T for minimum bias and 9 centrality classes according to the "*Fine*" type of centrality classes defined in Table. 4.1.4. The error bars on the π^0 data points include statistical and systematical errors on the $Au - Au$ data and the $N - N$ reference. The error bars on $(h^+ + h^-)/2$ data points are statistical errors only. The normalization errors on the reference common for charged hadrons and π^0s are added in quadrature with the uncertainty on $\langle N_{coll} \rangle$ and are indicated by the black bar on the left side of each panel. This error ranges from 15% to 36% from central to peripheral collisions and can shift all points in the charged and neutral pion R_{AA} up and down together. The shaded band on charged R_{AA} includes the remaining systematic errors on the charged $N - N$ reference summed in quadrature with the systematic errors from the $Au - Au$ spectra. This error amounts to -12.5% – +18% at low p_T and changes to ±12.5% at $p_T = 4.5$ GeV/c and ±18.5% at $p_T = 8$ GeV/c. 141

6.9 Charged hadron to π^0 ratios for minimum bias events and 9 centrality classes according to the "*Fine*" type of centrality classes defined in Table. 4.1.4. The error bars represent the quadratic sum of statistical and point-by-point systematic errors from $(h^+ + h^-)/2$ and π^0. The shaded band shows the percent normalization error (dominantly from $(h^+ + h^-)/2$ data) common to all centrality classes. The dashed line at 1.6 is the h/π ratio measured in $p - p$ [27] and e^+e^- [63] collisions. . . 142

6.10 $Au-Au$ yield integrated for $p_T > 4.5$ GeV/c over the $N-N$ yield, normalized using either N_{coll} (R_{AA} in the top panel) or N_{part} ($R_{AA}^{N_{part}}$ in the bottom panel), plotted as function of $\langle N_{part}\rangle$. "*Fine*" and "*Coarse*" types of the centrality classes defined in Table. 4.1.4 are used for $(h^+ + h^-)/2$ and π^0, respectively. Following errors are shown in both figures: **i).** The bands denoted by solid (dashed) lines represent the binary collision (participant pair) scaling. The width of the bands represent the systematic errors due to the normalization errors common to $(h^+ + h^-)/2$ and π^0 added in quadrature with the uncertainty on $\langle N_{coll}\rangle$ ($\langle N_{part}\rangle$). These errors can move $(h^+ + h^-)/2$ and π^0 up and down together in centrality correlated way, and are the same as the black error bars discussed in Fig. 6.8. **ii).** The error bars for each $(h^+ + h^-)/2$ data point are statistical error. The p_T correlated systematic errors from $Au-Au$ and the rest of the systematic errors on the charged hadron $N-N$ reference are represented by the brackets, within which the charged hadron data points can move up or down relative to π^0. **iii).** Dark shaded error bands around each π^0 data point include both statistical and point-to-point systematic errors on $Au-Au$ and the π^0 $N-N$ reference. 143

6.11 (a) CDF, UA1 and ISR transverse momentum dependence of the invariant cross section at seven center of mass energies from different experiments [27, 28, 110]. (b) The same data multiplied by $\sqrt{s}^{6.3}$, plotted as a function of $x_T = 2p_T/\sqrt{s}$. 146

6.12 (a) Transverse momentum dependence of the invariant cross section for π^0 at five center-of-mass energies from different experiments [122, 123, 124, 125, 29]. (b) The same data multiplied by $\sqrt{s}^{6.3}$, plotted vs $x_T = 2p_T/\sqrt{s}$. 147

6.13 x_T scaled spectra for central collisions and peripheral collisions at $\sqrt{s_{NN}} = 130$ and 200 GeV. The left figure shows the π^0 x_T spectra, and the right figure shows the $(h^+ + h^-)/2$ x_T spectra. The central (0-10%) x_T spectra are represented by triangular symbols, and the peripheral (60-80%) x_T spectra are represented by square symbols. The open symbols represent x_T spectra from $\sqrt{s_{NN}} = 130$ GeV scaled by a factor of $(130/200)^{6.3}$. The solid symbols represent x_T spectra from $\sqrt{s_{NN}} = 200$ GeV. The error bars are statistical only. 150

6.14 The x_T scaling power n (according to Eq. 6.13) plotted as function of x_T calculated for π^0 (top-left) and $(h^+ + h^-)/2$ (top-right) in central (0-10%) and peripheral (60-80%) collisions. The solid (and dashed) lines indicate a constant fit along with the fitting ranges to the central (and peripheral) $n(x_T)$ functions. The error bars at each data point include statistical and point-to-point systematic errors from $\sqrt{s_{NN}} = 130$ and 200 GeV. The scale errors on x_T spectra are 20.7% (15.9%) for π^0 x_T spectra ratio in central (peripheral) collisions, and 18.6% (15.7%) for $(h^+ + h^-)/2$ x_T spectra ratio in central (peripheral) collisions. These type of errors propagate into the systematic errors on x_T scaling power n listed in Table. 6.2. 151

6.15 HIJING predictions[133] of the inclusive charged hadron spectra in central $Au-Au$ and $p+Au$ collisions at $\sqrt{s_{NN}} = 200$ GeV. The competing effects of minijet production (dash-dotted), gluon shadowing (dashed) (assuming that gluon shadowing is identical to that of quarks), and jet quenching (solid) with $dE/dx =$ 2 GeV/fm are shown. $R^{AB}(p_T)$ is the ratio of the inclusive p_T spectrum of charged hadrons in $A-B$ collisions to that of $p-p$. In contrast to $Au-Au$, no significant quenching is expected in $p-A$ (or $d-Au$), since only the initial state shadowing effects (about $\sim 20\%$) and Cronin effects can modify the charged hadron spectrum at high p_T. 153

6.16 R_{AA} calculated from the BDMPS model [136] compared with PHENIX data. 154

6.17 The calculated nuclear modification factor $R_{AA}(p_T)$ for neutral pions at $\sqrt{s}_{NN} = 17$ and 200 GeV from Ref.[58]. Solid (dashed) lines correspond to the smaller (larger) effective initial gluon rapidity densities at given $\sqrt{s}$ that drive parton energy loss. Data on π^0 production in central $Pb-Pb$ at $\sqrt{s}_{NN} = 17.4$ GeV from WA98[140] and on π^0 and charged hadrons in central $Au-Au$ at $\sqrt{s}_{NN} = 200$ GeV from PHENIX are shown. 155

6.18 a) Calculated nuclear modification factor of π^0 p_T spectra for $d+Au$ and central $Au+Au$ collisions at $\sqrt{s} = 130$ (solid) and 200 GeV (dashed) as compared to PHENIX data. The lower dashed line [144] uses the energy loss including thermal absorption [139]. Figure from [48] b) The calculation for central $Au-Au$ collisions at $\sqrt{s_{NN}} = 200$ GeV from [145]including thermal absorption compared with charged hadron and neutral pion data from PHENIX. 156

6.19 The calculated centrality dependence of high p_T charged hadron $R_{AA}^{N_{part}}$ for BDMPS [113] (dotted line), WOGZ/WW [145] (dashed line) and our jet absorption model (solid line) compared with the charged hadron data. The thin dashed line at 1 represents the participant scaling, and the thin solid line represents the collisions scaling. 157

6.20 Saturation model calculation of the centrality dependence of hadron yields in $Au-Au$ collisions for different p_T at $\sqrt{s_{NN}} =$ 200 GeV. The band is the results from the calculation, and the thin line indicate the collision scaling. 158

6.21 a) Inclusive charged hadron yield at mid-rapidity for minimum bias $d-Au$ events, scaled by $\langle N_{coll}\rangle$. b) Minimum bias R_{dA} compared with R_{AA} for the 10% most central $Au-Au$ collisions, together with the saturation model predictions (CGC) shown by the solid line. Figure taken from [153, 154]. 160

6.22 a) Comparison of minimum bias R_{dAu} with a prediction from [150]. b) Comparison with prediction from [156]. 161

6.23 Comparison between R_{dAu} and R_{AA} for four centralities. The left column shows for $d-Au$, The right column shows $Au-Au$. From top to bottom, the centrality class goes from central to peripheral. The error bars on $d-Au$ are from Table.A.3 and Table.A.4. The $d-Au$ data points are provided by Sean Leckey. 162

6.24 h/π ratios for different centralities in $Au-Au$ collision compared with the calculation from[112]. 163

6.25 R_{dA} for charged hadrons (solid marker) and π^0 (open marker) in minimum bias collisions (from [153]). The lines are predictions from [112] for charged hadrons (solid line: without shadowing; dashed line: with EKS [40] shadowing) and π^0 (dotted line: without shadowing; dot-dashed line: with EKS shadowing). . . 164

6.26 R_{cp} for $\sqrt{s_{NN}} = 130$ and 200 GeV $Au-Au$ collisions for charged hadrons (closed markers) and π^0 (open markers). The thick black bar is the error from N_{coll} and is common for all four sets of data points. For charged hadrons, the error on the 200 GeV data is the same as shown in Fig. 6.4. The error bars and the brackets on 130 GeV data are statistical errors and the systematic errors that do not cancel in the ratio, respectively. For π^0, the error bar includes both the statistical errors and errors that don't cancel in the ratio. 166

6.27 Collision density $\rho_{coll}(x,y)$ (left) and participant density $\rho_{part}(x,y)$ (right) in transverse plane for central (0-5%) and peripheral (75-80%) collisions. 169

6.28 Origination point distribution in the transverse plane for jets that escape from the overlap region. 171

6.29 Centrality dependence of single hadron suppression, back-to-back suppression, and v_2 at high p_T. In all four panels, the thick solid line indicates the prediction from calculations based on Eqs. 6.19-6.20. a,b) R_{AA} (left) and $R_{AA}^{N_{part}}$ (right) for charged hadron and π^0 from PHENIX (Fig. 6.10) and charged hadrons from STAR [56]. The thin solid line indicates the N_{coll} scaling, and the dashed line indicates the N_{part} scaling limit. c) suppression of the charged hadron back-to-back correlation measured by STAR [65]. d) v_2 measured by PHENIX [68] using the BBC reaction-plane method, v_2 measured by the 2 particle cumulant in $4 < p_T < 5$ GeV/c [163] and the 4 particle cumulant in $5 < p_T < 7$ GeV/c [162] by STAR. 173

6.30 Calculation of R_{AA} (a) $R_{AA}^{N_{part}}$ (b), D_{AA} (c), and v_2 (d) using a Woods-Saxon nuclear profile for I_1 (solid line), I_2 (dashed line), and I_3 (dotted line) types of jet absorption. 175

6.31 Calculation of R_{AA} (a), $R_{AA}^{N_{part}}$ (b), jet correlation (c), and v_2 (d) assuming $\epsilon \sim \rho_{coll}$. The three curves are for I_1 (solid line), I_2 (dashed line), and I_3 (dotted line) types of jet absorption, respectively. 177

6.32 Origination point distributions in the transverse plane for jets that escape from the overlap region assuming a ρ_{coll} density profile. The three panels are for I_1 (left), I_2 (middle), and I_3 (right), respectively. 177

6.33 Calculation of $R_{AA}^{N_{part}}$, jet correlation, and v_2 for a hard-sphere nuclear profile (top panels) and a cylindrical nuclear profile (bottom panels) using the I_1 (solid line), I_2 (dashed line), and I_3 (dotted line) form of jet absorption. 178

7.1 a) $dE_T/dy|_{y=0}$ per pair of participants vs. $\sqrt{s_{NN}}$ for the most central collisions (the N_{part} are almost identical for all energies). Figure taken from [13]. b) The calculated R_{AA} as function of $\sqrt{s_{NN}}$ using the Woods-Saxon nuclear profile for the I_1 type of absorption (see Eq. 6.20). 181

A.1 Correction function for the RUN-1 charged hadron analysis [52], the decrease at high p_T is a result of poor momentum resolution. 195
A.2 a) The random association background. b) The signal/background ratio. 196
A.3 Occupancy correction. Triangles are for high quality tracks, boxes are for low quality tracks, and circles represent the average efficiency. 196
A.4 a) Distance distribution between the neutron and the proton inside a deuteron. b) The momentum distribution of the nucleons inside a deuteron [176]. 198
A.5 The four centrality classes used in the $d - Au$ analysis. 199
A.6 a) NBD distribution for BBCS hits from simulation. b) The BBCS hits distribution from real data, different curves represents events with different number of PC1 hits from real data. [173]. 200
A.7 Results of NBD fits to BBCS charges for minimum bias data. Figure from [173]. 200
A.8 a) Minimum bias trigger efficiency given by measured over calculated N_{hits}^{BBCS} distribution. b) Efficiency as a function of N_{coll}. Figure from [173]. 201
A.9 N_{coll} distributions for different centrality classes.[173] 202
A.10 Relative errors introduced by different systematic errors as function of centrality for most peripheral (left panel) and for most central (right panel) collisions.[173] 203
A.11 Efficiency of the BBC trigger for π^0 (left) [29] and charged hadrons (right) [174]. 203
A.12 The background subtraction for $d - Au$ minimum bias events for a sample p_T range of $5 < p_T < 6$ GeV/c. a) conversion background subtraction for $N_{PMT} \geq 0$ tracks, b) decay background subtraction for $N_{PMT} < 0$ tracks.[154] 205

List of Tables

2.1 Summary of the PHENIX Detector Subsystems [69]. 23
2.2 A list of physics run and corresponding parameters in the PHENIX experiment. 23
2.3 Performance of Pad Chambers in RUN-2 [77, 76]. 32

3.1 Potential and diameter for different types of wires used in the drift chamber 39
3.2 The average v_d and t_0 value in RUN-2 44
3.3 The estimated average single wire efficiency for east and west arm. 49
3.4 Matching resolutions in z and r-ϕ for various detectors in RUN-1 and RUN-2. 56
3.5 The width of the α distribution for zero-field data. The error is statistical only from the fitting procedure. 62

4.1 Centrality classes, average nuclear overlap function, average number of $N-N$ collisions, and average number of participant nucleons obtained from a Glauber Monte-Carlo simulation of the BBC and the ZDC responses for $Au-Au$ at $\sqrt{s_{NN}} = 200$ GeV. Each centrality class is expressed as a percentage of σ_{AuAu} = 6.9 b. Two sets of centrality definitions are used in this analysis: a "*Fine*" set of centralities, which corresponds to 0-5%, ...,15-20%,20-30%,...,80-92%, and a "*Coarse*" set of centralities, which corresponds to 0-10%,10-20%,20-30%,...,80-92%. 75
4.2 Number of background tracks with reconstructed $p_T > 5$ GeV/c from 100000 minimum bias Au HIJING events. 87
4.3 Parameters of the electron N_{PMT} distribution from data and Monte-Carlo. R_e is later used for background subtraction. . . 93
4.4 Yield of charged pions as function of p_T with different N_{PMT}, with random background subtracted. Charged pions are selected with 2 GeV/c energy cut in EMCal. 100

4.5 The systematic error on S_R, ϵ_π, due to pion over subtraction. The first row is used in the analysis. 101
4.6 K_s^0 background relative to primary $K^\pm$ as function of reconstructed p_T for different input spectral shapes. 105
4.7 Hyperon background relative to primary $p^\pm$ as function of reconstructed p_T for different input spectral shapes. 107
4.8 Remaining K_s^0 background relative to $K^\pm$ as function of p_T for different input spectral shapes. 111
4.9 Remaining hyperon background relative to $p, \bar{p}$ as function of p_T for different input spectral shapes. 112
4.10 Systematic errors on background subtraction. All errors are given in percent and are quoted as 1σ errors. These errors are correlated with p_T. 114

5.1 Ratio data/MC for different ϕ reference ranges. 123
5.2 Multiplicity dependent efficiency for various centrality classes. 126
5.3 Systematic errors on the hadron yields. All errors are quoted as 1σ errors. They are either normalization or are p_T correlated errors, but do not dependent on centrality. 128
5.4 Systematic errors on the central/peripheral ratio. All errors are given in percent and are quoted as 1σ errors. Most of the systematic errors listed in Table. 5.3 cancel in this ratio. Only those errors that are uncorrelated with centrality are shown here. 128

6.1 Systematic errors on the charged hadron $N-N$ reference spectrum. All errors are given in percent and are quoted as 1σ errors. Most of the errors are correlated with p_T. 138
6.2 Results of the simultaneous fit to $\sqrt{s_{NN}} = 130$ and 200 GeV data using Eq. 6.14. The fit ranges are $0.03 \leq x_T \leq 0.06$ for π^0 and $0.04 \leq x_T \leq 0.074$ for charged hadron. Only statistical and point-to-point systematic errors on the data points are included in the fit, which gives the statistical error on n. The normalization errors and other p_T correlated systematic errors are not included in the fit but are directly translated into a systematic error on n. 149
6.3 Glauber parameters calculated for a Woods-Saxon nuclear profile. 170

A.1 The comparison between different charged hadron analysis. . . 194
A.2 Upper bounds of the systematic error on the p_T dependent single particle correction function. This error table is taken from [52]. 197

A.3 $\langle N_{coll} \rangle$ and it errors and BBC trigger bias (see following discussion) for minimum bias collisions and the four centrality classes shown in Fig. A.5.[173] 202
A.4 Lists of all systematics uncertainties for charged hadron spectra in $d - Au$ collisions. All errors have been estimated as full extent errors. The total errors are the quadrature sum of all errors sources. To derive 1σ errors, all values should be divided by 1.73. 205

Chapter 1

Introduction

1.1 Quark Gluon Plasma and RHIC

Quantum-Chromo-Dynamics (QCD) is the fundamental theory that describes hadron-hadron collision on the fm scale. According to this theory, quarks and gluons (partons) are the basic building blocks of the hadrons, and gluons are the carriers of strong interaction. One of the key features of QCD is asymptotic freedom [1] due to the "anti-screening" feature of the QCD vacuum. According to asymptotic freedom, the coupling strength decreases with the increase of 4-momentum transfer (Q^2) of an interaction. One consequence is that interactions with Q^2 larger than a few GeV^2 can be calculated within the theory using the perturbation method, which allows its experimental verification in e.g. deep inelastic scattering. On the other hand, on a low energy scale (or large distance) , e.g. within hadrons, the coupling among partons is strong and the perturbation method is invalid. The only known non-perturbative method to compute QCD predictions in this regime from first principles is by simulations of lattice gauge theory [2], whose results are starting to give a quantitative description of the hadron spectrum.

At a critical temperature T_c ∼155-175 MeV, Lattice QCD predicts a phase transition to a deconfined phase of quarks and gluons. At the same temperature the weakly broken chiral symmetry, responsible for the existence of light pions, gets restored. Matter at this temperature, where partons are "deconfined", i.e. not confined together by the QCD force, is called Quark-Gluon-Plasma (QGP). Such a state of matter was realized in the early universe, a few μs after the "Big Bang". As the universe expanded and cooled down, the distance between partons grows. However, the binding force between partons increases, a phase transition eventually happens, when partons combine with each other, and colorless hadrons are formed.

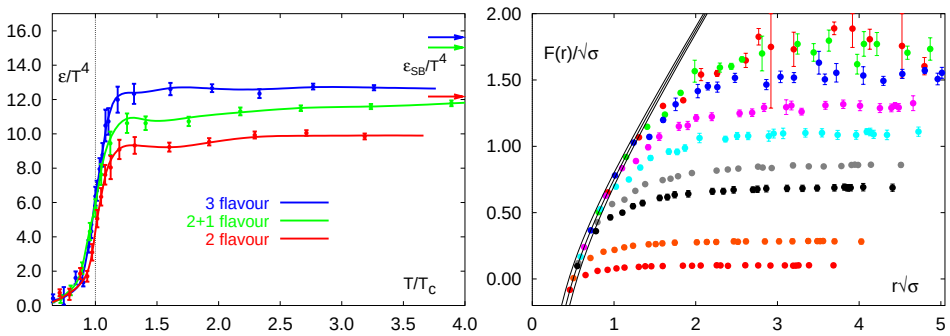

Figure 1.1: a) The energy density versus temperature calculated with improved staggered fermions on the lattice [3]. b) Static quark free energy for $N_f = 3$ at temperatures corresponding to T/Tc =0.58, 0.66, 0.74, 0.84, 0.9, 0.94, 0.97, 1.06 and 1.15 (from top to bottom) [5]. $F(r)$ is the free energy, $\sqrt{\sigma}$ is the string tension. Solid line is the $T = 0$ limit.

Fig. 1.1a shows the energy density as a function of temperature as calculated from Lattice QCD [3]. Current calculations indicate that the transition happens around a critical temperature $T_c = 155-175$ MeV, which corresponds to an energy density $\epsilon_c = 0.3-1.0$ GeV$/fm^3$ [3, 4]. Fig. 1.1b shows the Lattice QCD calculation of the temperature dependence of the heavy quark potential for 3 flavor QCD. Clearly, as the temperature exceeds the critical temperature T_c, the quark binding potential deviates from the vacuum potential and decrease zero, indicating that the interaction among partons becomes very weak above the critical temperature T_c.

The predicted QGP and its phase transition to hadronic matter can be realized in the laboratory by colliding high energy heavy nuclear ions, either in a fixed-target experiments like in the heavy-ion programs at the AGS and the SPS or in collider experiments at the RHIC and LHC. Energy is deposited in the overlap region of the two colliding nuclei, and is distributed among quarks and gluons that potentially form a QGP. However, due to the confining property of the QCD vacuum, the quarks and gluons are not directly measurable. Instead, experiments have to rely on the indirect observables that are sensitive to the transient QGP state. For this reason, the existence of the QGP can only be proved by a collection of indirect evidence from many observables. These observables include: dilepton production, J/Ψ production, photon production, radial and elliptic flow, the Hanbury-Brown-Twiss effect, strangeness production, and jet quenching. A detailed discussion of the relation of these

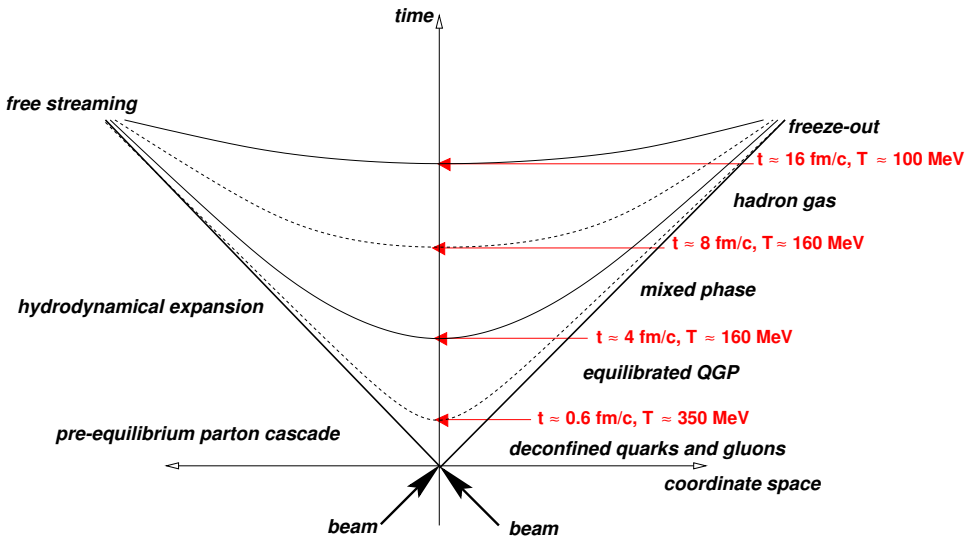

Figure 1.2: Space-time picture of a nucleus-nucleus collision. The times and temperatures for different phases are taken from [7].

observables to QGP formation can be found in [2, 6].

The evolution of the medium created in ultra-relativistic heavy-ion collisions may be viewed as evolving through the following stages as shown by the space-time diagram with the longitudinal coordinate z and the time coordinate t, as shown in Fig. 1.2,

1. pre-equilibrium:

   Parton-parton scattering happens. A large amount of energy is deposited in a space-time volume, the energy density is so high that the ground state of matter is in deconfined phase. The matter initially may not be in thermal equilibrium. It's dynamics can be described by a cascade of freely colliding partons.

2. chemical and thermal equilibrium of partons.

   Subsequent multiple scattering brings the matter to local equilibrium at the proper time τ_0, and the plasma then evolves according to hydrodynamics, with the possible formation of a mixed phase of QGP and hadron gas.

3. hadronization and freeze-out

As the plasma expands, its temperature drops. As it reaches T_c the plasma hadronizes. The hadrons keep interacting until the falls below the freeze-out temperature, and hadrons steam out of the collision region.

At AGS and SPS energies (center-of-mass energy $\sqrt{s_{NN}}$ = 4-20 GeV), despite suggestive hints [8], the experiments could not establish the creation of a QGP in the laboratory. Model calculations indicate that energy densities on the order of $\epsilon \approx 1-5$ GeV$/fm^3$ and temperatures on the order of $T \approx 140-200$ MeV have been achieved [6]. However, the size and lifetime of a partonic state could be too small to reach equilibrium. With the commissioning of the Relativistic Heavy-Ion Collider (RHIC) in June 2000, Au beams colliding with up to $\sqrt{s_{NN}} = 200$ GeV have been realized. The amount of energy available for creating a QGP is dramatically increased and a plasma that lasts as long as 4-5 fm$/c$ might be feasible [9].

In high energy nucleon-nucleon ($N-N$) collisions, e.g. at RHIC energy, the inelastic $N-N$ cross section is about 80% of the total cross section. A large fraction of the nucleon energy is deposit in the vicinity of mid-rapidity and subsequently carried away by pions. In one relativistic $Au-Au$ collisions at RHIC, many inelastic $N-N$ collisions occur, while the two colliding nuclei pass through each other in a very short time due to lorentz contraction. Thus, a large amount of energy is deposited in a small region of space during a very short time period. The spacial energy density (ϵ) in a relativistic collision can be estimated according to Bjorken [10] as:

$$\epsilon_{bj} = \frac{\langle E_T \rangle}{\tau_0 \pi r_0^2 A^{2/3}} dN/dy \qquad , \tag{1.1}$$

where $\tau_0 = 1fm/c$ is the typical formation time, $r_0 = 1.18fm$ is the nucleon radii, A is the number of participating nucleons, $\langle E_T \rangle$ is the mean transverse energy and dN/dy is the rapidity density of the multiplicity. In central collisions, the Bjorken energy density is estimated accordingly as ~ 2.9 GeV$/fm^3$ at SPS ($\sqrt{s_{NN}} = 17.2$ GeV) [11] and ~ 5 GeV$/fm^3$ at RHIC ($\sqrt{s_{NN}} = 200$ GeV) [12, 13]. These energy densities exceed the critical density at T_c, which is ~ 1 GeV$/fm^3$[4].

1.1.1 Collision Geometry for Heavy-Ion Collisions

A nucleus is an object composed of many-nucleons. The nucleon distribution inside the nucleus can be described by the Woods-Saxon density profile:

$$\rho(r) = \frac{\rho_0}{1 + e^{\frac{r-R}{a}}} \tag{1.2}$$

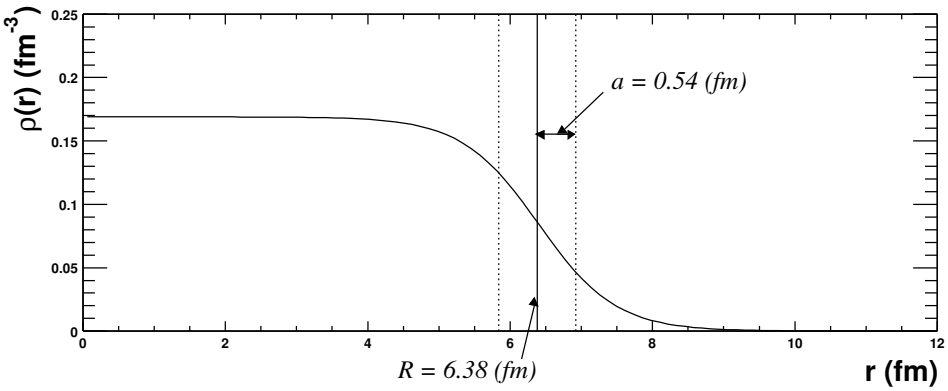

Figure 1.3: Woods-Saxon nuclear density profile for Au.

with

$$\begin{aligned} R &= (1.12A^{1/3} - 0.86A^{-1/3})fm \\ \rho_0 &= 0.169/fm^3 \\ a &= 0.54fm \end{aligned} \tag{1.3}$$

which gives $R = 6.40fm$ for a Au nucleus which is very close to 6.38 fm, the measured value from eA scattering [14]. a is called the diffusivity, and controls the thickness of the nucleus skin. The density profile for a Au nucleus is shown in Fig. 1.3. The integral $\int_0^\infty \rho(r)4\pi r^2 dr = 197$, is the total number of nucleons in a Au nucleus.

There are several general aspects regarding relativistic nucleus-nucleus $(A - A)$ collisions that are worth to point out. First, due to the large size of the nucleus, "*multiple scattering*" occurs, where a nucleon in one nucleus may collide with many nucleons in the other nucleus. In this process, an enhanced fraction of the initial energy carried by nucleons is deposited in the collision region. Meanwhile, nucleons lose energy and slow down. Second, as illustrated in Fig. 1.4, only the nucleons in the overlap region of the two nuclei participate in the collisions. These nucleons are usually called "*participants*" or "*wounded nucleons*", the rest that do not participate in the collision are called "*spectators*". The overlap region has a preferred direction, which is represented by the vector,$\vec{b}$, that connects the centers of the nuclei. The magnitude of $\vec{b}$ is referred to as the "*impact parameter*", which controls the size of the overlap region and the number of participants and, consequently, represents the "*centrality*" of the collision. The plane defined by the beam axis

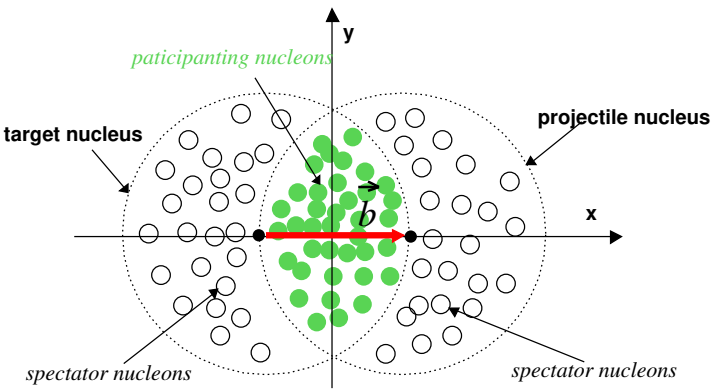

Figure 1.4: An illustration of the collision geometry for a non-headon nucleus-nucleus collision.

(z) and $\vec{b}$ is called "*reaction plane*", which represents the relative orientation of the colliding nuclei. Furthermore, depending on the underlying scale of the physical process, the nucleon-nucleon collisions may or may not be independent from each other. Processes involving large 4-momentum (Q^2) transfer, so called "*hard scattering*" processes, usually have a small cross section. For these processes, all nucleon-nucleon collisions are assumed to be independent of each other. Thus the cross section for hard scattering process should scale with the number of binary collisions, N_{coll}, among the participating nucleons. On the other hand, the production of soft particles is proportional to the amount of energy deposited in the overlap region, which is proportional to the number of participating nucleons, N_{part}.

The dynamics in nucleus-nucleus ($A-A$) collisions is complicated. The nucleons experience multiple scattering, and these scatterings are not independent of each other. The produced particles do not freely escape from the collision zone like in a $N-N$ collision. They have to traverse and interact with the medium created in the overlap region. Before we can understand the effects of the medium created in $A-A$ collisions, it is necessary to have a baseline to compare to. This baseline is provided by data from $N-N$ collision extrapolated to $A-A$. The Glauber model [15] provides a way to describe a high-energy heavy-ion collisions starting from $N-N$ collisions. The purpose of this model is not to try to describe the dynamics of the collision, but rather to describe the scaling behavior of the physics processes expected from the underlying collision geometry, in the absence of medium effects. It is based on

the concept of a mean-free path with the assumption of an elementary nucleon-nucleon cross section, σ_{nn}. A nucleon is assumed to travel on a straight line trajectory, independent of how many other nucleons it interacts with.

The quantities that characterize the collision geometry are number of binary collisions N_{coll}, number of participating nucleons N_{part}, the nuclear overlap function T_{AB}, and the eccentricity Ecc.[1] These quantities can be calculated analytically, see e.g. [2]. To relate the centrality classes defined in an experiment with those calculated in a Glauber model, one often assumes that the multiplicity dN/dy, and Glauber variables, N_{part} are proportional

$$\frac{dN}{dy} \propto N_{part}, \tag{1.4}$$

This is approximately correct at SPS energies [16], where the bulk particle production is dominated by soft processes that are usually proportional to N_{part} [2]. However, at RHIC energies, processes that violate N_{part} scaling become important. More realistic relations can be established from various models [18, 19, 20] that combine Glauber model with the details of the collision dynamics. For example, the HIJING model [18] assumes a two component modelling of the multiplicity,

$$\frac{dN}{dy} \propto (1-x)N_{part} + xN_{coll} \quad , \tag{1.5}$$

and KLN [20] predicts an increase faster than N_{part}

$$\frac{dN}{dy} \propto N_{part} log\left(\frac{Q_s^2}{\Lambda_{QCD}^2}\right) \quad . \tag{1.6}$$

where Q_s^2 is the saturation scale, which increases with N_{part}.

Experimentally, additional smearing effects due to limited detector acceptance and detector resolution have to be taken into account. For this reason, Glauber model calculations in a Monte-Carlo framework including simulations of detector effects are more robust than analytic calculations. We will discuss the implementation of the Glauber model for PHENIX in more detail in Chapter 4.1.3.

---

[1] The definition of these quantities and their relations can be found in Appendix B.

[2] The so called "wounded nucleon model", see [17].

1.2 Hard-scattering as Probe for QGP

One of the probes for quark matter is the so called "*hard-scattered*" partons, referring to partons scattered with large 4-momentum transfer (Q^2). At collider energies similar to RHIC, the importance of hard or semi-hard parton scattering is clearly seen in high-energy $p-p$ and $p-\bar{p}$ collisions [21]. They are also expected to be important in heavy-ion collisions at RHIC energies. These hard scatterings happen on a very short time scale and their production rates are calculable in perturbative QCD. If dense partonic matter is formed during the initial stage of a heavy-ion collision with a large volume and long life time (relative to the confinement scale $1/\Lambda_{QCD}$), the high p_T partons produced will interact with this dense medium and, according to theoretical studies [21, 22], will lose energy via induced gluon radiation. Unlike energy loss in QED, the radiative gluon energy loss per unit length dE/dx not only depends on the color charge density and momentum distribution of the medium, but also linearly depends on the thickness of the medium, due to the non-Abelian nature of gluon radiation in QCD [23, 24]. Thus the energy loss in a dense matter could be large, up to several GeV/fm. It softens the hard-scatted partons and effectively reduces the high p_T hadron yield, an effect known as "*jet quenching*". Therefore, the study of parton energy loss can directly probe the properties of the dense matter in the early stage of heavy-ion collisions.

1.2.1 Hard-scattering in $N-N$ Collisions

In nucleon-nucleon collisions, the standard perturbative QCD (pQCD) calculations of hard scattering processes rely on so called factorization theorems [25], which provides a way to separate long-distance non-perturbative effects from short-distance perturbative effects. Hard scattering is described by the lowest-order subprocesses which, for high-p_T particles, corresponds to a convolution of two-body scattering. This is shown schematically in Fig. 1.5. The corresponding expression for the inclusive particle production cross section in nucleon-nucleon collisions can be written as,

$$\begin{aligned}\frac{d\sigma^{NN}}{dyd^2p_T} &= \sum_{abcd}\int dx_a dx_b d^2k_{aT} d^2k_{bT} g_p(k_{aT},Q^2) g_p(k_{bT},Q^2) \\ &\quad f_{a/p}(x_a,Q^2) f_{b/N}(x_b,Q^2) \frac{D^0_{h/c}(z_c,Q^2)}{\pi z_c} \\ &\quad \frac{d\sigma}{d\hat{t}}(ab\to cd)\delta(\hat{s}+\hat{t}+\hat{u}),\end{aligned} \tag{1.7}$$

where $f_{a/p}(x_a, Q^2)$ is the parton distribution function, $D_{h/c}$ is the fragmentation function, and $\frac{d\sigma}{dt}$ is the parton-parton cross section. $N-N$ collisions are simply treated as the incoherent summation of all possible constituent scatterings, each weighted by the appropriate parton distribution and fragmentation functions. Parton distribution functions and fragmentation functions contain long-distance non-perturbative effects, and can be measured in other hard processes, e.g. e^+e^- and ep collisions.

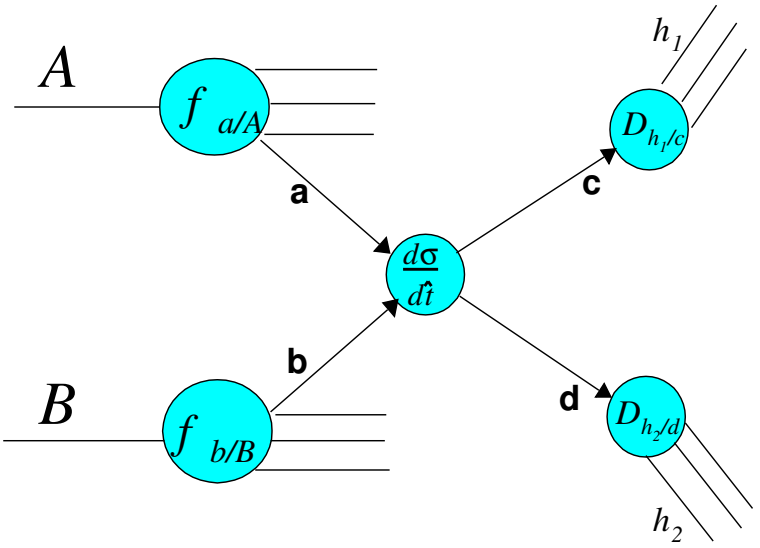

Figure 1.5: Schematic representation of a high-p_T reaction factorized into parton distribution functions (f), parton fragmentation functions (D), and a hard-scattering subprocess.

The pQCD calculations are rather successful in describing high p_T particle production in high-energy $N-N$ collisions [25, 26, 27, 28, 29]. As an example, Fig. 1.6 shows the π^0 spectra measured by PHENIX in $p-p$ collisions at $\sqrt{s} =$ 200 GeV/c [29], together with a next leading order pQCD calculation [30, 31, 32] based on the factorization theorem. These calculations are consistent with the data down to $p_T \sim 2$ GeV/c, indicating that the particle production is dominated by the fragmentation of hard-scatted partons and the production rate is well calibrated.

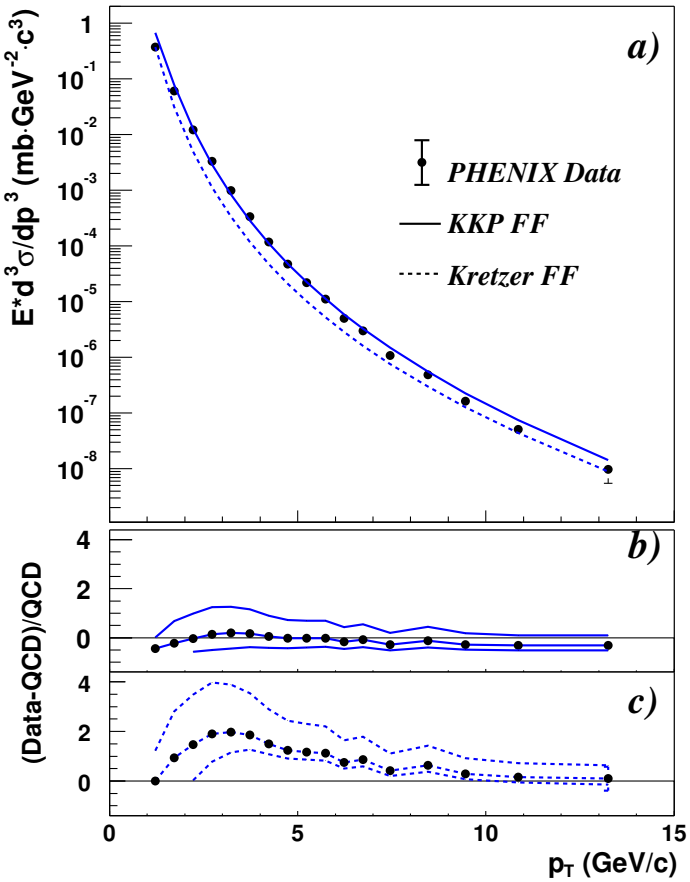

Figure 1.6: a) The invariant differential cross section for inclusive π^0 production (points) and the results from NLO pQCD calculations using the "KKP" [31](solid line) and "Kretzer" [32] (dashed line) sets of fragmentation functions. b,c) The relative difference between the data and the theory using KKP (b) and Kretzer (c) fragmentation functions with scales of $p_T/2$ (lower curve), p_T, and $2p_T$ (upper curve). This figure is taken from [29].

1.2.2 Hard-scattering as a Probe in Heavy-Ion Collisions

Hard-scattering scaled to Heavy-ion Collisions

Similar to $N-N$ collisions, the inclusive cross section for high p_T particle production in heavy-ion collisions is also given by single hard parton-parton

two-body scattering. The factorization theorem can be directly extrapolated to heavy-ion collisions. Naively, the hard-scattering cross section is proportional to the number of binary scaled $N-N$ collisions, N_{coll},

$$\frac{dN^{AA}}{dyd^2p_T} = \langle N_{coll}\rangle \frac{dN^{NN}}{dyd^2p_T} \tag{1.8}$$

Thus, the total hard-scattering cross-section for minimum bias $A-A$ collisions is related to that for $N-N$ collisions (Eq. 1.7) by,

$$\frac{1}{\sigma^{AA}_{inel}}\frac{d\sigma^{AA}}{dyd^2p_T} = \frac{\langle N_{coll}\rangle}{\sigma^{NN}_{inel}}\frac{d\sigma^{NN}}{dyd^2p_T} \tag{1.9}$$

Final State Jet Quenching

At the center-of-mass (c.m.) energy reached at RHIC, a bulk medium spanning a few hundred of fm^3 with energy density exceeding several GeV/fm^3 [12, 13] can be created 0.3-1 fm/c after the colliding nuclei pass through each other. This matter will leave its footprint on the properties of the experimentally observed particles. In particular, the energy loss of hard scattered partons should lead to a depletion or suppression of the high p_T hadron yields [3]. This suppression is quantified by the so called "*nuclear modification factor*" R_{AB}, which is defined by the ratio of the yield in nucleus-nucleus collisions to the yield in nucleon-nucleon collisions, normalized by the average number of independent nucleon-nucleon collisions in $A-B$ collisions, $\langle N_{coll}\rangle$.

$$R_{AB}(p_T,\eta) = \left(\frac{1}{N_{evt}}\frac{d^2N^{AB}}{dp_Td\eta}\right) / \left(\frac{\langle N_{coll}\rangle}{\sigma^{NN}_{inel}}\frac{d^2\sigma^{NN}}{dp_Td\eta}\right) \tag{1.10}$$

If there are no medium effects, this ratio should be 1. If jet energy losses strongly suppress the high p_T hadron yield, this ratio will be much smaller than 1. By studying the p_T, system size and $\sqrt{s_{NN}}$ dependence of R_{AB}, one may learn how the final state medium modifies the hard partons and thus deduce the properties of the medium.

Jet quenching is a final state effect, which happens after the hard parton-parton scattering. The modifications of jets in the final states are complicated by other nuclear effects in heavy-ion collisions which also affect the R_{AB} value. Although the fundamental QCD parton-parton processes are the same as in nucleon-nucleon case, the initial state of the matter in a nucleus

[3] High p_T hadron suppression is probably the most interesting discovery in the first three years running of RHIC [50, 51, 52, 53, 56, 55].

prior to parton-parton scatterings can be significantly modified compare to those in $N-N$ collisions. The main initial state effects are "k_T *broadening*" or "*Cronin effect*" [33], "*parton shadowing*" [34, 42] and more recently proposed"*Gluon saturation*" effect [36, 37]. These nuclear effects can modify the initial hard-scattering processes such that the high p_T hadron production rates are affected. In order to study the property of QGP using hard-scattering partons as probe, it is very important to understand these initial state effects present in heavy-ion collisions.

Initial State Effects

- The Cronin effect [33] from initial state multiple scattering

  Due to the finite thickness of heavy nuclei, a parton may suffer multiple soft scatterings while travelling through the nuclear matter before the final hard parton-parton scattering. This is illustrated in Fig. 1.7. The initial partons in general have small transverse momenta but large c.m. energies. The soft scatterings increase the transverse momenta of the partons, and can be treated as an effective broadening of the initial transverse momentum k_T of the beam partons. This so called Cronin effect [33] leads to a smearing of the p_T spectra. Since the particle production cross section falls steeply towards high p_T, this smearing effect leads to an enhancement of particle production typically around 1.5-4 GeV/c compared to $N-N$ collisions [38]. The hadron yield,

  $$E\frac{d\sigma^{pA}}{d^3p} = E\frac{d\sigma^{pp}}{d^3p}A^{\alpha(p_T)} \tag{1.11}$$

  scales faster than the nucleon number A at $p_T \gtrsim 2$ GeV/c, i.e $\alpha(p_T) > 1$. This was first observed by James Cronin [33] and indicates such an enhancement. The Cronin effect can be studied in $p-A$ or $d-A$ collisions.

- Initial state deformation of parton distribution functions of nuclei

  Since the incoming nuclei are large, the composite nucleons wave functions can interact coherently among each other. The results from deeply inelastic lepton-nucleus scattering (DIS) [34] indicate clearly that the parton distribution function of the bound nucleons, are different from those of the free nucleons, $f_{i/A}(x,Q^2) \neq f_{i/n}(x,Q^2)$. These initial state

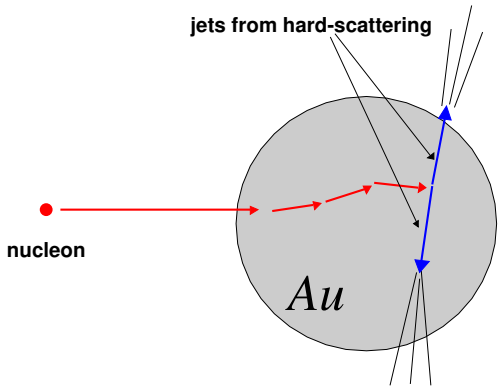

Figure 1.7: A Schematic view of k_T broadening before hard-scattering.

nuclear effects can be quantified by the ratio of the parton structure functions of nuclei relative to deuterons $R_{F_2}^A = F_2^A(x,Q^2)/F_2^D(x,Q^2)$ and are also shown in Fig. 1.8: Shadowing ($R_{F_2}^A \leq 1$) at $x \lesssim 0.1$, anti-shadowing ($R_{F_2}^A \geq 1$) at $0.1 \lesssim x \lesssim 0.3$, EMC effect [39] ($R_{F_2}^A \leq 1$) at $0.3 \lesssim x \lesssim 0.7$, and Fermi motion ($R_{F_2}^A \geq 1$) towards $x \to 1$ and beyond. Recent measurements also revealed a Q^2 dependence of $R_{F_2}^A$ at small value of x [35]. According to LO QCD, the parton structure function F_2 is directly related to the parton distribution function as, $F_2 = \sum_i e_i^2 x f_i(x,Q^2)$. So the same nuclear effects for parton structure function also applies to the parton distribution function.

Assuming that the leading hadron on average carries half of the parton energy, the high p_T range from 2-10 GeV/c, currently accessible at RHIC, corresponds to x range of 0.04-0.2, which is at the shadowing region. The nuclear shadowing refers to the suppression of the nuclear structure function relative to a sum of free nucleon structure function (see in Fig. 1.8) at small x. This suppression is caused by the coherent multi-gluon interaction at small x, where the gluon density becomes very large [42].

- Gluon Saturation - Strong Shadowing Limit

Nuclear shadowing effects increase for smaller x and larger nuclei, and at certain small x, QCD analysis suggests that gluon density saturates

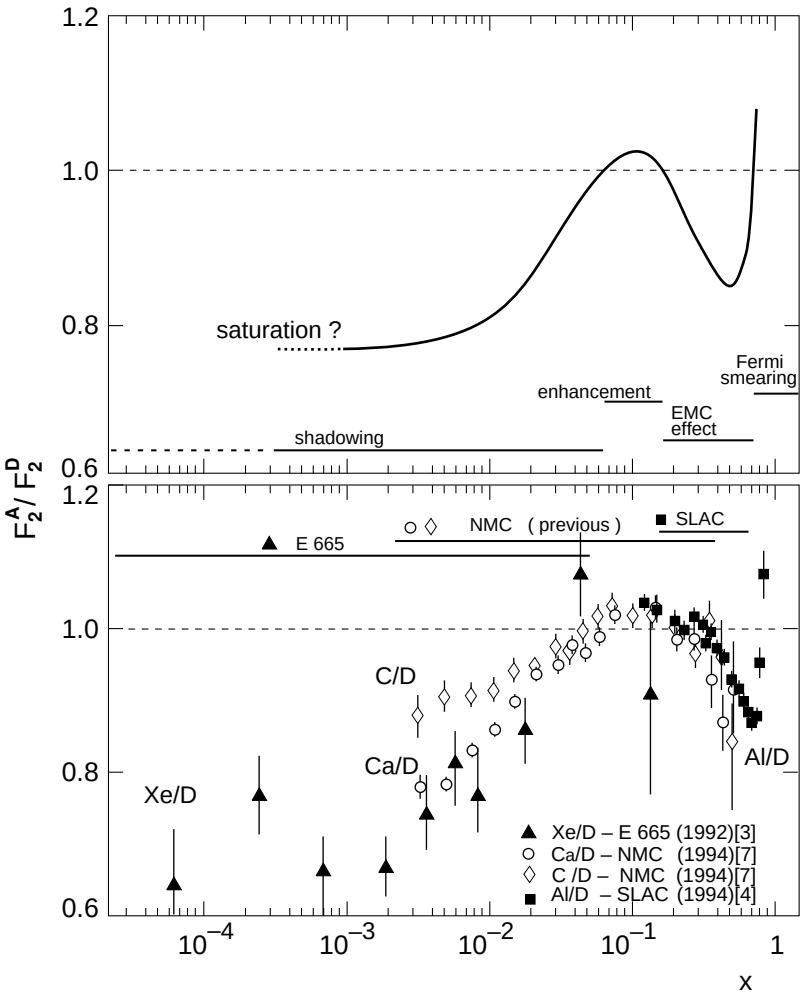

Figure 1.8: a) Schematic view of the structure function, F_2^A/F_2^D. b) Partial compilation of results for F_2^A/F_2^D (from [41]). Note that below $x \approx 0.01$, the average Q^2 value of the data is smaller than 2 GeV^2.

as a result of non-linear corrections to DGLAP evolution [42], an effect also found in classical Yang-Mills models [43]. Due to soft gluon bremsstrahlung of hard valence partons, the total parton density increases rapidly with decreasing x. However, parton recombination, $gg \rightarrow g$, and screening effects become important and eventually "saturate" the rapid growth of parton density at certain x. A "*saturation scale*", which is proportional to the gluon density per unit area and grows as

$Q_s^2 \sim A^{1/3}/x^\delta (\delta \approx 0.2 - 0.3)$, determines the critical values of the momentum transfer at which the parton systems becomes dense and recombination happens (see Fig. 1.9). Both the shadowing and saturation effect are present in large nuclei and can be studied in $e-A, p-A, d-A$ collisions.

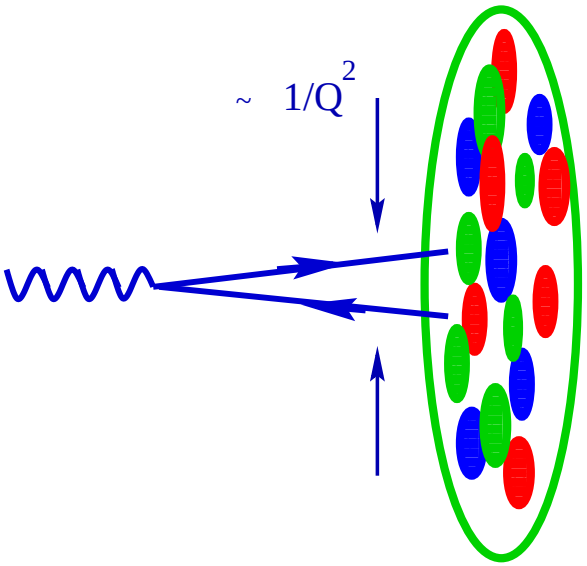

Figure 1.9: parton interacting with the nuclear target resolves the transverse area $\sim 1/Q^2$ and, in the target rest frame, the longitudinal distance $\sim 1/(mx)$ [44], where m is the parton mass.

Factorization Theorem in Heavy-ion Collisions

The factorization theorem including initial state nuclear effects and final state jet quenching can be written as [9]:

$$\begin{aligned}\frac{d\sigma^{AB}}{dyd^2p_T} &= K\sum_{abcd}\int d^2bd^2rt_A(r)t_B(|\mathbf{b}-\mathbf{r}|)\int dx_a dx_b d^2k_{aT}d^2k_{bT} \\ &\quad g_A(k_{aT},Q^2,r)g_B(k_{bT},Q^2,|\mathbf{b}-\mathbf{r}|)f_{a/A}(x_a,Q^2,r)f_{b/B}(x_b,Q^2,|\mathbf{b}-\mathbf{r}|) \\ &\quad \frac{D_{h/c}(z_c,Q^2,\Delta L)}{\pi z_c}\frac{d\sigma}{d\hat{t}}(ab\to cd),\end{aligned} \tag{1.12}$$

where t_A is the nuclear thickness function, g_A takes into account the k_T broadening, $K \approx 1.3-2$ is used to account for higher order pQCD correction, $f_{a/A}$ is the parton distribution function in nuclei, z_c is the fractional momentum of the hadron relative to the fragmenting parton c, and $D_{h/c}(z_c, Q^2, \Delta L)$ is the modified effective fragmentation function for produced parton c which has to travel an average distance ΔL inside a dense medium, this term includes parton energy losses in the final state.

The philosophy underlying the study of high p_T physics in heavy-ion collisions in the quest for a QGP is simple. The results measured in complicated heavy-ion collisions can only be interpreted based on the understanding obtained from simpler system like $p-p$, e^+-e^-, $p-A$, and $e-A$. On the one hand, characteristics of hard-scattered partons are rather well understood in $p-p$ and e^+e^- collisions, they can be used as a calibrated probe for heavy-ion collisions. On the other hand, the knowledge learned from $e-A$ and $p-A$ collisions about the nuclear parton distributions and k_T broadening can help us to fix the initial conditions prior to the hard-scattering processes in heavy-ion collisions. By combining this knowledge with the measurements of jet production in heavy-ion collisions, one expects to disentangle various nuclear effects, and learn about the modifications of jets in the medium in the final state.

1.3 High p_T Observables

In this work, we focus on high p_T observables. The hard-scatted partons can be used as a probe for the dense medium created in heavy-ion collisions. However, the constituents that interact with the medium, partons, can not be observed directly. Experimentally, we have to rely on hadrons from parton fragmentation that carry the reminiscent information about the original partons. The fragments (or jet) from a high energy parton usually have a very small angular spread and focus around the "*leading particle*" which carries the major fraction of the energy of the original parton. In high energy elementary collisions, where the event multiplicity is low, these jets of particles can be directly identified by applying an energy cut on a cluster of particles that falls within small cone, $\Delta r = \sqrt{(\Delta\eta)^2 + (\Delta\phi)^2}$ [45, 46, 47]. This method works well for events containing only a few separated jets. However, in heavy-ion collisions, the soft background and multi-jet production makes it impossible to identify jets directly. The amount of total energy from the soft background in a typical jet finding cone of $\Delta r = 0.7$ [45] is 100 GeV at RHIC. Experimentalists have to rely on indirect methods to characterize the jet yield and shape in heavy-ion collisions. Right now, there are two statistical methods to extract information on jet production: single hadron high p_T spectra, and two particle correlation. Since hadrons with $p_T > 2$ GeV/c are dominantly from leading hadrons from jet fragmentation, the first method measures the yield of semi-hard and hard jets. Since the jet fragments are focused in a small cone, they are highly correlated in angular space. By correlating the leading particle with soft particles, one can learn the shape of the jet fragmentation.

The results obtained so far from RHIC have proven that these two ob-

servables are extremely useful to probe the dense medium. I will discuss them separately in the rest of this section.

1.3.1 Suppression of High p_T Hadrons

At the energies reached at the RHIC, hard scattering rate becomes sufficiently large. Due to the large Q^2, the hard-scattered partons are created early in the collisions, at times $\delta\tau \sim 1/m_T\ fm/c$ (m_T is the transverse energy of the parton, so $\delta\tau \sim 0.2fm$ for 1 GeV/c parton), while most of the partons of the plasma with temperature T form and equilibrate at later times $\sim 1/gT \sim 0.5$ fm/c [48]. The hard scattered partons propagate along approximately straight eikonal lines through the plasma until $\tau \sim R \sim 5$ fm/c in central $Au - Au$ collisions. Thus these partons may directly probe the subsequently produced hot, dense, and strongly interacting medium. When an energetic parton propagates through a QGP, it suffers both elastic energy losses from simple scatterings and radiative energy loss due to induced radiations from multiple scatterings. The elastic energy loss of partons in a QCD plasma of temperature $T \sim 300$ MeV is small ($dE/dx < 0.5GeV/fm$ for a quark jet with E=30 GeV [49]). However, due to the non-Abelian nature of gluon radiation in QCD, the radiative gluon energy loss, dE/dx, depends linearly on the thickness of the medium, and could be much larger than the elastic energy loss. Jet quenching due to gluon radiation in QGP should become observable as a suppression of high p_T hadron yields in heavy-ion collisions.

The suppression is usually quantified through R_{AB} defined in Eq. 1.10. Initial measurements of hadron p_T spectra in $Au - Au$ collisions at $\sqrt{s_{NN}} =$ 130 GeV have indeed demonstrated a substantial suppression of hadron yields per nucleon-nucleon collision relative to pp data [50, 51, 52]. Data from $\sqrt{s_{NN}}$ = 200 GeV confirm these results [53, 54, 56]. The suppression is observed in central but not in peripheral collisions. These observations points towards strong medium effects, which are confirmed quantitatively in several model calculations that include parton energy loss in dense matter [58, 57].

A very different interpretation of the suppression observed in central $Au - Au$ collisions is based on the initial-state gluon saturation effects [59] which was introduced in Chapter 1.2.2. Saturation effectively modifies the parton distribution function such that the number of hard scatterings and consequently the high p_T hadron yield is reduced. In Ref. [59], it was proposed that gluon saturation phenomena alone may account for a significant part of the observed high p_T hadron suppression pattern. Current $Au - Au$ collisions can not unambiguously distinguish between these two scenarios. Fortunately, like other initial-state effect, saturation is expected to be present in $d - Au$

collisions and should result in a $\sim 30\%$ suppression in minimum bias $d-Au$ collisions [59]. Recent results from $d-Au$ collisions at $\sqrt{s_{NN}} = 200$ GeV thus provide an unique opportunity to determine experimentally the modification, if any, of high p_T hadron yields due to initial state nuclear effects for a system in which a hot, dense medium is not produced in the final state.

In addition to hadron suppression, an unexpectedly large fraction of baryons has been observed in central $Au-Au$ collisions for p_T up to 4–5 GeV/c [60, 61, 62], which complicates the interpretation of the high p_T results. The observed ratio of baryons to mesons from PHENIX [61] is inconsistent with jet fragmentation in $p-p$ [27] and e^+e^- collisions [63]. While the origin of this effect is unclear, it could point towards bulk particle production ("soft physics") contributing to the p_T spectra out to 4–5 GeV/c. It has been suggested that coalescence of thermalized quarks combining with energy loss of hard-scattered partons can account for the unusual particle composition, which shifts the region dominated by hard-scattering to higher p_T [64].

1.3.2 Jet Angular Correlation

In heavy-ion collisions, due to the large soft backgrounds ($\sim 100 GeV/srd$), a jet signal can not be identified directly. A measurement of the jet structure has to rely on two-particle correlation methods. The results from $Au-Au$ collisions at $\sqrt{s_{NN}} = 200$ GeV reveal a significant modification of hard-scattered partons in the medium, with a strong dependence on the collision geometry. In central collisions, the jet near angle correlation strength is found to be similar to $p-p$, while the away side correlation is strongly suppressed [65]. This observation hints towards energy loss and surface emission of jets.

Meanwhile, a large elliptic flow (v_2) has been observed in intermediate centrality classes [66, 67, 68]. The v_2 results from the anisotropy of the pressure gradient in the overlap region and leads to more high p_T particles emitted into the reaction plane where the pressure gradient is larger than in the direction normal to reaction plane where the pressure gradient is the weakest. The elliptic flow produces a $cos(2\phi)$ type of correlation which peaks at 0 and 180°, similar to the jet correlation signals. As we shall discuss in Chapter. 6.7, the surface emission naturally leads to a correlation between jet emission direction and the reaction plane which mimics v_2. On the other hand, current correlation methods rely on the fit of correlation signal which can also be affected by the genuine flow. It remains a challenge for RHIC to disentangle contributions from jets and elliptic flow.

1.3.3 Collision Geometry and High p_T Observable

In relativistic heavy-ion collisions, energy is deposited in the overlap region between two colliding nuclei. The size, shape, and energy density of the medium formed in this region strongly depends on the impact parameter of the collision. The amount of medium a hard scattered parton traverses, and consequently its energy loss, varies with the centrality of the collision and also the azimuthal angle with respect to the reaction plane. If the parton energy loss is large, the surviving partons will be emitted dominantly from the surface of the overlap region. The partons moving towards the surface (near side) traverse on average less material than those going in opposite direction (away side). Thus partons scattered to the near side are likely to escape with little energy loss, while the away side partons are likely to lose significant energy and thus will be suppressed more strongly.

1.4 Organization of the Work

In this work, we present new data on inclusive charged hadron production for $0.5 < p_T < 10$ GeV/c, measured over a broad range of centrality in $Au-Au$ collisions at $\sqrt{s_{NN}} = 200$ GeV by the PHENIX Collaboration at RHIC. These data are compared to data on neutral pion production [54] and to data from $Au-Au$ collisions at $\sqrt{s_{NN}} = 130$ GeV [50, 52], all measured within the same experiment. To help in addressing the question whether the observed suppression is an initial or final state effect, we compare the results to data from $d-Au$ collisions at $\sqrt{s_{NN}}$ =200 GeV [153].

In Chapter 2, we discuss the PHENIX detectors relevant to our analysis. Chapter 3 gives a detailed account of the calibrations needed for the charged hadron analysis, focusing on the charged particle tracking and momentum measurement. Chapter 4 describes the techniques used in the data reduction, in particular the background subtraction method which is crucial to extend the charged hadron measurement to high p_T. The corrections and systematic errors on the charged hadron measurement are discussed in Chapter 5.

In Chapter 6, we first present the main results from $Au-Au$ collisions at $\sqrt{s_{NN}}$ =200 GeV, which are divided into three sections: centrality and p_T dependence of the charged hadron p_T spectra are discussed in Chapter 6.1. Chapter 6.2 focuses on the charged hadron suppression and the comparison to π^0 data. In Chapter 6.3, we discuss the $\sqrt{s_{NN}}$ dependence of both charged hadron and neutral pion production and test possible x_T-scaling. The next three sections of Chapter 6 focus on the discussion and comparison of the

$Au-Au$ results to existing theoretical models (Chapter 6.4) and $d-Au$ results (Chapter 6.5 and Chapter 6.6). In the last section of that chapter, we discuss the centrality dependence of high p_T results on the basis of a jet absorption model. We argue that the high p_T phenomena observed at RHIC are governed by the collision geometry. The calculations are compared with the centrality dependence of the high p_T hadron yield, back-to-back jet angular correlations and the azimuthal anisotropy.

In Chapter 7, we give a summary of the work and the outlook of the high p_T physics.

The charged hadron analysis techniques for $Au-Au$ collisions at $\sqrt{s_{NN}}$ = 130 GeV and $d-Au$ collisions at $\sqrt{s_{NN}}$ = 200 GeV are very similar to those for $Au-Au$ collisions at $\sqrt{s_{NN}} = 130$ GeV. We discuss briefly these two analysis in Appendix. A, focusing on their differences from that for $Au-Au$ collisions at $\sqrt{s_{NN}} = 200$ GeV.

Chapter 2

PHENIX Experiment

2.1 PHENIX Detector

PHENIX is a sophisticated detector system composed of 11 subsystems, which allows the measurement of hadrons, leptons and photons with excellent momentum and energy resolution. Another prime advantage of the PHENIX experiment is the ability to study rare physics using Level-1 and Level-2 triggers to sample events with potential physics interest at the highest luminosity expected at RHIC. The PHENIX subsystems are grouped into four spectrometer arms − two around mid-rapidity (the central arms) and two at forward rapidity (the muon arms) − and a set of global detectors. The east and west central arms are centered around rapidity zero and are instrumented to detect electrons, photons, and charged hadrons. The north and south forward arms have full azimuthal coverage and are instrumented to detect muons. Each of the four arms has a geometric acceptance of approximately 1 steradian. The global detectors measure the time and the position of the interactions, and the multiplicity of produced particles. The baseline layout of the PHENIX detector is shown in Fig. 2.1. The rapidity and azimuthal angle (ϕ) coverages, together with the physics abilities of each subsystems are listed in Table 2.1.

The PHENIX coordinates are defined relative to the beam axis, and can be easily visualized from Fig. 2.1. The origin is located at the middle point between the two Beam Beam Counter along the beam axis. In cartesian coordinate system, the z axis is along the beam axis pointing to the north muon arm. The x axis is pointing horizontally to the west arm. The y axis points upwards.

Since the commissioning of RHIC in June 2000, there have been three running periods which have delivered two $Au-Au$ physics runs, one $d-Au$ physics run and two $p-p$ physics runs. The collision species, energy, and integrated luminosity are listed in Table. 2.2. The detector setups for three

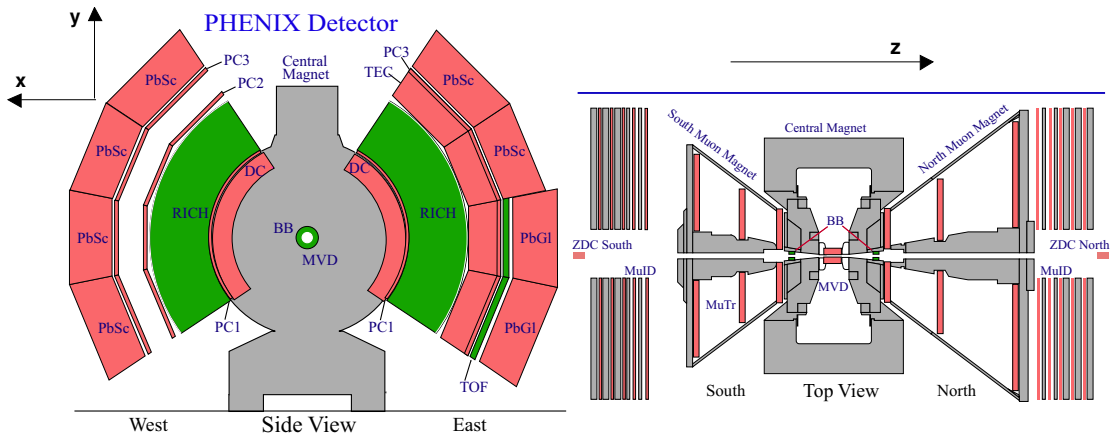

Figure 2.1: The baseline PHENIX experiment. The left panel shows the PHENIX central arm spectrometers viewed along the beam axis. The right panel shows a side view of the PHENIX muon arm spectrometers.

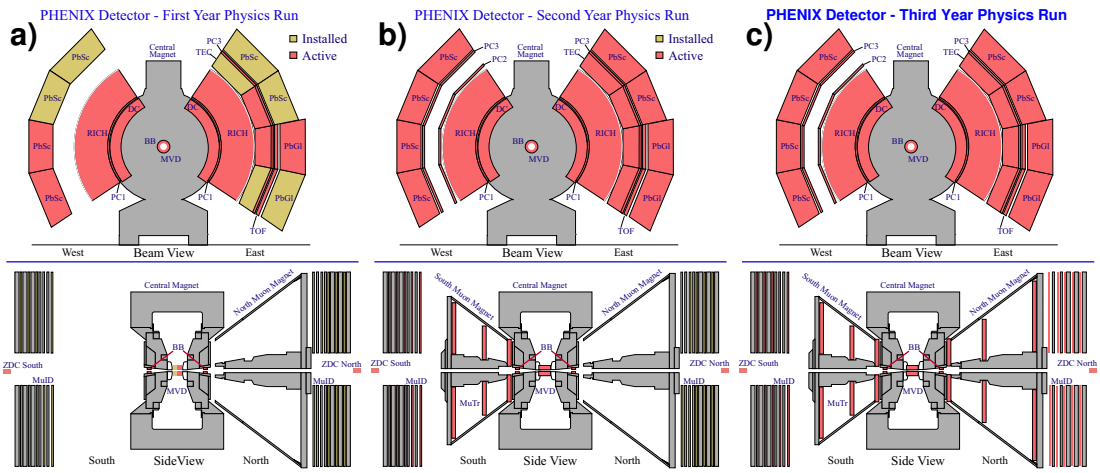

Figure 2.2: Layout for PHENIX Experiments in RUN-1 (left panel), RUN-2 (middle panel) and RUN-3 (right panel).

running periods are shown in Fig. 2.2. The charged hadron analysis discussed in the present work focuses on the data taken in the second heavy-ion run, or RUN-2. This analysis uses the global detectors and a subsets of the central arm detectors, which shall be introduced in the following.

Table 2.1: Summary of the PHENIX Detector Subsystems [69].

Element	$\Delta\eta$	$\Delta\phi$	Purpose and Special Features
Magnet: central (CM)	$\pm$0.35	360°	Up to 1.15 T·m.
muon (MMS)	-1.1 to -2.2	360°	0.72 T·m for $\eta = 2$
muon (MMN)	1.1 to 2.4	360°	0.72 T·m for $\eta = 2$
Silicon (MVD)	$\pm$2.6	360°	$d^2N/d\eta d\phi$, precise vertex, reaction plane determination
Beam-beam (BBC)	$\pm$(3.1 to 3.9)	360°	Start timing, fast vertex.
NTC	$\pm$(1 to 2)	320°	Extend coverage of BBC for p-p and p-A.
ZDC	$\pm$2 mrad	360°	Minimum bias trigger.
Drift chambers (DC)	$\pm$0.35	90°×2	Good momentum and mass resolution, $\Delta m/m = 0.4\%$ at $m = 1$GeV.
Pad chambers (PC)	$\pm$0.35	90°×2	Pattern recognition, tracking for nonbend direction.
TEC	$\pm$0.35	90°	Pattern recognition, dE/dx.
RICH	$\pm$0.35	90°×2	Electron identification.
ToF	$\pm$0.35	45°	Good hadron identification, σ <100 ps.
T0	$\pm$0.35	45°	Improve ToF timing for p-p and p-A.
PbSc EMCal	$\pm$0.35	90°+45°	For both calorimeters, photon and electron detection.
PbGl EMCal	$\pm$0.35	45°	Good $e^{\pm}/\pi^{\pm}$ separation at $p > 1$ GeV/c by EM shower and $p < 0.35$ GeV/c by ToF. $K^{\pm}/\pi^{\pm}$ separation up to 1 GeV/c by ToF.
μ tracker: (μTS)	-1.15 to -2.25	360°	Tracking for muons.
(μTN)	1.15 to 2.44	360°	Muon tracker north installed for year-3
μ identifier: (μIDS)	-1.15 to -2.25	360°	Steel absorbers and Iarocci tubes for
(μIDN)	1.15 to 2.44	360°	muon/hadron separation.

Table 2.2: A list of physics run and corresponding parameters in the PHENIX experiment.

Run	Year	Species	$\sqrt{s}$[GeV]	$\int Ldt$	$N_{events}(10^6)$
RUN-1	2000	$Au-Au$	130	$1mb^{-1}$	10
RUN-2	2001/2002	$Au-Au$	200	24 mb^{-1}	170
		$p-p$	200	0.15 pb^{-1}	3700
RUN-3	2002/2003	$d-Au$	200	2.74 nb^{-1}	5500
		$p-p$	200	0.35 pb^{-1}	6600

2.1.1 Global Detectors

The global properties of the collision used in this analysis, including the collision vertex along the beam direction, the trigger and timing information,

the impact parameter $\vec{b}$, and the charged particle multiplicity are characterized by a set of global detectors around the beam-line. These detectors include the Zero Degree Calorimeters (ZDC), the Beam Beam Counters (BBC), and the Multiplicity Vertex Detector (MVD).

The ZDCs are small transverse area hadron calorimeters that are installed at each of the four RHIC experiments with an angular acceptance of $|\theta| < 2mrad$. Each ZDC is positioned 18 m up and downstream from the interaction point along the beam axis. They are located in the beam line behind the beam bending magnets and measure the energy deposited by spectator neutrons from the collisions. Charged particles are deflected out of the ZDC acceptance by the beam bending magnets leading to a measurement of neutron energy with very low background. A single ZDC consists of 3 modules each with a depth of 2 hadronic interaction lengths, which are read out by a single PMT. Both time and amplitude are digitized for each of the 3 PMTs, and an analog sum is determined of all three PMTs for each ZDC. The energy resolution at the one neutron peak is approximately 21% [70, 71]. The coincidence neutron signal from the two ZDC can be used as a minimal bias selection for heavy-ion collisions. This makes it useful as an event trigger and a luminosity monitor [72].

The PHENIX beam-beam counters (BBC) are arrays of quartz Cerenkov detectors which measure relativistic charged particles produced in cones around each beam ($3.0 \leq \eta \leq 3.9$, with 2π azimuthal coverage). There are two identical Beam-Beam counters each positioned 1.4 m from the interaction point, just behind the central magnet poles around the beam axis. The inner(outer) radius of the BBC is 5cm(30cm), leaving about 1cm space from the beam-pipe. Each counter consists of 64 photomultiplier tubes equipped with quartz Cerenkov radiators in front. The BBC is designed to operate under various collision species (dynamic range 1-30 MIP), high radiation and large magnetic field (0.3 T). The main role of the BBC is to provide the start time for the TOF measurement, to serve as a crucial component for PHENIX Level-1 trigger, and to measure the collision vertex point (z_{vtx}). Interestingly, the large charged particle multiplicity ($\approx$1000 in central $Au - Au$ collision) in the BBC acceptance allows the measurement of the reaction plane on an event by event basis [68]. Due to the 3 units of rapidity gap from mid-rapidity, the reaction plane determined by the BBC is less sensitive to the non-flow effects [68] in the PHENIX central acceptance.

For both the ZDC and the BBC, the time and vertex position are determined using the measured time difference between the north and the south detectors and the known distance between the two detectors. The start time

(T_0) and the vertex position along the beam axis (z_{vtx}) are calculated as

$$\begin{aligned} T_0 &= (T_1 + T_2)/2 \\ z_{vtx} &= (T_1 - T_2)/2c \end{aligned} \tag{2.1}$$

where T_1 and T_2 are the average timing of particles in each counter and c is the speed of light. In Run-2, with an intrinsic timing resolution of 150 ps, the ZDC vertex is measured with a resolution of 3 cm, while the BBC timing resolution of 40 ps results in a vertex position resolution of 0.6 cm [73].

Since the multiplicity of both the neutrons in the ZDC and the charged particles in the BBC are correlated with the collision geometry, they can also be used to measure the collision centrality (impact parameter $|\vec{b}|$). While the ZDCs measure forward neutrons that result from fragmentation of the colliding nuclei(mostly spectators), the BBCs are sensitive to charged particles produced in the collisions (produced by participants). Together, both detectors yield information on the impact parameter of the nuclear interaction. These observables, combined with a Glauber model for the collision geometry, allow us to determine different centrality classes. The details on a Glauber simulation in PHENIX are discussed in Chapter 4.1.3.

2.1.2 The Central Arm Detectors

Each of the west and the east central arm spectrometers covers the pseudorapidity range $|\eta| < 0.35$ and 90 degrees in azimuthal angle ϕ. As shown in the upper panel of Fig. 2.1, each of the spectrometers consists of layers of tracking and particle identification subdetectors. Viewed from the inner radius outward, the west arm spectrometer is composed of Drift Chamber (DC) at 2-2.4m, Pixel Pad Chambers (PC1) at 2.45m, Ring Image Cerenkov Counters (RICH) at 2.6-4.0m, Pixel Pad Chambers (PC2) at 4.2m, Pixel Pad Chambers (PC3) at 4.9m, and Lead Scintillator electromagnetic calorimeters (PbSc) at 5.07-6m. The east arm spectrometer consists of similar detectors as the west arm at the same radial locations, but it does not have PC2, and in addition, it has 2 sectors of a Time-of-Flight Scintillator Wall (TOF) at 5.06m, four layers of Time Expansion Chambers (TEC) at 4.1-4.8m between TOF and PC3, two sectors of PbSc and 2 sectors of Lead Glass electromagnetic calorimeters (PbGl) at 5.07m and 5.4 m, respectively.

The tracking system of PHENIX operates in an environment of high track density of up to 500 charged tracks in the acceptance. The system is designed to: (i) locate all charged tracks of interest within the fiducial volume, (ii) measure the particle momenta, (iii) contribute information to the PHENIX

Level-2 trigger. The baseline tracking system consists of three components: (i) The DCs provide precise projective tracking and excellent momentum measurement (ii) Each of the PC1, PC2, and PC3 provide a three-dimensional position measurement to aid in pattern recognition and to determine p_z/p_T. (iii) The TEC assists pattern recognition and can improve the momentum resolution at $p_T > 5$ GeV/c. All three components have been successfully used in Run-2 to provide charged high p_T Level-2 triggers

Particle identification is provided by RICH, TEC, TOF, PbSc and PbGl. Electron identification is performed using the following detector subsystems: (i) Cerenkov radiation detected in the RICH, (ii) energy loss dE/dx of the charged particles in the TEC, and (iii) time-of-flight and electromagnetic showers in PbSc and PbGl calorimeters. Photons are detected with good energy resolution using the electromagnetic showers in PbSc and PbGl, which can then be used to measure the π^0 and η production rate from their 2γ decay. Good time-of-flight is the key element for charged hadron identifications. This is realized in PHENIX by the TOF in a small acceptance ($\sim 1/3sr$) with accurate timing resolution, and also by PbSc and PbGl in the full central arm acceptance of PHENIX($\sim 2sr$) with less accurate timing resolution.

In what follows, we will discuss the PHENIX central spectrometers, focusing on the subsystems which are used in this analysis: the magnet, DC, PC1, PC2, PC3, RICH, EMC, and TOF. More details about the design and performance of PHENIX can be found in [75].

2.2 The Central Arm Detectors

2.2.1 The Central Arm Magnet

The PHENIX magnet system is composed of three spectrometer magnets, the Central Magnet (CM) and the north and south Muon Magnets (MMN and MMS). The Cental Magnet is energized by two pairs of concentric coils and provides an axially symmetric field parallel to the beam and around the beam axis. Charged particles bend in a plane perpendicular to the beam axis. The bending angles are accurately measured by the DCs, from which the charged particle momenta can be accurately determined.

Fig. 2.3a shows the cutaway drawing of the PHENIX magnets showing the CM and MM field lines. The magnetic field for the central spectrometer is axially symmetric around the beam axis. Its component parallel to the beam axis has an approximately Gaussian dependence on the radial distance from the beam axis. At the center close to beam axis, the field line uniformly points

along the beam direction. However, the residual field at the DC distance (2-2.4m radially) is highly non-uniform, the field line is parallel to the beam near $z = 0$, but has a significant r component at large z. The z dependence of the field is better illustrated in Fig. 2.3b, where B_z as function of radius r along the lines connecting origin and different z at the DC radius is shown. The field strength is about 0.48 T at the beam line ($r = 0$), and decreases as r increases. The field is almost uniform for different z at $r < 2m$. But in the drift chamber region, the residual field strength strongly varies with z. At around $z = 0$, the field is about 0.096 T (0.048 T) at the inner (outer) radius of the DC. At large z (80cm), the field changes direction and is much weaker(0.04 T(0.02 T) at the inner (outer) radius of the DC).

For the charged hadron analysis, tracking starts at the Drift Chamber, which sits at the edge of the magnetic field. Due to the lack of tracking devices between the collision vertex and the DC, a background from decay and conversion secondaries contaminates the spectra at high p_T. These background tracks usually have genuine low momenta, and bend significantly from the field inside and after the DC. As we will show in Chapter 4.4 and 4.5, this residual bend can be harnessed to help reject background charged particles at high p_T, and is the basis of the background rejection and subtraction techniques we have developed.

2.2.2 The Drift Chamber

The functions of the DC include:

- Accurate measurement of charged particle trajectories in r-ϕ direction to determine their transverse momentum (p_T), and the invariant mass of pairs of particles.
- Together with the hits measured by the PC1 and collision z_{vtx} measured by the BBC, determine the track polar angle θ.
- Participates in the pattern recognition by providing tracking information that is used to link together tracks and hits in various PHENIX central detector subsystems.

In order to achieve these functionalities, the DC performance has to satisfy the following main requirements:

- Single wire resolution better than 150 um in r-ϕ direction

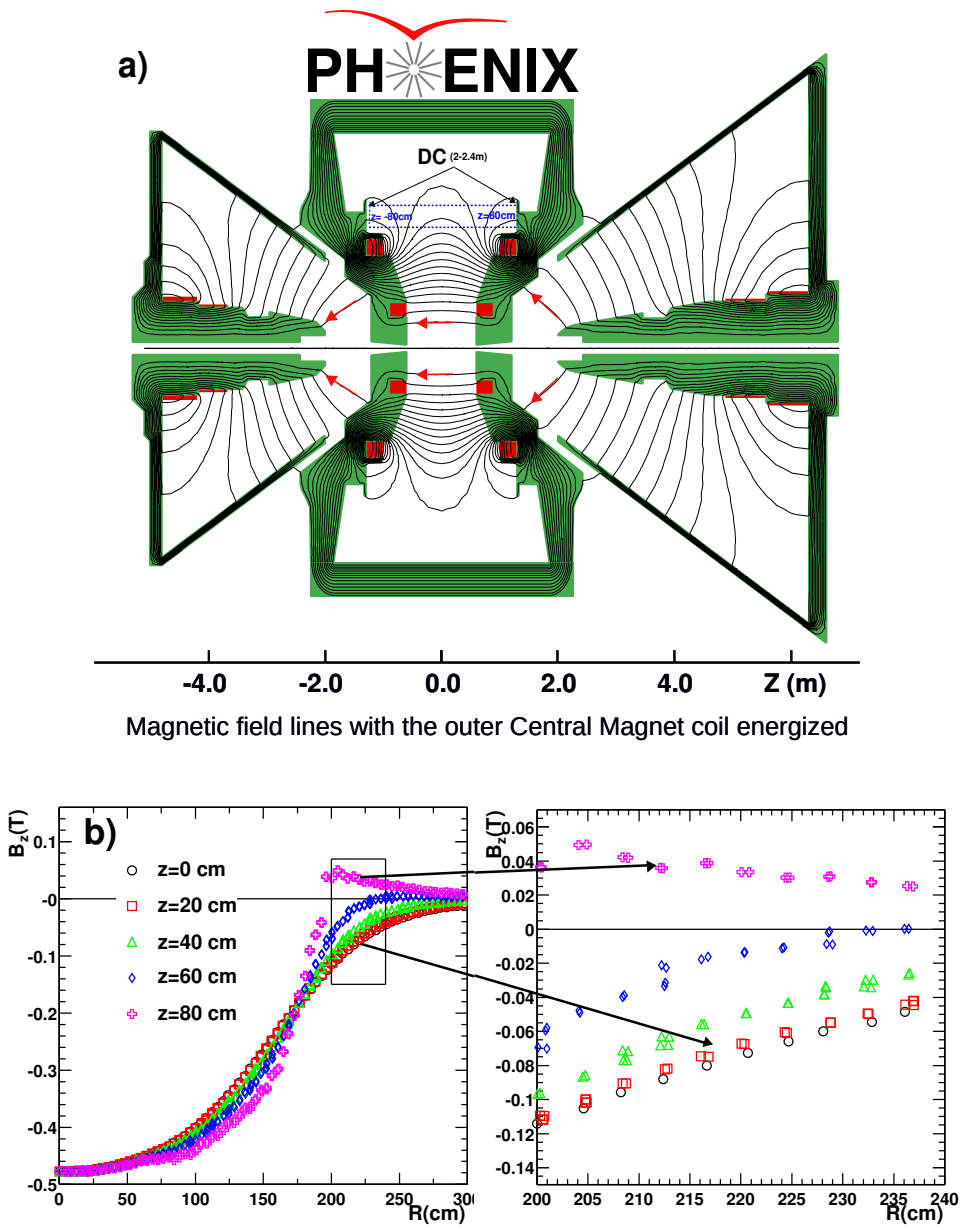

Figure 2.3: a) CM and MM field lines shown on a cutaway drawing of the PHENIX magnets. The beams travel along the z axis in this figure and collide at $z = 0$. b) z component of the magnetic field, B_z, as a function of, R, the radial distance along the line connecting origin and different z locations at the DC (it is the z component of the magnetic field that bends the track).

- Single track reconstruction efficiency better than 99%
- Two track resolution better than 1.5 mm.
- Spacial resolution in the z direction better than 2 mm.

The PHENIX Drift Chambers are of cylindrical shape and are located in the region from 2–2.4 m in radial direction from the beam axis. Their length is 1.8 m along the beam direction. Each DC covers 90° in azimuthal angle ϕ and consists of 40 planes of sensing wires subdivided into 80 drift cells, each cell spanning 1.125° in azimuth. The wire planes are arranged in six types of wire modules stacked radially in the following order, X1, U1, V1, X2, U2, V2. Each of the X and U,V modules contains 12 and 4 sense wires, respectively. The X, U, V wire orientations are shown in Fig. 2.4. The X1 and X2 wire modules run in parallel to the beam to perform precise track measurements in r-ϕ. U1,V1 and U2,V2 wire modules are placed after X1 and X2, respectively. They have stereo angles about ±5° relative to the X wires and measure the z coordinate of the track. The stereo angle is selected to match with the z resolution of the pad chambers and minimize tracking ambiguities.

In typical central $Au - Au$ collisions, there are as many as 200 tracks in each DC. In order to reduce the occupancy and keep good track reconstruction efficiency, each sensing wire is separated electrically in the center by a low mass kapton strip and are read out separately. This way, the number of DC readout channels is doubled with little additional material in the fiducial volume of the chamber. In total, each DC contains roughly 3200 anode wires and ,therefore, about 6400 readout channels. The measured occupancy in central $Au - Au$ collisions is about 2 hits per wire.

2.2.3 The Pad Chambers

The primary functions of the PCs are [69]:

- Measurement of non-projective three dimensional spatial points, which are used for both momentum determination (p_z) and pattern recognition.
- Reject decays and photon conversion background at high p_T by tight matching requirement to the track measured by the DC(see Chapter 4.4).
- Distinguish electrons from other particles by accurate pointing of charged track to the RICH and EMCal.
- Charged particle veto in front of EMCal.

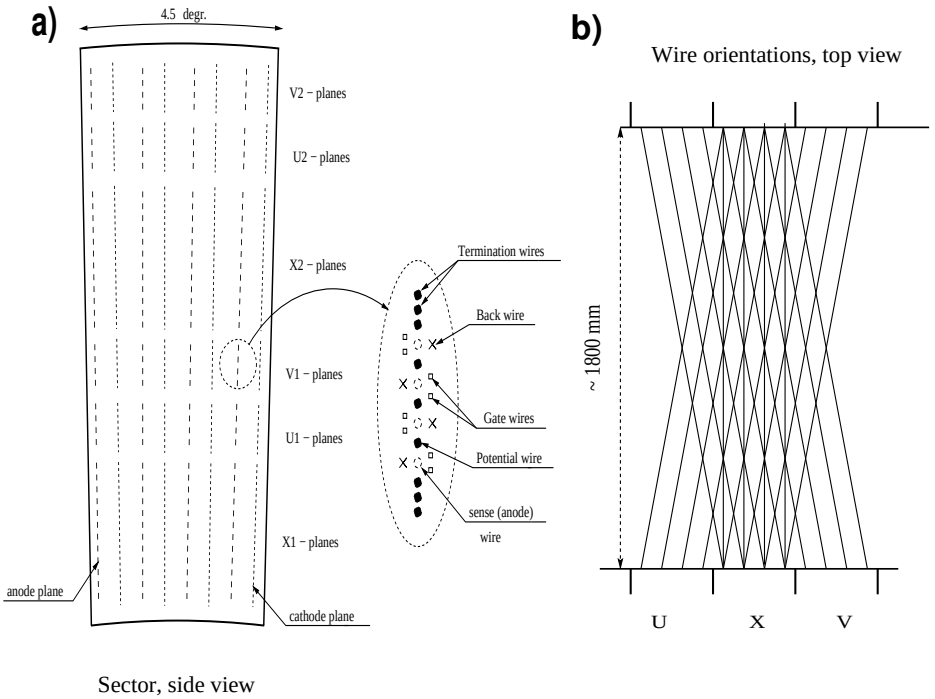

Figure 2.4: a) Layout of the wire position for 4 cells and a blow up drawing of the wire arrangement for a V1 net (the arrangement are similar for other wire nets). b) Top view of a schematic diagram of the stereo wire orientation.

- Providing seed for tracks in charged high p_T Level-2 triggers and electron Level-2 triggers.

The design of the pad chambers is driven by the following considerations [76]

- Very high efficiency ($> 99\%$) and low occupancy(few % in most central $Au - Au$ collisions).
- Good spatial resolution.
- Low mass, in order to minimize secondary particle production and multiple scattering.

The PCs are multiwire proportional chambers that form three separate layers of the PHENIX central tracking system. Each detector contains a single

plane of wires inside a gas volume bounded by two cathode planes. One cathode is finely segmented into an array of pixels. The charged induced on a number of pixels when a charged particle starts an avalanche on an anode wire is read out through specially designed readout electronics.

The 3D view of the pad chamber system is shown in Fig. 2.5. The important PC specifications achieved in RUN-2 are listed in Table 2.3. The pad size for PC1 is 0.84 $cm\times$ 0.845 cm to achieve less than 8% occupancy in most central $Au-Au$ collisions. This gives a position resolution of 1.7 mm along z and 2.5 mm in r-ϕ. The pad size for PC2 and PC3 is chosen such that they have similar angular resolution compared to PC1. The use of a frameless wire chamber held by honeycomb sandwich minimize the amount of material in the PC [76].

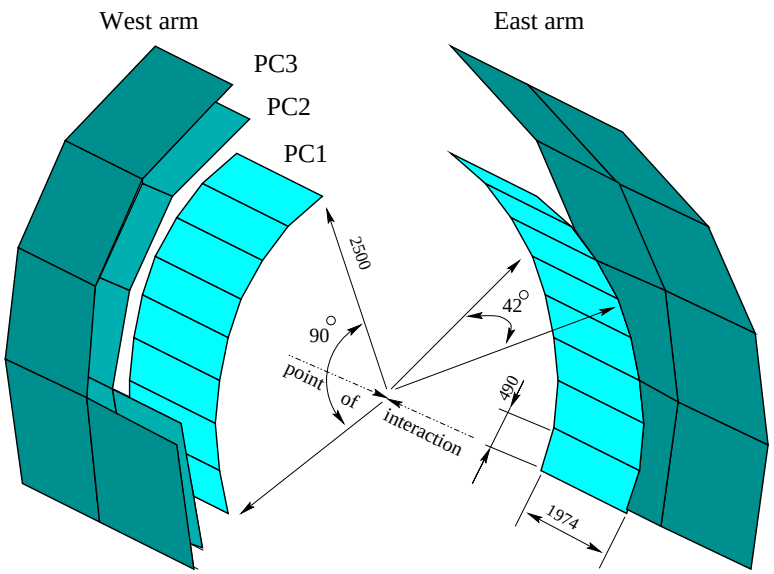

Figure 2.5: The Pad Chamber system in PHENIX. Several sectors of PC2 and PC3 in the west arm are removed for clarity of the picture. Figure from Ref. [76].

2.2.4 The Ring Imaging Cerenkov Detectors

The primary functions of the RICH are:

- Identification of electrons below $p_T < 4.8$ GeV/c.

Table 2.3: Performance of Pad Chambers in RUN-2 [77, 76].

Parameters	PC1	PC2	PC3
Pad Size (r-$\phi \times z$)(cm^2)	0.84×0.845	1.355×1.425	1.6×1.67
Single hit resolution (r-ϕ, z) in mm	(2.5,1.7)	(3.9,3.1)	(4.6,3.6)
Double hit resolution (r-ϕ, z) in cm	(2.9,2.4)	(4.6,4.0)	(5.3,5.0)
Radiation Length (% X_0)	1.2	2.4	2.4
Efficiency	>99%	>99%	>99%

- Help charged pion identification at $p_T > 4.8$ GeV/c. The thresholds are flexible with different radiation gases.
- One of the primary PHENIX electron Level-1 trigger devices and the core for numerous Level-2 triggers, e.g. single electron trigger, $J/\Psi \rightarrow e^+e^-$ trigger, $\phi \rightarrow e^+e^-$, high p_T pion trigger.

In order to achieve these functionalities, the RICH performance has to satisfy the following specifications [69]:

- e/π separation at the 10^4 level for single tracks.
- The Photo Multiplier Tube (PMT) should have high single photon efficiency ($\sim$ 100%). It should also have good timing resolution to reduce noise and contamination from background electrons.
- Minimal radiation length to reduce conversions inside RICH.

The RICH detector is located between the inner and outer tracking units. Fig. 2.6 shows a cutaway drawing of one RICH detector revealing the internal components. Each RICH detector has a volume of 40 m^3 with an entrance window area of 8.9 m^2 and an exit window area of 21.6 m^2. The spherical mirrors focus Cerenkov light onto two arrays of PMTs, each located on one side of the RICH entrance window. The PMTs are fitted with Winston cones of 50 mm diameter and have magnetic shields that allow them to operate in magnetic fields up to 100 Gauss. The radiator gas length seen by charged particles is 87 cm at $\eta = 0$ and 150 cm at $\eta = 0.35$, the average path length through radiator gas is 120 cm.

The RICH is filled with CO_2 gas at a pressure slightly above ambient air pressure. It has a Cerenkov threshold of $\gamma_{thr} = 35$ which is about 17 MeV/c for electrons and 4.8 GeV/c for charged pions. So, e/π separation is possible

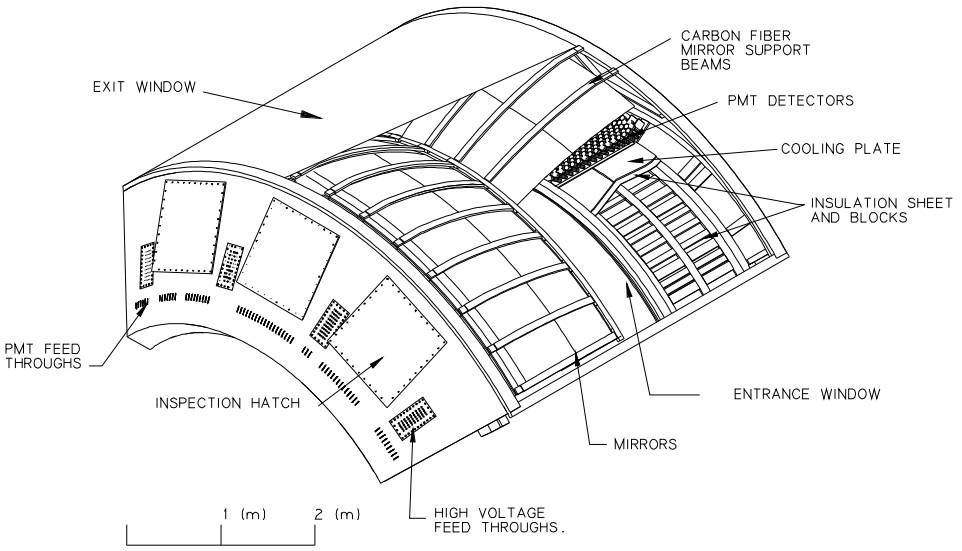

Figure 2.6: A cutaway view of the RICH detector [78].

below 4.8 GeV/c. The RICH can also be used to identify pions at $p_T > 4.8$ GeV/c. Fig. 2.7 illustrates the principle of electron detection in the RICH. The Cerenkov photons generated by e^+, e^- and high momentum hadrons are reflected by spherical mirrors placed within the radiator volume. The photons are focused onto PMTs placed just behind the PHENIX central magnet. The pole tips of the magnet thus serve as hadron shields for the PMTs.

Cerenkov photons are emitted at an angle $\theta = cos^{-1}(1/(\beta n))$. These photons are focused as a ring of photons onto the PMT array, and are converted into photo electrons in the PMT. The total number of photo electrons for a charged particle above the Cerenkov threshold can be written as [79]

$$\begin{aligned} N_{npe} &= L\frac{\alpha^2 z^2}{r_e m_e c^2}\int \epsilon_c \epsilon_d sin^2\theta dE, \text{ where} \\ &\quad \frac{\alpha^2 z^2}{r_e m_e c^2} = 370 cm^{-1} eV^{-1}. \end{aligned} \tag{2.2}$$

Here, L is path length of particles in the radiator; ϵ_c is the PMT Cerenkov light collecting efficiency, and ϵ_d is the quantum efficiency of the PMT. Usually a "*figure of merit*" N^0_{npe} is defined,

$$\begin{aligned} N_{npe} &= N^0_{npe} L sin^2\theta \qquad \text{, where} \\ N^0_{npe} &= \frac{\alpha^2 z^2}{r_e m_e c^2}\langle\epsilon_c\rangle\langle\epsilon_d\rangle. \end{aligned} \tag{2.3}$$

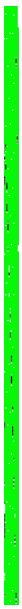

Figure 2.7: Schematic r-z view of the RICH and its optics. A typical electron (400 MeV/c) produces Cerenkov photons, which are reflected by the mirror into a ring at the focal plane where they are collected by the PMT array. Hadrons with $\gamma < 35$ do not produce photons in the RICH [79].

which quantifies the RICH electron detection performance. This number takes into account acceptance and quantum efficiency of the PMT and the property of the gas. In RUN-2, it is measured to be 116 cm^{-1} for CO_2 gas.

Each PMT has a diameter of about 2.5 cm, while the ring of photons reflected onto the PMT array has a radius of 11.8 cm. Usually, one electron fires several PMTs located along the ring. This is illustrated by Fig. 2.8, where a contour plot of a residual distribution of RICH hits associated with the tracks from the track projection point are shown. Peripheral events are used to reduce the accidental associations. The RICH ring can be clearly seen as expected from the ring diameter for CO_2 gas. To reduce false hits, the number of PMTs for a given charged track are counted within 3.4-12.8cm from the projection. This quantity, N_{PMT}, is used to separate electrons from hadrons as will be later discussed in Chapter 4.5.

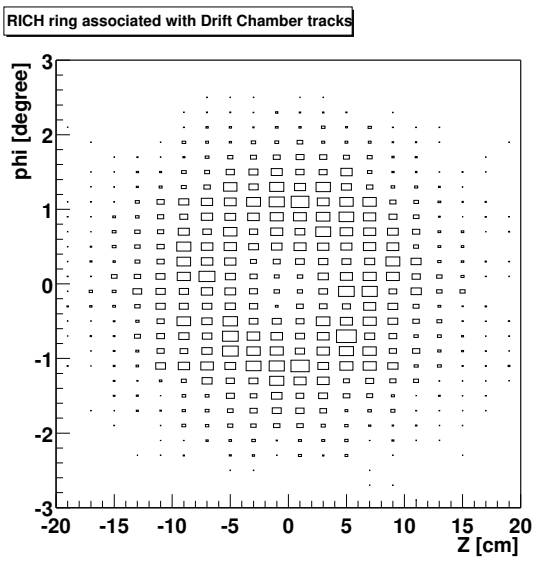

Figure 2.8: Box plot for RICH PMT hits relative to the track projection point in the RICH, accumulated over many tracks [78].

2.2.5 The Electromagnetic Calorimeters

The Electromagnetic Calorimeter (EMCal) is used to measure the spatial position and energy of electrons and photons produced in heavy ion collisions. It covers the full central arm acceptance of $70° \leq \theta \leq 110°$ and 180° in azimuth. There are two types of calorimeters, Lead Scintillator (PbSc) sampling calorimeters and Lead Glass (PbGl) Cerenkov calorimeters, populated in the radial direction within 5-6m. There are 4 sectors of PbSc in west arm, 2 sectors of PbSc and PbGl in the east arm. Both detectors have very good energy,

spatial and timing resolution, while the PbSc excels in timing and PbGl in the energy measurement.

The EMcal is mainly designed for electron identification, direct photon measurements, neutral meson (e.g. π^0, η.) measurements via their $\gamma\gamma$ decay channel, and low p_T charged hadron identification from their time-of-flight. However, since both types of calorimeters have 0.85 units of hadronic interaction length, high p_T charged hadrons also have a large probability of depositing a large fraction of their energy. Thus they can provide a background veto for charged hadrons.

For the charged hadron analysis, the EMCals has been used to select a clean sample of high p_T charged hadrons. These high p_T hadrons have been used to study the systematics of the momentum resolution (see Chapter. 3.3.1). A clean sample of high p_T pions can also be selected [80] by requiring a confirming hit in the RICH and a high energy cut in the EMCal. These pions are used to obtain the N_{PMT} distribution, which are used in the charged hadron analysis.

In both RUN-2 and RUN-3 and also in future RHIC runs, EMCal has been and will be a crucial Level-1 trigger device. A large sample of events, corresponding to integrated luminosity many times that of minimum bias events, which contains high energy candidate particles can be recorded. These triggered events can potentially increase the p_T limit that can be reached with only minimum bias events [1], and also allow for a correlation study with high p_T particles.

2.2.6 The Time Of Flight

The PHENIX Time of Flight (ToF) detector is the most important device for identifying charged hadrons in a wide range of p_T. ToF contains 960 scintillator slats oriented along the r-ϕ direction, covering $\pi/4$ in azimuthal direction in the lower part of the east arm. Particle identification is achieved by correlating the time-of-flight to the measured momentum of the charged particles. With the large distance (5.05 m) and good timing resolution (100ps), ToF can provide 3σ π/K separation up to 2.4 GeV/c and 3σ K/p separation up to 4 GeV/c.

For charged hadron analysis, the ToF has been used to determine the DC momentum resolution and momentum scale, based on the width and mean

[1]Since EMCal only catches a fraction of the high p_T hadron energy, the main difficulty in using the triggered data for charged hadron or charged pion analysis is in extracting the EMCal trigger efficiency.

location of m^2 for identified particles as function of p_T. The details of this measurement are discussed in Chapter. 3.3

Chapter 3

The Calibration Marathon

3.1 The Drift Chamber Calibration

A drift cell in the Drift Chamber is approximately 4 *cm* wide[1] in azimuthal direction and 6 *mm* high in radial direction. The wire configuration and the drift lines are shown in Fig. 3.1 for a drift cell under operating potentials. The sensitive region of a drift cell is created by the anode and the cathode wire, with field lines running from the anode wire to the cathode wire. In order to assure an uniform electric field in the cell, several "field shaping" wires with different voltages are introduced to "shape" the field lines to the desired geometry. Since electrons originating at the same distance from both sides of the anode wire have the same drift time, this causes a left-right ambiguity in the hit reconstruction. This is solved by implementing *back-drift wires* alternately with *gate wire* pairs at an 2 *mm* distance from the anode wires. The back-drift wire has a low voltage and catches the field lines from the cathode wire at one side of the drift cell, thus only electrons ionized on the other side can reach the anode wire. This way, the left-right ambiguity is removed, except for a 2 *mm* window between the back-drift wire and the anode wire, where a fraction of the electrons can still reach the anode. The back-drift wire reduces the effective length of the drift region by half to be about 2 *cm*. The gate wire operates at a high voltage to constrain the drift lines in 4 *mm* region (half height of a cell). This reduces the average width of the hits and improve the single hit resolution. In the region between the back wire and the gate wire, the charge amplification happens, so potential wires are mounted between anode wires on the cell boundary to shape the field line such that the charge

[1]Due to the increasing radial distance, the outer drift cells have slightly larger width.

Table 3.1: Potential and diameter for different types of wires used in the drift chamber

wire type	Anode(sense)	Cathode	Gate	Potential	Back drift
voltage (kV)	0	-4 to -4.7	-1.5 to -1.6	-2.3 to 2.65	-0.8 to -0.9
diameter(μm)	25	90	90	90	90

passing the gate is amplified and collected on the corresponding anode wire. The default voltage configurations for different wires are listed in Table. 3.1.

The Drift Chamber operates with 50% Ar and 50% C_2H_6 gas. The drift velocity of the electrons from ionization, v_d, depends on the electric field strength (E), temperature (T), pressure (P), and the composition of the gas as,

$$v_d = \epsilon \frac{ET}{P}, \tag{3.1}$$

where ϵ is a constant related to the gas. The relationship between drift velocity and ratio of field strength and pressure (E/P) for the DC working gas is shown in Fig. 3.2. The nominal working point of the PHENIX DC is chosen to be on the relatively flat part of the function: $E/P = 3V/(cmTorr)$, where the drift velocity v_d is about 4.8 $cm/\mu s$.

The charge signal is collected by the anode wire and passed to the Amplifier Shaper Discriminator (ASD) chip, which amplifies pulses from the wires and discriminates against a predetermined threshold. A TMC (Time Memory Cell) digitizes both the rise time (Leading edge t_L) and the fall time(Trailing edge t_T) when the pulses pass the threshold, as illustrated by Fig. 3.3. The resolution of digitization (time bin) corresponds to 0.82 ns at a clock frequency of 38 MHz. t_L represents the drift time and can be used to calculate the distance between the hit and the anode wire, $d = v_d t_L$. However, this time has to be corrected for signal travelling time and Level-1 trigger decision time. So a time offset t_0 has to be subtracted to obtain the absolute drift time t_a,

$$t_a = (t_L - t_{bbc}) - t_0, \tag{3.2}$$

where t_{bbc} is the event start time recorded by the PHENIX beam-beam counters (BBC).

The time difference between the leading edge and trailing edge, $t_T - t_L$, characterizes the spread of the charge clouds from the ionization. Due to the finite rise time of the pulses and the spread of the charge clouds, the recorded leading time t_L is usually different from the nominal drift time, t_a, for electrons

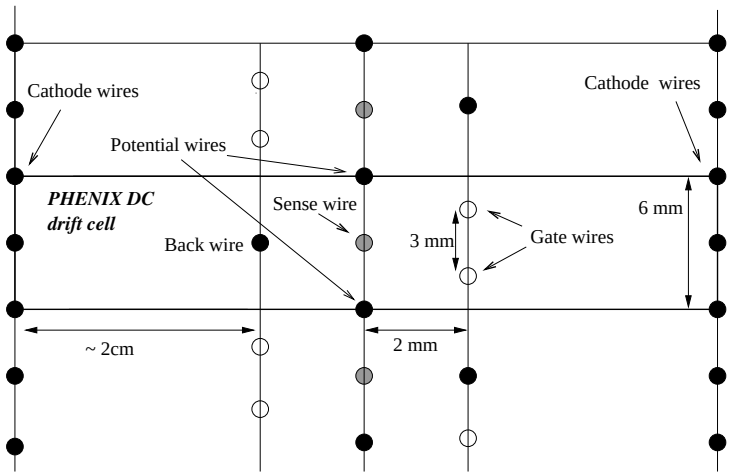

Figure 3.1: a) A typical drift cell with the wire positions. [81] b) The drift lines for six wire planes in an X1 net, different types of wires are marked by arrows. The drift lines are in blue (or dark colored line in black and white). A typical track trajectory is illustrated by the boundary of drift lines to the right. The electrons clouds from the ionization are illustrated by the red dots [82]. (courtesy of Sergy Butsyk).

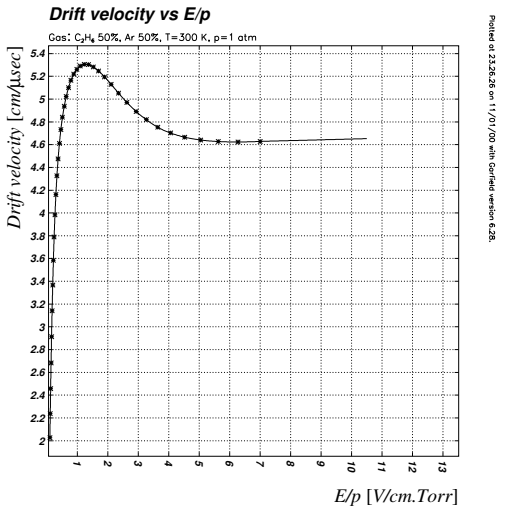

Figure 3.2: Drift velocity as function of E/P in the DC working gas mixture. Figure taken from [81].

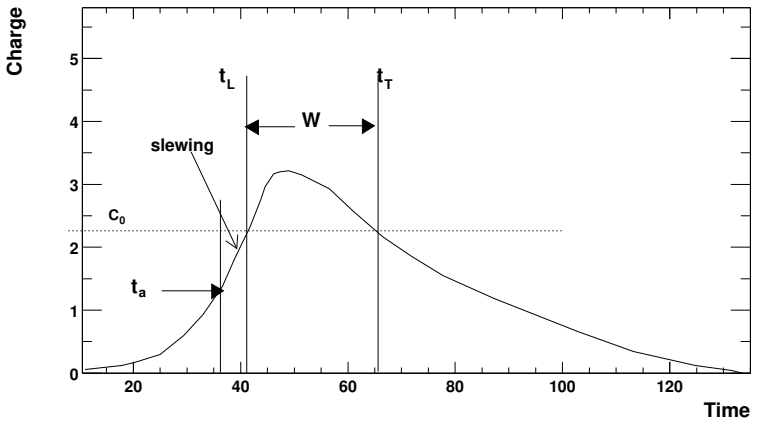

Figure 3.3: A schematic illustration of the drift time measurement for a drift chamber hit. The curve shows the amplified analog signal from a hit. The horizontal dashed line is the charge threshold in the ASD. The difference between leading edge and trailing edge $t_T - t_L$ gives the width of the hit. The short solid vertical line indicate the true drift time, t_a. Thus $t_L - t_a$ is the slewing correction.

ionized at the middle of the drift region (along the line connecting the anode and cathode wires). The difference between the t_a and t_L is called "slewing time" as illustrated by Fig. 3.3, and needs to be corrected as a function of the width of the hit.

The Drift Chamber calibration task can be roughly divided into the following list,

v_d and t_0 calibration In addition to a global v_d and t_0 calibration, a detailed plane-by-plane v_d and wire-by-wire t_0 calibration has also been performed in Run-2. They are among the most important calibration parameters for the Drift Chamber.

Slewing and Drift Correction Since the hit arriving time depends on the hit width, the hit arrival time needs to be adjusted. This is referred to as slewing correction. Drift corrections refer to corrections due to the distortion of electric field for wires close to the mylar entrance window of the DC (see Fig. 3.1b).

Single Wire Efficiency and Tracking Efficiency Single wire efficiency and tracking efficiency are among the most important parameters that benchmark the performance of the DCs. The design goal is $> 96\%$ for the single wire efficiency and $> 99\%$ for the tracking efficiency.

Noisy and Dead Channel The loss of acceptance and tracking efficiency due to noisy and inactive channels needs to be investigated.

3.1.1 v_d and t_0 calibration

The data read out of the drift chamber is driven by events triggered on by the BBC. The BBC measures the collision start time t_{bbc}. According to Eq. 3.2, this time has to be subtracted from the DC start time. Fig. 3.4 shows the t_{bbc} distribution, the distribution has a 1 ns offset from zero and 0.8 ns width.[2]

After the subtraction of t_{bbc}, the time distribution of the Drift Chamber hits is used to extract the average drift velocity, v_d, and the time offset, t_0. Fig. 3.5 shows the time distribution for two drift planes at radius $r = 206$ cm and 232 cm, respectively. The time distribution has a characteristic shape: (i) The sharp rise at the left edge is the start time, corresponds to the ionization very close to the anode wire; (ii) The region of enhancement ($< 100ns$) corresponds to the region within 2 mm from the anode wires, where the anode wires can receive charges from both sides; (iii) The fall off at large time represents hits generated close to the cathode wire. Thus the time at the rising edge

[2]The intrinsic BBC timing resolution is much narrower (about 20 ps), the width is mostly dominated by the spread of beam bunches.

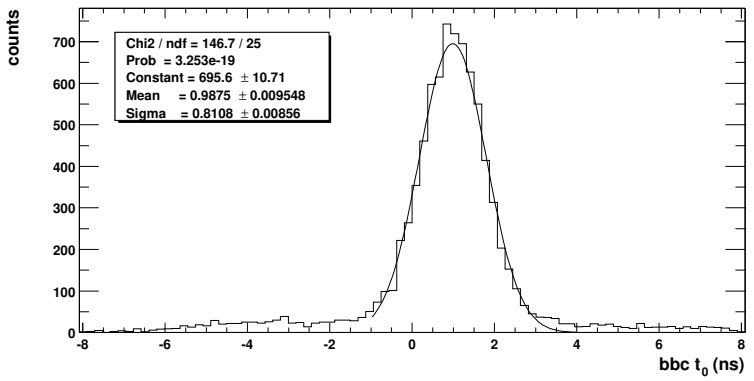

Figure 3.4: The measured BBC start time distribution.

gives the time offset t_0 and the width of the distribution corresponds to the maximum drift time for the full drift region, which is about 2 cm. One can also notice that the time range for the outer drift plane is larger, reflecting the linear increase of the drift cell length with the running radial position, since they are at larger radius. A fermi function fit is used to determine the times for the two edges, t_0 and t_1. Since the drift length for each cell is given by drift chamber wire geometry, we can calculate the drift velocity by dividing the known maximum drift length d by the time difference:

$$v_d = \frac{d}{t_1 - t_0} \tag{3.3}$$

As an example, the cell length for plane 2 and 31 are $2.02cm$ and $2.28cm$, respectively. Their v_d calculated from Eq. 3.3 are 5.17 and 5.12 cm/ns,[3] respectively.

In the RUN-2 offline reconstruction, the v_d and t_0 for every single run have been automatically determined and the values are saved into the database. Fig. 3.6 shows the run-by-run variation of v_d and t_0. The average global t_0 and v_d are listed in Table. 3.2. During most of the RUN-2 period, t_0 and v_d are very stable. The run-by-run variation of t_0 and v_d is about 1 ns and 0.3%, respectively[4]. This leads to a run-by-run variation of the single hit resolution of 2 $cm \times 0.3\% = 64$ μm.

[3]The difference is $\sim$1% level, which should disappear after the plane by plane v_d correction.

[4]The sudden jump in the t_0 value around run 28450 is due to a hardware change

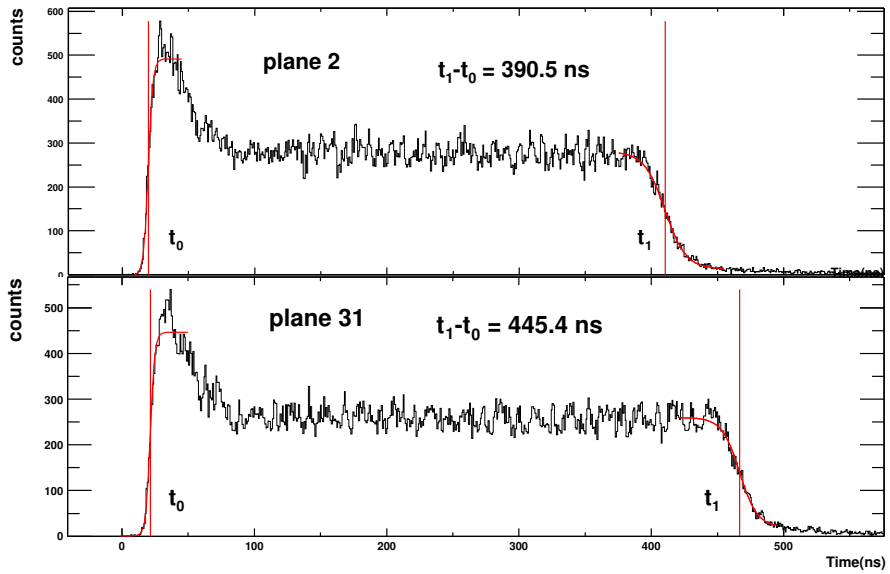

Figure 3.5: The time distribution for two X planes in the west arm (The third plane in X1, and the second to last plane in X2) from RUN-2 data. Also shown is a fit to the leading and trailing edge of the timing distribution.

Table 3.2: The average v_d and t_0 value in RUN-2

arm	$v_d(\mu m/ns)$	$t_0(ns)$	$t_{bbc}(ns)$
west	0.00516 ± 0.000015	20 ± 0.3	$1. \pm 0.8$
east	0.00519 ± 0.000014	21.3 ± 0.3	

Fig. 3.7 shows the wire-by-wire t_0 variation and plane-by-plane v_d variation. Most of the variations result from imperfections of the DC internal geometry. These imperfections lead to small deviation of the anode wires from their ideal location. Consequently, the drift lengths are also different from the ideal cell length. In addition, wire-by-wire t_0 offsets can also result from channel-by-channel timing variation of the DC electronics. These varia-

in the Drift Chamber time delay, so the time digitization of the TMC chip is shifted by about 100 ns. Also around run 27500, alcohol has been added to the DC gas to improve the high voltage stability of DC wires. This leads to a 2% change in the drift velocity v_d.

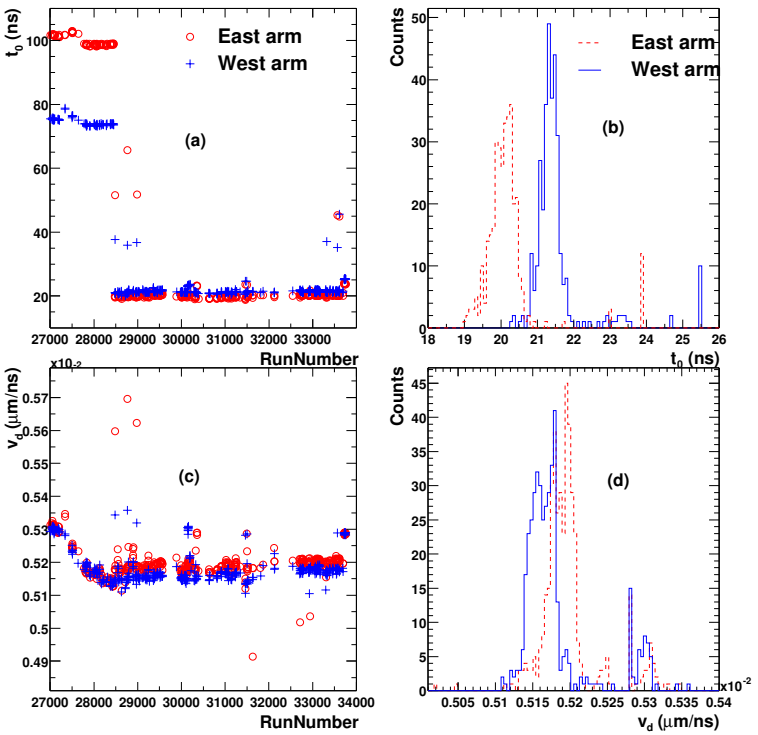

Figure 3.6: The run-by-run variation of t_0 and v_d for the east arm and west arm separately. (a) t_0 versus run number. (b) The t_0 distribution for all runs. (c) v_d versus run number. (d) The v_d distribution for all runs.

tion constants are determined from a large dataset, saved in the database and applied in the offline reconstruction.

3.1.2 Slewing and Drift Correction

A robust approach to calibrate the wire alignment and determine the slewing correction is given by the so called "*three-point*" method [83]. The method is based on the fact that a track is a straight line for zero-field within the Drift Chamber such that the distance calculated from drift time t_L should linearly depend on the plane number. This idea is illustrated in Fig. 3.8. Since t_L is proportional to drift distance, the leading times of the hits from the same track should fall on a straight line in zero-field, i.e. the residual $\Delta T = (T_1 + T_5)/2 - T_3$ should be zero. The calibration is performed by minimizing the offset and the width of ΔT distribution.

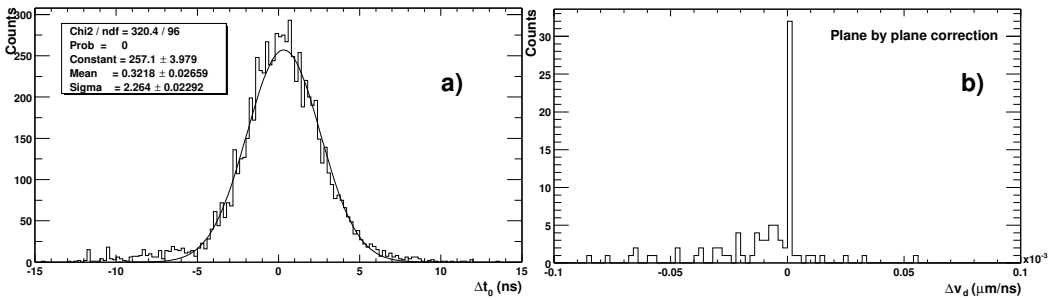

Figure 3.7: a) Channel-by-channel t_0 variation. b) Plane-by-plane v_d variation.

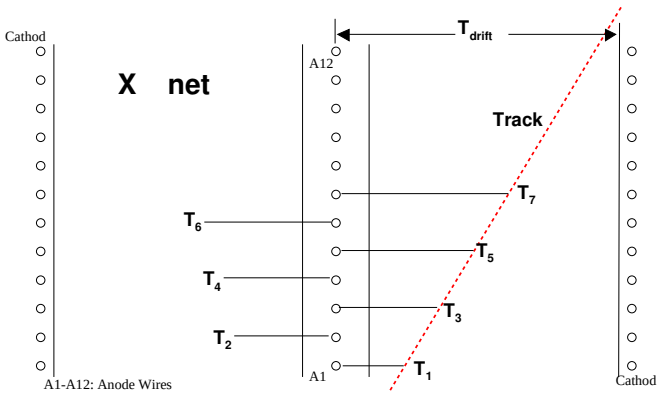

Figure 3.8: Illustration of three-point method.

A charge signal from the anode wire has a certain rise time. The larger the signal, the wider the hit, and the faster it rises to the threshold. So a certain delay should be added to compensate for the shaping time as function of the signal width as shown in Fig. 3.3. This delay is studied from the systematic shift of the mean of the residual distribution of hit width, $\langle \Delta T \rangle$. As an example, Fig. 3.9a shows ΔT distributions for hits with two different widths. Clearly, the slewing offset, $\langle \Delta T \rangle$, depends on the hit width. As shown in Fig. 3.9b, the slewing offset is parameterized as function of hit width and applied in the offline hit reconstruction software.

The electrons from ionization are assumed to travel along a straight line in the drift valley between the cathode wire and the anode wire. However, for the first few wire planes close to the mylar window, the electric field is distorted and becomes less uniform. This distortion was studied [82] using the GARFIELD simulation as shown in Fig. 3.10. The thin lines show the isochrones. Electrons starting from the same line will arrive at the anode wire simultaneously. For the first few planes in the X1 net, the normal drift region

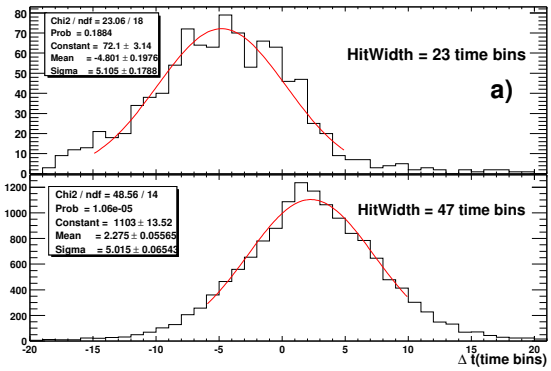

Figure 3.9: a) The residual ΔT distribution for hits with 23 time bins and 47 time bins (1 timebin = $0.822ns$), together with Gauss fits. b) The $\langle \Delta T \rangle$ as function of hit width and a 2 order polynomial fit. This figure is for east arm X1 wires [82].

become much narrower (indicated by the small dots along the isochrones) and the drift lines for electrons generated outside the drift region are not straight but are significantly curved. The distortion becomes negligible beyond the fifth plane. This effect is parameterized for each X wire plane and corrections are applied in the offline hit reconstruction software.

Fig. 3.11 shows the residual distribution from the three-point method after all above correction have been applied. The measured single hit resolution is close to or better than the design resolution of 150 μm.

3.1.3 Single Wire Efficiency and Tracking Efficiency

The charge threshold of the ASD chip is typically chosen such that the DC has almost 100% single hit efficiency. However, occasionally noise hits can be created by sparks from the high voltage cathode and other field wires. These sparks usually are localized in space, thus the corresponding noise hits have a very short width. Fig 3.12 shows the width distribution for the east and west arm separately as obtained from data. The width of signal hits peaks around 46 and 43 timebins for east and west respectively, while the noise hits peak around 10 timebins. The east arm has more noise than the west arm, probably due to a different voltage configuration. To suppress these noise hits, an offline requirement of 20 timebins is applied on the hit width as indicated by the dashed line. The fraction of real hits that are rejected by this cut is

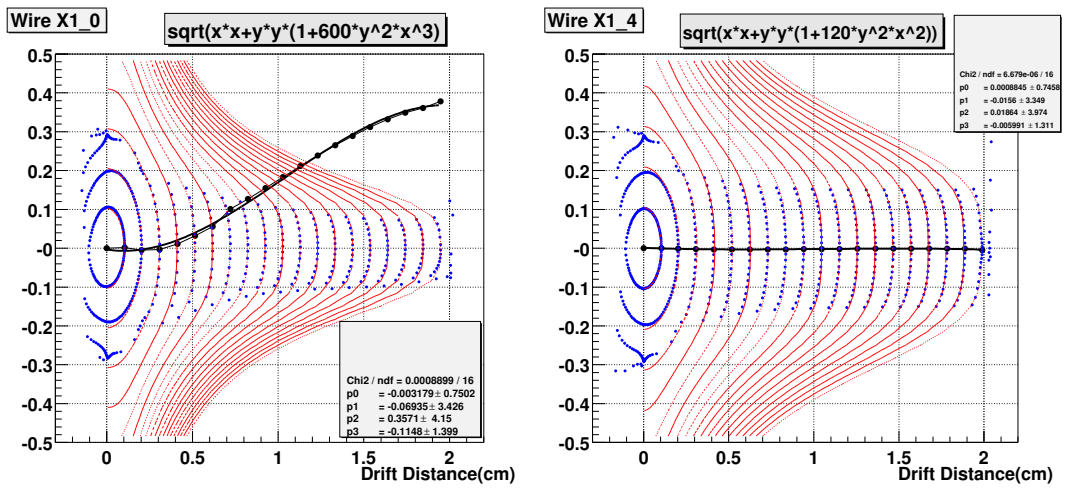

Figure 3.10: The contours of the drift lines for the first (left panel) and the fifth (right panel) X1 plane. The thin contour lines indicate the isochrones. The small dots on the isochrones indicate the normal drift region, where electrons drift along a straight line. The think black lines indicate the typical drift trajectories [82].

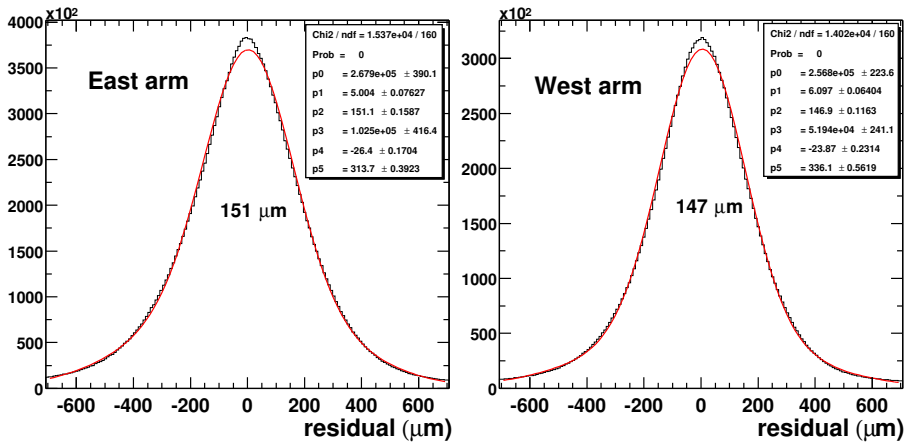

Figure 3.11: Single hit resolution for the east arm (left) and the west arm (right) in μm.

Table 3.3: The estimated average single wire efficiency for east and west arm.

arm	Gauss extrapolation (%)	linear extrapolation(%)	average(%)
East	99.24	96.53	97.89
West	98.11	94.22	96.17

estimated by a Gaussian and linear extrapolation to small widths. This fraction is estimated to be 2.1% and 3.8% for east and west arm respectively. The remaining fraction of signal hits determines the average single wire efficiency, which is 97.9% (96.2%) for east (west) arm. (see Table 3.3).

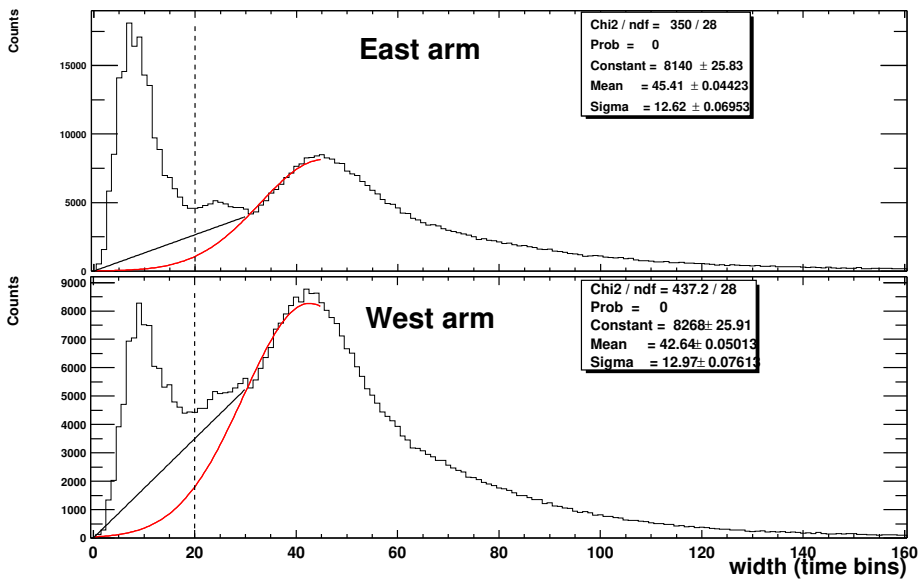

Figure 3.12: The width distribution of the DC hits as function of time bins. offline width cut is illustrated by the vertical dashed line. The solid curve (dotted line) are Gaussian (linear) extrapolation of signals to the small width region.

The three-point method serves as an independent method to study the single wire efficiency. The idea is illustrated in Fig. 3.8. For a given drift cell, if a hit is found in each of the two neighboring cells and if they belong to the same track, this track can be fixed by a straight line connecting the two hits. Then one should expect to find a hit where the track crosses the current drift

cell. By counting the fraction of missing hits, one can determine the single wire efficiency for each every cell.

Fig. 3.13 shows the DC single wire efficiency averaged over 4 cells and separately for X1 and X2 wire nets. The blank areas are due to inactive regions in the drift chamber. However, most of the channels have well above 90% efficiency in the active detector area.

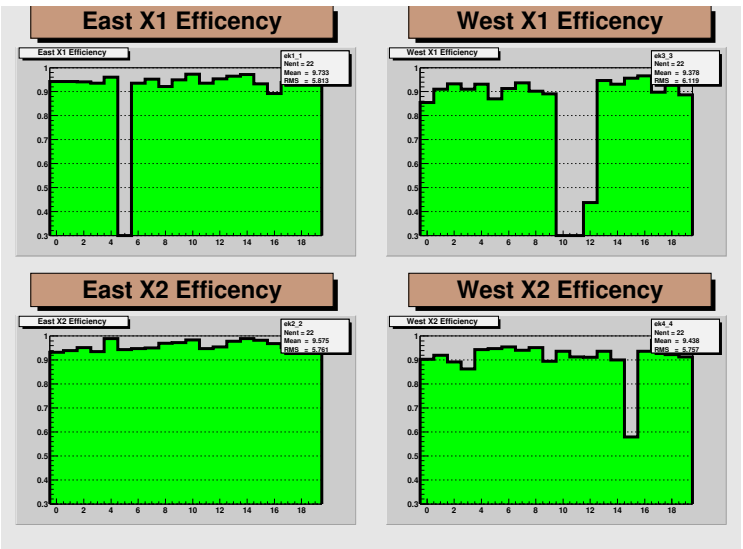

Figure 3.13: The single wire efficiency calculated by 3-point method from online monitoring.

As a result of the high single wire efficiency, the DCs have very good tracking efficiency. The tracking efficiency in low multiplicity environments[5] can directly be calculated from the single wire efficiency based on simple binomial statistics. A track requires a minimum 8 hits found out of 12 possible hits. This gives more than 99% tracking efficiency in the active area of the DC.

3.1.4 Noisy and Inactive Channels

A small fraction of the DC channels are either noisy or inactive in RUN-2. The noisy channels are masked out in the offline reconstruction, and effectively

[5]In high multiplicity environment, the tracking efficiency deteriorate due to hit overlap and the limitations of the pattern recognition, see Chapter. 5.6.

become inactive channels, that way. Fig. 3.14 shows the noisy and inactive channels for a typical run. Out of 12400 total DC channels, there are about 1000 bad channels in both arms, corresponding to about 10%. However, in our analysis, tracks are required to have at least two hits in each of the X1 and X2 wire nets. The effective acceptance is reduced to about 85% (70%) for the east (west) arm.

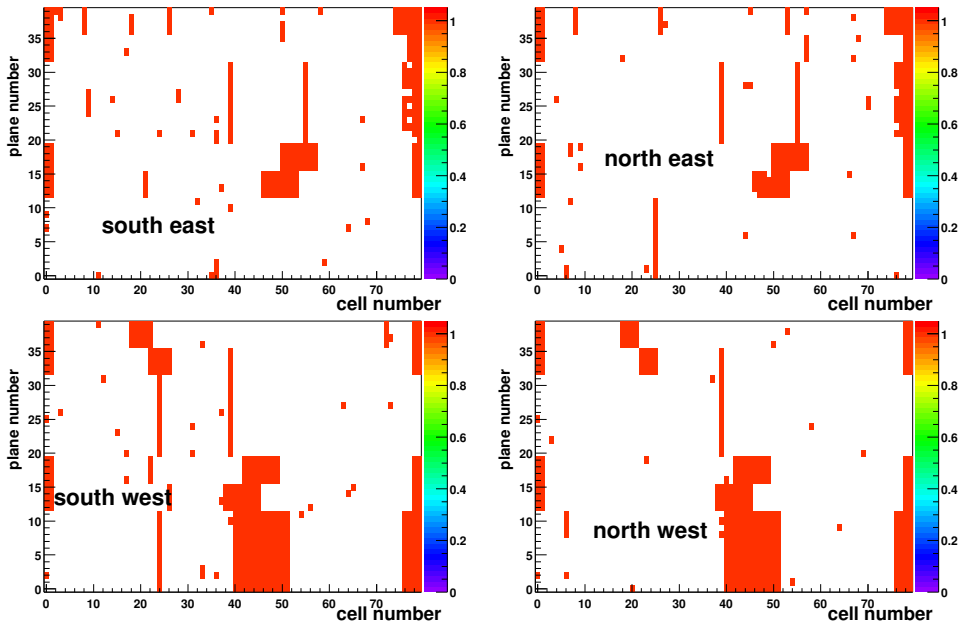

Figure 3.14: The DC inactive area shown separately for the east arm (top) and the west arm (bottom), as well as for the north side (right) and the south side(left).

3.2 Track Reconstruction

3.2.1 DC-PC1 Tracking

A typical track in the DC main bend plane is illustrated in Fig. 3.15a. The coordinates we chose to describe tracks in the drift chamber are ϕ, the azimuthal angle at the intersection of the track with a "reference radius" at the mid-radius of the drift chamber, and α, the inclination of the track at that point. In principle, ϕ and α are equivalent to a slope and intercept; the

main difference is that ϕ and α are limited to a given range of possible values while slope and intercept are not. Fig. 3.15b shows the track in the r-z plane, perpendicular to the bend plane. Because the magnetic field is along the beam direction, tracks usually have a very small bend in this plane. Therefore, it is called the non-bend plane. The coordinates used in this projection are *zed* or z_{dc}, the z coordinate of the intersection point, and β, the inclination of the track at the reference radius.

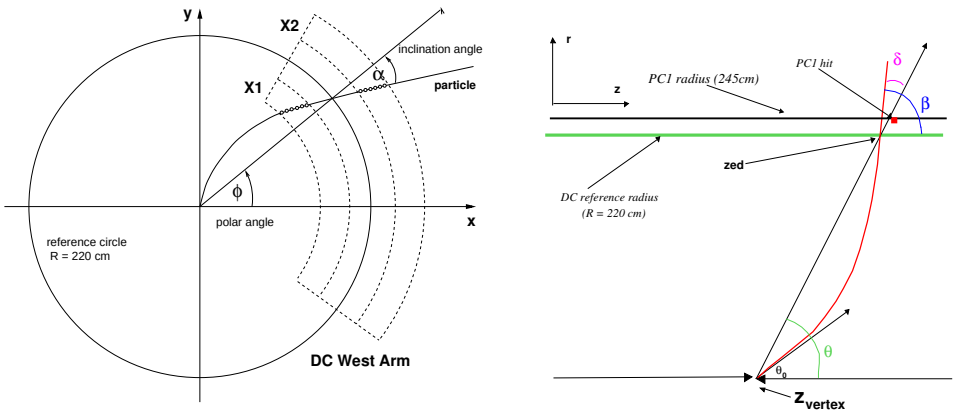

Figure 3.15: a) A schematic cutaway view of a track in the DC x-y (or r-ϕ) plane. The X1 and X2 hits in the drift chamber are shown as small circles within an outline of the drift chamber. ϕ and α are the feature space variables in the CHT transform (see text). b) A schematic cutaway view of a track in the DC r-z plane. The track polar angle is β. The associated PC1 hit is indicated by the box marker. The track bending angle is δ, which is small, such that the track can be approximated by the straight line linking the PC1 hit and collision vertex measured by the BBC.

In order to find a track, hits produced in the detector by the same charged particle have to be found and combined. The tracking is done separately in the r-ϕ and the r-z plane. The track reconstruction in r-ϕ is realized using a combinatorial hough transform technique(CHT) [85], where any pair of hits can be mapped to a point in the space defined by azimuth angle ϕ and track bending angle α. The basic assumption is that tracks are straight lines within the DC. In this case, all hit pairs for a given track will have the same ϕ and α, thus resulting in a local maximum in the feature space spanned by these variables. For a track with n hits, the pair wise combination leads

to a peak height proportional to $n(n-1)/2$, while random pairs of hits from different tracks result in a flat background. The granularity of the feature space variables are chosen to match the DC spacial resolution. The CHT technique is especially suitable for the DC because it places a track with typically 12 hits well above the background even in most central $Au-Au$ collisions, where the hit density is extremely high. Fig 3.16 shows an example of a portion of the drift chamber hits (left panel) together with the associated feature space (right panel) for a central $Au-Au$ collision. The tracks are clearly distinguishable in the feature space and a simple threshold can identify the peaks. In central $Au-Au$ collisions at RHIC, over 95% of the tracks originating from the event vertex and passing completely through the drift chamber are found by the CHT transform. The false track rate is less than 1%. The DC tracking efficiency in a high multiplicity environment is estimated based on an embedding technique, which will be discussed in Chapter. 5.6.

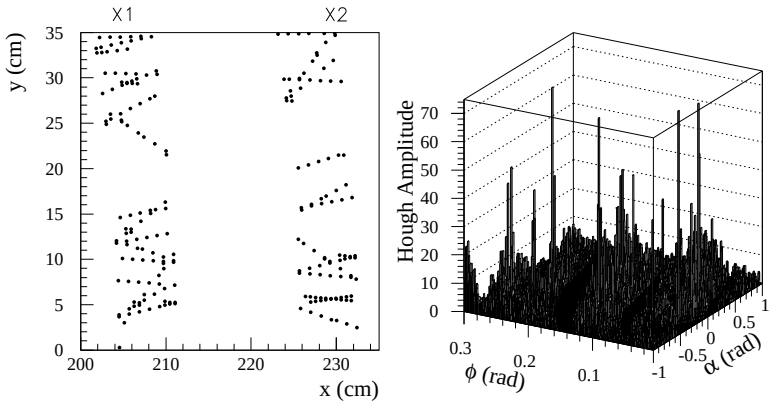

Figure 3.16: Hits in a portion of the drift chamber (left panel) and the corresponding feature space distribution for X1 and X2 wires (right panel) [85].

After the reconstruction of the track in the main bend plane, the direction of the track is specified by ϕ and α. Tracks are then reconstructed in the non-bend plane by combining the information from the PC1 reconstructed hits and the collision's z_{vtx} as measured by the BBC. First, PC1 candidate hits within 2 cm distance from the track in the r-ϕ plane are identified. Then a straight line connecting z_{vtx} and PC1 z fixes the direction of the track in z. The intersection points between the r-z plane and UV hit lines are calculated. UV1 hits are associated to the track if they are within ± 5 cm from the track in the r-z plane. If there is more than one PC1 association, the one with more

associated UV hits is accepted to be the correct track.

3.2.2 Momentum Determination and Global Tracking

The α measured in the drift chamber is closely related to the field integral along the track trajectory. For tracks emitted perpendicular to the beam axis, this relation can be approximated by

$$\alpha \simeq \frac{K}{p_T} \quad , \tag{3.4}$$

where $K = 87$ mrad GeV/c is the effective field integral. However, due to the small non-uniformity of the focusing magnetic field along the flight path of charged particles, an accurate analytical expression for the momentum of the particles can not be determined. A four-dimensional field integral grid was constructed within the entire radial extent of the central arm for momentum determination based on drift chamber hits. The variables in the grid are z_{vtx}, the polar angle θ_0 of the particle at the vertex, the total momentum p, and radius r, at which the field integral $f(p, r, \theta_0, z)$ is calculated. The field integral grid is generated by explicitly swimming particles through the magnetic field map from survey measurement and numerically integrating to obtain $f(p, r, \theta_0, z)$ for each grid point. An iterative procedure is used to determine the momentum for reconstructed tracks, using Eq. 3.4 as an initial guess. The details of the iteration procedure can be found in [84, 85, 86].

In addition to the charged particle momentum, the track model also determines the trajectory within the central arm magnetic field, which can be used to calculate the track intersections with each detector, and thus facilitate inter-detector hit association (see next section). The length of the trajectories to the TOF and the EMCal are also calculated to provide an estimate of the flight distance, which, together with the time-of-flight measurement, are used for the particle identification.

3.2.3 Matching to Outer Detectors

The ability to accurately associate hits to outer detectors (detectors after PC1) is crucial for the rejection of high p_T background in the charged hadron analysis. As we shall discuss in Chapter 4.4, the background rejection heavily relies on the matching distribution of associated hits in PC2 and PC3. In this section, we discuss the matching to outer detectors focusing on the matching to PC2 and PC3.

Tracks are reconstructed by DC-PC1 and projected to the outer tracking detectors by the track model. These detectors are two dimensional walls extending in r-ϕ and z direction, and sandwiched one after the other. Each of them provides a 3-dimensional hit at the detector wall. A wide window around the track intersection point with the detector plane is searched for a list of candidate hits. The one with the closest distance to the intersection point is identified as the hit associated with the track.

For primary tracks, the distance in both the r-ϕ and the z direction between the track projection point and the associated hit position is approximately Gaussian with a width given by,

$$\sigma_{match} = \sqrt{\sigma_{det}^{match\,2} + (\frac{\sigma_{ms}^{match}}{p\beta})^2} \quad , \tag{3.5}$$

where σ_{det}^{match} is the finite detector resolution, which includes the DC pointing (or α) resolution and the detector spacial resolution, and σ_{ms}^{match} is the multiple scattering contribution. The mean of the residual distribution, $mean_{match}$, is typically small compared to σ_{match} after detector alignment (see next section). A non-zero value of $mean_{match}$ usually results from imperfections in the detector alignment or the magnetic field map used by the track model. These imperfections can lead to a momentum and charge sign dependence of $mean_{match}$.

In this work, the residual distribution of the difference between hit position and track intersection is also referred as the matching distribution. The matching distribution needs to be parameterized separately for all tracking detectors (PC2, PC3, TOF, PbSC, PbGl) for both positive and negative charged particles in r-ϕ and z direction. For both r-ϕ and z of each detector, the mean and width are extracted by a Gauss fit to the matching distribution, and parameterized as function of p_T. As an example, Fig. 3.17 shows $mean_z$, $mean_{r\text{-}\phi}$, σ_z, $\sigma_{r\text{-}\phi}$ and their parameterizations as function of p_T for PC2. The typical matching resolutions for these variables at $p_T = 2$ GeV/c are listed in Table. 3.4, together with the values obtained in RUN-1.

The run-by-run variation of the matching parameterizations are checked. We found that the matching distribution is very stable across the whole RUN-2 period. So a single set of parameterizations is used in the data analysis. Fig. 3.18 shows the run-by-run variation of $\sigma_{r\text{-}\phi}$ at 2 GeV/c in momentum (top panel), and the fitting parameters (bottom panel) according to Eq. 3.5.

Since the track reconstruction in the r-z plane requires the BBC vertex information, uncertainties associated with that measurement can affect the track projection and hence the matching distribution in z at outer detectors.

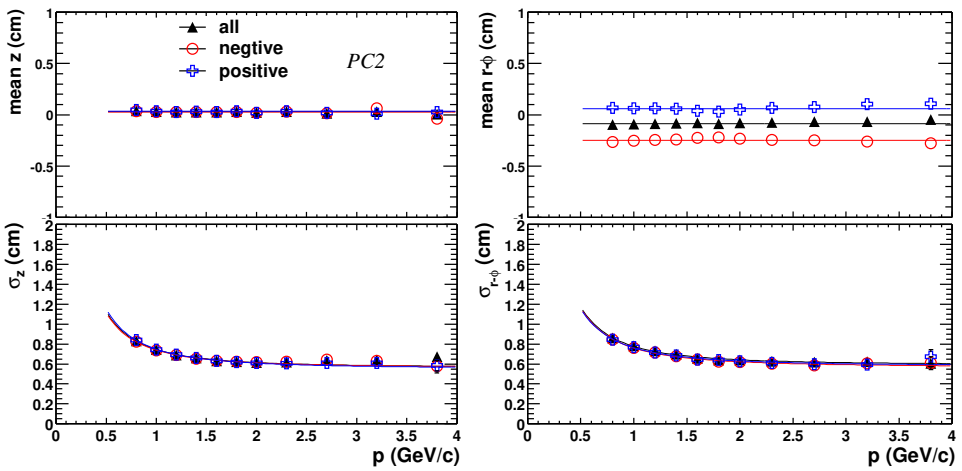

Figure 3.17: PC2 matching variables as function of momentum and charge. From left to right and top to bottom, four panels represents, $mean_z$, $mean_{r\text{-}\phi}$, σ_z and $\sigma_{r\text{-}\phi}$.

Table 3.4: Matching resolutions in z and r-ϕ for various detectors in RUN-1 and RUN-2.

	values for RUN-1		values for RUN-2	
	$\sigma_z(cm)$	$\sigma_{r\text{-}\phi}(cm)$	$\sigma_z(cm)$	$\sigma_{r\text{-}\phi}(cm)$
PC2 West	N/A		0.7	0.63
PC3 East	1.31	1.74	0.9	0.79
PC3 West	N/A		0.9	0.79
TOF East	1.2	2.53	0.92	1.82
PbGl East	N/A		2.16	1.95
PbSc East	N/A		2.23	2.38
PbSc West	2.73	2.76	2.29	2.33

Fig. 3.19 shows this centrality dependence of the matching distribution at the PC2. Three observations can be made from this figure: 1) $mean_z$ systematically drifts to one side, indicating that the BBC measurement systematically deviates from the true vertex location; 2) σ_z increases from central to peripheral collisions, indicating that the BBC z_{vtx} resolution is centrality dependent; 3) No centrality dependency is observed in $mean_{r\text{-}\phi}$ and $\sigma_{r\text{-}\phi}$, which is expected since the collision vertex in the r-ϕ plane is fixed at $r = 0$ and BBC is not used. In data analysis, the centrality dependence of the matching distributions caused by the BBC vertex determination is corrected.

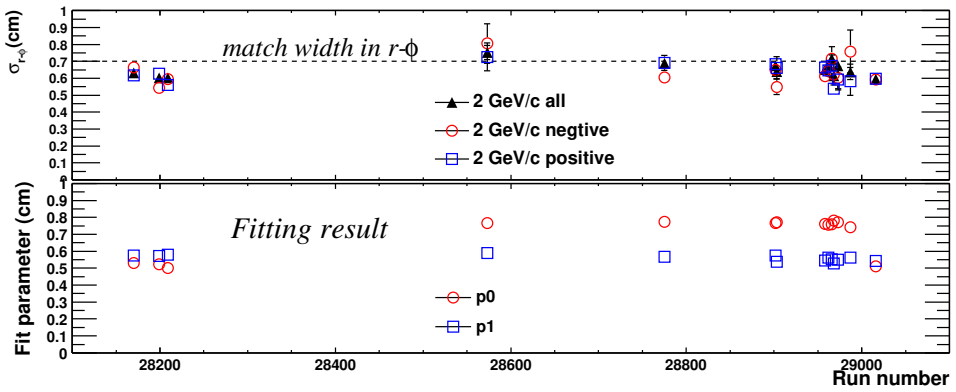

Figure 3.18: Run-by-run variation of the $\sigma_{r\text{-}\phi}$ at 2 GeV/c in momentum (top panel), and the fitting parameters (bottom panel) according to Eq. 3.5. The dashed line at the top panel represents the average.

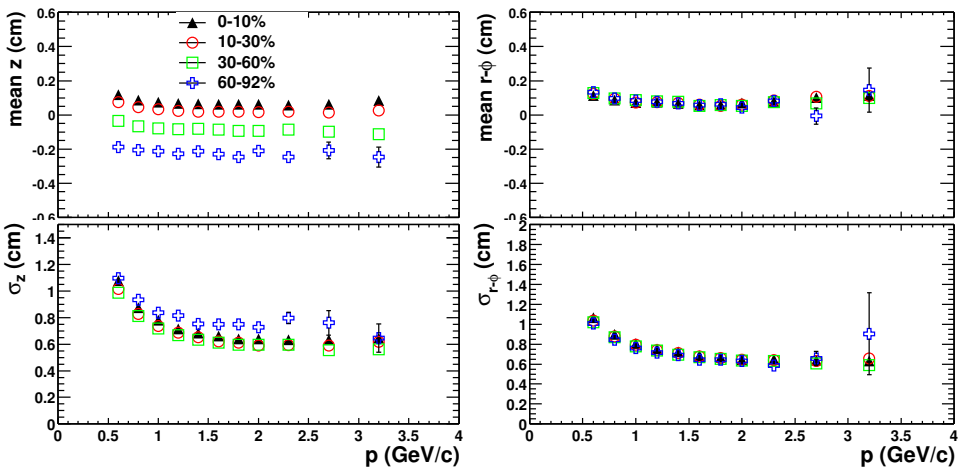

Figure 3.19: Centrality dependence of the matching variables as function of p_T. A centrality dependent variation can be seen in $mean_z$ and σ_z, but not in $mean_{r\text{-}\phi}$ and $\sigma_{r\text{-}\phi}$.

3.2.4 Detector Alignment

From the single hit resolution of 150 μm, the ideal momentum resolution of the DC should be $\delta p/p = 0.4\%p$ (GeV/c) at high p_T. However, the track reconstruction procedure assumes a certain wire geometry, which may be different from the actual wire locations. The measured momentum resolution

could be worse if the detector geometry is not accurately known. Thus a significant effort has been devoted to aligning the wire geometry used in the offline reconstruction. The DC alignment is composed of two tasks: (i) determination of the the location of the DC frame in PHENIX coordinate system, and (ii) the alignment of internal wires relative to the DC frame [88]. The detector alignment is performed using zero-field data, where all tracks are basically straight lines originated from the collision vertex. The systematic deviation of the measured track from the expected location is studied to determine the DC global position and wire positions.

Each DC arm can be shifted or rotated as a solid body relative to the ideal location in the PHENIX coordinate system. The frame has a cylindrical shape. When aligned in global space, the center of the cylinder in the r-ϕ plane should coincide with the collision vertex. Since trajectories are straight lines in zero-field, their α distribution should be centered around zero, and the width should be given by multiple scattering and detector resolution. If the frame is shifted in the r-ϕ plane, the α distribution should systematically deviate from 0. This deviation depends on the azimuthal angle ϕ of the track at the reference radius R_{ref} as,

$$\langle \Delta\alpha(\phi) \rangle = \frac{\Delta y cos\phi}{R_{ref}} - \frac{\Delta x sin\phi}{R_{ref}} + \mathcal{O}\left(\frac{1}{\mathrm{R}^2_{\mathrm{ref}}}\right), \tag{3.6}$$

where, Δx and Δy are the shift of the frame center in x and y direction, respectively. To determine Δx and Δy, we measure $\langle \Delta\alpha \rangle$ for different ϕ slices and then fit with Eq. 3.6 to extract Δx and Δy. The result is shown in Fig. 3.20. The shift $(\Delta x, \Delta y)$ is determined to be (-0.061 cm,-1.012 cm) and (-1.361 cm,-1.132 cm) for the west and the east arm respectively.

The DC X wires are built into wire nets, which are solid cards each holding 12 X wires. The wire position inside the card may not be perfectly aligned with respect to each other. Beyond that, the azimuthal location of the card could also be imperfect. A rotation of the card changes the ϕ of individual wires in a correlated manner. Based on these considerations, the drift chamber internal wire alignment is divided into three tasks: (i) Wires in each card have to be aligned with respect to each other, i.e. they should sit on a straight line. (ii) Each card has to be rotated such that the α distribution in zero-field is centered around zero. (iii) Each X1 and X2 card pair must be relatively aligned, i.e. the pair has to be placed at the same and correct ϕ.

Step i) and ii) are done in a single procedure. The idea is illustrated in Fig. 3.21. The mis-alignment is indicated by the spread of the anode wires around the card and an overall rotation, $\Delta\alpha$, of the card relative to the ideal

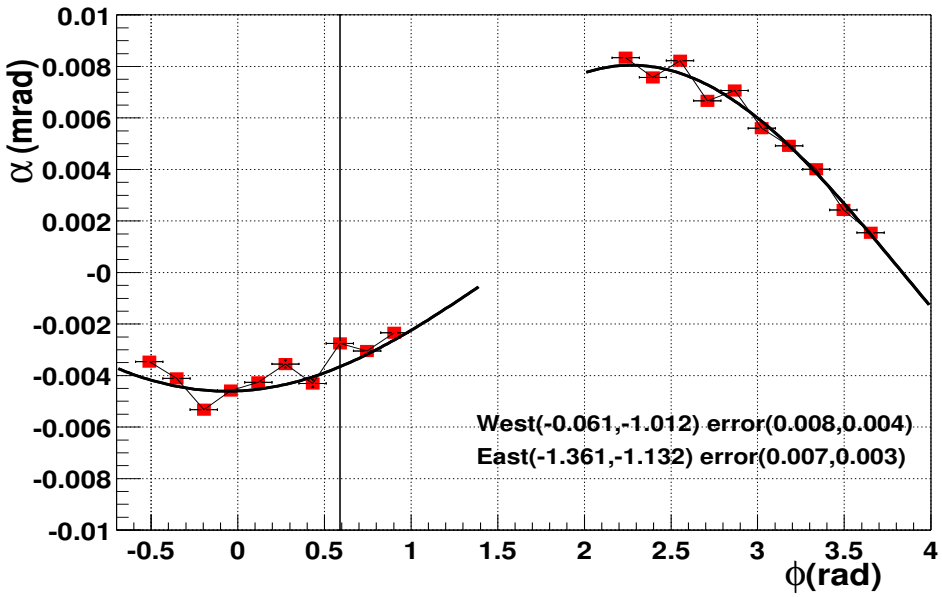

Figure 3.20: $\langle \Delta\alpha \rangle$ as function of ϕ. The marker and the black curve represent the data and the fit, respectively.

direction. The card internal wire alignment is taken into account by a wire-by-wire t_0 correction as discussed in Chapter. 3.1.1. By adjusting the t_0 shift for a given wire, we minimize the residual of the hits to the track using the three-point method, thus effectively aligning the anode wires with respect to each other. The rotation in α is then corrected by a plane dependent t_0 shift

$$\Delta t = n \times \Delta t_0, \tag{3.7}$$

where n is the plane number and Δt_0 is a card dependent constant, to rotate the card to the correct direction.

Step (iii) is performed using the PC1 information. The determination of the cell-by-cell spacing in ϕ direction is based on the precisely known pad spacing of PC1 along ϕ [76] and achieved by minimizing the residual of the track to the PC1 cluster. After all DC X1,X2 cards are placed at their correct locations, the relative alignment between X1 and X2 is checked. The final result is shown in Fig 3.22. The width of the residual distribution is 0.15 and 0.18 $mrad$ for the east and the west arm, respectively. Recall that the single wire resolution is 150 μm, which leads to 0.3 $mrad$ spread in the relative alignment of X1 and X2 cards. The achieved X1 vs X2 alignment is well within this spread.

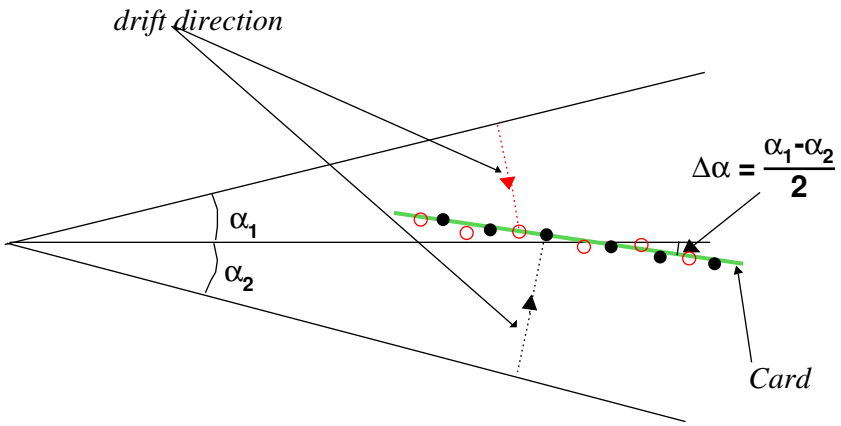

Figure 3.21: A schematic view of the idea for card alignment. The card is indicated by the thick line. The wires with different drift directions are indicated by the open and closed marker. α_1 and α_2 represent the angles corresponding to the drift boundary on each side of the card.

Figure 3.22: The difference in ϕ between X1 card and X2 card for the east and the west arm. The histogram is the distribution and the line is a fit with two Gaussian functions.

3.3 Momentum Calibration

The precise determination of the momentum resolution and the momentum scale is crucial for the high p_T spectra. From Eq. 3.4, one can derive the

following relation between the momentum resolution and the α resolution,

$$\begin{aligned} \delta p/p &= \delta\alpha/\alpha \\ &= \frac{1}{K}\sqrt{(\frac{\sigma_{ms}}{\beta})^2 + (\sigma_\alpha p)^2} \quad , \end{aligned} \tag{3.8}$$

where $\delta\alpha$ is the measured angular spread, which can be decomposed into the contribution from multiple scattering (σ_{ms}) and the contribution from the intrinsic pointing resolution (σ_α) of the DC. At high p_T (> 2 GeV/c), σ_α is the dominating contribution, i.e.

$$\delta_\alpha \simeq \sigma_\alpha \quad . \tag{3.9}$$

Currently, there are two independent methods to determine the momentum resolution. The first method is based on genuine high momentum tracks from zero-field data, which are selected by requiring an association to an energetic hadronic shower in the electromagnetic calorimeters. The angular spread of high momentum particles directly measures the angular resolution of the drift chamber from Eq. 3.9, and thus determines the momentum resolution at high p_T, i.e. $\sigma_\alpha/\alpha \simeq \delta_p/p$. The second method relies on the time-of-flight measurement of identified hadrons by combining information from the BBC and TOF detectors. The width of the mass distribution of identified hadrons can be used to determine the momentum resolution after properly subtracting the contributions from the TOF resolution and the multiple scattering.

Finally, the momentum scale can be determined from the deviation of the measured particle mass from the Particle Data Book value. In this section we discuss in detail the momentum resolution and momentum scale determinations in RUN-2.

3.3.1 Momentum Resolution

Fig. 3.23 shows the α distribution without energy cut for tracks in both the west and the east arm. The same distribution requiring an successively increasing energy cut of 1 GeV, 1.5 GeV, and 2 GeV is shown in Fig. 3.24. We use a double Gauss fit to extract the widths of these distribution. They are summarized in Table. 3.5. The energy cuts reduce the multiple scattering contribution, thus the α widths gets smaller. A 2 GeV energy cut in the EMCal corresponds to on average 4 GeV/c momentum cut [91]. With this cut, the multiple scattering effects become negligible, and the α width is equal to the DC intrinsic angular resolution. Thus $\sigma_\alpha \sim 0.89 \pm 0.03\ mrad$ [6].

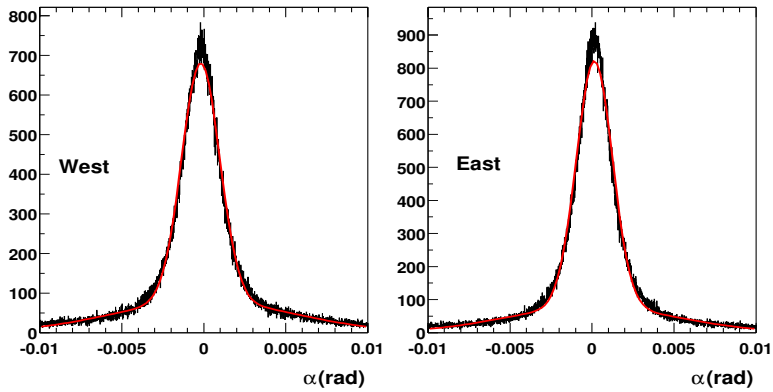

Figure 3.23: α distribution for tracks passing a 2 σ PC3 z matching cut.

Table 3.5: The width of the α distribution for zero-field data. The error is statistical only from the fitting procedure.

Cut	West arm ($mrad$)	East arm ($mrad$)
≥ 2 hits in both X1,X2 X1,X2, $D_z^{PC3} < 2\sigma$	1.16 ± 0.004	1.1 ± 0.004
plus $E > 1$GeV	0.98 ± 0.01	0.88 ± 0.01
plus $E > 1.5$GeV	0.92 ± 0.02	0.88 ± 0.02
plus $E > 2$GeV	0.89 ± 0.03	0.89 ± 0.03

The particle identification ability of the TOF detector provides an independent method to extract both σ_α and σ_{ms}. The TOF distinguishes different particles by the particle mass (m), calculated from the measured momentum (p) and path-length (L) from the track model, and time-of-flight (t) measured by the TOF,

$$m^2 = p^2(\frac{t^2c^2}{L^2} - 1), \tag{3.10}$$

where c is the speed of light. The width of the m^2 distribution depends on the DC angular resolution, multiple scattering, and the TOF resolution. A simple

[6] σ_α can also be measured from the PC3 matching distribution for high p_T tracks using field-on data. This technique is less accurate and was used in RUN1 where the momentum resolution was worse. The details can be found in [87].

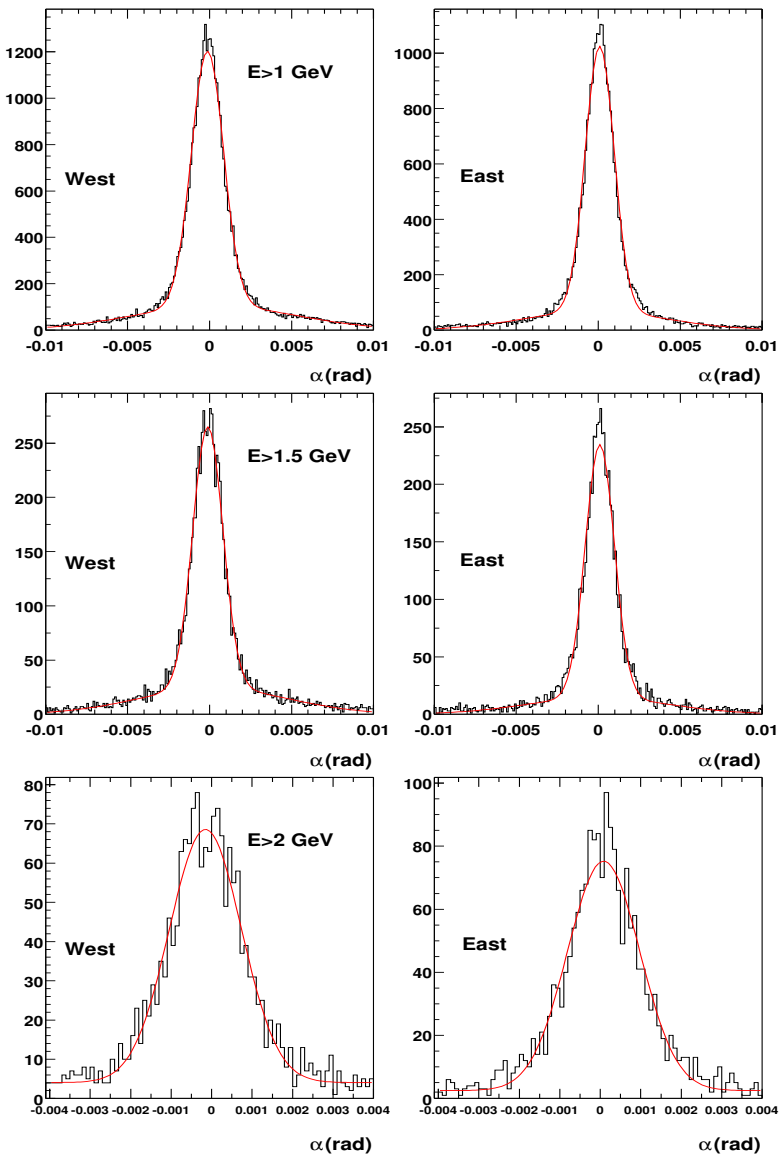

Figure 3.24: α distribution for tracks passing different energy cuts at the EMCal.

error propagation of Eq. 3.10 gives following formula for the width of m^2,

$$\sigma^2_{m^2} = 4m^4\frac{(\delta p)^2}{p^2} + 4p^4\frac{tc}{L}\frac{\sigma_T^2}{t}. \tag{3.11}$$

Combining with Eq. 3.8, one arrives at,

$$\sigma^2_{m^2} = \frac{\sigma^2_\alpha}{K^2}\left(4m^4p^2\right) + \frac{\sigma^2_{ms}}{K^2}\left[4m^4\left(1+\frac{m^2}{p^2}\right)\right] + \frac{\sigma^2_{tof}c^2}{L^2}\left[4p^2\left(m^2+p^2\right)\right] \quad (3.12)$$

This function can be rewritten to represent the width relative to the particle's true m^2,

$$\frac{\sigma_{m^2}}{m^2} = \sqrt{\frac{4\sigma^2_\alpha}{K^2}\left(p^2\right) + \frac{4\sigma^2_{ms}}{K^2}\left[\left(1+\frac{m^2}{p^2}\right)\right] + \frac{4\sigma^2_{tof}c^2}{L^2}\left[\frac{p^2}{m^2}\left(1+\frac{p^2}{m^2}\right)\right]} \quad (3.13)$$

A typical m^2 distribution is shown in Fig. 3.25. The width and centroid of the m^2 for each particle species are extracted by a Gauss fit, and the width as function of p_T is parameterized according to Eq. 3.12 with σ_α,σ_{ms} and σ_{tof} as free parameters. The momentum dependence of the width and centroid from minimum bias data are shown in Fig. 3.26, together with the parameterization. The results obtained are [89, 90],

- $\sigma_\alpha = 0.84\ mrad$
- $\sigma_{ms} = 0.86\ mrad$
- $\sigma_{tof} = 120\ ps$

The momentum resolution is measured to be $\delta p/p \simeq 0.9 \pm 0.1\% \oplus 1.0 \pm 0.1\%\ p$ (GeV/c).

Fig. 3.27 shows the three different contributions to the mass resolution for pions and protons. Since the pion mass is small, the m^2 width in the measured momentum range is dominated by σ_{tof} according to Eq. 3.13, and the pion m^2 width alone can constraint σ_{tof} very well. For protons, the three terms have different contributions at different momenta. The multiple scattering term dominates at low momentum ($p < 0.8$ GeV/c). The momentum resolution term is important for intermediate momenta($0.8 < p < 1.5$ GeV/c) and the TOF resolution starts to become important at $p > 0.8$ GeV/c and dominates the high momentum region ($p > 1.5$ GeV/c). The three terms are roughly equal around 1 GeV/c. Thus this method can give very accurate σ_{ms} and σ_{tof} values, but a less accurate σ_α compared to the first method.

3.3.2 Momentum Scale

In RUN-2, it was found that the magnetic field map used by the track model does not match the real magnetic field perfectly. This lead to a systematic momentum shift which is reflected by a shift of the proton and antiproton

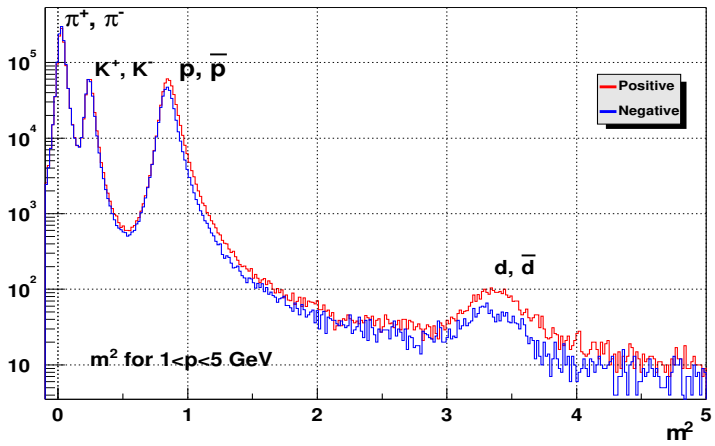

Figure 3.25: m^2 distribution from the TOF in RUN-2.[89]

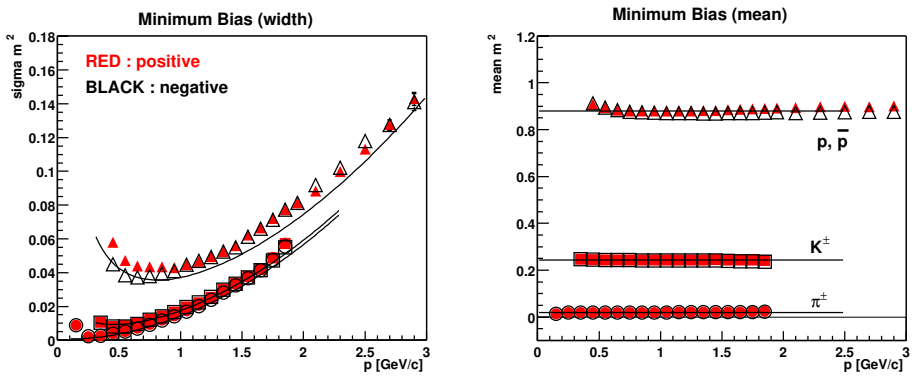

Figure 3.26: Momentum dependence of the width (left) and the centroid (right) of m^2 distributions for each identified particle.[90]

m^2 distributions. This shift, Δ_{m^2}, can be calculated from the momentum shift, Δ_p, as,

$$\Delta_{m^2} = \frac{2m^2\Delta_p}{p} \quad . \tag{3.14}$$

Since Δ_{m^2} is proportional to the particle m^2, a heavy particles like the protons are more sensitive to the momentum scale. Fig. 3.28a shows the measured proton and antiproton m^2 centroid as function of momentum. A 4% shift in the proton's m^2 is clearly visible, which corresponds to a 2% downward momentum

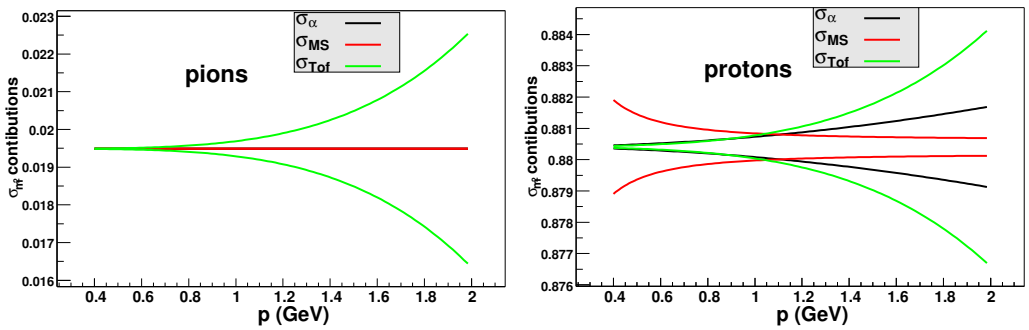

Figure 3.27: The three contributions to the 1σ m^2 width for pions(left) protons(right). Each contribution is shown by a band with different color around the expected m^2 value. [89]

shift. After a factor of 1.022 is applied as momentum scale correction in the offline analysis, the ratio of the calculated m^2 to the Particle Data Book value for all momenta is almost consistent with 1, as shown in Fig. 3.28b. The corrected m^2 value is still about 1% lower than the Particle Data Book value, but it is momentum independent. Given the fluctuation of the points, we quote an error of 0.7% on the uncertainty of the momentum scale, which corresponds to $\pm 1.4\%$ uncertainty on m^2, which is a conservative estimate.

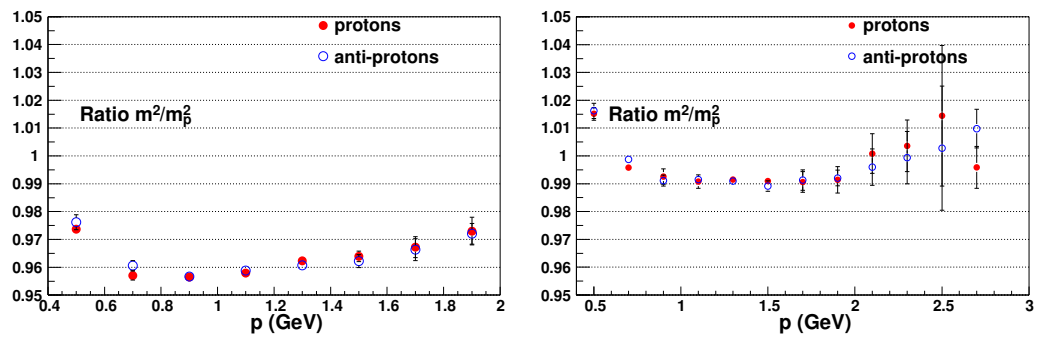

Figure 3.28: Ratio of measured m^2 centroid to the nominal value for protons and antiprotons as function of momentum before (left) and after (right) a momentum scale correction factor of 1.022 has been applied.[89]

Chapter 4

Data Analysis

In this chapter, we describe event selection, the background rejection and background subtraction. We focus on the reduction of the p_T spectra above 4.5 GeV/c. Many of the ingredients necessary but not specific for this analysis have been discussed in Chapter 2 and 3.

4.1 Event Selection and Centrality

4.1.1 Minimum Bias Trigger Definition and Efficiency

During RUN-2, PHENIX sampled an integrated luminosity of 24 μb^{-1} (see Table. 2.2) for $Au-Au$ collisions at $\sqrt{s_{NN}} = 200$ GeV. A sample of minimum bias events used in this analysis is selected according to following conditions on the BBC and the ZDC:

1. BBC conditions
    - A coincidence between the north and south BBC with at least two PMTs fired in each BBC is required. The collision vertex has to satisfy $|z_{vtx}| < 75\ cm$. These cuts are performed by the BBC Level-1 (BBCLL1) trigger online.
    - An offline collision vertex cut of $|z_{vtx}| < 30\ cm$ is required.
2. ZDC conditions
    - At least one forward neutron has to be registered in each of the two ZDCs.

The trigger efficiency for minimum bias $Au-Au$ nuclear interactions related to these cuts is studied by a detailed simulation of the BBC and the

ZDC[92, 93]. First, response for all 124 PMT tubes and the BBCLL1 board logic are tuned in the simulation to match the real data. Then HIJING [18] simulated events are used to determine the BBC trigger efficiency. Fig. 4.1 shows the extracted the BBC trigger efficiency as a function of z_{vtx}. The systematic errors are studied by varying the TDC (Time Digital Convertor) threshold for each PMT (used by the BBCLL1 trigger) and the input dN/dy and collision vertex distribution from HIJING.

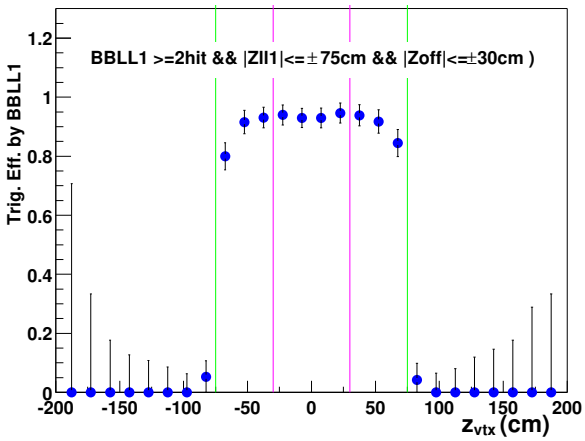

Figure 4.1: the BBC trigger efficiency as function off z_{vtx} from Ref.[92].

The extracted BBC trigger efficiency is

$$\epsilon_{bbc}^{trigger} = 93.1\% \pm 0.4\%(stat.) \pm 1.6\%(sys.) \quad . \tag{4.1}$$

To reject the small percentage of BBC triggers that are "background" events, a ZDC coincidence with at least one neutron on both sides is required. The fraction of BBC triggers that also satisfy the ZDC condition, $\epsilon_{zdc|bbc}^{trigger}$, is shown in Fig. 4.2 as function of run number. The ratio has a maximum value around 97.5% (indicated by the horizontal line). The fact that the ratio drops to lower values in some later runs is in agreement with observations during these runs that the luminosity was high, and the BBC trigger had a higher background rate. It is also possible that the BBC had a "hot" tube in some of these runs. A conservative estimate for the 2.5% exclusive BBC triggers is that 40% of these events are due to ZDC inefficiencies and 60% are "background" events. The ZDC trigger efficiency for events that also satisfy the BBC trigger is

$$\epsilon_{zdc|bbc}^{trigger} = 99^{+1.0}_{-1.5}\% \quad . \tag{4.2}$$

The minimum bias trigger efficiency with the BBC and ZDC coincidence can be calculated as,

$$\epsilon_{minbias}^{trigger} = \epsilon_{bbc}^{trigger} \times \epsilon_{zdc|bbc}^{trigger} = 92.2^{+2.5}_{-3.0}\% \quad . \tag{4.3}$$

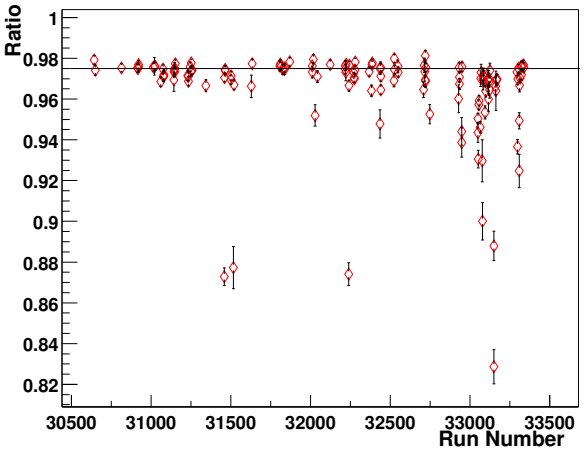

Figure 4.2: $\epsilon^{trigger}_{zdc|bbc}$ as function of run number. The error bars shown are statistical only. (from [93])

4.1.2 Centrality Definition

Both the total energy measured by the ZDC and the total charge measured by the BBC are sensitive to the impact parameter of the $Au-Au$ collisions. Thus each of them can provide an independent centrality definition. The ZDCs measure spectator neutrons that are not bound in deuterons or heavier fragments. The BBC measures the number of charged particles at forward rapidity, $(3.0 < \eta < 3.9)$. The collision centralities are determined from the measured correlation between the fractional charge deposited in the BBC and the fractional energy deposited in the ZDC, using the fact that the charge measured in the BBC is monotonically related to the centrality.

Fig. 4.3a shows the measured correlation between the ZDC fractional energy and the BBC fractional charge during RUN-2. The centrality classes are defined by the so called "clock"-method. For a given (ZDC, BBC) on the ZDC vs. BBC plane, one can calculate the angle ϕ relative to a fixed origin, chosen as $(BBC_0, ZDC_0) = (0.2, 0)$. The full ϕ range is then divided into a certain number of bins, each bin with the same number of counts. The centrality range covered by the minimum bias trigger, (0,92.2%), is divided by the same number of bins with equal ranges. Then we obtain a mapping between the ϕ cut and the centrality ranges in percentages. Fig. 4.3b shows the corresponding charged track multiplicity distribution for some of the centrality classes defined. The more central events have a larger number of tracks per event than the more peripheral events.

Figure 4.3: Centrality definition in PHENIX. The left panel shows the ZDC energy vs. BBC charge, together with centralities defined by the clock method. The right panel shows the corresponding track multiplicity for minimum bias events and the four most central centrality classes.

4.1.3 Glauber Simulation

To estimate the average number of binary collisions $\langle N_{coll} \rangle$ and participating nucleons $\langle N_{part} \rangle$ for each centrality class defined by the clock method, a Glauber model Monte-Carlo simulation that includes the responses of the BBC and ZDC is used. The idea of the Glauber model is introduced in Chapter 1.1.1 and the Glauber variables can be found in Appendix B. In the simulation, 79 protons and 118 neutrons are randomly distributed for each of the two Au nuclei. These two nuclei then collide with each other at random impact parameter. For a given collision, the neutrons that do not collide with other nucleons are counted as forward going neutrons towards the ZDC. In real collisions, these spectator neutrons may miss the ZDC acceptance due to the intrinsic p_T from their fermi motion inside the Au nuclei or because they may be bound in deuterons or heavier fragments and thus swept away by the magnets. This "*neutron loss probability*" is larger in peripheral collisions, because a larger fraction of the spectator neutrons may reside in composite fragments. NA49 experiment has separately measured the number of neutrons, protons, and fragments in the forward direction in $Pb - Pb$ collisions at $158A$ GeV [94]. An approximately linear relation between the spectator-neutron loss probability and the impact parameter b is seen. In PHENIX, the neutron loss probability is determined from data and a slightly different parameterization

is used [95, 96],

$$p_{loss} = 1 - (1 - p_{loss}^{frag.})(1 - p_{loss}^{accep.}). \quad (4.4)$$

where

$$p_{loss}^{frag.} = 0.3305 + 0.0127b + e^{(b-17)/2}, \quad (4.5)$$

is the probability of the neutron bound in charged composite fragments, and

$$p_{loss}^{accep.} = 0.2857. \quad (4.6)$$

is the acceptance loss probability for free neutrons. The energy carried by the remaining spectator neutrons is smeared according to the measured ZDC resolution [70],

$$\frac{\sigma_E}{E} = \frac{218\%}{\sqrt{E/GeV}}. \quad (4.7)$$

For the simulation of the BBC signal [97], we have to assume a relation between N_{part} and the number of charged particles registered by the BBCs. A monotonic relation

$$dN/d\eta \propto N_{part}^{\alpha} \quad (4.8)$$

is assumed and, by default, a linear scaling of the charged particle multiplicity with N_{part} is used in the simulation ($\alpha = 1$). We later vary α to test the sensitivity of the result of the calculation. To take into account of the fluctuation of the number of charged particles for a given N_{part}, the number of charged tracks is sampled according to a poisson distribution for each participant,

$$p(k, \mu) = \frac{\mu^k}{k!} e^{-\mu}. \quad (4.9)$$

The mean value, μ, is chosen such that the condition of having at least two particles in the two BBCs is consistent with the BBC trigger efficiency of 93%. This is true when the mean number of charged particles per participant in one BBC is about 0.5. Finally, in order to take into account the fluctuations in the BBC detector response. For each charged particle, the amount of charge deposited in the BBC is sampled from a Landau distribution.

In the simulation, events are generated in a certain impact parameter range, e.g. $0 - 20\ fm$. The default calculation assumes a radius of the Au nucleus of $R = 6.38fm$, a diffusivity of $a = 0.54\ fm$ and a nucleon-nucleon cross section of $\sigma_{nn} = 42\ mb$. For each event, all Glauber quantities (i.e. N_{coll}, N_{part}, $\langle T_{AuAu} \rangle$ and Ecc), the ZDC energy and the BBC charge are calculated.

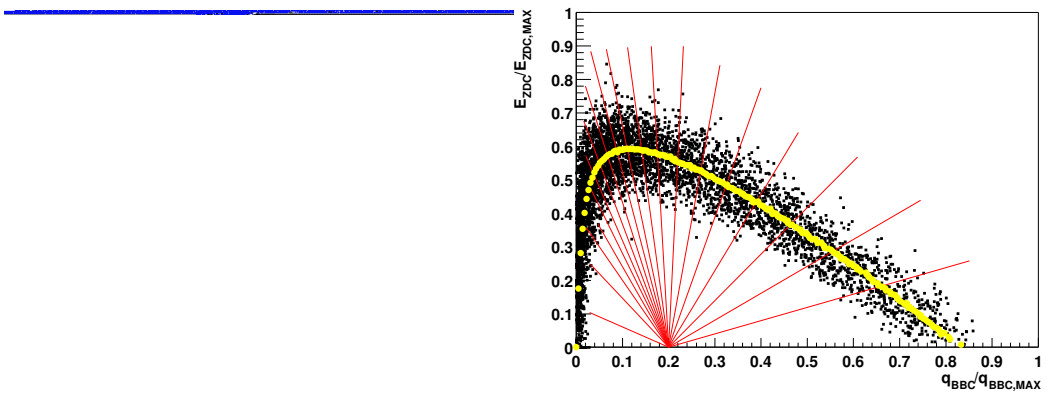

Figure 4.4: The ZDC vs BBC for different number of participants (left panel) The clock-method to define centrality classes for Monte-Carlo (right panel). Figure from Ref.[97].

The left panel of Fig. 4.4 shows how the ZDC and BBC signals vary with an increasing number of participants. The i-th blob corresponds to a cut of $25(i-1) \leq N_{part} < 25i$. The same clock-method discussed in the previous section is used to define the same centrality classes as for data. This is illustrated in the right panel of Fig. 4.4. For each centrality class, the average Glauber quantities, b, N_{part}, N_{coll}, $\langle T_{AuAu} \rangle$ and Ecc are readily obtained.

The systematic errors of the Glauber quantities are estimated by varying the model assumptions [98], e.g.:

1. $\sigma_{nn} = 39\ mb$ and $\sigma_{nn} = 45\ mb$ (default $\sigma_{nn} = 42\ mb$)

2. Woods-Saxon parameters, $R = 6.65\ fm$, $a = 0.55\ fm$ and $R = 6.25\ fm$, $a = 0.53\ fm$. (defaults : $R = 6.38\ fm$, $a = 0.54\ fm$)

3. an alternative neutron loss function in the ZDC

4. a different smearing function for the BBC response.

5. Each nucleon is assumed to have a hard core of 0.4 fm, the distance between the centers of the two nucleons is always greater than 0.8 fm in the Au nucleus.

Fig. 4.5 shows the systematic errors for the total geometric cross section. Fig. 4.6 shows the systematic errors for $\langle N_{coll} \rangle$, $\langle N_{part} \rangle$, $\langle T_{AuAu} \rangle$, and $\langle b \rangle$.

Figure 4.5: Total geometrical cross section for Glauber calculation with different parameters. Figure from [98].

Figure 4.6: Systematic errors on $\langle N_{coll} \rangle$, $\langle T_{AuAu} \rangle$, $\langle N_{part} \rangle$ and $\langle b \rangle$. Figure from [98].

The total inelastic $Au - Au$ cross section at $\sqrt{s_{NN}} = 200$ GeV calculated form Glauber model is,

$$\sigma_{geo}^{Au-Au} = 6847 \pm 542mb \tag{4.10}$$

4.1.4 Centrality Selection for the Charged Hadron Analysis

The centrality classes used in this analysis and corresponding values of $\langle N_{coll} \rangle$, $\langle N_{part} \rangle$ and $\langle T_{AuAu} \rangle$ are listed in Tab. 4.1.4. Two sets of centrality definitions are used: a "*Fine*" set of centralities, which corresponds to 0-5%, ...,15-20%, 20-30%,..., 80-92%, and a "*Coarse*" set of centralities, which corresponds to 0-10%, 10-20%, 20-30%,..., 80-92%. The calculated values of $\langle N_{coll} \rangle$, $\langle N_{part} \rangle$ and $\langle T_{AuAu} \rangle$ for each centrality class are listed in Tab. 4.1.4. The total number of minimum bias events after an offline collision vertex cut, $|z_{vtx}| < 30$ *cm* is 27×10^6. These events are analyzed to obtained the charged hadron spectra presented in this work.

4.2 Tracking and Momentum Measurement of Charged Hadrons

In the charged hadron analysis, tracks are reconstructed using the DC, PC1, PC2, PC3 detectors of the west central spectrometer and the BBC. Tracks are first reconstructed by DC-PC1 (Chapter. 3.2.1), then projected to PC2 and PC3 (Chapter. 3.2.3). Trajectories are confirmed by requiring matching hits in both PC2 and PC3 to reduce the secondary background (Chapter 4.4). The track momenta are measured by a track model using the information from DC and PC1 (Chapter. 3.2.2).

4.3 Background Problem at High p_T

As a first order approximation, the momentum reconstruction is based on Eq. 3.4. Due to the lack of a tracking detector between the beam-axis and the DC, secondary particles from hadron decay and e^+e^- from the conversion of photon in materials before the DC become a background to the charged particle measurement. The background is studied by propagating simulated HIJING [18] events through the GEANT [100] Monte-Carlo simulation of the PHENIX. Fig. 4.7a shows the spatial origin of the background with

Table 4.1: Centrality classes, average nuclear overlap function, average number of $N-N$ collisions, and average number of participant nucleons obtained from a Glauber Monte-Carlo simulation of the BBC and the ZDC responses for $Au-Au$ at $\sqrt{s_{NN}} = 200$ GeV. Each centrality class is expressed as a percentage of $\sigma_{AuAu} = 6.9$ b. Two sets of centrality definitions are used in this analysis: a "*Fine*" set of centralities, which corresponds to 0-5%, ...,15-20%,20-30%,...,80-92%, and a "*Coarse*" set of centralities, which corresponds to 0-10%,10-20%,20-30%,...,80-92%.

Centrality	$\langle N_{coll} \rangle$	$\langle N_{part} \rangle$	$\langle T_{AuAu} \rangle (mb^{-1})$
0 - 5%	1065 ± 105.5	351.4 ± 2.9	25.37 ± 1.77
5 - 10%	854.4 ± 82.1	299 ± 3.8	20.13 ± 1.36
10 - 15%	672.4 ± 66.8	253.9 ± 4.3	16.01 ± 1.15
15 - 20%	532.7 ± 52.1	215.3 ± 5.3	12.68 ± 0.86
0 - 10%	955.4 ± 93.6	325.2 ± 3.3	22.75 ± 1.56
10 - 20%	602.6 ± 59.3	234.6 ± 4.7	14.35 ± 1.00
20 - 30%	373.8 ± 39.6	166.6 ± 5.4	8.90 ± 0.72
30 - 40%	219.8 ± 22.6	114.2 ± 4.4	5.23 ± 0.44
40 - 50%	120.3 ± 13.7	74.4 ± 3.8	2.86 ± 0.28
50 - 60%	61.0 ± 9.9	45.5 ± 3.3	1.45 ± 0.23
60 - 70%	28.5 ± 7.6	25.7 ± 3.8	0.68 ± 0.18
70 - 80%	12.4 ± 4.2	13.4 ± 3.0	0.30 ± 0.10
80 - 92%	4.9 ± 1.2	6.3 ± 1.2	0.12 ± 0.03
60 - 92%	14.5 ± 4	14.5 ± 2.5	0.35 ± 0.10
min. bias	257.8 ± 25.4	109.1 ± 4.1	6.14 ± 0.45

reconstructed $p_T > 2$ GeV/c from the HIJING simulation. Most background originates from the beam pipe and the pole tips, while some background is generated close to the DC. Fig. 4.7b shows the fraction of background tracks in the total track sample as a function of the real p_T. The fraction of background at any p_T is typically less than 5%.

Fig. 4.8 shows the fractional difference between the p_T (p^G) generated in the simulation and the reconstructed p_T (p^R) relative to p^G. For most of the background tracks p^G is close to p^R. However, depending on how close the conversion or the decay point is to the DC, some background tracks may have a small deflection angle α at the DC. Thus, according to Eq. 3.4, they are incorrectly assigned a large momentum. Since the spectra are steeply falling as function of p_T, this background becomes a severe contamination at high p_T. In this analysis, the p_T range over which charged particle production is accessible is limited by this background. In what follows, we exploit the track match to PC2 and PC3 to reject as much of the background as possible, then employ a statistical method to measure and subtract the irreducible background.

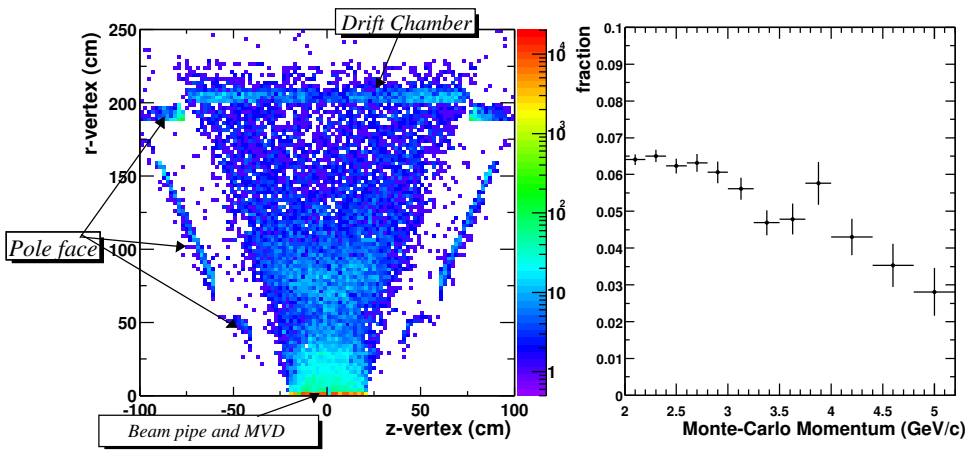

Figure 4.7: a) The background origination point in r-z plane. b) The fraction of backgrounds as function of Monte-carlo p_T.

Figure 4.8: The fractional difference between the generated p_T (p_T^G) and reconstructed p_T (p_T^R) relative to p_T^G.

4.4 Background Rejection

4.4.1 Random Association Background

After tuning the track matching to PC2 and PC3, the displacement in both the r-ϕ and the z direction (represented by D_ϕ and D_z, respectively) between the track projection point and the measured PC hit position is approximately Gaussian with a mean of 0 and a width given by Eq. 3.5 (see Chapter 3.2.3). The width of the Gaussian has two contributions. One is due to the DC and PC detector resolutions, the other is due to multiple scattering.

Fortunately, despite being incorrectly reconstructed with large p_T, the majority of the background particles have low momenta. While travelling from the DC to the PC2 and PC3, they multiple scatter and receive an additional deflection (or residual bend) from the residual (or fringe) field. This deflection enhances the displacement D_ϕ and D_z at PC2 and PC3 and leads to a long tail in the D_ϕ distribution as shown in Fig 4.9a. This tail extends in opposite direction for particles with different charge sign, since they bend in opposite directions. This residual effect is absent in D_z as shown by Fig 4.9b.

The background tail in the matching distribution can simply be removed by applying a tight matching cut at PC2 and PC3. Fig. 4.10a shows the p_T distribution for tracks reconstructed by DC-PC1 only and for tracks with an additional 2σ D_ϕ and 2σ D_z matching cut at the PC3. Fig. 4.10b shows the ratio of the two distributions. The ratio is almost flat at $p_T < 2$ GeV/c around 0.5, indicating that the two spectra are almost parallel to each other. The 50%

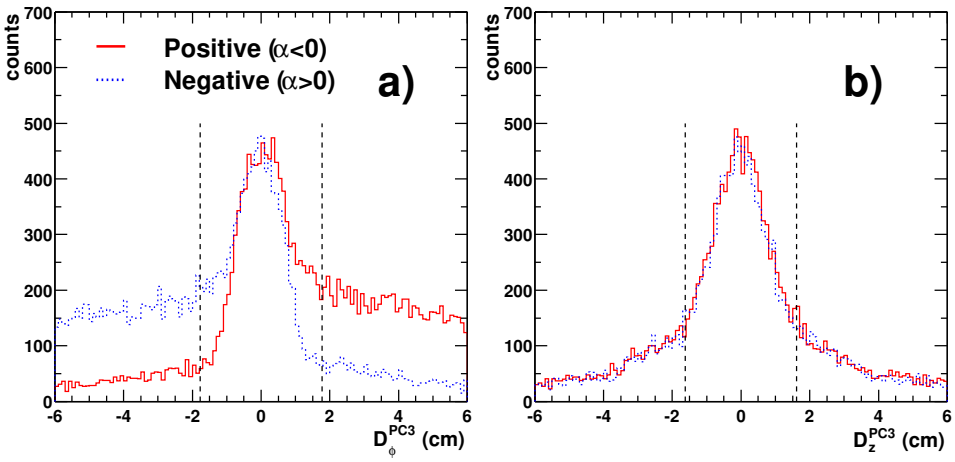

Figure 4.9: a) The displacement in r-ϕ, D_ϕ^{PC3}, for both negative and positive tracks in $5 < p_T < 7$ GeV/c. A 3 σ cut on D_z^{PC3} has already been applied to reduce the background. b) The same distribution in z direction, where a 3 σ cut on D_ϕ^{PC3} has been applied.

reduction of the track yield is due to the loss of acceptance at PC3, hadron decays between DC and PC3, and the matching cut efficiency. However, the fraction of tracks rejected by the PC3 match increases rapidly at $p_T > 2.5$ GeV/c. Since the loss of acceptance and hadron decays between DC and PC3 does not increase with p_T, this increase indicates that the fraction of background in DC-PC1 tracks increases with p_T. These tracks have intrinsically low momenta, and thus they have a bad match at the PC3. At $p_T \sim 5$ GeV/c, more than 95% of the DC/PC1 tracks are background and are rejected by the PC3 match. However, the PC3 matching can not reject all background. In fact, above p_T >5-6 GeV/c, the ratio becomes flat again, indicating a saturation of the PC3 rejection power around a factor of 50. The spectra are once again dominated by background beyond 5-6 GeV/c with only 2 σ PC3 match.

In central $Au - Au$ collisions, the PC2 and PC3 occupancy is about a few percent. The average distance between two PC hits is about 25 cm (assuming 200 hits in each arm). The hit association algorithm assigns the hit closest to the track projection to the track. Occasionally, a track can be wrongly associated to a hit that belongs to a different track. This random association probability p_{ran} is negligible in peripheral collisions, but is about

$$p_{ran} \sim \frac{4\sigma_{D_\phi} \times 4\sigma_{D_z}}{25\ cm \times 25\ cm}$$

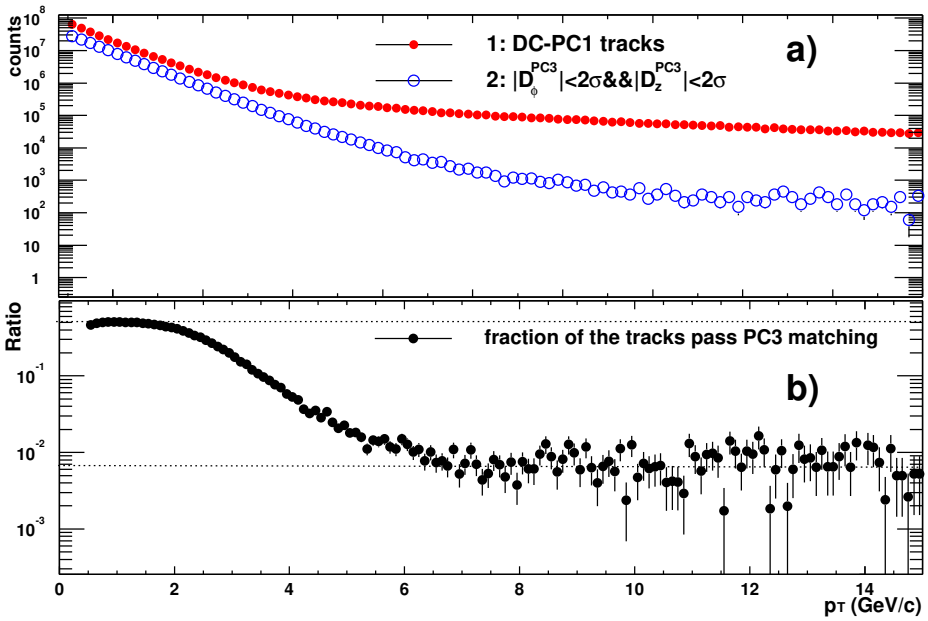

Figure 4.10: a) All tracks from DC/PC1 for minimum bias events and tracks that satisfy 2 σ match at PC3. b) Ratio of the two spectra.

$$= (4 \times 0.63\ cm \times 4 \times 0.6\ cm)/625\ cm^2$$
$$= 1\% \quad (4.11)$$

in central collisions for a $\pm 2\sigma$ matching window in r-ϕ and z. Although the real PC3 hit for most of the background tracks falls outside the matching window, they have this finite probability of 1% in central collisions to randomly associate a hit inside the 2σ matching window. Since more than 90% of the DC/PC1 tracks at $p_T > 5$ GeV/c are background (from Fig. 4.10b), the tracks with random association become comparable in yield to the signal. If the fraction of signal in DC/PC1 tracks is $f < 5\%$ at 4 GeV/c, then the fraction of random background relative to signal tracks is $(p_{ran} \times (1 - f))/f > 20\%$.

One way to estimate the random association background is to randomize the hits at PC3, re-run the track association and study the probability to find a randomly associated hit in the matching window. What has been done here is the following: the track's direction is swapped between north and south and the hit-association between these swapped tracks and hits at all outer detectors is repeated. The swapping is done for every reconstructed track for three different cases, depending on the track z position at the reference radius of the DC:

- For $|z_{DC}| > 35.0$, $z_{DC}^{swap} = -z_{DC}$.
- For $0 < z_{DC} < 35.0$, $z_{DC}^{swap} = z_{DC} - 35.0$ cm.
- For $-35.0 < z_{DC} < 0$, $z_{DC}^{swap} = z_{DC} + 35.0$ cm.

This is called the "*flip-and-slide*" method [99]. this method ensures that the swapped tracks are relatively far from the original direction but have approximately the same rapidity. Fig. 4.11a shows the random association background spectra as function of p_T from minimum bias events. Fig. 4.11b shows its fraction among all DC/PC1 tracks ($\frac{spec3}{spec1}$) and among the PC3 associated tracks ($\frac{spec3}{spec2}$) as function of p_T. $\frac{spec3}{spec1}$ is simply the random association probability and is proportional to the DC/PC1 track density: the increase at low p_T is because of a wider matching window according to Eq. 3.5. At $p_T > 2$ GeV/c, this ratio saturates, which indicates that the random association probability is 0.6% for minimum bias events. Meanwhile, the fraction of random background relative to tracks satisfying the PC3 matching cut ($\frac{spec3}{spec2}$) increases and saturates at about 30%, which indicates that about 30% of the tracks satisfying the PC3 matching come from random association at high p_T. This random association probability is proportional to the event multiplicity and becomes about 70% at 5 GeV/c for the 0-5% most central collisions.

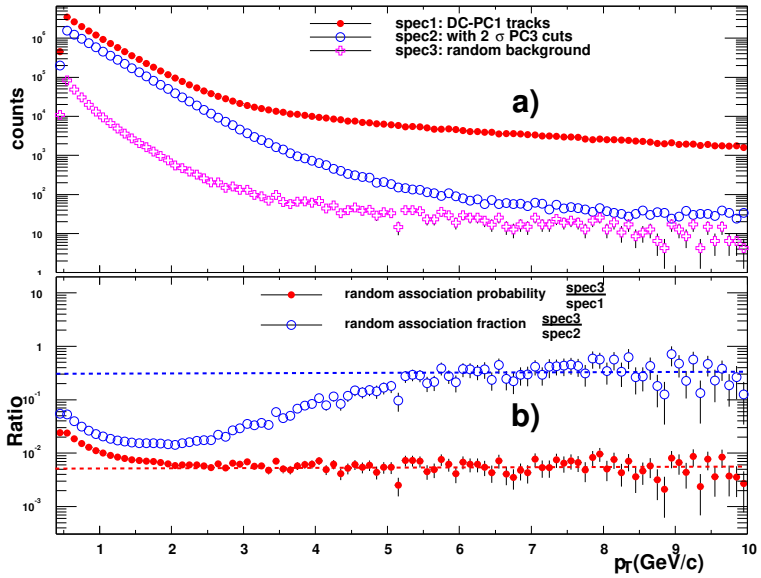

Figure 4.11: a) The same as Fig. 4.10a, but including the random association spectra at PC3 (curve with cross markers). b) The random association probability, and random association fraction relative to tracks that satisfy PC3 match.

Since we know how to estimate the random background statistically, in principle, we can directly subtract this background from the tracks with PC3 match. This subtraction is small for peripheral collisions and for central collisions at $p_T < 3$ GeV/c, but is large for central collisions at $p_T > 4$ GeV/c (see Fig. 4.11b). This technique was used for the RUN-1 analysis [171, 50, 52] and is limited to $p_T < 5$ GeV/c, at which point the random background may exceed the signal for the most central collisions. Fortunately, in RUN2 the PC2 detector is installed in the west arm, which provides an additional veto on the random association background [1]. When PC2 is used, the random association probability is significantly reduced to p^2_{ran} 0.01%. [2] Fig. 4.12 shows the ran-

[1]Since the PC2 only exists in the west arm, we didn't use the east arm for charged hadron analysis.

[2]The random background refers to those tracks with randomly associated hit at both PC2 and PC3. The tracks which have only one random hit at either PC2 or PC3 are not random tracks, because if they have correctly pointed to PC2, then they should also correctly point to PC3 and vice verse. In this case, both the true

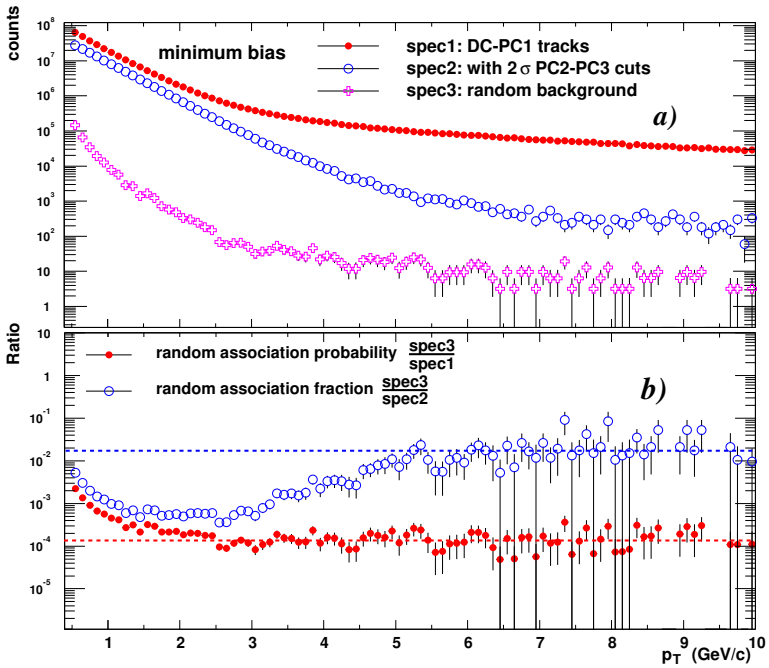

Figure 4.12: a) Same as Fig. 4.11a, but also requiring a 2σ match to PC2. b) The random association probability, and random association fraction relative to tracks that satisfy the PC2, PC3 match cut.

dom association background for minimum bias collisions. The spectra in this figure are the same as in Fig. 4.11, except that a 2σ matching is required for both PC2 and PC3. The p_T dependence of the ratios in Fig. 4.12b is similar to those in Fig. 4.11b. However, the constant levels are significantly reduced. The random association probability drops to 0.012%, while the fraction of random background relative to tracks with 2σ PC2 and 2σ PC3 match is about 1.7%. Fig. 4.13 shows the same curves for the 0-5% most central collisions. The fraction of random background increases to 3%, but is still low enough that we can ignore this contamination to the charged hadron spectra.

4.4.2 Better Matching Variables

Fig. 4.14a shows a schematic view of the track matching to PC2 and PC3 in the west arm. Since both the multiple scattering and the residual

and the randomly associated hits are inside the matching window.

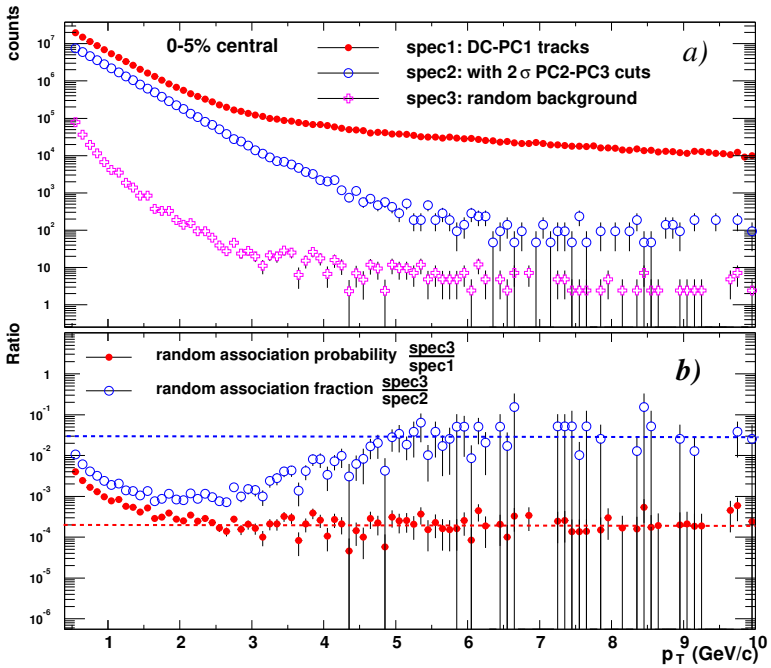

Figure 4.13: Same as Fig. 4.12 for the 0-5% most central collisions.

bend systematically bend the track in one direction, the displacements D_ϕ and D_z are correlated between PC2 and PC3. The correlation in D_ϕ at PC2 and PC3 is shown in Fig. 4.14b. Most of the tracks lie in a narrow window around the diagonal line. The width of this window is given by the PC2 and PC3 detector resolutions, which are on the order of a few millimeters (see Table. 2.3). Multiple scattering and residual bend within and following the DC broaden the matching distribution along the diagonal line. The double-peak structure along D_ϕ^- is related to the finite granularity of PC2 and PC3 pads. The positive directions of D_ϕ^+ and D_ϕ^- are indicated by the arrows. A $\pm 2\sigma$ cut on these variables is illustrated by the dashed box. Similar correlations are also observed in D_z, however, matching distributions for same charge signed particles are symmetric along the diagonal line because there is no residual bend in z direction. To optimize the background rejection, we define two sets of orthogonal variables for D_ϕ and D_z,

$$D_\phi^+ = \frac{1}{\sqrt{2}}(D_\phi^{PC2} + D_\phi^{PC3})$$

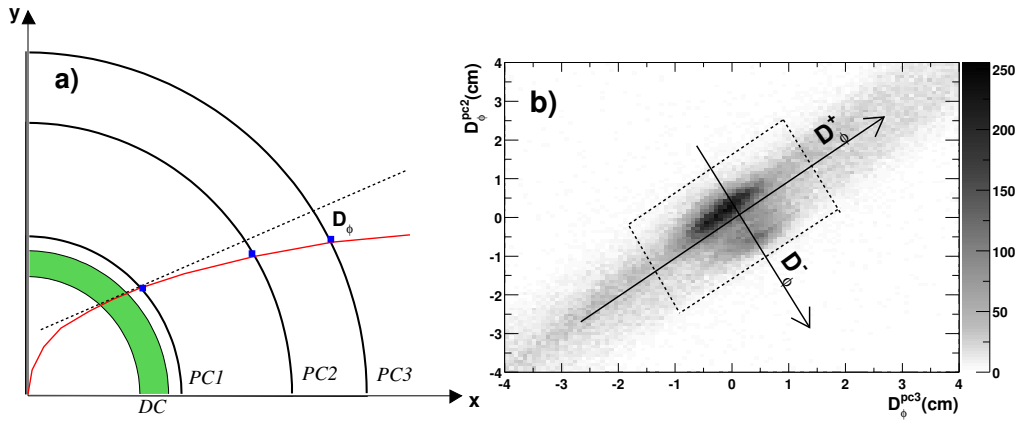

Figure 4.14: a) a schematic view of the matching of tracks to PC2 and PC3. b) D_ϕ^{PC2} versus D_ϕ^{PC3} for tracks with reconstructed $p_T > 4$ GeV/c.

$$
\begin{aligned}
D_\phi^- &= \frac{1}{\sqrt{2}}(D_\phi^{PC2} - D_\phi^{PC3}) \\
D_z^+ &= \frac{1}{\sqrt{2}}(D_z^{PC2} + D_z^{PC3}) \\
D_z^- &= \frac{1}{\sqrt{2}}(D_z^{PC2} - D_z^{PC3}) \qquad (4.12)
\end{aligned}
$$

D_ϕ^+, D_z^+ are the variables along the correlated direction. D_ϕ^-, D_z^- are along the direction normal to D_ϕ^+ and D_z^+, respectively. A $\pm 2\sigma$ cut on these variables is applied in the data analysis. In the remaining discussion, unless stated otherwise, only tracks satisfying these cuts are included.

As shown in Fig. 2.3b, the z component of the fringe field B_z has a strong dependence on the Drift Chamber z , z_{DC}. Since the residual bend is proportional to B_z, it also has a strong dependence on z_{DC}. The z_{DC} dependence of D_ϕ^+ is shown in Fig. 4.15. For tracks with $|z_{DC}| < 40cm$, the displacement D_ϕ^+ at the PC2 appears as two peaks for genuine positive and negative particles due to the fringe field [3]. These displacements decrease towards large z_{DC}, eventually, the two peaks merge with each other and become a single

[3]The charge of the track is given by the α angle measured by the DC: positive for $\alpha < 0$, negative for $\alpha > 0$. However, for background particles, the charge sign based on α angle is not necessary correct. The displacements are caused by the fringe field and their directions reflect the true charge.

peak. The lack of residual bend at large z_{DC} leads to a larger background contamination at large z_{DC}. This is reflected by Fig. 4.16, where the track z_{DC} distribution is plotted for tracks with reconstructed $p_T > 5$ GeV/c. The track density increase rapidly towards high z_{DC}. In order to ensure a significant, almost z independent residual bend, a fiducial cut of $|z_{DC}| < 40cm$ is applied at the DC, which effectively corresponds to a pseudo-rapidity cut of $|\eta|$ <0.18.

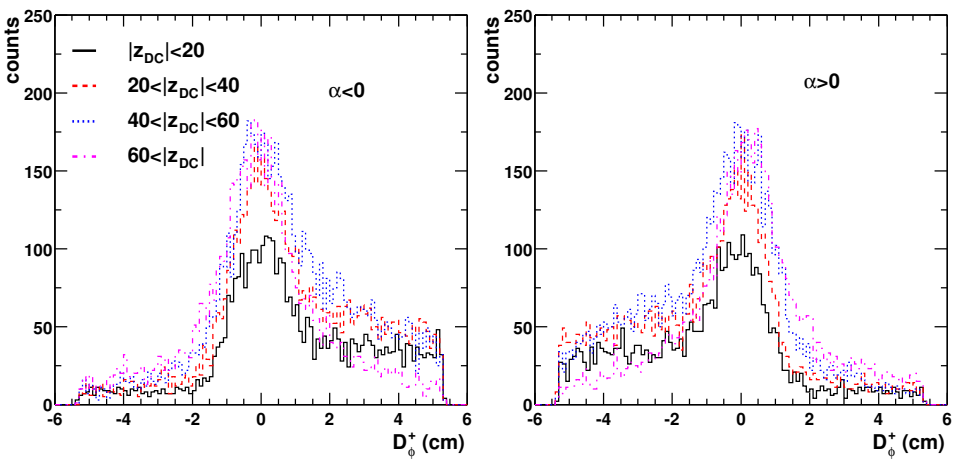

Figure 4.15: The D_ϕ^+ distribution for different z_{DC} ranges for positive (left) and negative (right) particles in $5 < p_T < 7$ GeV/c.

Fig. 4.17 shows the background level after a 2σ matching cut on the variables defined in Eq. 4.12 and a $|z_{DC}| < 40cm$ cut at the DC have been applied. The background level is about 6% for $p_T < 4$ GeV/c, but increases rapidly towards higher p_T. These background tracks are not the random association background discussed in the previous section, but are true decays or conversion tracks which happen to have a good match at both PC2 and PC3. In the next section, we discuss the statistical background subtraction method which subtracts this irreducible background in the 5 to 10 GeV/c range.

4.5 Subtraction of the Irreducible Background

The irreducible background contribution can be subtracted statistically if the shapes of the matching distributions for background and signal are known in detail. In this section, we shall discuss the statistical method we have

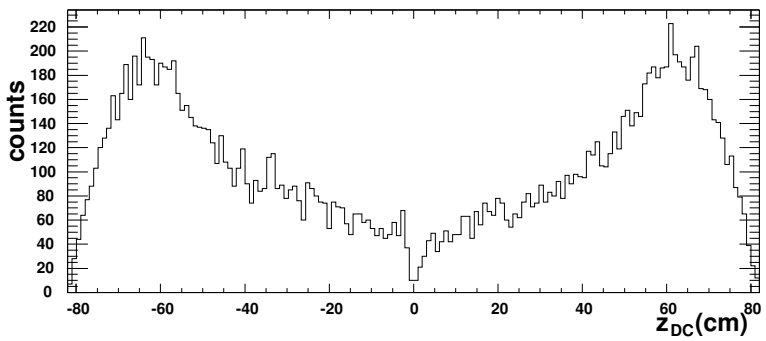

Figure 4.16: Track density as function of z_{DC}

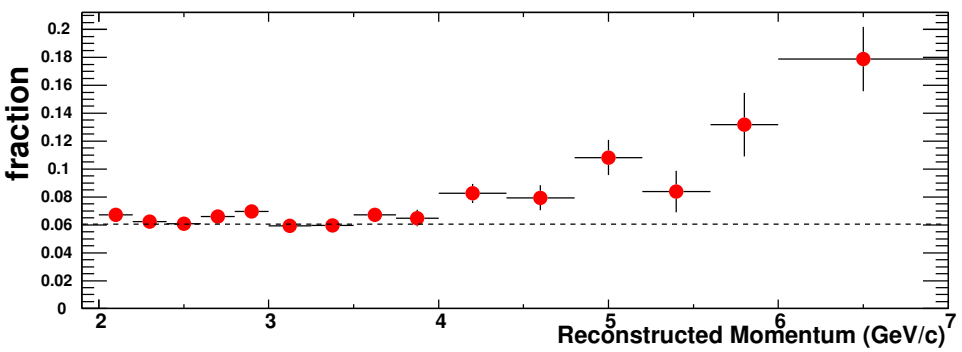

Figure 4.17: HIJING [18] simulation of the background level with 2σ matching cut on matching variables as defined in Eq. 4.12.

Table 4.2: Number of background tracks with reconstructed $p_T > 5$ GeV/c from 100000 minimum bias Au HIJING events.

$\gamma \rightarrow e^+e^-$	Hadron decay	
	$K^{\pm}, K^0_L$	$K^0_s, \Lambda, \Sigma^0, \Sigma^+, \Xi^0, \Xi^-$ and antiparticles
345	132	79

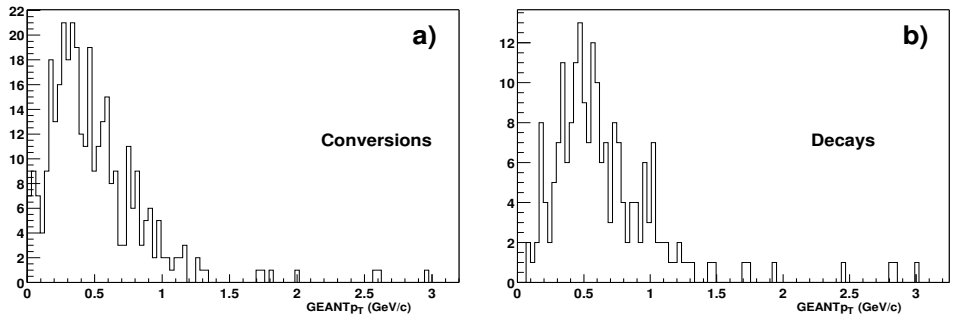

Figure 4.18: True p_T distribution of background tracks from conversions (panel a)) and decays (panel b)).

developed to extract the signal yield based on the detailed knowledge of the matching distributions for background.

4.5.1 Background Sources and Why

After the matching and $|z_{DC}| < 40\ cm$ cuts, the background level is about 6% for $p_T < 4$ GeV/c, but increases rapidly towards higher p_T. This is also indicated by the flat tails at high p_T in Fig. 4.12. Based on full HIJING simulation of 100000 events, we find that at high p_T the background can generally be decomposed into a conversion background (60%) and a decay background (40%) as summarized in Table. 4.2. Fig. 4.18 shows the true transverse momentum distributions of these two kinds of backgrounds. They both average around 0.5 GeV/c. A detailed study of both background sources is presented below. This study is based on another Monte-Carlo HIJING simulations.

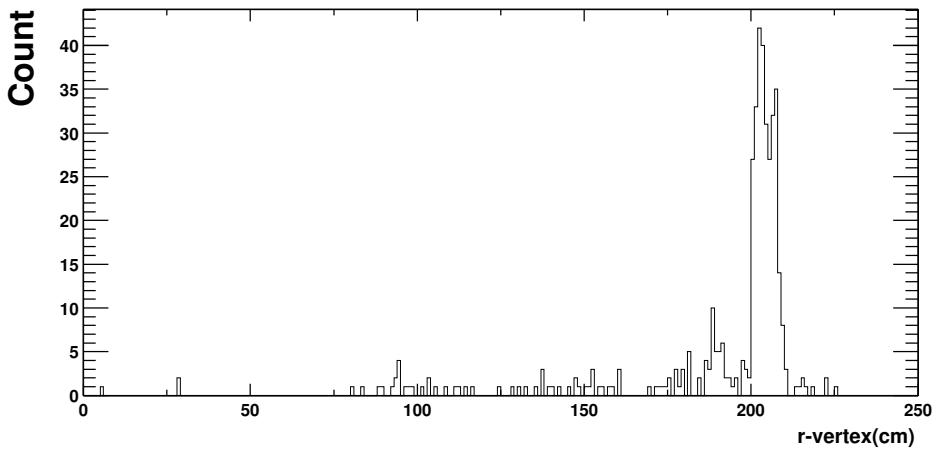

Figure 4.19: Conversion background vertex distribution in radial direction from simulation. These tracks have a reconstructed $p_T > 5$ GeV/c.

Photons from π^0 decays are the major source of conversion background at high p_T. Fig. 4.19 shows the vertex distribution of e^+e^- with a reconstructed $p_T > 5$ GeV/c. Most of the conversion background tracks are generated between the DC entrance window and the X1 nets. The region between beam-axis and the DC also produces some background, but most of these electrons are deflected by the strong magnetic field. The conversion electrons are produced in pairs. The conversion angular distribution is [101],

$$\frac{d\sigma}{d\theta} \propto \frac{\gamma^2\theta}{(1+\gamma^2\theta^2)^2} \quad . \tag{4.13}$$

For 0.5 GeV/c electrons, the half width is roughly $\theta \sim 1/\gamma \sim 1\ mrad$. The conversion pair usually splits in the main bend plane due to the residual bend, but remains close in z direction. Because conversions happen close to the DC, it is very likely that both e^+ and e^- are reconstructed. In principle, a fraction of the conversions can be removed by a close track cuts. [4]

The decay background is more complicated because there are several different sources and the decay kinematics depends on the particle type. We shall discuss in more detail the decay background and how it is falsely reconstructed at high p_T. Recall that the momentum reconstruction relies on Eq. 3.4, which

[4]We haven't exploited this approach in the current analysis.

can be derived as following (in cylindrical coordinates),[5]

$$\begin{aligned}\alpha_1 &= \int_0^R \frac{d|\bar{p}|r}{pR} \\ &= \int_0^R \frac{eB_z r dl}{pR} \\ &= \frac{\frac{e}{R}\int_0^R B_z r dl}{p} \\ &= \frac{K}{p}. \end{aligned} \tag{4.14}$$

where $R = 220\ cm$ is the DC reference radius where α_1 is measured. $K = 86$ MeV/c is the total effective momentum kick at the radius R from the magnetic field.

If a particle decays at radius r, the daughter particles usually receive a momentum kick Δp, which leads to an additional change of α at the reference radius.

$$\alpha_2 = \frac{\Delta p cos(\theta) sin(\phi) r}{pR} \leq \frac{\Delta p}{p}\frac{r}{R} \tag{4.15}$$

where θ,ϕ are the polar and azimuth emission angles of the daughter particle relative to the parent flight direction in the parent's rest frame. α_2 reaches its maximum at $r = R, \theta = 0, \phi = \pm 90°$, i.e. when the particle decays in the main bend plane and the daughter emission angle is perpendicular to the parent's flight direction. The total α angle for the daughter track is,

$$\alpha = \alpha_1(0 \rightarrow r) + \alpha_2 + \alpha_3(r \rightarrow R) \tag{4.16}$$

where α_1 and α_3 are the bend from the field before and after the decay point, respectively. If the momentum kick from the decay is larger than the total effective kick from the field ($\Delta p > K$ according to Eq. 4.14–4.15), the daughter particle can have a decay angle such that the total α in Eq. 4.16 becomes zero. In other words, the daughter particle can be reconstructed with arbitrary p_T depending on the value of r, θ, ϕ.

For example, charged kaons have a large decay length $c\tau$ for the $K \rightarrow \nu_\mu \mu$ decay channel. The daughter muons get a large momentum kick $\Delta p = (m_K^2 - m_\mu^2)/(2m_K) \approx 236\text{MeV}/c > K$. So the muon can have any reconstructed momentum. The same is true also for daughter pions in the $K \rightarrow \pi^0 \pi$ decay channel.

[5]Note that $d\alpha_1 = d|\bar{p}|r/(pR)$ and $d\bar{p} = ed\bar{l} \times \bar{B}$.

K_s^0 and Λ are neutral. Therefore, the magnetic field only affects the daughter particles and Eq. 4.15 becomes $\alpha = \alpha_2 + \alpha_3$. Because of their small $c\tau$ (2.67 cm,7.89 cm for K_s^0, Λ), most of these particles decay very close to the collision vertex. In this case, $\alpha \sim \alpha_3 \sim K/p$. Most of the particles have the correct reconstructed momenta. But as they decay further away from the vertex, the contribution from α_2 becomes important and their daughter particles may have large reconstructed momenta. Interestingly, at a certain decay radius α may become zero. This condition is given by,

$$\begin{aligned} \alpha &= \alpha_2 + \alpha_3 \\ &= \frac{\Delta p}{p}\frac{r}{R} + \frac{K_1}{p} = 0. \end{aligned} \tag{4.17}$$

where $K_1 < K$ is the field integral from r to R. This happens when

$$r = \frac{K_1(r)}{\Delta p} R \tag{4.18}$$

For the $K_s^0 \to \pi^+ + \pi^-$ decay channel, $\Delta p = \sqrt{m_K^2/4 - m_\pi^2} = 206$ MeV/c, which gives $r \approx 50 - 60$ cm. Around this radius, the secondary pions can be reconstructed with any p_T. Fig. 4.20 shows the fractional differences between the reconstructed p_T and the true p_T of the secondary particles from K_s^0 (left panel) and Λ (right) as function of the decay vertex. At about 50-60 cm, the reconstructed p_T of decays πs from K_s^0 can become much larger than the true value. For $\Lambda \to \pi + p$, $\Delta p = 101$MeV/c and the critical radius is about 100 cm.

Because of the differences in the decay kinematics the background matching distributions at high p_T are different for different sources. These differences are shown in Fig. 4.21. We can distinguish three types of background sources based on their matching distributions.

1. e^+e^- **from photon conversions**

   As discussed earlier, most of the e^+e^- reconstructed at high p_T have true p_T around 0.5 GeV/c. The opening angle of e^+e^- relative to the parent photon are very small and most of them are generated close to or within the DC. The residual magnetic field thus splits them in ϕ direction, but not in z because the r component of the magnetic field B_r is very small. As a result, there are two distinct peaks in the D_ϕ^+ distribution but only one centered around zero in D_z^+. However, the width σ of the D_z^+ distribution is about 50% larger than the one for signal tracks because

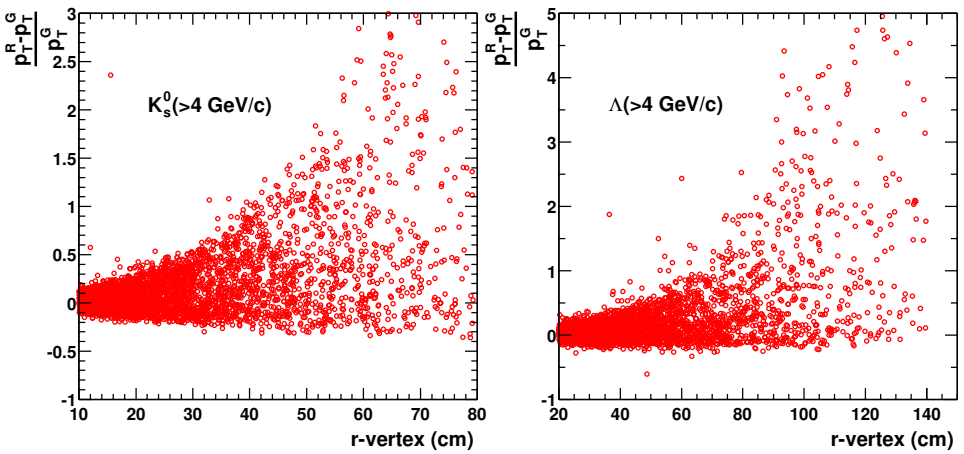

Figure 4.20: The fractional difference between reconstructed p_T^R and true p_T^G for the secondary particles from K_s^0 (left) and Λ (right). The K_s^0 and Λ are required to have $p_T > 4$ GeV/c.

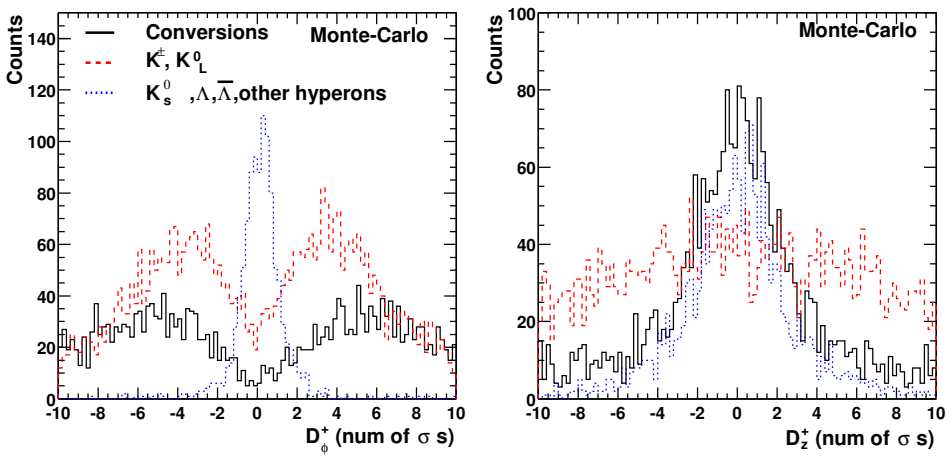

Figure 4.21: The matching distribution in D_ϕ^+(left) and D_z^+(right) for difference background sources from simulation.

of the strong multiple scattering of e^+e^-. Interestingly, since the D_ϕ^+ distribution for conversion electrons is so broad, we can select almost pure electron candidates by:

$$|D_\phi^-| < 2\sigma \&\& |D_z^-| < 2\sigma \&\& |D_z^+| < 2\sigma \&\& |z_{DC}| < 40 \\ \&\& N_{PMT} > 0 \&\& 3\sigma < |D_\phi^+| < 9\sigma \qquad (4.19)$$

where N_{PMT} is the number of PMTs fired in the RICH, which is used to distinguish electrons and high p_T pions from kaons and heavier hadrons (see next section).

2. **Secondary background from weak decays of the long lived strange particles, $K^\pm$ and K_L^0**

   The secondary pions or muons significantly deviate from the original kaon flight direction, much more than conversion electrons. The residual bend produces a similar double-peak structure in the $D^+\phi$ distribution as conversions, but the momentum kick from the decay somewhat smears the distribution. On the other hand, the D_z^+ distributions are dominated by the decay angle and the matching distribution is essentially flat [102].

3. **Secondary background from weak decays of short lived strange particles: K^s and Λ (including other hyperons) decay**

   No double-peak structure is observed in the D_ϕ^+ distribution. Since the decays occur close to the vertex, the reconstructed momenta are usually not very different from the true momenta (like a momentum smearing effect). Because of this, the secondary pion, muon and proton background at high p_T is very rigid. The particles are less influenced by the residual magnetic field and have a narrow D_ϕ^+ match compared to the previous two sources of background. The D_z^+ distribution, however, is about 50% wider than for signal particles, most likely due to the momentum kick from the decay.

4.5.2 Separation of Conversion and Decays

To distinguish between conversion background and decay background, we take advantage of the RICH to tag electrons. Charged particles with velocities above the Cerenkov threshold ($\gamma_{th} = 35$) emit Cerenkov photons, which are detected by the photo multiplier arrays in the RICH (see Chapter 2.2.4 and Ref. [78]). The average Cerenkov radiation length is about $120cm$, which

Table 4.3: Parameters of the electron N_{PMT} distribution from data and Monte-Carlo. R_e is later used for background subtraction.

	Monte-Carlo	Data(min bias)	Data(0-10%)	Data(60-92%)
$\langle N_{PMT} \rangle$	4.69	4.4	4.37	4.28
fraction of Random subtracted	-	6.3%	9.9%	1.4%
$R_e = \frac{N_{PMT} \geq 5}{N_{PMT} > 0}$	58%	47.4%	48.6%	44.4%

leads to about 12 Cerenkov photons for every electron. We characterize the Cerenkov photon yield for a charged particle by N_{PMT}, the number of photon multiplier tubes(PMT) with signals above threshold and within 3.4-12.8 cm distance from the track projection point.

To study the electron's N_{PMT} distribution, we need a sample of pure electrons. One way to obtain pure electrons is to use Eq. 4.19. The electrons satisfying this condition come mostly from photon conversions and have a mean p_T of about 0.5 GeV/c. However, a small fraction of contamination could result from random associations of charged tracks with RICH hits. This contamination is again estimated using the "*flip and slide*" method introduced in Chapter. 4.4.1. Fig. 4.22a shows the raw N_{PMT} distribution[6](solid line), together with the one for fake electrons from random association (dashed line). After the random background is subtracted, the integral of the resulting distribution is then normalized to 1. Fig. 4.22b shows the normalized distribution, together with the distribution from simulation. Some of the parameters of the N_{PMT} distribution are summarized in Table 4.3. The average $\langle N_{PMT} \rangle$ from data is $\approx$ 4.4. Since the N_{PMT} distribution follows Poisson statistics, this corresponds to more than 99% probability to fire at least one PMT. The $\langle N_{PMT} \rangle$ value from simulation is larger, the reason is not completely known, but could indicate that the "*figure of merit*" defined in Eq. 2.3 still needs some fine tuning.

The Cerenkov threshold for pions is $\gamma_{th} m_\pi = 4.8$ GeV. The number of Cerenkov photo electrons detected for a charged track is proportional to $sin^2\theta$ (see Eq.2.3), where $\theta = arccos(1/(\beta n))$ is the Cerenkov angle. Since

$$sin^2\theta \approx \theta^2 \approx 2(1 - \frac{\beta_{th}}{\beta}) \approx \frac{4}{\gamma_{th}^2}(1 - \frac{\gamma^2}{\gamma_{th}^2}) \quad , \tag{4.20}$$

[6]In PHENIX software, the fired N_{PMT} are great or equal to zero. The N_{PMT} for hadrons which do not fire RICH is set to be -1.

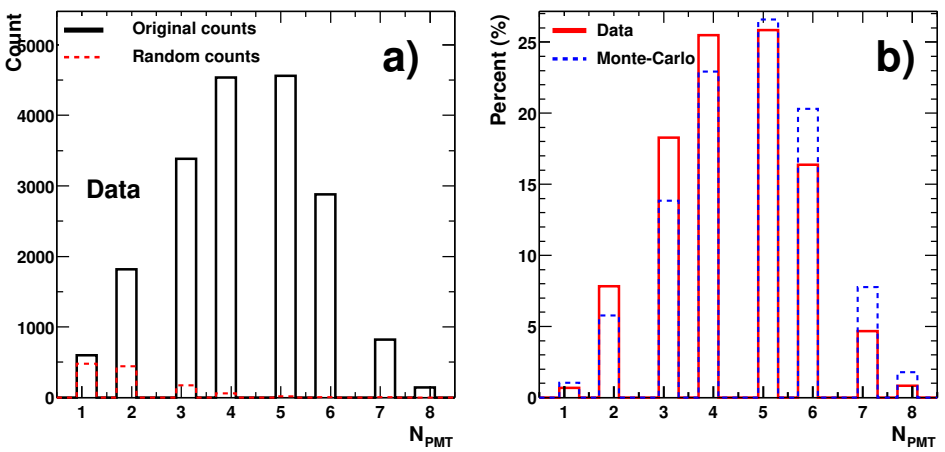

Figure 4.22: a) Raw N_{PMT} distribution (solid line) and the estimated random association background (dashed line). b) The probability distribution of N_{PMT} for data after subtracting random background(solid line) and for Monte-Carlo (dashed line).

θ increases slowly as function of p_T. Consequently, the number of associated PMTs reaches its asymptotic value only well above 10 GeV/c[7]. Fig. 4.23 shows the $\langle N_{PMT} \rangle$ distribution for charged pions as function of p_T from Monte-Carlo. The $\langle N_{PMT} \rangle$ increases from 1.4 at 6 GeV/c to 2.9 at 8 GeV/c and 3.7 at 10 GeV/c. Note that since the Monte-Carlo overestimated the $\langle N_{PMT} \rangle$ for electrons, these values should be smaller for real data.

Based on the discussion above, we can split the charged track sample with $p_T > 5$ GeV/c using the RICH as following,

$$\begin{aligned} N_A(all\ tracks) &= N_R(tracks\ with\ N_{PMT} \geq 0) + N_{NR}(tracks\ with\ N_{PMT} < 0) \\ N_R &= S_R(signal\ \pi^{\pm}) + N_e(conversions) \\ N_{NR} &= S_{NR}(signal\ \pi^{\pm}, K^{\pm}, p^{\pm}) + N_{decay}(decays) \end{aligned} \tag{4.21}$$

The corresponding p_T distributions for N_A, N_R, N_{NR} are shown in Fig. 4.24.

[7]In addition, pions just above threshold have a very small ring radius. Since N_{PMT} is counted within 3.4-12.8 cm from the ring center, this further reduces the N_{PMT} for low p_T pions.

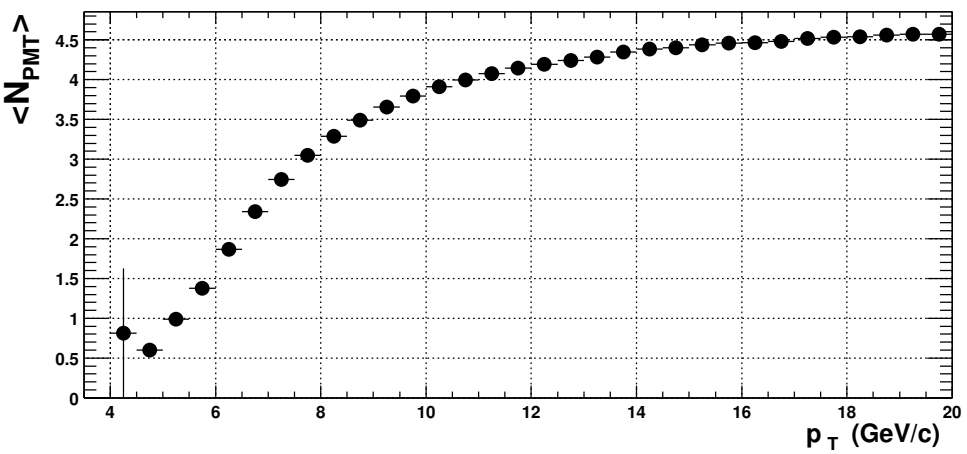

Figure 4.23: The $\langle N_{PMT} \rangle$ as function of p_T for $\pi^+ + \pi^-$ from Monte Carlo.

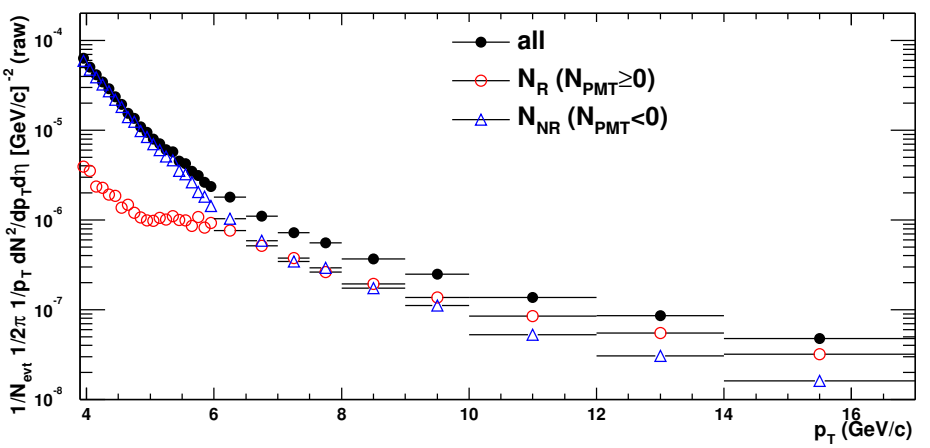

Figure 4.24: Raw spectra for all tracks (N_A), tracks with RICH hit (N_R) and tracks without RICH hit (N_{NR}) according to Eq. 4.21.

4.5.3 Conversion Background Subtraction

Tracks (N_R) with at least one associated RICH PMT contain both conversion electrons and real pions. The shoulder structure between 5-7 GeV/c for N_R tracks in Fig. 4.24 already indicates that there is a large fraction of pions in this sample. For pions with $p_T < 10$ GeV/c, $\langle N_{PMT} \rangle$ has not reached its asymptotic value. So for the p_T range of 5-10 GeV/c, a requirement of $N_{PMT} \geq 5$ can reject most of the pions (see the later part of this section starting from page 98.) while preserving a well-defined fraction

$$R_e = \frac{N_e^{N_{PMT} \geq 5}}{N_e} \quad , \tag{4.22}$$

of the electrons, where $N_e^{N_{PMT} \geq 5}$ is the number of electrons with $N_{PMT} \geq 5$. Once R_e is known, the total electron background can be calculated from Eq.4.22 as

$$N_e = \frac{N_e^{N_{PMT} \geq 5}}{R_e} \quad . \tag{4.23}$$

The the number of real pions in the RICH-associated sample is then obtained by subtracting the electrons from N_R,

$$S_R = N_R - \frac{N_e^{N_{PMT} \geq 5}}{R_e} \quad . \tag{4.24}$$

Fig. 4.25 shows the measured $R_e^m = \frac{N_e^{N_{PMT} \geq m}}{N_e}$ as function of p_T below 11 GeV/c for different N_{PMT} threshold, m. Electrons are selected based on Eq. 4.19 and with random association background subtracted. From 5 to 11 GeV/c, the variation of R_e^m as function of p_T for different N_{PMT} cuts is very small, specifically, the variation of $R_e = R_e^5$ is less than $\pm 3\%$ (absolute error, bracketed by the dashed line). The fitted value for $N_{PMT} \geq 5$ is $46.7 \pm 0.8\%$. As we extend the p_T range as shown in Fig. 4.26, however, we do see a weak p_T dependence. The origin is not clear yet, but this variation is included in the systematic error estimation of R_e. Fig. 4.27 shows the R_e values as function of p_T from Monte-Carlo simulation. Clearly, the simulation has a larger R_e than observed in real data.

R_e also needs to be studied as function of centrality, Table 4.3 already listed R_e for several centrality classes. The complete centrality dependence of R_e is shown in Fig. 4.28. We have bracketed the variation of R_e for all centralities with $\pm 4\%$ absolute error. For peripheral collisions, R_e values are slightly different, but they still agree within 1σ statistical error [8]

[8] For peripheral collisions, the measured spectra reach only about 7 GeV/c. At

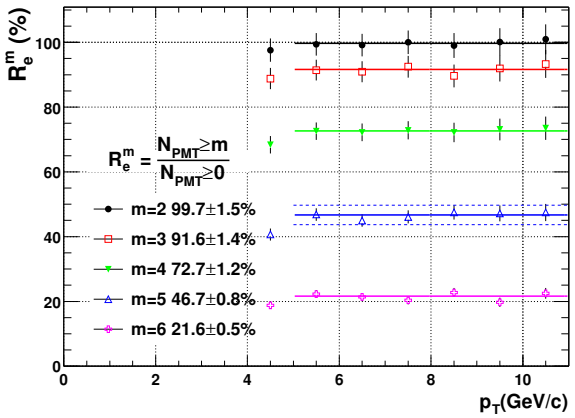

Figure 4.25: R_e^m as function of reconstructed p_T for different N_{PMT} threshold m for minimum bias data. The definition of R_e^m is given in the figure.

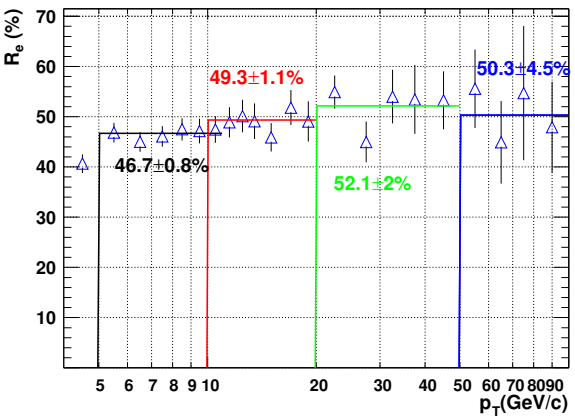

Figure 4.26: The fitted $R_e = R_e^5$ value for different reconstructed p_T ranges from data.

7 GeV/c, the amount of conversion background contamination is small. Even if we double the error on R_e, the systematic error from background subtraction is not the dominate systematic error.

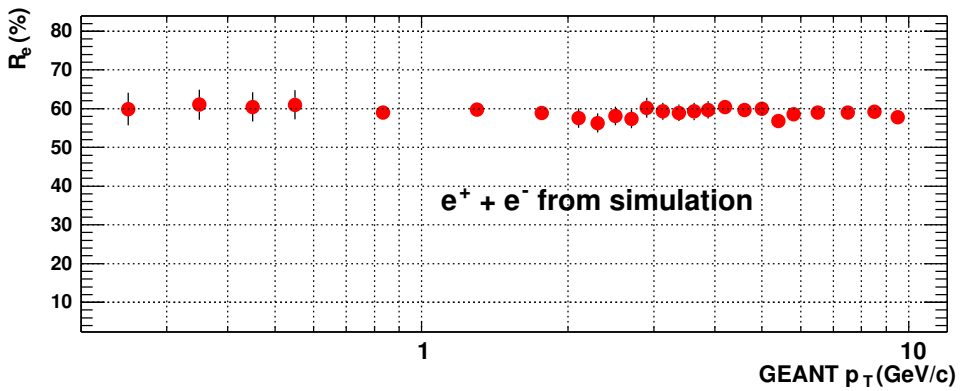

Figure 4.27: R_e as function of true p_T from the simulation of single e^+ and e^-.

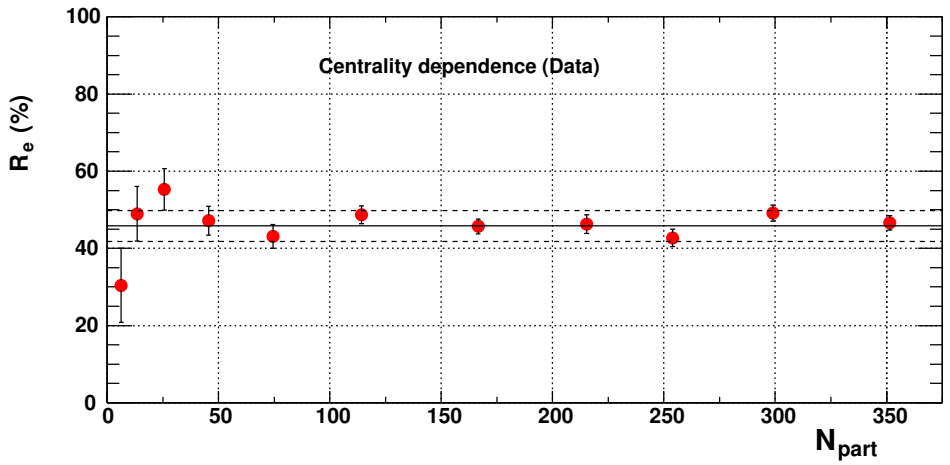

Figure 4.28: R_e as function N_{part}. The solid line indicates the average value, and the dashed line indicates the estimated systematic uncertainties.

In conclusion, the measured value for R_e is,

$$R_e = 0.458 \pm 0.03(p_T \ dependent) \pm 0.04(N_{part} \ dependent) \tag{4.25}$$

The R_e is the average from Fig.4.28, the errors take into account the variation as function of p_T and centrality.

The conversion background subtraction based on Eq. 4.22–4.24 is presented in Fig. 4.29 for a sample range of $6 < p_T < 7$ GeV/c in the D^+_ϕ distribution. Also shown is the matching distribution for conversion electrons from the Monte-Carlo simulation. The contributions from pions and electrons are clearly distinguishable. The shape of the simulated electron background matching distribution agrees with that from real data very well. In Fig. 4.30, the raw minimum bias p_T spectrum for tracks with RICH association is decomposed into the estimated electron spectrum and pion spectrum, the spectrum for random association tracks is also shown.

With this method, a small fraction of genuine pions, which satisfy $N_{PMT} \geq 5$, is subtracted. This fraction, R_π, is negligible below 7 GeV/c, but increases rapidly towards higher p_T. We can estimate R_π from a clean sample of high p_T pions, which are selected by requiring a $N_{PMT} > 0$ and a 2 GeV/c energy cut in EMCal. This cut removes most of the electron backgrounds, since most

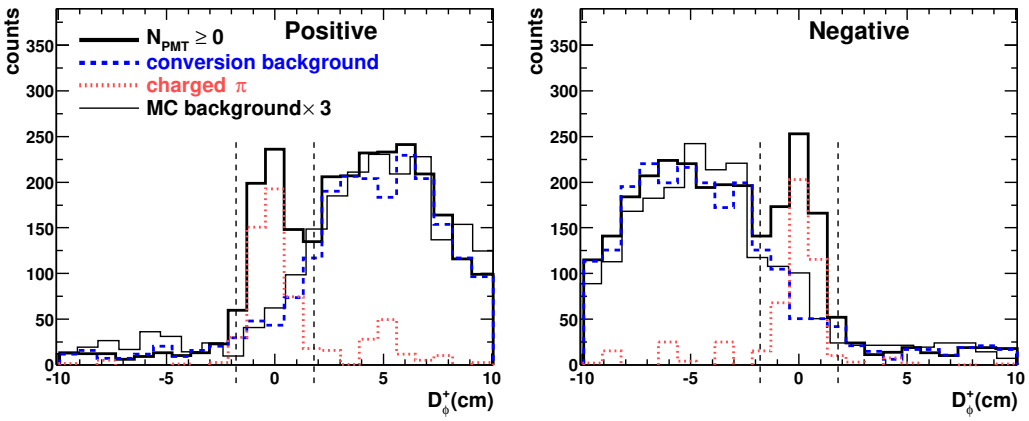

Figure 4.29: An illustration of the background subtraction in D^+_ϕ for tracks with associated RICH PMTs and $6 < p_T < 7$ GeV/c. The subtraction is shown for minimum bias events and separately for positively (left) and negatively (right) charged tracks. Since e^+ and e^- are deflected in opposite directions by the fringe field, they are shifted to positive and negative directions, respectively. The first three distributions represent the raw counts for all tracks with RICH association (solid line), the estimated conversion background based on R_e method (dashed line) and the charged π (dot-dashed line) that were obtained by subtracting the dashed line from the solid line. The thin solid line represents the matching distribution of background electrons from the Monte-Carlo simulation, arbitrarily scaled to match the data. The 2 σ matching window is illustrated by the vertical dashed line.

Figure 4.30: Background subtraction for N_R tracks. There are very little random associates left at $p_T > 6$ GeV/c.

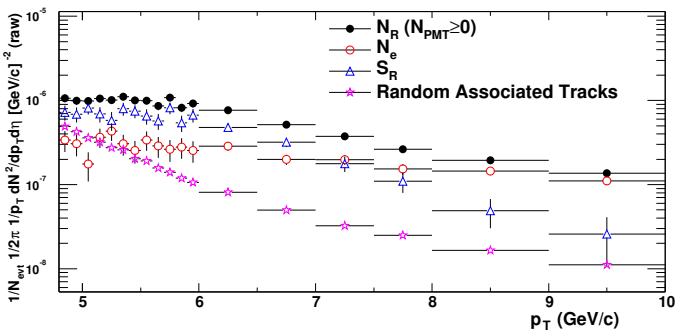

of the electrons have energies below 2 GeV/c (see Fig. 4.18). The R_π values are listed in Table. 4.4.[9] Despite of the limited statistics, R_π steadily increases

[9]Negative counts are an artifact of the random background subtraction procedure on a distribution with limited statistics.

Table 4.4: Yield of charged pions as function of p_T with different N_{PMT}, with random background subtracted. Charged pions are selected with 2 GeV/c energy cut in EMCal.

p_T (GeV/c)	N_{PMT}						R_π(%)
	0	1	2	3	4	≥ 5	
5-6	61	224	130	23	13	23	5
6-7	24	141	157	53	22	9	2.3
7-8	7	40	86	40	20	7	3.6
8-9	2	7	35	31	16	8	9
9-10	0	-1	16	16	9	6	15
10-20	1	-1	13	18	25	31	55

with p_T as expected. R_π is less than 5% for $p_T < 8$ GeV/c and $< 15\%$ for $p_T < 10$ GeV/c (with some uncertainties due to the limited statistics).

The pion over-subtraction can also be estimated from Monte-Carlo simulation. Fig. 4.31 shows the RICH response for pions as function of p_T. R_π continuously increases with p_T until 20 GeV/c. R_π is 0 at $p_T < 6$ GeV/c, 3% for 6-7 GeV/c, 10% for 7-8 GeV/c, 17% for 8-9 GeV/c and 23% for 9-10 GeV/c. Since we know that our simulation overestimates R_e, it is reasonable to assume that it also overestimates R_π, and the Monte-Carlo value can serve as an upper limit on R_π. From R_e and R_π, the over-subtraction of pions can be readily calculated. First, similar to Eq. 4.23,

$$N_\pi = \frac{N_\pi^{N_{PMT}\geq 5}}{R_\pi} \quad , \tag{4.26}$$

where N_π is the total number of pions. If the total number of tracks with $N_{PMT} \geq 5$ is $N^{N_{PMT}\geq 5}$, then $N^{N_{PMT}\geq 5} = N_e^{N_{PMT}\geq 5} + N_\pi^{N_{PMT}\geq 5}$, and the total number of tracks S_R after background subtraction is,

$$S_R = N_\pi - \frac{N^{N_{PMT}\geq 5}}{R_e} = N_\pi(1 - \frac{R_\pi}{R_e}) \quad , \tag{4.27}$$

and the number of over-subtracted pions is

$$N_\pi \frac{R_\pi}{R_e} = S_R(\frac{1}{\frac{R_e}{R_\pi} - 1}) \quad . \tag{4.28}$$

We only have limited information about R_π from data and simulation. We do know that the Monte-Carlo gives an upper limit on the R_π value. So

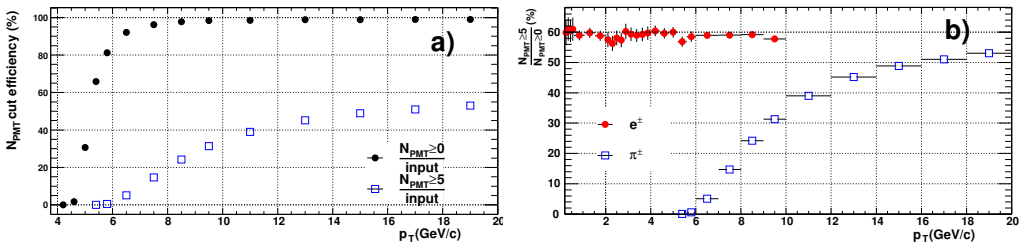

Figure 4.31: a) RICH efficiency for charged pions as function of generated p_T. b) R_e and R_π from the MC simulation as function of generated p_T.

Table 4.5: The systematic error on S_R, ϵ_π, due to pion over subtraction. The first row is used in the analysis.

p_T (GeV/c)	< 6	6-7	7-8	8-9	9-10
ϵ_π (MC)	$< 1\%$	4%	13%	28%	55%
ϵ_π Data	$< 1\%$	4%	5%	18%	31%

the approach we follow here is to correct the measured yield up by 50% of the estimated π over-subtraction estimated from Monte-carlo,

$$\epsilon_\pi = 0.5 \times (\frac{1}{\frac{R_e}{R_\pi} - 1}), \tag{4.29}$$

and assign a 100% systematic error on the correction. The values of ϵ_π are summarized in Table. 4.5, where the first row lists the values used in this analysis.

Based on Fig. 4.31a, an $N_{PMT} \geq 0$ cut is $> 95\%$ efficient for pions in the p_T range of 7-10 GeV/c. So the pion spectra obtained after conversion background subtraction, pion over-subtraction correction, and the full efficiency correction (see Chapter 5) can be compared directly with published π^0 spectra [54]. This comparison is shown in Fig. 4.32 for three centrality selections. The two spectra agree quite nicely, although the statistical error bar for charged pions are quite large.

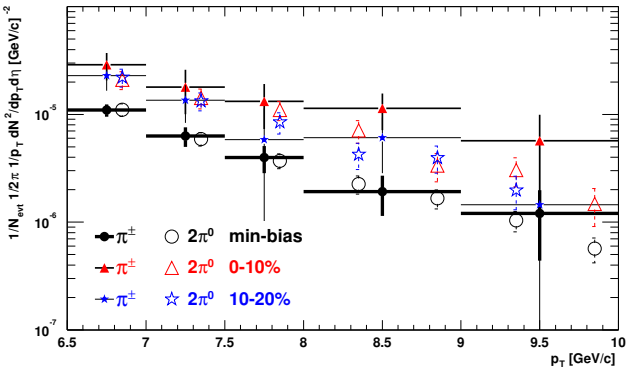

Figure 4.32: Fully corrected charged pion spectra compared to π^0 spectra for three centrality classes. The π^0 data points have been shifted to the right by 0.1 GeV/c for better distinction.

4.5.4 Decay Background Subtraction

The tracks with no associated RICH PMT (N_{NR}) includes π, K, p [10], contaminated by the decay background. The two decay background sources, $K^{\pm}, K^0_L$ and K^0_s, Λ, have very different decay kinematics and thus very different matching distribution. To study them in detail, we run a large statistics HIJING simulation (about 7 million central HIJING events) and propagated events through the full PHENIX detector response simulation. For each of the decay background sources, we obtain the input p_T spectrum of the parent particle and also the reconstructed p_T spectrum for daughters. The HIJING input spectra do not match exactly with the identified spectra measured by PHENIX [103], we need to tune the simulation accurately.

Fig. 4.33a shows the primary charged kaon p_T spectra together with the spectra from parent kaons and secondary particles from the HIJING simulation. As we change the threshold on the reconstructed p_T of the daughter particles from 5 to 10 GeV/c, the shape of the parent kaon p_T distributions does not change. This indicates that the background above 5 GeV/c is not correlated with the true p_T and thus the matching distributions should become independent of reconstructed p_T as confirmed in Fig. 4.33b.

Due to the isospin symmetry, the K^0_s, K^0_L, K^+, and K^- primary yields should be equal to each other. Thus the K^0_s decay contribution is better constraint by comparing it relative to the primary $K^{\pm}$ yield. This is shown in Fig. 4.34. The p_T dependence of the K^0_s decay background is similar to the primary kaon distribution. This is different from Fig 4.33, where the kaon decay spectra shape is insensitive to the actual kaon spectra at high p_T. The reason is that the matching distributions for K^0_s decay products are

[10] At $p_T > 7$ GeV/c, more than 95% of all charged π fire the RICH, so only a negligible fraction of pions is included in N_{NR}.

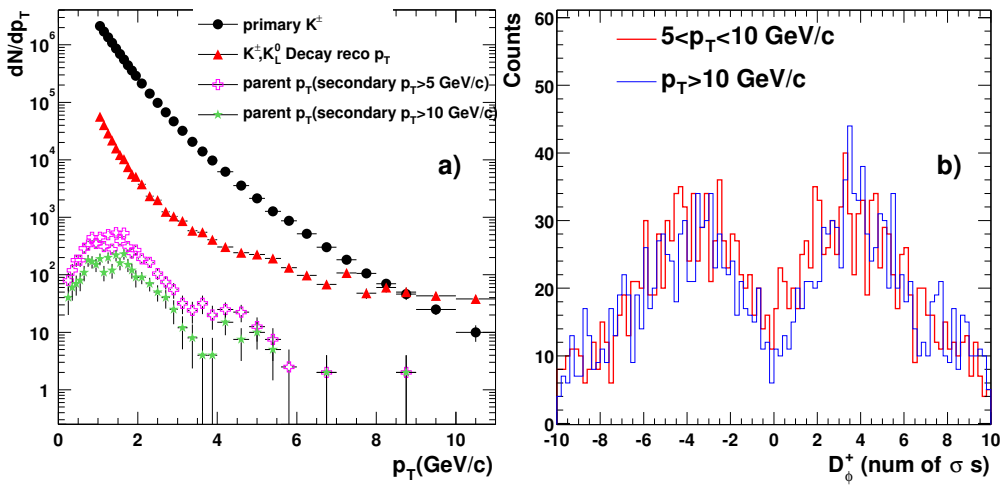

Figure 4.33: a) Charged kaons and their decay particle p_T distributions. b) The matching distribution for decays in two different reconstructed p_T ranges.

almost indistinguishable from those from signal tracks, because they decay close to the vertex and the reconstructed p_T is close to the true momentum. The background from K_s^0 decays relative to $K^+ + K^-$ is about 10% below 5 GeV/c, and increases up to 25% at 8 GeV/c and 50% at 10 GeV/c. The 10% level at intermediate p_T can be treated as an average feed down. The increase towards high p_T can be interpreted as an effective momentum smearing effect due to the non-zero error on the momentum measurement. This error results from the distance between the collision vertex and the K_s^0 decay point.

Similarly, the hyperon (mainly Λ and $\bar{\Lambda}$) decay contribution is studied by comparing with primary proton and anti-proton yields from HIJING. HIJING gives $\Lambda/p \sim 0.5$ at $p_T > 2$ GeV/c. However, both PHENIX [103, 104, 105] and STAR [106] have measured $\Lambda/p \sim 0.9$. So we scaled the $\Lambda, \bar{\Lambda}$ yields from HIJING up by a factor of 1.64. The comparison of the reconstructed background spectra with the primary $p, \bar{p}$ is shown in Fig. 4.35. The hyperon decays amount to 30% of the proton yield below 5 GeV/c, and the fraction increases to 40% at 6 GeV/c, 70% at 8 GeV/c, and 120% above 9 GeV/c.

The background p_T distributions from K_s^0 and hyperon decays closely follow their parent p_T distributions (represented by the open square marker in Fig. 4.34 and 4.35). This kind of background, in contrast to background from $K^\pm$ decays, falls quickly as function of p_T. Although it is difficult to subtract this from the matching distribution, we can estimate the contribution relative

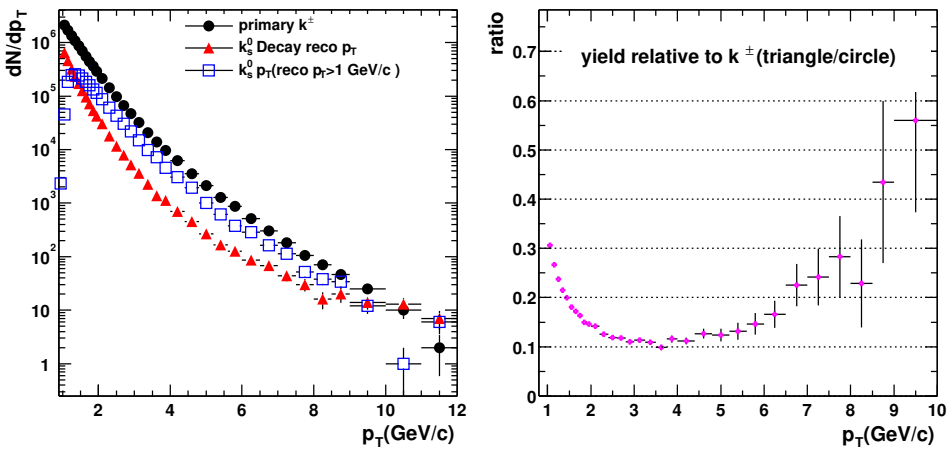

Figure 4.34: Background level from K_s^0 decay relative to primary $K^{\pm}$. The left figure shows the reconstructed spectra from HIJING(except for the open square marker, which represents the parent K_s^0 true p_T distribution for daughter particles with reconstructed $p_T > 1$ GeB/c). The right figure shows the K_s^0 feed down contribution relative to the $K^{\pm}$ yield.

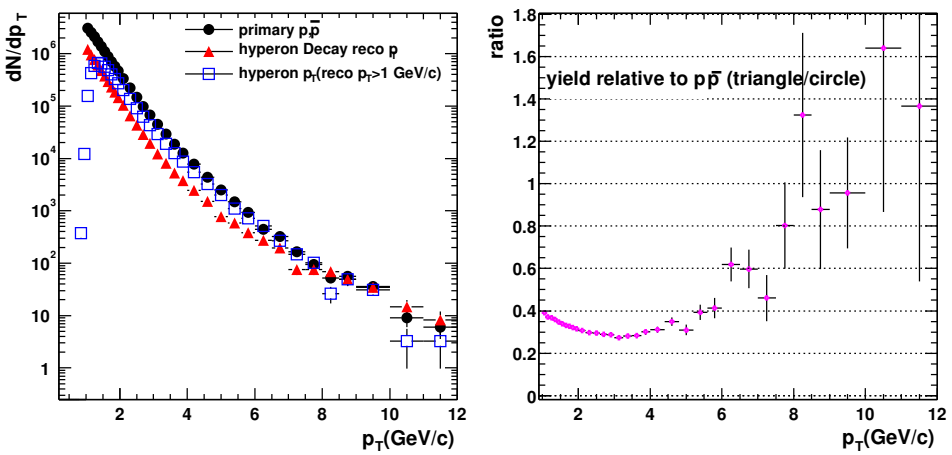

Figure 4.35: a) Hyperon and anti-hyperon decay contribution compared to primary $p + \bar{p}$ spectra. The HIJING input has been scaled up by a factor 1.64 to match the measured Λ/p ratio (0.9). b) hyperon feed relative to $p + \bar{p}$.

Table 4.6: K^0_s background relative to primary $K^{\pm}$ as function of reconstructed p_T for different input spectral shapes.

p_T (GeV/c)	< 4	4-5	5-6	6-7	7-8	8-9	9-10
$\epsilon^{decay}_{K^0_s}(\%)$	< 12	12	13	20	25	30	50
central $\epsilon^{decay}_{K^0_s}(\%)$	9	12	20	35	40	30	40
peripheral $\epsilon^{decay}_{K^0_s}(\%)$	10	12	15	25	35	40	70

to the parent's yield (or particles with similar yield as the parent) as function of the reconstructed p_T. The input spectral shapes of the parent particles are tuned to match those measured from real data. Two spectral shapes are used for this study: one is a fit to central $Au-Au$ charged hadron spectrum (0-5% central), the second is a fit to a peripheral $Au-Au$ charged hadron spectrum (60-70% central).[11] For both spectral shapes we determine a p_T dependent background from K^0_s relative to $K^{\pm}$, and background from hyperons relative to $p+\bar{p}$. The results are presented in Fig. 4.36 and Fig. 4.37. We define

$$\epsilon^{decay}_{K^0_s}(p_T) = \frac{\text{yield from } K^0_s \text{ decay}}{\text{yield of primary } K^+ + K^-} \quad , \tag{4.30}$$

to quantify the background contribution from K^0_s decay and

$$\epsilon^{decay}_{hyperon}(p_T) = \frac{\text{yield from hyperon decay}}{\text{yield of primary } p+\bar{p}} \quad , \tag{4.31}$$

to quantify the background contribution from hyperon decays. We calculate for each input spectral shape the $\epsilon^{decay}_{K^0_s}$ and $\epsilon^{decay}_{hyperon}$ as function of p_T, the results are shown in the right panels of Fig. 4.36 and Fig. 4.37. The background contributions are sensitive to the weight used. We summarize them in Table. 4.6 and Table. 4.7.

The decay background subtraction is performed in two steps. First, most of the decay background, mainly from $K^{\pm}$ and K^0_L, is subtracted from the track D^+_ϕ distribution. Then the remaining decay background, mainly from $K^0_s, \Lambda, \bar{\Lambda}$ and other hyperon decays, is estimated using the results from Table. 4.6 and 4.7.

To estimate the decay matching distribution, a sample of almost pure decay background tracks is selected by requiring $10 < p_T < 20$ GeV/c and

[11] This procedure is iterative. The results presented here use fits to the final spectra.

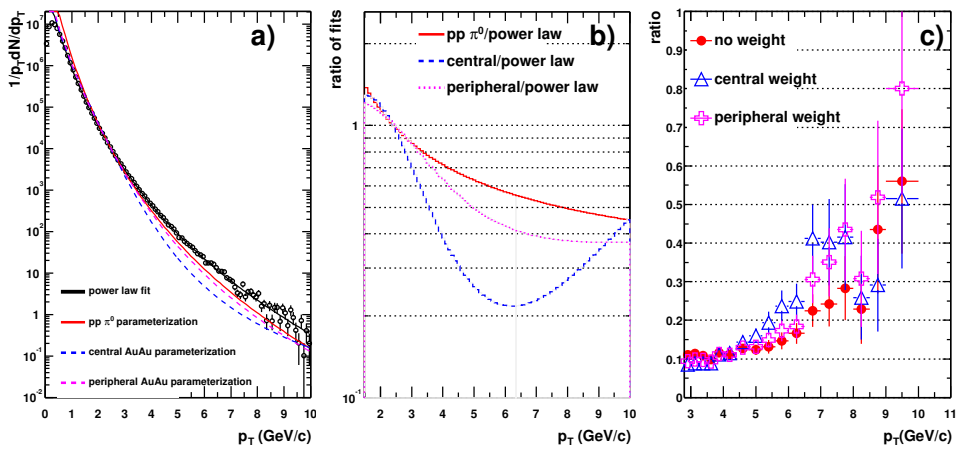

Figure 4.36: a) Primary $K^+ + K^-$ reconstructed p_T spectra from HIJING with various fits. b) Ratios of different fits to the power-law fit of the HIJING input. c) The K^0_s background relative to $K^{\pm}$, $\epsilon^{decay}_{K^0_s}(p_T)$(Eq. 4.30), for different fits.

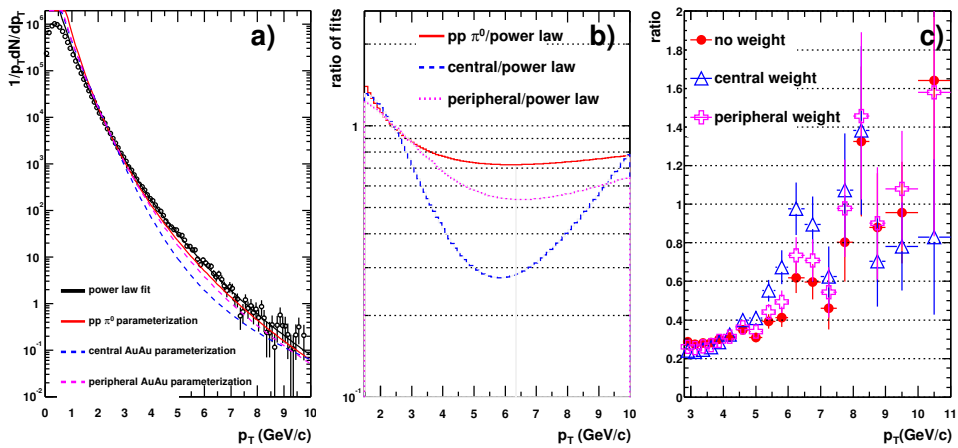

Figure 4.37: a) Primary $p + \bar{p}$ reconstructed p_T spectra with various fits. b) The ratios of different fits to the power-law fit of the HIJING input. c) The hyperon background relative to $p + \bar{p}$, $\epsilon^{decay}_{hyperon}(p_T)$(Eq. 4.31), for different fits.

$N_{PMT} < 0$. Once the shape of the decay background's D^+_ϕ distribution is established from this sample, we can subtract the decay background statisti-

Table 4.7: Hyperon background relative to primary $p^{\pm}$ as function of reconstructed p_T for different input spectral shapes.

p_T (GeV/c)	< 4	4-5	5-6	6-7	7-8	8-9	9-10
$\epsilon^{decay}_{hyperon}(\%)$	30	30	40	60	70	110	90
central $\epsilon^{decay}_{hyperon}(\%)$	30	35	60	90	90	120	70
peripheral $\epsilon^{decay}_{hyperon}(\%)$	30	32	50	70	80	125	100

cally. Fig. 4.38 shows the p_T distribution of tracks without associated RICH hits (N_{NR}), and the estimated contribution from signal tracks for $p_T > 6$ GeV/c. The shape of the signal track distribution is assumed to be the same as measured for π^0 in $p+p$ collisions at $\sqrt{s_{NN}} = 200$ GeV from Ref. [29]. The signal distribution is normalized to N_{NR} at 7 GeV/c and extrapolated to higher p_T [12]. The estimated integrated signal is 5% within 10-20 GeV/c. However, since the decay background at 7 GeV/c is already about 50%, so the integrated signal is only about 2.5% of N_{NR} within 10-20 GeV/c.

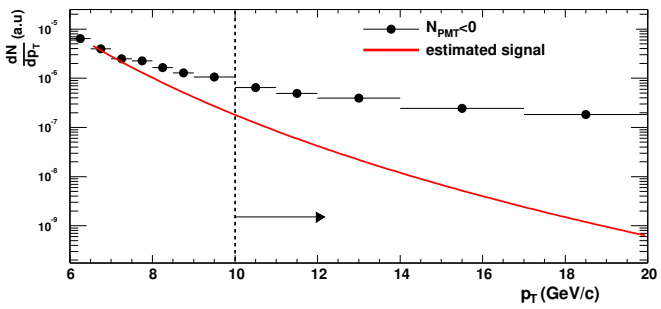

Figure 4.38: The p_T distribution for tracks without RICH hits (N_{NR}) for minimum bias collisions, the curve is the upper limit of the extrapolation of the signal shape to high p_T.

We determine a ratio R_{NR}, defined as the number of tracks within $|D^+_\phi| < 2\sigma$ relative to the number of tracks in the interval $3\sigma < |D^+_\phi| < 9\sigma$:

$$R_{NR}(p_T) = \frac{N_{NR}(|D^+_\phi| < 2\sigma)}{N_{NR}(3\sigma < |D^+_\phi| < 9\sigma)} \quad (4.32)$$

Since $N_{NR} = S_{NR} + N_{decay}$, it becomes

$$R_{NR}(p_T) = R^S_{NR} + R_{decay} \quad , \quad (4.33)$$

[12] We can do this because above this p_T, N_{NR} contains all protons and kaons, and small fraction of pions (see Fig. 4.31. Also the correction function is independent of p_T (see Chapter 5.1).

where R_{NR}^{S} is defined as

$$R_{NR}^{S} = \frac{S_{NR}(|D_{\phi}^{+}| < 2\sigma)}{N_{NR}(3\sigma < |D_{\phi}^{+}| < 9\sigma)} \quad , \tag{4.34}$$

and R_{decay} is defined as

$$\begin{aligned} R_{decay} &= \frac{N_{decay}(|D_{\phi}^{+}| < 2\sigma)}{N_{NR}(3\sigma < |D_{\phi}^{+}| < 9\sigma)} \\ &\approx \frac{N_{decay}(|D_{\phi}^{+}| < 2\sigma)}{N_{decay}(3\sigma < |D_{\phi}^{+}| < 9\sigma)} \end{aligned} \tag{4.35}$$

The last relation is true since the number of signal tracks in $3\sigma < |D_{\phi}^{+}| < 9\sigma$ is negligible. Since the integrated signal yield is negligible at $p_T > 10$ GeV/c (see Fig. 4.38), we also have $R_{NR}(10 - 20\text{GeV}/c) \sim R_{decay}(10 - 20\text{GeV}/c)$.

Fig. 4.39a shows R_{NR} as function of p_T from data. R_{NR} is consistent with 0.43 ± 0.03 at $10 < p_T < 20$ GeV/c. Below 10 GeV/c, R_{NR} increases mainly because of the rapid increase of the signal yield. Fig. 4.39b shows both R_{NR} and R_{decay} as function of p_T from Monte-Carlo simulation. We notice that R_{NR} and R_{decay} increase towards lower p_T. The increase of R_{decay} comes from the increase of the feed down contribution from K_s^0 and hyperons (see Fig. 4.34 and Fig. 4.35). The faster increase of R_{NR} is due to the increase of signal.

In the p_T range from 10 to 20 GeV/c, $R_{NR} \approx R_{decay}$ and is approximately constant around 0.424 ± 0.04. We calculate this constant level for different centrality classes and plot it in Fig. 4.40. No apparent centrality dependence is observed. The measured value is fitted as $R_{NR} = 0.424 \pm 0.03$. This value agrees well with the value determined from simulation, $R_{NR} = 0.45 \pm 0.02(stat)$.

The final R_{decay} value measured between 10-20 GeV/c is

$$R_{decay}^{10<p_T<20} = 0.424 \pm 0.04\ (p_T\ dependent) \pm 0.03\ (N_{part}\ dependent) \quad . \tag{4.36}$$

From this result, we estimate the decay contribution as a function of p_T to be $N_{NR}(3\sigma < |D_{\phi}^{+}| < 9\sigma) \times R_{decay}^{10<p_T<20}$ and the number of signal tracks is calculated as

$$\begin{aligned} S_{NR} &= N_{NR}(|D_{\phi}^{+}| < 2\sigma) - \\ &\quad N_{NR}(3\sigma < |D_{\phi}^{+}| < 9\sigma) \times R_{decay}^{10<p_T<20} \quad . \end{aligned} \tag{4.37}$$

The decay background subtraction based on Eqs. 4.35–4.37 in D_{ϕ}^{+} is presented in Fig. 4.41 for a sample range of $6 < p_T < 7$ GeV/c. Also shown

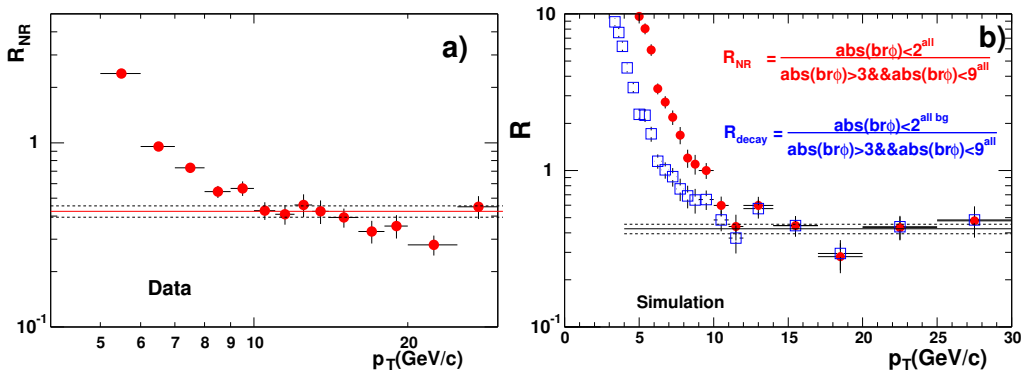

Figure 4.39: a) The p_T dependence of R_{NR} form data. b) The p_T dependence of R_{NR} and R_{decay} from simulation. The solid line in both panels is at 0.424, the dashed lines indicate a ± 0.04 variation.

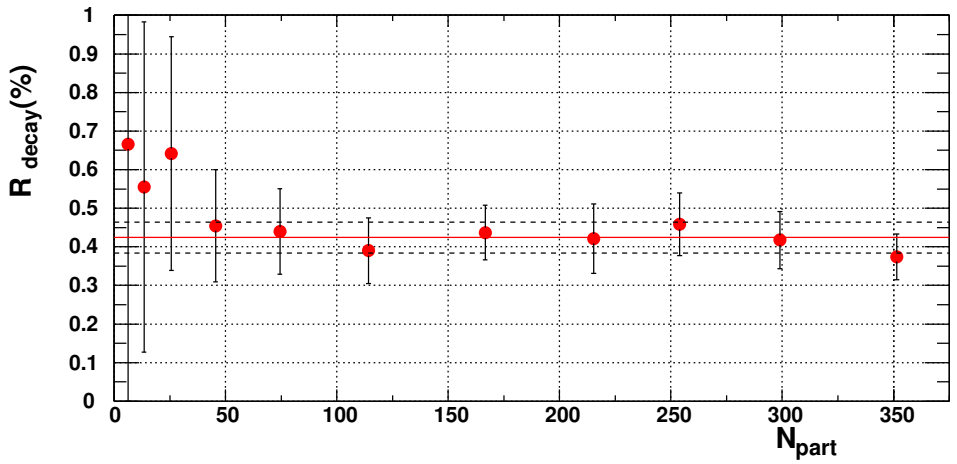

Figure 4.40: The centrality dependence of $R_{decay}^{10<p_T<20}$. The solid line is at 0.424, the dashed lines indicate a ± 0.03 variation.

is the matching distribution for decay particles from Monte-Carlo simulation. Outside the signal window, the shape of the estimated background matches the data rather well, the average difference is at the 10% level and is taken into account in the error estimation of $R_{decay}^{10<p_T<20}$. In Fig. 4.42, the raw minimum bias p_T spectrum for tracks without RICH association is decomposed into the estimated decay spectrum and signal spectrum.

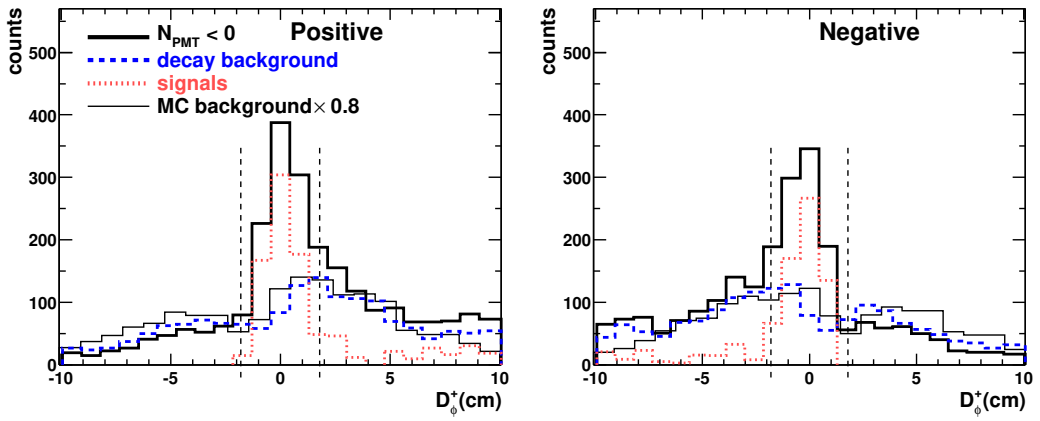

Figure 4.41: Background subtraction in D^+_ϕ for tracks without an associated RICH PMT and with $6 < p_T < 7$ GeV/c. The subtraction is shown for minimum bias events and separately for positively (left) and negatively (right) charged tracks. The first three distributions represent the raw counts for all tracks without a RICH association (solid line), estimated decay background based on the R_{decay} method (dashed line), and signal tracks (dot-dashed line) that were calculated as the difference of the first two distributions. The thin solid line represents the matching distribution of decay background from Monte-Carlo simulation, arbitrarily scaled to match the data. The 2 σ matching windows are illustrated by the vertical dashed lines.

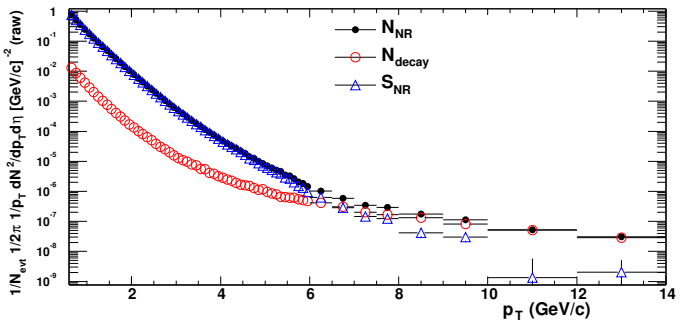

Figure 4.42: Background subtraction for N_{NR} tracks (Eq. 4.37) in minimum bias events.

The fact that R_{decay} in Fig. 4.39b increases towards low p_T indicates that background inside the matching window, mainly from $K^0_s, \Lambda, \bar{\Lambda}$, increases faster than outside the matching window. Since a constant R_{decay} is assumed in Eq. 4.37, we under-subtract the decay background. The amount of remaining background is estimated from the same MC simulation. Fig. 4.43 shows the result. The fraction of background subtracted from R_{decay} method, $\epsilon^{decay}_{subtracted}$, is close to 80% around 9 GeV/c, but rapidly decreases towards lower p_T. Since

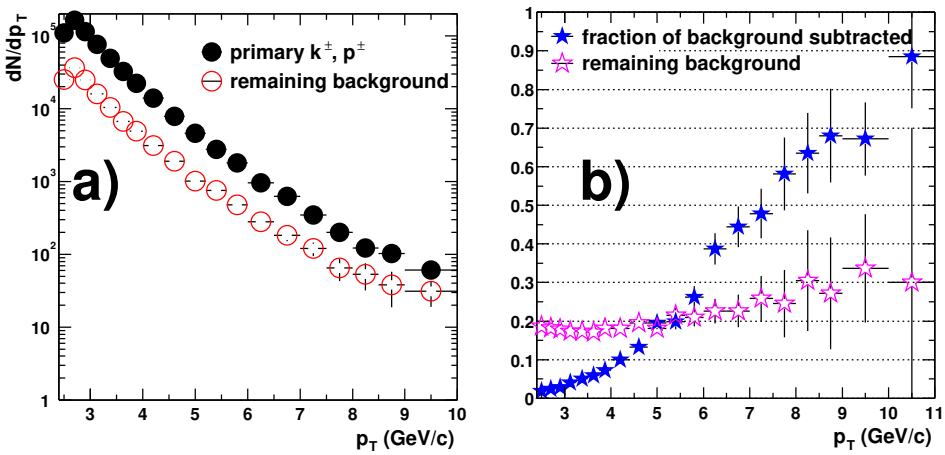

Figure 4.43: a) Signal tracks (closed circles) and remaining background tracks (open circles). b) The fraction of background subtracted (close stars), and remaining background relative to all tracks after subtraction (open stars).

Table 4.8: Remaining K^0_s background relative to $K^{\pm}$ as function of p_T for different input spectral shapes.

p_T (GeV/c)	< 4	4-5	5-6	6-7	7-8	8-9	9-10
$\epsilon^{remain}_{K^0_s}(\%)$	< 11.3	10.6	10.4	12	11.3	10.5	17.5
central shape $\epsilon^{remain}_{K^0_s}(\%)$	9.4	10.6	12	15	15.8	14	24.5
peripheral shape $\epsilon^{remain}_{K^0_s}(\%)$	9.4	10.6	12	15	15.8	14	24.5

the fraction of decay background from K^0_s and Λ relative to the signal increases towards high p_T (see Fig. 4.34 and 4.35), the fraction of remaining background is almost constant at a level of 20-30% relative to the primary $K^{\pm}, p, \bar{p}$.

The remaining background can be calculated as,

$$\epsilon^{remain}_{K^0_s} = \epsilon^{decay}_{K^0_s} \times (1 - \epsilon^{decay}_{subtracted}) \tag{4.38}$$

for K^0_s, and

$$\epsilon^{remain}_{hyperon} = \epsilon^{decay}_{hyperon} \times (1 - \epsilon^{decay}_{subtracted}) \tag{4.39}$$

for hyperons. $\epsilon^{remain}_{K^0_s}$ and $\epsilon^{remain}_{hyperon}$ can be calculated from Table. 4.6 and 4.7. The results are listed in Table. 4.8 and 4.9.

Table 4.9: Remaining hyperon background relative to $p, \bar{p}$ as function of p_T for different input spectral shapes.

p_T (GeV/c)	< 4	4-5	5-6	6-7	7-8	8-9	9-10
$\epsilon^{remain}_{hyperon}$(%)	28.2	26.4	32	36	31.5	38.5	31.5
central shape $\epsilon^{remain}_{hyperon}$(%)	28.2	30.8	48	54	40.5	42	24.5
peripheral shape $\epsilon^{remain}_{hyperon}$(%)	28.2	28.2	40	42	36	43.8	35

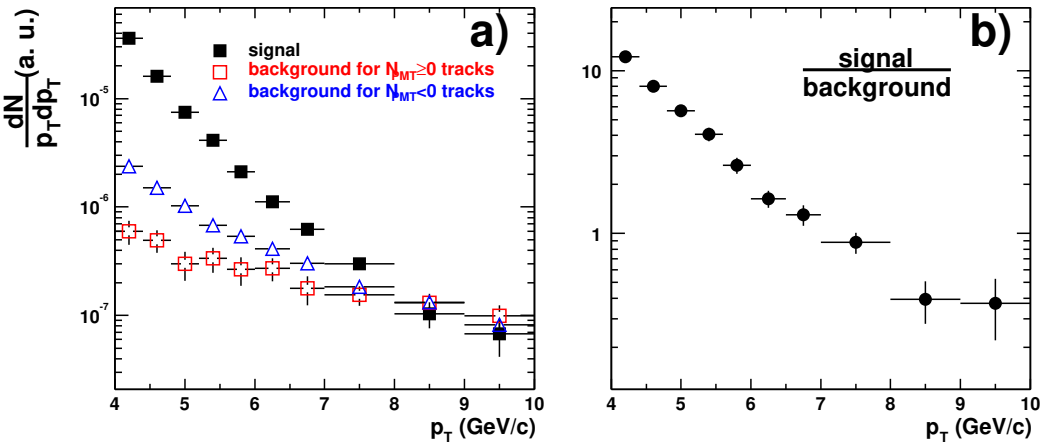

Figure 4.44: Amount of background estimated as function of p_T for minimum bias collisions. The left figure shows the arbitrarily normalized spectra for the signal (filled squares), e^+e^- from conversion (open squares) and decays (open triangles). The right figure shows the signal to background ratio. Only statistical errors are shown.

4.5.5 Systematic Errors on Background Subtraction

Fig. 4.44 shows the total signal, obtained from $S_R + S_{NR}$, with the decay and conversion backgrounds subtracted. The right hand shows the signal-to-background ratio. The background increases with increasing p_T. At 4 GeV/c the signal-to-background ratio is about 10. It decreases to 1 at 7.5 GeV/c and to ∼0.3 at 10 GeV/c. Fig. 4.45 shows the relative contributions of $N_{PMT} \geq 0$ tracks (S_R) and $N_{PMT} < 0$ tracks (S_{NR}) to the total background subtracted spectra. At $p_T > 7$ GeV/c, where most of the pions are included in S_R, the π fraction is about 60%, while $K^{\pm}, p, \bar{p}$ contribute about 40%.

Tab. 4.10 summarizes the systematic errors on the background subtrac-

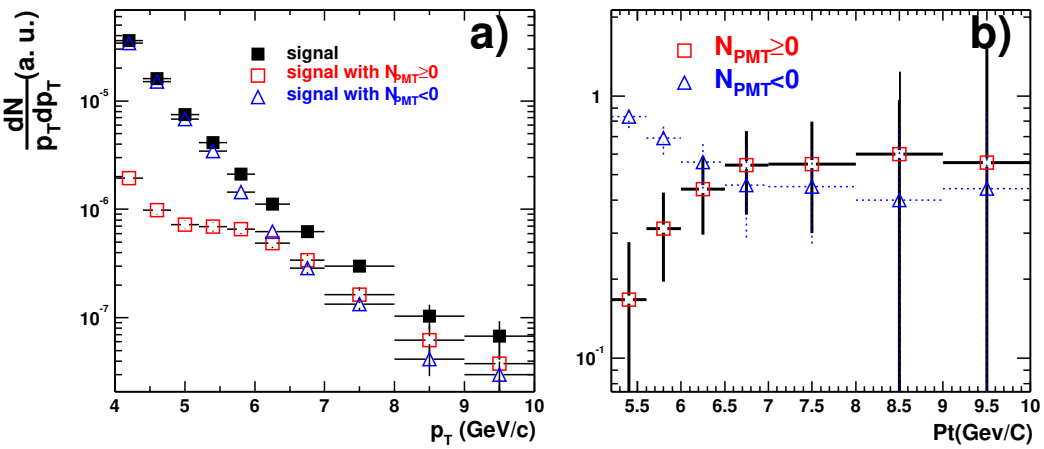

Figure 4.45: a) The signal spectra decomposed into $N_{PMT} \geq 0$ (S_R) and $N_{PMT} < 0$ (S_{NR}). b) The fraction of these two samples relative to the total raw signal yield.

tion. These systematic errors have been adjusted to 1σ errors [13] [14]. These errors are correlated with p_T and are presented relative to the charged hadron yield. There are three types of errors:

- The uncertainty of the pion-loss is $\delta_{\pi loss}$ (see Table. 4.5). This error is re-scaled by the fraction of signal tracks with RICH association, i.e. $S_R/(S_R + S_{NR}) \sim 0.6$ from Fig. 4.45.

- $\delta_{R_e \oplus R_{decay}}$ accounts for systematic errors due to the uncertainties on R_e and R_{decay}, with $R_e = 0.458 \pm 0.05$ and $R_{decay} = 0.424 \pm 0.05$. Both quantities are varied up and down within their errors and propagated as an uncertainty in the final yield. The resulting uncertainties on the charged yields are then added in quadrature to obtain $\delta_{R_e \oplus R_{decay}}$.

- The uncertainty of the K^0_s, Λ, and $\bar{\Lambda}$ feed-down subtraction is denoted by $\delta_{feeddown}$. As summarized in Table. 4.8 and Table. 4.9, the final feed-down contribution depends sensitively on the choice of the Λ and K^0_s p_T spectra and of their yields in the high p_T range where they are not measured. Both the yields and their spectral shapes are varied within limits

[13] The error quoted so far in the text are full extent errors, they have to be divided by $\sqrt{3}$ to obtained 1σ errors.

[14] From now on, all errors quoted in tables for the charged hadron analysis are 1σ errors.

Table 4.10: Systematic errors on background subtraction. All errors are given in percent and are quoted as 1σ errors. These errors are correlated with p_T.

p_T (GeV/c)	$\delta_{\pi loss}$ (%)	$\delta_{R_e \oplus R_{decay}}$(%)	$\delta_{feeddown}$ (%)	total(%)
< 5	0.3	0.3	5	5
5 - 6	0.6	1.8	5	5.3
6 - 7	1.4	4.1	8.5	9.5
7 - 8	4.6	7.1	7.8	11.5
8 - 9	9.9	17.6	6	21.1
9 - 10	19.4	23.5	6	31.1

imposed by the $N_{PMT} < 0$ spectrum. The average feed-down contribution depends on p_T and varies between 6 to 13% relative to the total charged hadron yield; it is subtracted from the charged spectra. The systematic uncertainties are estimated from the spread of the feed-down contributions obtained with different assumptions. The uncertainties are approximately 60% of the subtraction, and depend on p_T and centrality.

Chapter 5

Corrections and Systematic Uncertainties

After background subtraction, the charged hadron raw p_T spectra have to be corrected for

1. Geometrical acceptance and decay losses
2. Matching cut efficiency
3. Reconstruction efficiency
4. Momentum resolution and scale
5. Run-by-run variation
6. Occupancy dependent efficiency loss

These corrections are determined using a GEANT [100] Monte-Carlo simulation of the PHENIX detector in which simulated tracks are reconstructed using the same analysis chain applied to the real data. For each of π^+, π^-, K^+, K^-, p, $\bar{p}$ species, 5 million tracks are generated uniformly in event vertex ($-30 < z_{vtx} < 30cm$), rapidity ($-0.6 < y < 0.6$), azimuth ($0 < \phi < 2\pi$), and p_T ($0 < p_T < 10$ GeV/c). The procedure for calculating the correction function is iterative. Initially, the generated particles are assigned a weight such that the input spectrum matches the charged hadron raw spectral shape. The ratio of the input p_T spectrum to the reconstructed p_T spectrum gives the first correction function, which in turn gives the first corrected spectrum. The generated particles are then assigned a new weight such that the input spectrum matches the first corrected charged hadron spectrum. This new weight is then used to obtain a new correction function, which in turn gives a new corrected charged hadron spectrum. This procedure is repeated until the final spectrum does not change. The weighting procedure is necessary to take into account the momentum resolution effect and other detector smearing effects which are sensitive to the spectral shape.

5.1 Geometrical Acceptance and Decay Losses

Fig. 5.1 show the geometrical acceptance for charged hadrons as function of p_T. Due to the strong magnetic field, charged tracks with $p_T < 0.15$ GeV/c originating from the vertex will not reach the Drift Chamber. For the same reason, the track reconstruction efficiency strongly depends on p_T for $p_T < 2$ GeV/c. However, the p_T dependence becomes relatively small above 2 GeV/c.

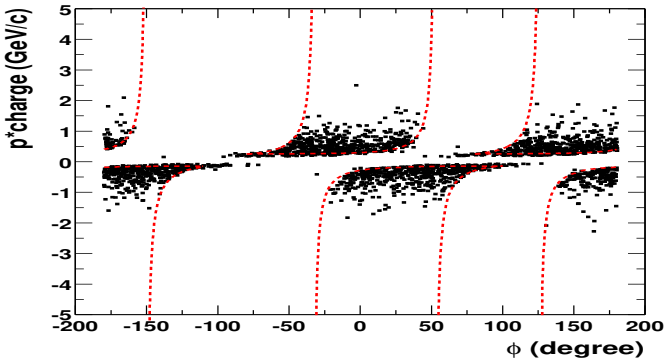

Figure 5.1: Geometrical acceptance for charged particles in azimuth ϕ as function of p_T.

The dominant measured charged hadrons are $\pi^{\pm}, K^{\pm}, p$, and $\bar{p}$. Since they have different decay probabilities and multiple scattering, the efficiency correction depends on particle species but not on charge. This is reflected in Fig. 5.2, where the correction functions averaged separately over π^+ and π^-, K^+ and K^-, and p and $\bar{p}$ are shown. For $p_T < 3$ GeV/c, the kaon correction function is significantly larger than those for pions and protons, reflecting the relatively short lifetime. This difference become less than 15% at $p_T > 3$ GeV/c. The input p_T distributions for different particle species are weighted by the measured p_T-dependent particle composition from Ref. [103]: [1]

$$input = pion + \lambda_1 \times kaon + \lambda_2 \times proton \tag{5.1}$$

where λ_1 is the yield ratio of charged kaons to charged pions, and λ_2 is the yield ratio of protons to charged pions. The final correction function is obtained as the ratio of the weighted input p_T spectra to the reconstructed p_T spectra. To account for the centrality dependence of the particle composition, λ_1 and λ_2 are determined for one central (0-5%) and one peripheral (60-70%) centrality

[1] Note that because charged hadron yield is measured per unit of peusdo-rapidity, the pion, kaon, and proton yields are converted from dN/dy to $dN/d\eta$ before calculating the ratio.

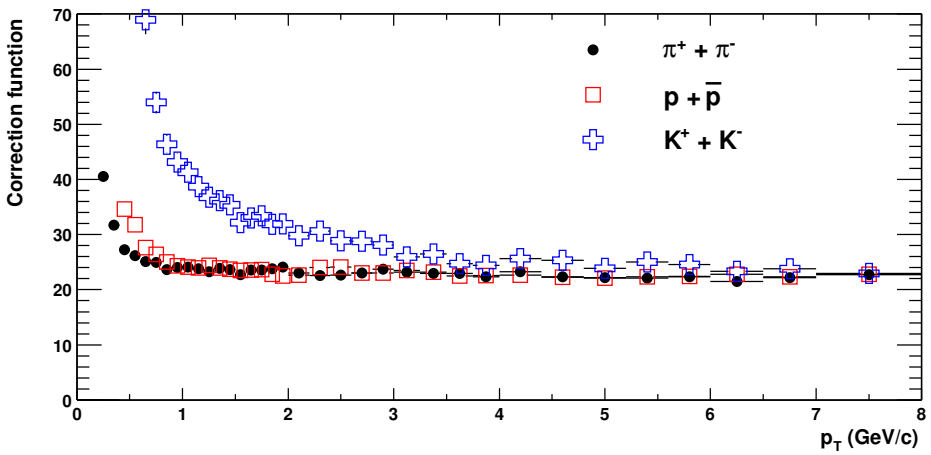

Figure 5.2: Averaged correction functions for π^+ and π^-, p and $\bar{p}$, and K^+ and K^-.

class. There is some difference in λ_1 and λ_2 for the two sets of weights as shown in Fig. 5.3. However, since the correction functions are similar for pions and protons, the combined correction function is insensitive to changes in λ_2. Below 1 GeV/c, the kaon correction is significantly larger than that for pions and protons, but the kaon yield is small and λ_1 is much less than 1. Above 2 GeV/c, λ_1 increases, but the difference between the correction functions for pions and kaons decreases. Combining all these dependencies, the variation of the particle composition for the two centrality classes leads to less than 2% difference in the combined correction functions at $p_T > 0.5$ GeV/c. Since no kaon data are available above 2 GeV/c, we assume a constant K/π ratio within $\pm$10% from the value observed at 2 GeV/c. This assumption leads to an additional 2.5% systematic error in the combined correction function above 2 GeV/c.

5.2 Matching Cut Efficiency

To correctly estimate the efficiency of various cuts, the same analysis cuts used in the real data analysis must also be applied to the simulated tracks, and the variables describing the cuts in the simulation have to be tuned to match those from the data. The matching parameters are among these variables and have to be tuned to the data. In particular, the widths of the $D^+_\phi, D^-_\phi, D^+_z$, and D^-_z distributions have to be similar for data and simulation, and any

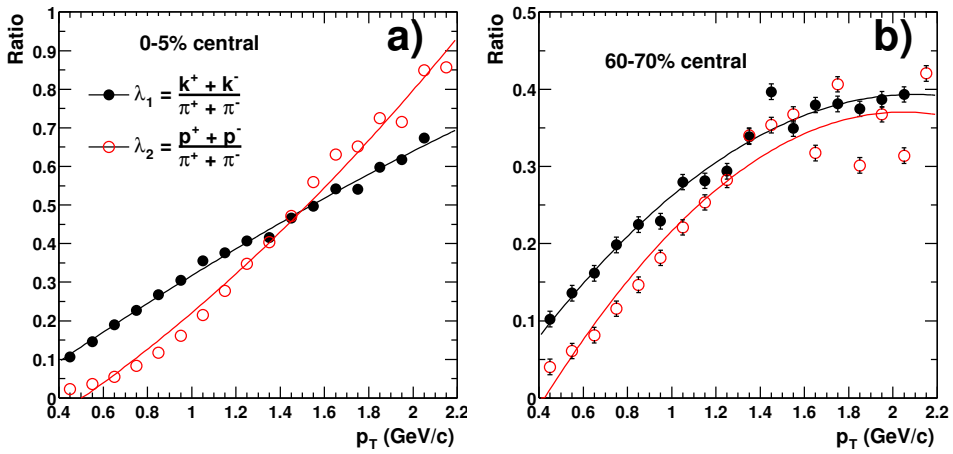

Figure 5.3: The K/π and p/π ratio for central (panel a)) peripheral (panel b)) collisions.

remaining differences have to be included in the systematic error estimation.

In both real data and simulation, a 2σ matching cut is applied on D^+_ϕ, D^-_ϕ, D^+_z, and D^-_z. The widths of the matching distributions in the simulation have been tuned to match those from the data within 10%. The systematic errors due to the remaining differences are given by the change of the hadron yields when simultaneously widening and narrowing all four matching variables by 10%. The results of this study are shown in Fig. 5.4. The differences between the data (open symbols) and the simulation (solid symbols) reflect the differences in the width of the matching variables. The error bars on each set of points are obtained by simultaneously enlarging/narrowing the matching window by 10%, which creates a $\pm 3\%$ variation. The Monte-Carlo cut efficiency is 4% higher than that from data at $p_T < 1$ GeV/c, but both values agree within 2% above 2 GeV/c. In the end, the matching systematic error, σ_{match}, is estimated to be $4 \oplus 3(MC) \oplus 3(data)\% = 6\%$ for $p_T < 1$ GeV/c, and $2 \oplus 3 \oplus 3\% = 5\%$ for $p_T > 1$ GeV/c.

As a consistency check, the full analysis procedure, including background subtraction and Monte-Carlo correction, is repeated with different matching cuts. The ratios of the fully corrected spectra for two different matching cuts to the default matching cuts ($1.6\sigma/2\sigma$ and $2.5\sigma/2\sigma$) are presented in Fig. 5.5 for central (0-5%) and peripheral (60-92%) collisions. The variation for different matching cuts is less than 10%.

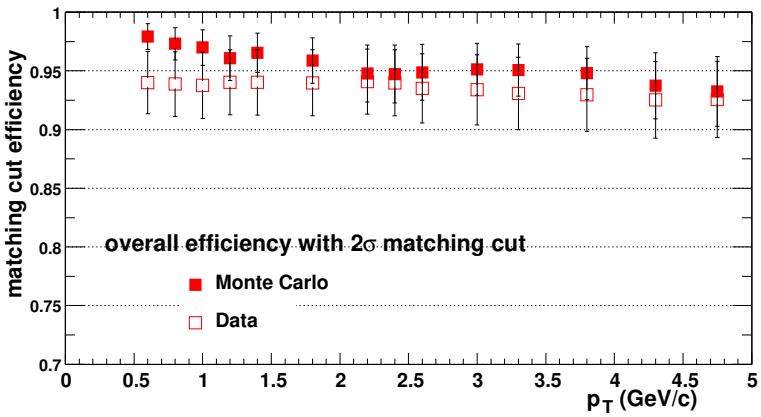

Figure 5.4: The overall 2σ matching cut efficiency for MC (solid) and data (open).

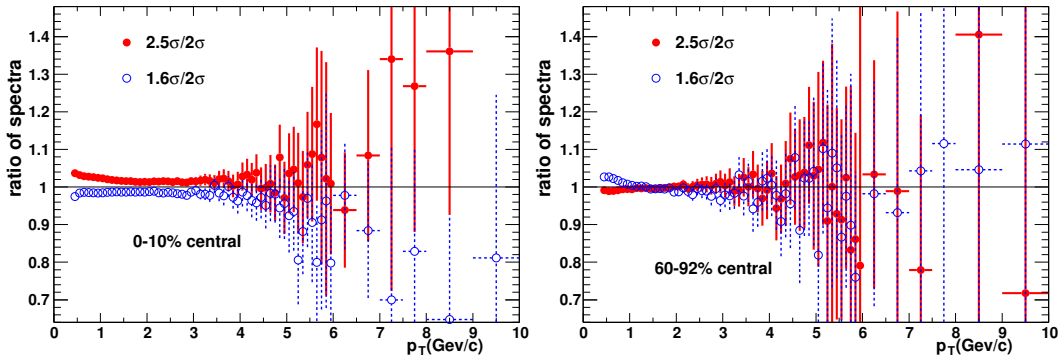

Figure 5.5: The ratio of fully corrected spectra for different matching windows for central(left) and peripheral(right) events.

5.3 Reconstruction Efficiency

The reconstruction efficiency refers to the probability to find a track located in the active area of the tracking detectors used in this analysis. The Drift Chamber tracking efficiency is well above 99% in its active area (Chapter. 3.1.3). The PC1, PC2 and PC3 also have very good efficiency in their active area (99% for PC1, 98% for PC2 and PC3). Thus we quote the systematic errors on the tracking efficiency as: $\sigma_{track} = 1 \oplus 1 \oplus 2 \oplus 2\% = 3.2\%$.

5.4 Momentum Resolution and Scale

The measured momentum resolution is accurate within 10% (see Chapter 3.3). The systematic errors due to the momentum resolution are checked by a simple Gaussian smearing of the measured p_T spectra according to the following two limits of resolution:[2]

$$\begin{aligned} \frac{\delta p}{p} &= 0.5\% \oplus 0.8\% p \\ \frac{\delta p}{p} &= 0.9\% \oplus 1.2\% p \end{aligned} \tag{5.2}$$

The result is shown in the bottom panel of Fig. 5.6. The difference is ±1% at 5 GeV/c and ±3% at 10 GeV/c.

Since the momentum smearing effect depends sensitively on the steepness of the spectra, as a second check, we have fitted the spectra for central and peripheral collisions and used these fits as the weights to determine the correction. The results are shown in the upper panel of Fig. 5.6. The differences again are small but become significant above 5 GeV/c. The difference increases from about ±1% at 8 GeV/c to ∼ ±5% at 10 GeV/c.

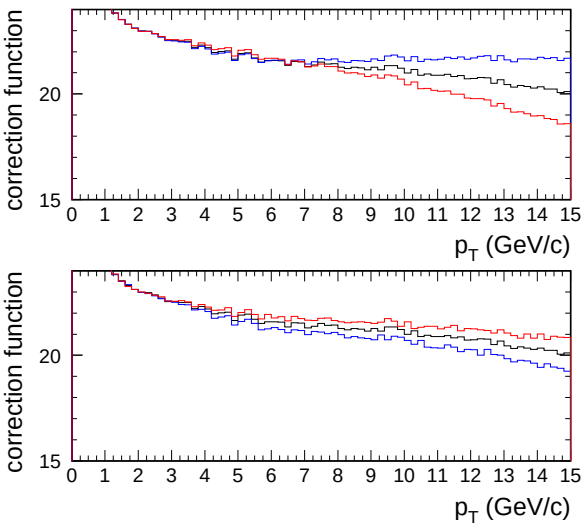

Figure 5.6: Systematic checks of correction functions. Top panel shows the variations using fits to p_T spectra from minimum bias (middle curve), central (bottom curve) and peripheral (top curve) data as weighting functions. The bottom panel compares corrections obtained by varying the momentum resolution by ±20%.

The momentum scale is known within 0.7% (Chapter 3.3.2). The systematic errors due to this uncertainty are estimated from the change in yields

[2]Since the data could have momentum smearing that is non-Gaussian, we vary the resolution by 20% to give an upper limit on the systematic errors.

resulting from shifting the measured p_T up and down by 0.7% $\times$ p_T. The calculated errors depend on p_T and the local spectral shape. Although the p_T shift due to the momentum scale error is small at low p_T, the change in yield can be enhanced due to a steeper spectral shape at low p_T compared to high p_T. Fig. 5.7 shows the fractional variation of the yields for central (solid) and peripheral (open) collisions. The maximum change is about $\pm$6.8% around 4 GeV/c and the difference between central and peripheral collisions is $\sim$ 2%.

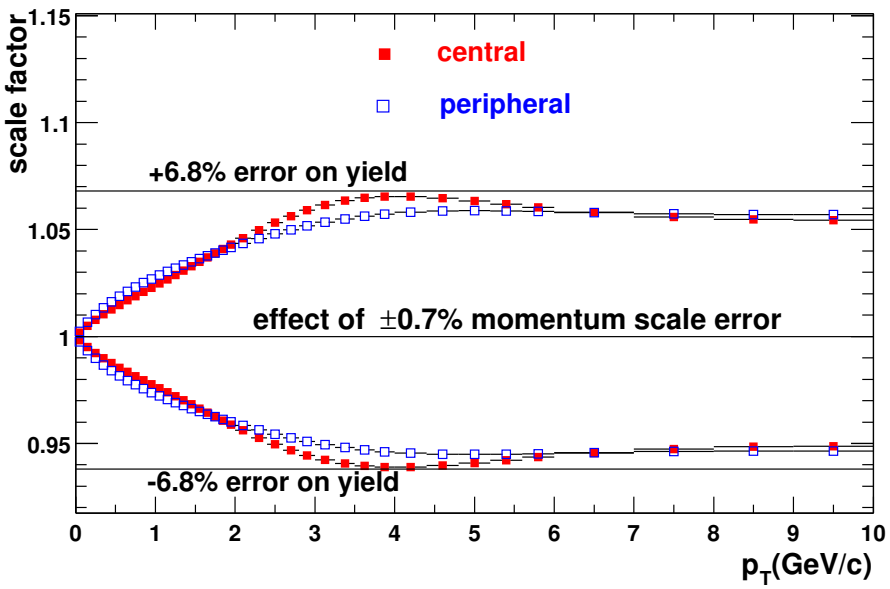

Figure 5.7: Upper and lower limit on the yield assuming a 0.7% momentum scale error for central (solid marker) and peripheral (open marker) collisions.

The average p_T within a given bin of the spectrum is not at the center of the bin because the spectra are steeply falling. The deviation from the bin center depends on the bin width and the local inverse slope and needs to be corrected. In the charged hadron analysis, we use a slightly different but equivalent approach. Instead of shifting the data points to the correct average p_T value, the yields are reduced by an amount calculated from the local spectral shape to reflect the correct yield at the center of the p_T bin.

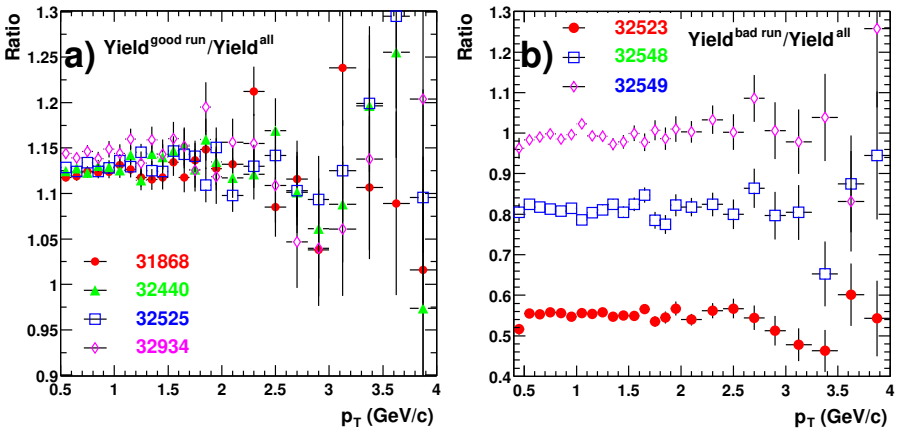

Figure 5.8: Raw spectra for a given run divided by raw spectra for the full data set. a) Ratios of good runs to the full data set. b) Ratios of bad runs to the full data set.

5.5 Run-by-Run Variation and Acceptance Normalization

The performance of the tracking detectors is not uniform over the whole RUN-2 period. The degradation of the west arm DC performance and high voltage problems in PC2 and PC3 create run-by-run dependent inactive area and thus effectively reduces the acceptance for the full data set. This is corrected by introducing an overall scale factor on the spectra.

For minimum bias events, Fig. 5.8a shows the ratios of the raw p_T distributions for several good runs to that for all runs (normalized per event). The ratio of spectra from good runs to spectra from the full data set is around 1.135 ± 0.02, and there is no observable difference in the slope of the spectra. Similar ratios are plotted in Fig. 5.8b for some of the "bad" runs which have additional inactive area. There is an effective overall reduction of the yield. It is this reduction of 13.5% that leads to the 13.5% run-by-run correction.

In addition to the run-by-run variation of the acceptance, we also need to make sure that the acceptance for good runs correctly match the one from Monte-carlo. In order to do that, we compare the spatial distribution of tracks from good runs (run 31868, 32440, 32525, 32934 from Fig. 5.8) to the same distribution for simulated tracks as shown in Fig. 5.9. For normalization, we picked regions in ϕ where the DC has high tracking efficiency and the

Table 5.1: Ratio data/MC for different ϕ reference ranges.

ϕ range	[-0.45,-0.41]	[-0.34,-0.25]	[0.48,0.51]	[0.7,0.77]
North side	0.98 ± 0.04	0.94 ± 0.05	1.08 ± 0.06	1.04 ± 0.04
South side	0.94 ± 0.04	1.04 ± 0.05	1.02 ± 0.06	0.96 ± 0.04

corresponding PC1, PC2 and PC3 acceptance contains no inactive area. The north side yield and south side yield in those ϕ regions are also required to be roughly equal. From Fig. 5.9, we have identified four such ϕ ranges:
$[-0.45, -0.41], [-0.34, -0.25], [0.48, 0.51], [0.7, 0.77]$

Fig. 5.10 shows ϕ distributions for data (solid line) and Monte-Carlo (dashed line), separately for tracks in the north (left panel) and south (right panel) side of the DC. These distributions are obtained by projecting the track acceptance distributions shown in Fig. 5.9 to the vertical axis. The Monte-Carlo curves in Fig. 5.10 have been scaled to have the same total integral as the data. For each of the selected ϕ ranges, the ratio of the integrals between data and Monte-carlo are calculated and listed in Table. 5.1. Any deviation from 1 will reflect an uncertainty in the overall normalization. We find that the acceptance from Monte-Carlo agrees with that for the good runs within $\pm 3\%$.

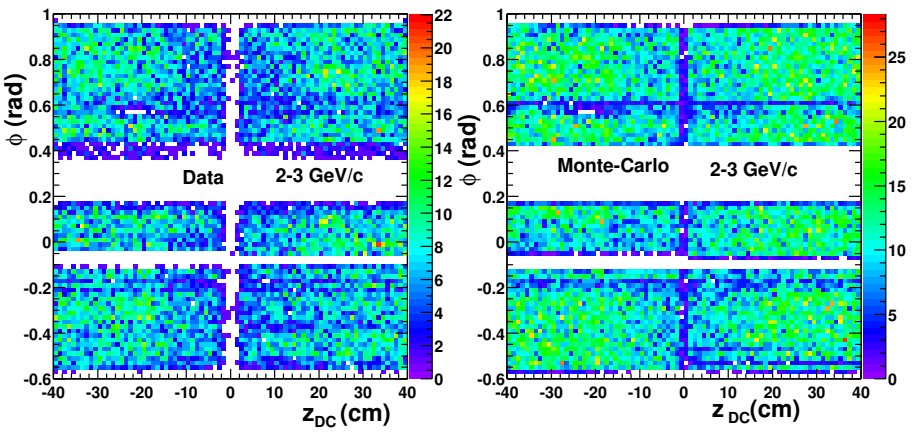

Figure 5.9: ϕ vs z_{DC} distribution for tracks with $2 < p_T < 3$ GeV/c from good runs (left) and Monte-Carlo simulation (right).

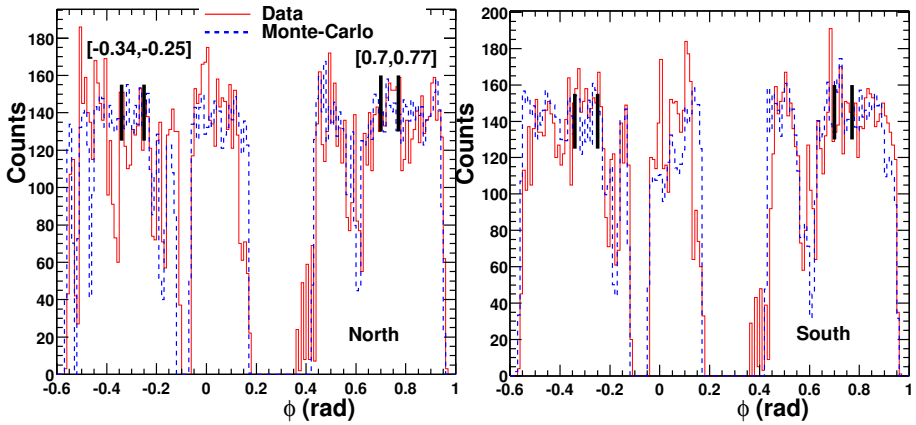

Figure 5.10: ϕ distributions of the tracks with $2 < p_T < 3$ GeV/c. Several good ϕ ranges used for normalization are indicated by the black bar. a) Tracks at the north side of the DC. b) Tracks at the south side of the DC. MC statistics have been scaled to match the data.

5.6 Occupancy Dependent Correction

An effect that is difficult to avoid in for high multiplicity environments, such as in heavy-ion collisions is a loss in tracking efficiency due to limitations associated with the pattern recognition algorithms and due to hit merging effects. Although these losses are small for peripheral collisions, they are sizable in central collisions. The multiplicity(or occupancy) dependent track reconstruction efficiency is estimated by embedding single simulated tracks into real events. The merged events are then reconstructed and the probability of finding the embedded track is evaluated. The main reason for the decrease in tracking efficiency is the merging of hits in the Drift Chamber and the Pad Chambers. Also the inability of the pattern recognition software to find tracks in the high occupancy environment. Due to the merging, the hit is either lost (associated to another track) or it is shifted in location. Thus the embedded tracks either are not reconstructed, or lose it's associated hits in PCs.

The occupancy dependent efficiencies are shown for four different centrality classes in Fig. 5.11. The efficiencies are almost constant as function of p_T for $p_T > 1.5$ GeV/c, but first increase then decrease towards lower p_T. The increase is due to the fact that at low p_T, the PC2 and PC3 2σ matching windows are larger to account for multiple scattering (see Eq. 3.5). Thus tracks are less vulnerable to hit merging at PC2 and PC3, and the efficiency increases. However, at very low $p_T (< 0.4$ GeV/$c)$, the bending angle becomes

very large. The track segments inside the DC become longer ($\approx 40cm/cos(\alpha)$). These tracks have a larger probability of being distorted by other tracks. This results in a decrease of the efficiency[3].

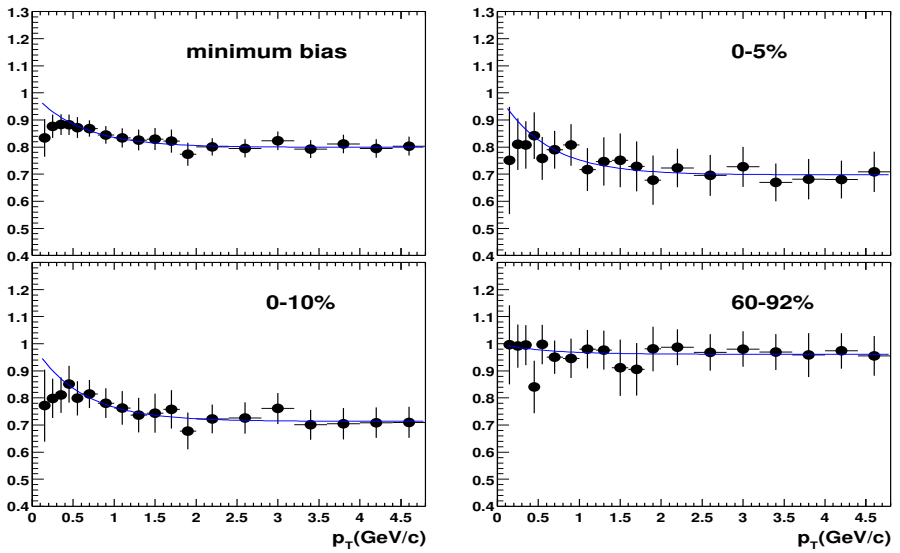

Figure 5.11: The occupancy dependent efficiency as function of p_T for four centrality classes.

The observed p_T dependence at low p_T has been taken into account by applying a slightly smaller, p_T-dependent, occupancy correction for $p_T < 1.5$ GeV/c, given as:

$$\epsilon(p_T, N_{part}) = \epsilon_0(N_{part}) + (1 - \epsilon_0(N_{part}))e^{-1.7p_T} \tag{5.3}$$

For $p_T > 1.5$ GeV/c, the multiplicity dependence correction ϵ_0 only depends on centrality.

The values of ϵ_0 for various centrality classes are summarized in Table. 5.2.

5.7 Systematic Uncertainties

The final correction functions used are summarized in Fig. 5.12. The combined single particle correction function determined from $\pi^{\pm}, K^{\pm}, p$ and $\bar{p}$

[3]However, since the charged hadron spectra start at 0.5 GeV/c, this decrease is irrelevant.

Table 5.2: Multiplicity dependent efficiency for various centrality classes.

Centrality	minbias	0-5%	5-10%	10-15%	15-20%	20-30%	30-40%
ϵ_0 (%)	80 ± 1.5	70 ± 3	73.6 ± 3	78.2 ± 3.1	82 ± 3.2	87 ± 2.6	90.2 ± 2.7
Centrality	40-50%	50-60%	60-70%	70-80%	80-92%	0-10%	60-92%
ϵ_0 (%)	95 ± 2.8	95.8 ± 2.8	97.5 ± 3	99.3 ± 2	99.7 ± 2	71.4 ± 3	98 ± 3

is plotted in Fig. 5.12a. This correction function can be simply parameterized as

$$c(p_T) = \frac{4.0165}{p_T} + 23.52 - 0.3135 p_T + 0.0108 {p_T}^2 \tag{5.4}$$

for $p_T < 10$ GeV/c. The sharp rise below 2 GeV/c is due to a loss in acceptance and decays in flight. Above 2 GeV/c, the correction decreases only slowly with p_T. For $p_T > 4$ GeV/c, the correction varies by less than $\pm 5\%$. Fig. 5.12a also shows the systematic error on the correction function. This error includes not only the errors on the correction itself, but also the uncertainty due to the background subtraction procedure.

Fig. 5.12c shows the ratio of the correction functions for central and peripheral collisions. The ratio is above 1 indicating that central collisions have a larger occupancy correction. However, as Fig. 5.12c shows, the occupancy correction is independent of p_T within a $\pm 3\%$ systematic uncertainty from 1.5 to 10 GeV/c. The full correction is thus factorized into a centrality-dependent (i.e. detector occupancy dependent) correction function, $c(N_{part}) = 1/\epsilon_0$, and a p_T-dependent correction function, $c(p_T)$. The centrality-dependent correction function, $c(N_{part})$, is shown on the upper right panel of Fig. 5.12.

Finally, the inclusive charged hadron spectra are obtained by multiplying the full correction function with the background subtracted raw spectra, and dividing by the number of events for every centrality class:

$$\frac{dN}{2\pi p_T dp_T d\eta} = \frac{1}{N_{events}} \times c(p_T) \times c(N_{part}) \times \left(\frac{dN}{p_T dp_T}\right)^{bgr-subtracted} \tag{5.5}$$

The systematic errors on the spectra, which are common to all centrality classes, are listed in Table. 5.3. Sources of systematic uncertainties are: the matching cuts (δ_{match}), normalization (δ_{norm}), particle composition (δ_{mix}), momentum resolution (δ_{reso}), momentum scale (δ_{scale}), and background subtraction (δ_{bgr}) from Table. 4.10. The normalization error is independent of p_T. All other errors vary with p_T but are highly correlated bin-to-bin, which means that points in neighboring p_T bins can move in the same direction by similar factors.

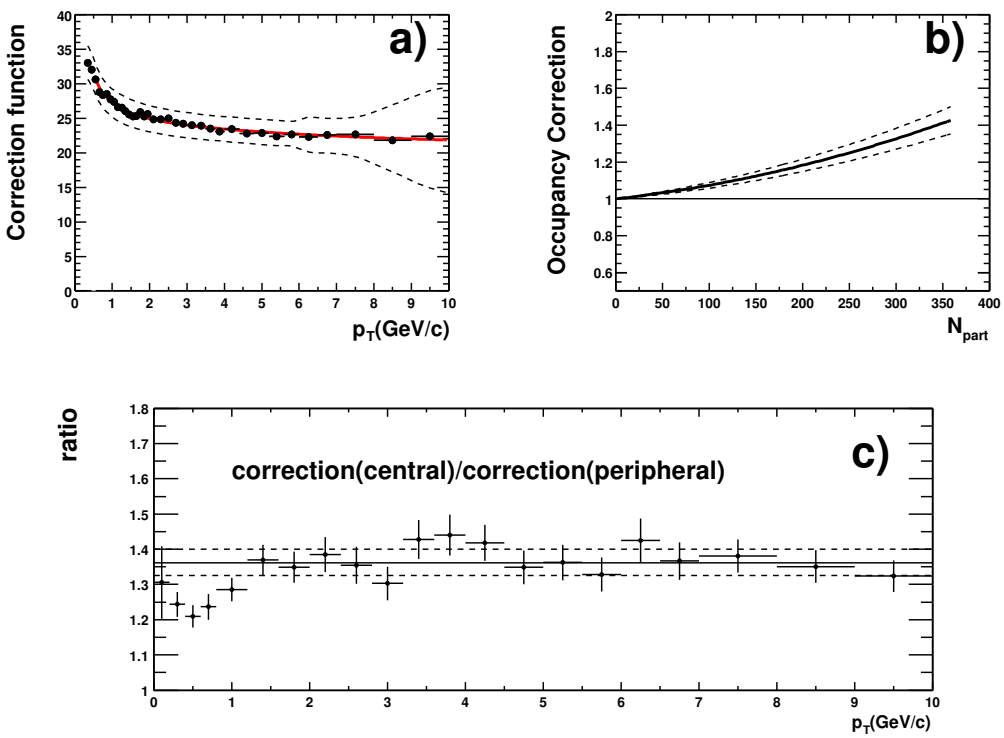

Figure 5.12: Functions used to correct the charged particle p_T spectra. The upper left panel shows the p_T dependent correction, $c(p_T)$. The upper right panel shows the centrality dependent correction, $c(N_{part})$. Systematic uncertainties are indicated by the dashed lines. The two corrections factorize at $p_T > 1.5$ GeV/c, so that for any centrality the full correction function is given by $c(p_T) \times c(N_{part})$. The accuracy of this factorization is demonstrated in the lower panel. The ratio of the full correction for central collisions (5% most central) to the correction for single particle events varies by less than 3% above 1.5 GeV/c (the error bar is the statistical error from the Monte-Carlo calculation).

The centralitydependent systematic errors are quantified in terms of the central-to-peripheral ratio, R_{cp}, shown in Table. 5.4. Besides the uncertainty of the occupancy correction ($\delta_{occupancy}$) illustrated in Fig. 5.12b, the background subtraction procedure has a centrality-dependent uncertainty. As shown in Eq.4.25 and Eq. 4.36, the errors on R_e and R_{decay} reflect the p_T and centrality dependencies. The centrality dependent part contributes about half of the error on both R_e and R_{decay}, and hence does not cancel in R_{cp}. Since the errors on

Table 5.3: Systematic errors on the hadron yields. All errors are quoted as 1σ errors. They are either normalization or are p_T correlated errors, but do not dependent on centrality.

p_T (GeV/c)	δ_{match}(%)	δ_{norm}(%)	δ_{mix}(%)	δ_{reso}(%)	δ_{scale}(%)	δ_{bgr}(%)	total(%)
< 1	3.5	3.2	2.4	0.6	0.6	5	7.3
1 - 5	3	3.2	2.4	0.6	3	5	7.6
5 - 6	3	3.2	1.8	0.6	3.6	5.3	7.9
6 - 7	3	3.2	1.8	0.6	3.3	9.5	11.1
7 - 8	3	3.2	1.8	0.6	3.1	11.5	12.8
8 - 9	3	3.2	1.8	0.9	3.1	21.1	21.9
9 - 10	3	3.2	1.8	5.3	3.1	31.1	32.1

Table 5.4: Systematic errors on the central/peripheral ratio. All errors are given in percent and are quoted as 1σ errors. Most of the systematic errors listed in Table. 5.3 cancel in this ratio. Only those errors that are uncorrelated with centrality are shown here.

p_T (GeV/c)	$\delta_{occupancy}$(%)	$\delta_{feeddown}$(%)	$\delta_{R_e \oplus R_{decay}}$ (%)	total(%)
< 6	5	5	1.8	7.3
6 - 7	5	5	4.1	8.2
7 - 8	5	5	7.1	10
8 - 9	5	5	17.6	19
9 - 10	5	5	23.5	24.6

R_e and R_{decay} are independent, the uncertainty on R_{cp} is approximately equal to $\delta_{R_e \oplus R_{decay}}$ from Table. 4.10. Finally, $\delta_{feeddown}$ is the centrality-dependent error from the feed-down subtraction.

5.8 Comparison with Identified Charged Hadron Spectra

Recently, PHENIX has published spectra of identified charged hadrons [103]. The charged hadron spectra can be compared to the sum of $\pi^{\pm}, K^{\pm}$, p and $\bar{p}$ to check the accuracy of our systematic error analysis. Since the kaon spectra are measured only up to 2 GeV/c, this comparison is also limited to 2 GeV/c.

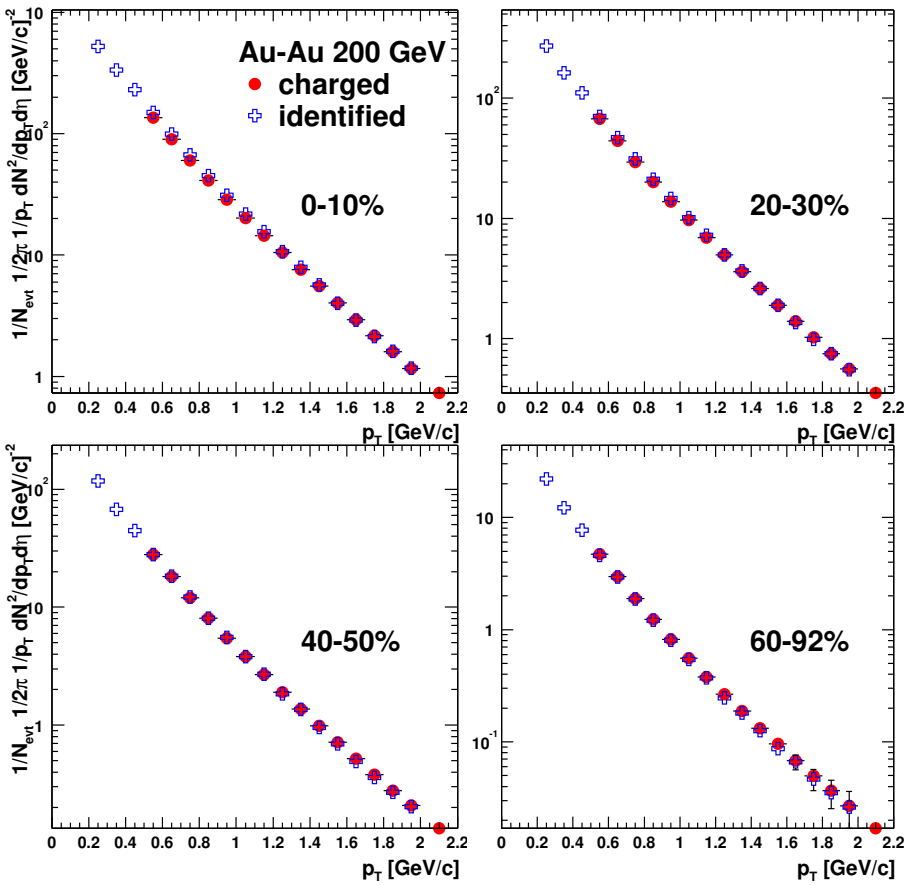

Figure 5.13: The comparison between the sum of the identified charged hadron spectra and unidentified charged hadron spectra from the same experiment for four centrality classes. The errors shown are statistical only.

The result of the comparison is shown in Fig. 5.13. The identified hadron spectra have been converted from $dN/dy \rightarrow dN/d\eta$ before the summation. From Ref. [103], the typical systematic errors for the identified hadron spectra is 8-14% (1σ), depending on particle species. So, the error on the summed spectra is around 10%. From Table. 5.3, the total error on the charged hadron spectra is about 5% for $p_T < 5$ GeV/c. This gives $10 \oplus 5 \approx 11\%$ error on the difference between charged hadron and the summed spectra. As Fig. 5.13 shows, the overall agreement between the two spectra is indeed better than 10%.

Chapter 6

Results and Discussion

6.1 Inclusive Charged Hadron p_T Spectra

Fig. 6.1 shows the inclusive charged hadron p_T spectra for various centrality classes. All spectra exhibit power-law tails at high p_T. But for peripheral collisions, the power-law shape is more concave than for central collisions. More details of the centrality dependence of the spectral shape can be seen from Fig. 6.2, which shows for each centrality class the ratio of the spectra to the minimum-bias spectrum. In these ratios, most systematic errors cancel or affect the overall scale only. The characteristic centrality dependence of the shape already observed in $\sqrt{s_{NN}} = 130$ GeV $Au-Au$ collisions [51, 52] is more apparent at $\sqrt{s_{NN}} = 200$ GeV. In peripheral collisions, the ratio decreases up to $p_T \sim 2$ GeV/c and then rises up to about 4 GeV/c. The trends are reversed in the most central collisions. In the range above 4–5 GeV/c, all ratios appear to be constant as function of p_T, which would imply that they have a similar centrality independent shape.

Based on the different trends observed in Fig. 6.2, we can distinguish three p_T regions: 0.5–2, 2–4.5 and > 4.5 GeV/c. The different centrality dependence of the spectral shape in these regions can be quantified by a truncated average p_T:

$$\langle p_T^{trunc} \rangle \equiv \frac{\int_{p_T^{min}}^{8\ GeV/c} p_T \cdot dN/dp_T}{\int_{p_T^{min}}^{8\ GeV/c} dN/dp_T} - p_T^{min}, \tag{6.1}$$

which is insensitive to the normalization of the spectra. The upper bound of 8 GeV/c in the integral is given by the limited p_T reach for peripheral centrality classes as shown in Fig. 6.1. In Fig 6.3, the values of $\langle p_T^{trunc} \rangle$ for the three p_T^{min} values are plotted as function of centrality, represented by the average number of participating nucleons (N_{part}) for each centrality class.

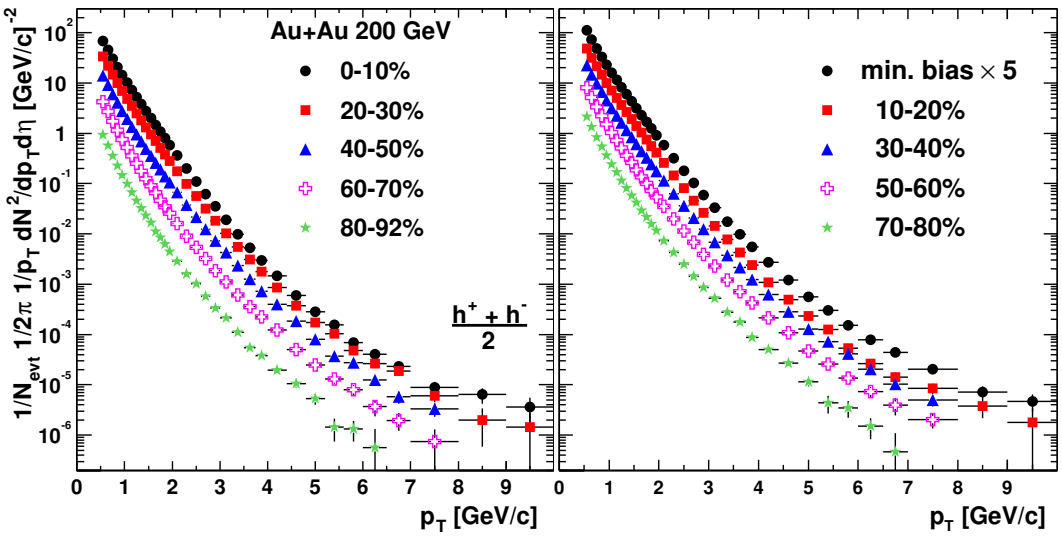

Figure 6.1: p_T spectra of charged hadrons for minimum bias collisions along with spectra for 9 centrality classes. The minimum bias spectrum has been multiplied by 5 for visibility. Only statistical errors are shown in the spectra. Most of the p_T dependent systematic errors are independent of centrality and are tabulated in Table. 5.3.

For $p_T^{min} = 0.5$ GeV/c, where particle production is expected to be governed by soft physics, $\langle p_T^{trunc} \rangle$ increases with N_{part}. This trend is also seen for the average p_T of identified charged hadrons, and reflects the increased radial flow of soft particles in more central collisions [103]. For $p_T^{min} = 2$ GeV/c, the trend is significantly different. For peripheral collisions, $\langle p_T^{trunc} \rangle$ is substantially larger than the value obtained with $p_T^{min} = 0.5$ GeV/c due to the presence of the power-law tail. With increasing N_{part}, $\langle p_T^{trunc} \rangle$ for $p_T^{min} = 2$ GeV/c decreases and the values obtained with $p_T^{min} = 0.5$ and 2 GeV/c approach each other, which indicates an almost exponential spectrum in central collisions around ~ 2 GeV/c. For the highest p_T range ($p_T^{min} = 4.5$ GeV/c), $\langle p_T^{trunc} \rangle$ is approximately constant. This implies that the shape of the spectrum is nearly independent of centrality, as would be expected if this region is dominated by hard scattering.

However, the yields at high p_T do not scale with the number of nucleon-nucleon collisions; they are suppressed comparing to the binary collision scaling expected for hard scattering processes. This can be clearly seen from Fig. 6.4, which shows R_{cp}, the ratio of yields for central and peripheral collisions nor-

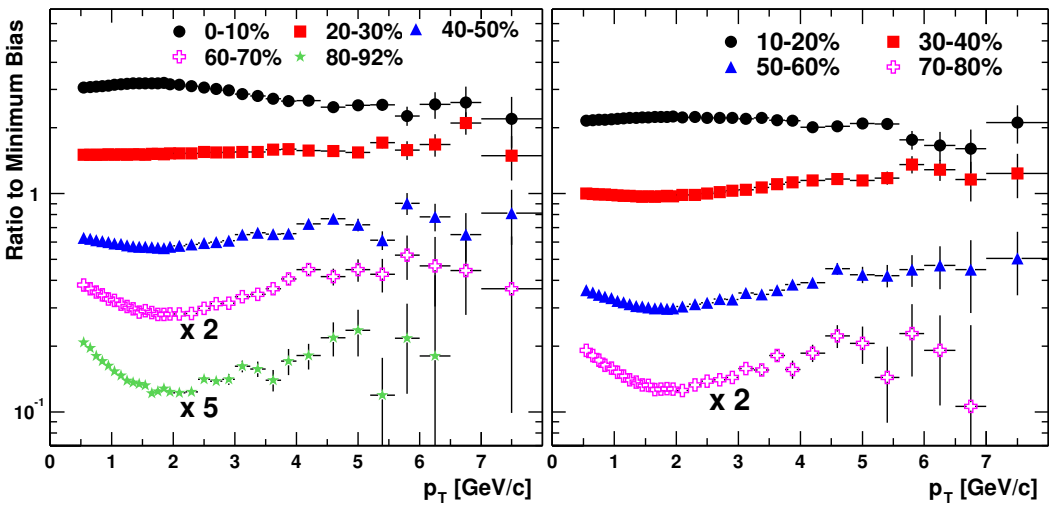

Figure 6.2: Ratios of centrality selected p_T spectra to the minimum bias spectrum. Ratios for peripheral classes are scaled up for clarity. For the p_T range shown, most of the systematic errors cancel in the ratio. The remaining systematic errors that can change the shape are less than 10% (see Table. 5.4) and are correlated bin-to-bin in p_T.

malized to the average number of nucleon-nucleon collisions in each event sample. The ratio is below unity for all p_T. The three p_T regions show different trends as outlined in the discussion of Fig. 6.3: (i) In the "soft" region with $p_T < 2$ GeV/c, the ratio increases as function of p_T. (ii) In the "hard" region with $p_T > 4.5$ GeV/c, the suppression appears to be constant at ~ 0.3, which again indicates that the spectra have a similar shape, but with the yield in central collisions being suppressed by a constant factor from 4.5 to 10 GeV/c. (iii) In the transition region from 2 to $\sim$4.5 GeV/c, the ratio decreases as a function of p_T.

6.2 Suppression of High p_T Hadrons

At finite Q^2, nuclear modifications of the parton distribution [40] and initial [33, 59] and final state [22] interactions of the scattering partons can modify the high-p_T hadron production rates in hard scattering processes. Medium modifications of hadron spectra are often quantified by the "nuclear modification factor" R_{AA}, which we calculate for each centrality class as the ratio of the

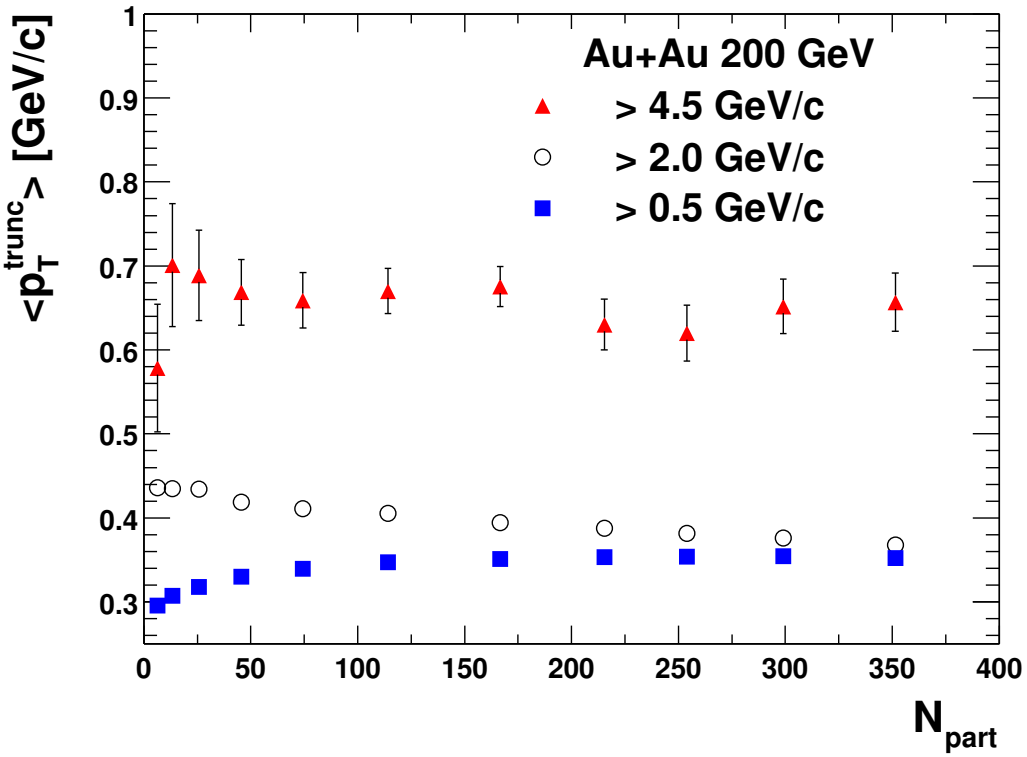

Figure 6.3: Centrality dependence of $\langle p_T^{trunc} \rangle$, defined as the average p_T of charged particles with p_T above a threshold p_T^{min} minus the threshold p_T^{min}(see Eq. 6.1). Shown are $\langle p_T^{trunc} \rangle$ values for three p_T^{min} cuts, with $p_T^{min} = 0.5$, 2 and 4.5 GeV/c respectively. Only statistical errors are shown.

yield per nucleon-nucleon collision in $Au - Au$ to the yield in nucleon-nucleon collisions:

$$R_{AA}(p_T, \eta) = \left(\frac{1}{N_{evt}} \frac{d^2 N^{A+A}}{dp_T d\eta} \right) / \left(\frac{\langle N_{coll} \rangle}{\sigma_{inel}^{N+N}} \frac{d^2 \sigma^{N+N}}{dp_T d\eta} \right) \tag{6.2}$$

$\langle N_{coll} \rangle / \sigma_{inel}^{N+N}$ is the average Glauber nuclear overlap function, $\langle T_{AuAu} \rangle$, for each centrality class. In order to calculate R_{AA}, we need a reference spectrum for nucleon-nucleon collisions. Due to the lack of charged hadron data with sufficient reach in p_T from our own experiment, we construct the $N - N$ reference for charged hadrons from the π^0 spectra in $p - p$ collisions at $\sqrt{s} = 200$ GeV/c measured by PHENIX [29], and the charged hadron to pion ratio observed in other experiments, as described below.

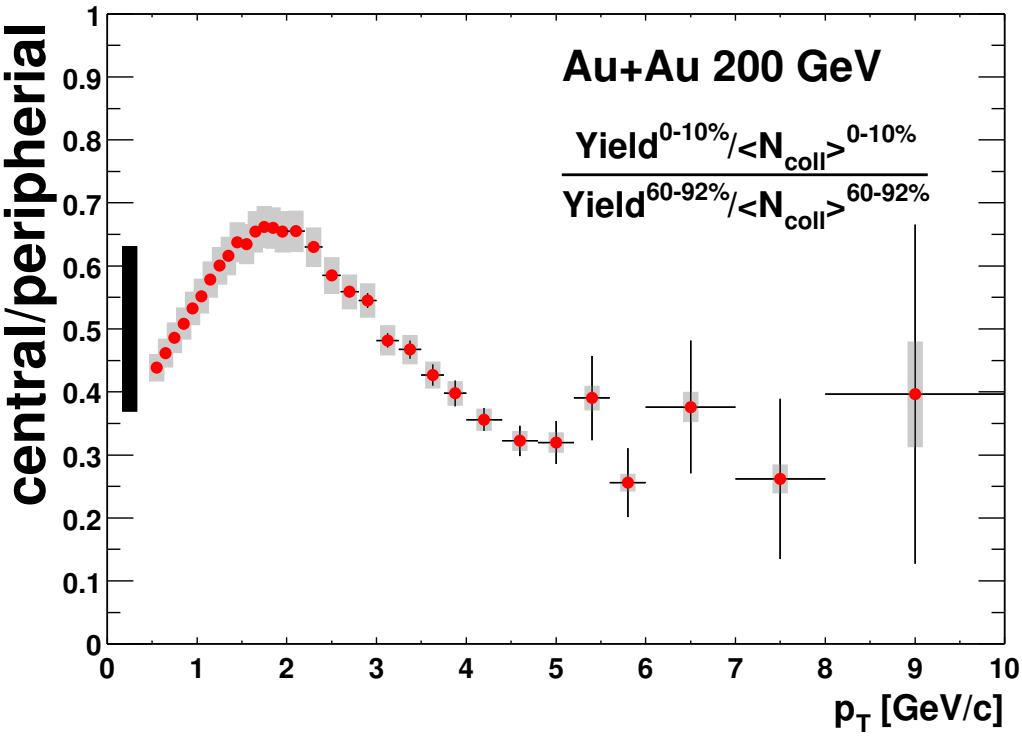

Figure 6.4: Ratio of charged hadron yields per nucleon-nucleon collision between central (0-10%) and peripheral (60-92%) $Au-Au$ collisions. In this ratio, most of the systematic errors cancel. The solid error bars on each data point are statistical. The error bar on the left hand side of the figure is the overall scale error relative to 0.5, which is the quadrature sum of (i) the uncertainty of $\langle N_{coll} \rangle$ (see Table. 4.1.4) and (ii) the uncertainty on the occupancy correction ($\delta_{occupancy}$). The shaded error band on each data point is the p_T dependent systematic error from $\delta_{R_e \oplus R_{decay}}$ and centrality dependent feed down correction ($\delta_{feeddown}$) as given in Table. 5.4.

The PHENIX π^0 spectrum from $p-p$ collisions is measured out to 14 GeV/c. These data can be parameterized by a power-law function,

$$\frac{d^2\sigma^{\pi^0}_{N+N}}{\sigma^{N+N}_{inel} dp_T d\eta} = \frac{A}{\sigma_{inel}} \left(\frac{p_0}{p_0 + p_T} \right)^n \quad , \tag{6.3}$$

with A = 386 mb/GeV^2, p_0 = 1.219 GeV, and n = 9.99 [29]. Fig. 6.5a shows the p_T spectra for neutral pions and the power-law fit (Eq. 6.3) to the data.

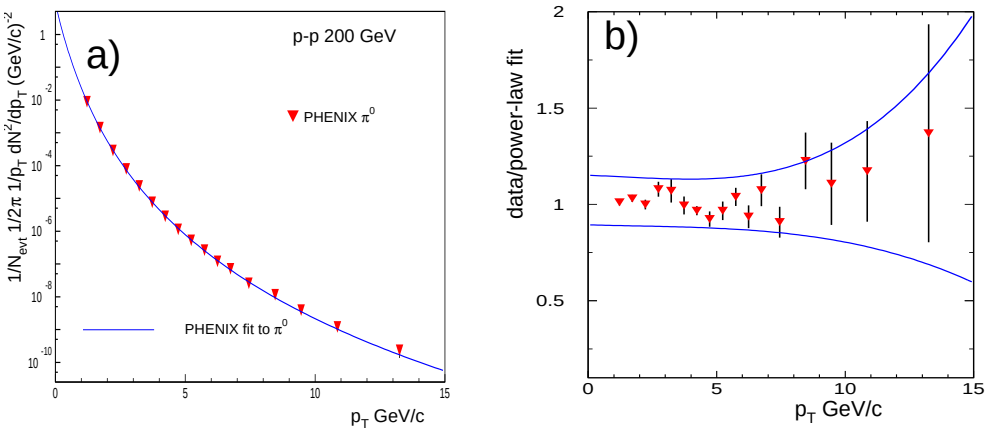

Figure 6.5: a) PHENIX π^0 spectrum from $p-p$ collisions at $\sqrt{s} = 200$ GeV together with the power-law fit Eq. 6.3. b) Ratio of the data to the fit together with the systematic error band.

Fig. 6.5b shows the ratio of the data to the power-law fit. At larger p_T, the power-law fit underestimates the data. To estimate the uncertainty of the parameterization, the following errors are added in quadrature,

1. Statistical errors and p_T correlated systematic errors from [29, 107] are added in quadrature. Below $p_T \leq 10$ GeV/c the statistical errors are negligible, but they dominate at higher p_T. The combined errors increase with p_T.

2. The absolute normalization error is 9.6% [108], plus 4% uncertainty of the geometrical acceptance [107].

3. The systematic deviation of the data from the power-law fit at $p_T > 8$ GeV/c is compensated by an offset, which we add to the systematic error. The offset is calculated by fitting the ratio with a second order polynomial.

The resulting total systematic error is $< 15\%$ at $p_T < 10$ GeV/c, and increase towards higher p_T.

In $p-p$ experiments at the ISR, the h/π ratio was measured to be 1.6 ± 0.16, independent of p_T from 1.5 to 5 GeV/c, and independent of $\sqrt{s}$ from 23 to 63 GeV [27]. Below 1.5 GeV/c, h/π decreases towards lower p_T. The ISR data are consistent with data on π, K, p production from the FNAL

E735 experiment [109] at $\sqrt{s} = 1.8$ TeV. The h/π ratio computed from these data increases with p_T and reaches a value of 1.6 at the end of the measured p_T range, $\sim$1.5 GeV/c. At high momentum, an h/π ratio of $\sim$ 1.6 is also observed for quark and gluon jet fragmentation in e^+e^- collisions at LEP by the DELPHI Collaboration [63]. Finally, charged hadron data measured by PHENIX in $p-p$ collisions and UA1 [110] in $\bar{p}+p$ collisions, both at $\sqrt{s} =$ 200 GeV/c, give consistent h/π ratios when compared to the PHENIX $p-p$ π^0 data. These agreement are summarized in Fig. 6.6, where the 10% systematic error bands on the h/π ratio are shown.

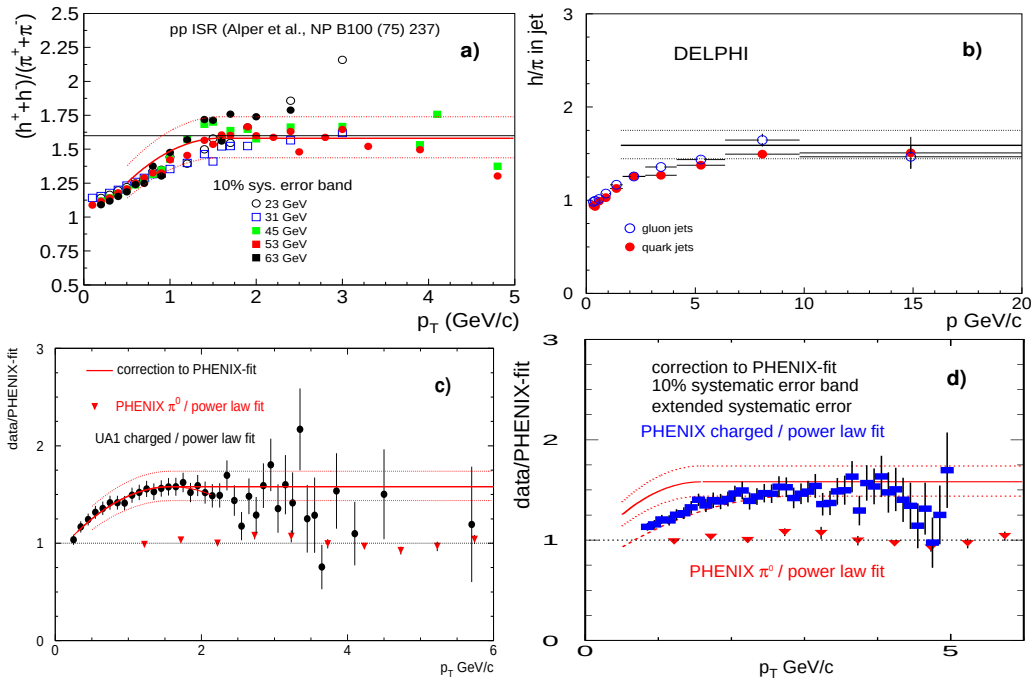

Figure 6.6: a) ISR data from Ref. [27]. π,K,p are summed to give the h/π ratio. b) h/π ratio as function of momentum found in quark and gluon jets in DELPHI [63]. c) Ratio of PHENIX π^0 data and UA1 [110] charged data to the PHENIX power-law fit. The fit to the UA1/power-law ratio is used to correct the power law to represent the charged hadron reference for 200 GeV. d) Same as c), but using the PHENIX data.

Based on these findings, we assume that h/π is constant above 1.5 GeV/c in $p-p$ collisions at RHIC and that we can scale up the π^0 cross section (Eq. 6.3) by this factor to obtain a reference for charged hadron production.

To be consistent with the data described above, we correct this reference below 1.5 GeV/c using,

$$r(p_T) = \begin{cases} R_{h/\pi} - a(p_{max} - p_T)^2 & \text{for } p_T \leq p_{max} \\ R_{h/\pi} & \text{for } p_T > p_{max} \end{cases} \quad , \tag{6.4}$$

where $R_{h/\pi} = 1.6$, $p_{max} = 1.6$ GeV/c and a = 0.28 GeV^{-2}. This function is obtained from the fit to the UA1/power-law-fit ratio as shown in Fig. 6.6c. As shown in Fig. 6.6a,b, and c, this correction together with 10% error bands covers the variations from different data sets. However, there are some deviations at low p_T in Fig. 6.6d, these deviations are covered by introducing an asymmetric systematic error. This error is shown by the dashed line for $p_T < 2$ GeV/c.

Finally, the charged hadron reference used in this analysis is given by the product of the power-law function from Eq. 6.3 and the empirical correction from Eq. 6.4 as:

$$\frac{d^2\sigma_{N+N}^{h^+ + h^-}}{\sigma_{inel}^{N+N} dp_T d\eta} = \frac{A}{\sigma_{inel}} \left(\frac{p_0}{p_0 + p_T} \right)^n \times r(p_T) \quad . \tag{6.5}$$

The final charged hadron reference is compared with PHENIX and UA1 data in the left panel of Fig. 6.7. A more quantitative comparison is obtained by dividing the data by the reference, and is shown in the right panel of Fig. 6.7.

The 1σ systematic errors on the charged hadron $N - N$ reference are summarized in Table. 6.1. The main sources of uncertainties include: (i) the systematic errors on the absolute normalization of the PHENIX π^0 data ($\delta_{norm}^{\pi^0}$), which are independent of p_T, (ii) uncertainties due to the power-law fit to the π^0 data ($\delta_{fit}^{\pi^0}$), and (iii) uncertainties on $R_{h/\pi}$ ($\delta_{h/\pi}$), which are estimated from the spread of $R_{h/\pi}$ obtained from different data sets used to constrain h/π^0.

Fig. 6.8 shows the nuclear modification factor $R_{AA}(p_T)$ for charged hadrons from minimum bias and nine centrality classes. The systematic errors on R_{AA} are described in the figure captions. At low p_T, the charged hadron R_{AA}s increases monotonically up to 2 GeV/c for all centrality classes. At $p_T > 2$ GeV/c, the R_{AA}s remains constant and close to unity for the most peripheral centrality class. However, in central collisions, it decreases at higher p_T, down to an approximately constant value of 0.2–0.3 for $p_T > 4$–5 GeV/c. This is consistent with Fig. 6.4, where the central to peripheral ratio also saturates above 4–5 GeV/c. This approximately p_T independent suppression pattern

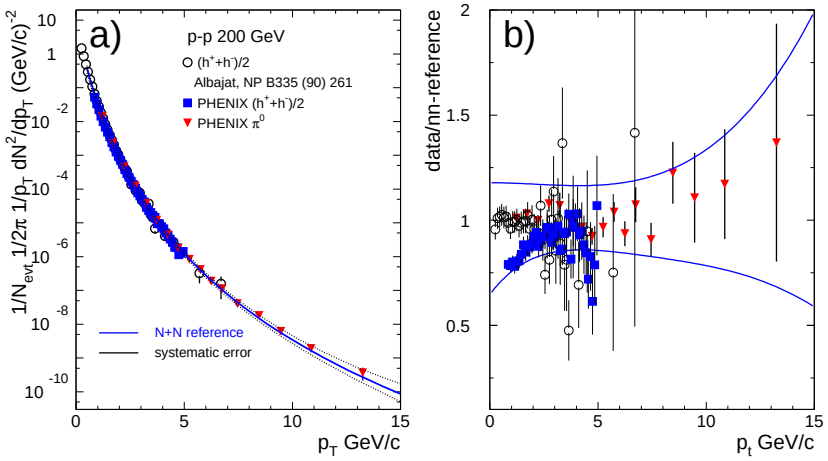

Figure 6.7: a) PHENIX charged hadron data compared with UA1 [110] and neutral pions from PHENIX [29] scaled by 1.581. Also shown is the $N-N$ reference and its systematic uncertainty. b) Ratio of the data to the reference. The lines indicates the systematic uncertainty on the reference distribution.

Table 6.1: Systematic errors on the charged hadron $N-N$ reference spectrum. All errors are given in percent and are quoted as 1σ errors. Most of the errors are correlated with p_T.

p_T (GeV/c)	$\delta^{\pi^0}_{norm}$(%)	$\delta^{\pi^0}_{fit}$(%)	$\delta_{R_{h/\pi}}$(%)	total (%)
0.75	10.4	-3.9 + 9.1	-15.1 + 5.9	-18.7 + 15.0
1.00	10.4	-4.1 + 8.9	-14.4 + 5.9	-18.3 + 14.9
1.50	10.4	-4.6 + 8.3	-11.6 + 5.9	-16.3 + 14.6
2.00	10.4	-5.1 + 7.7	-7.9 + 5.9	-14.0 + 14.2
2.50	10.4	-5.5 + 7.2	-5.9 + 5.9	-13.1 + 13.9
3.00	10.4	-5.9 + 6.7	-5.9 + 5.9	-13.3 + 13.7
3.50	10.4	-6.4 + 6.4	-5.9 + 5.9	-13.5 + 13.5
4.50	10.4	-7.5 + 6.5	-5.9 + 5.9	-14.1 + 13.6
5.50	10.4	-8.9 + 7.9	-5.9 + 5.9	-14.9 + 14.3
6.50	10.4	-10.7 + 10.5	-5.9 + 5.9	-16.0 + 15.9
7.50	10.4	-12.9 + 14.3	-5.9 + 5.9	-17.6 + 18.7
8.50	10.4	-15.8 + 19.4	-5.9 + 5.9	-19.8 + 22.8
9.50	10.4	-19.3 + 25.9	-5.9 + 5.9	-22.7 + 28.5

has been interpreted as a result of the detailed interplay between the Cronin effect, nuclear shadowing, and partonic energy loss [58].

Also shown in Fig. 6.8 are R_{AA} for neutral pions from ref. [54]. The neutral pion R_{AA} values also seem to reach a maximum around 2 GeV/c, but the changes are smaller than those for charged hadrons. Except for the most peripheral bin, the neutral pion R_{AA} is always below the charged R_{AA} in the range of $2 < p_T < 4.5$ GeV/c. However, at $p_T > 4.5$ GeV/c, R_{AA} for both neutral pions and hadrons saturates at roughly the same level, indicating a similar suppression for neutral pions and charged hadrons at high p_T.

The fact that the neutral pion R_{AA} values are smaller than the inclusive charged hadron R_{AA} at intermediate p_T ($2 < p_T < 4.5$ GeV/c) has already been observed at $\sqrt{s_{NN}} = 130$ GeV [50]. This difference can be explained by the large p/π ratio observed in the same p_T range in central $Au - Au$ collisions [60, 61]. This large relative proton and anti-proton yield indicates a deviation from the standard picture of hadron production at $p_T > 2$ GeV/c, which assumes that the hadrons are created by the fragmentation of energetic partons. Such a deviation has led to models of quark coalescence [64] or baryon junctions [111] as the possible mechanisms to enhance the proton production rate at medium p_T . Both models predict that baryon enhancement is limited to $p_T < 5$ GeV/c, beyond which jet fragmentation should eventually become the dominant production mechanism for all particle species. In that case, one would expect a similar suppression factor for charged hadrons and π^0, in agreement with the data at $p_T > 4.5$ GeV/c. Recently, the difference of R_{AA} between charged hadrons and pions was also argued as the consequence of centrality and particle species dependent $\langle k_T \rangle$ broadening effect [112].

If hard-scattering dominates charged hadron production at $p_T > 4.5$ GeV/c, the particle composition should be determined by the jet fragmentation function, similar to nucleon-nucleon collisions. Fig. 6.9 shows h/π^0 for all centrality classes. The systematic errors are explained in the figure captions. In the most peripheral collisions, the h/π^0 ratio is consistent with the $p - p$ values down to $p_T = 2$ GeV/c. In central collisions, the h/π^0 ratio is enhanced by as much as 50% above the $p - p$ value in the region $1 < p_T < 4.5$ GeV/c. This enhancement gradually decreases towards more peripheral collisions and reflects the difference of R_{AA} between the charged hadrons and π^0s, which is due to the large baryon contribution. The enhancement also strongly depends on p_T: It reaches a maximum between 2.5 and 3.5 GeV/c, then decreases. At $p_T > 4.5$ GeV/c, the h/π^0 ratios for all centralities reach an approximately constant value of 1.6, which is consistent with the h/π value observed in $p - p$ [27] collisions and in jet fragmentation in e^+e^- [63] collisions. The similarity of the spectral shape and of the particle composition between $Au - Au$ and $p - p$

collisions suggest that fragmentation of hard-scattered partons indeed is the dominant mechanism of particle production in $Au-Au$ collisions above p_T of 4–5 GeV/c, regardless of the fact that the yields do not scale with N_{coll}.

Since R_{AA} values for charged hadrons and π^0s are approximately constant at $p_T > 4.5$ GeV/c, we can quantify the centrality dependence of the R_{AA} value by calculating it from yields integrated above 4.5 GeV/c. The upper panel of Fig. 6.10 shows R_{AA} for $p_T > 4.5$ GeV/c as function of N_{part}. The R_{AA} values for charged hadrons and π^0 agree for all centrality classes within errors. In peripheral collisions with $N_{part} < 50$, R_{AA} is consistent with binary collision scaling. With increasing N_{part}, R_{AA} decreases monotonically, reaching a value of 0.23 ± 0.03 (0-5% most central) for charged hadrons and 0.24 ± 0.02 (0-10% most central) for π^0s. There is an additional 14% error common to charged hadrons and π^0s, which originates from the uncertainty on the NN reference and N_{coll}.

To address suggestions that the yield of high p_T hadrons in $Au-Au$ collisions may be proportional to N_{part} instead of N_{coll} [59, 113], we have investigated a different ratio,

$$R_{AA}^{N_{part}} = 2\langle N_{coll}\rangle / \langle N_{part}\rangle \times R_{AA} \qquad . \tag{6.6}$$

$R_{AA}^{N_{part}}$ for $p_T > 4.5$ GeV/c is shown in the lower panel of Fig. 6.10, together with solid (or dashed) bands representing the allowed range if the data follow binary collision (or participant) scaling. As discussed above, for peripheral collisions, $R_{AA}^{N_{part}}$ follows more closely the binary collision scaling. Above 50 participants, $R_{AA}^{N_{part}}$ varies by only $\pm 20\%$. However, it peaks at $\langle N_{part}\rangle = 100$ and decreases monotonically towards more central collisions.

The decrease of $R_{AA}^{N_{part}}$ could be a natural consequence of energy loss of hard scattered partons in the medium [113]. If the energy loss is large, hard scattered partons may only escape near the surface of the reaction volume. In a cylindrical collision geometry, for which the number of collisions from the surface is proportional to N_{part}, binary collision scaling is reduced to an approximate participant scaling. Detailed calculations show that in this case, $R_{AA}^{N_{part}}$ slightly decreases with N_{part} depending in details on how the energy loss is modelled [113]. This interpretation is also consistent with our previous conclusion that, above 4.5 GeV/c, hadron production is dominated by hard-scattering although the yield does not scale with the number of binary collisions. Gluon saturation scenarios [59] also suggest approximate participant scaling. However, the same models suggest a 30% increase in $R_{AA}^{N_{part}}$ over the p_T range 4.5–9 GeV/c in central collisions that is not observed in the data (compare with the upper right panel in Fig. 6.8).

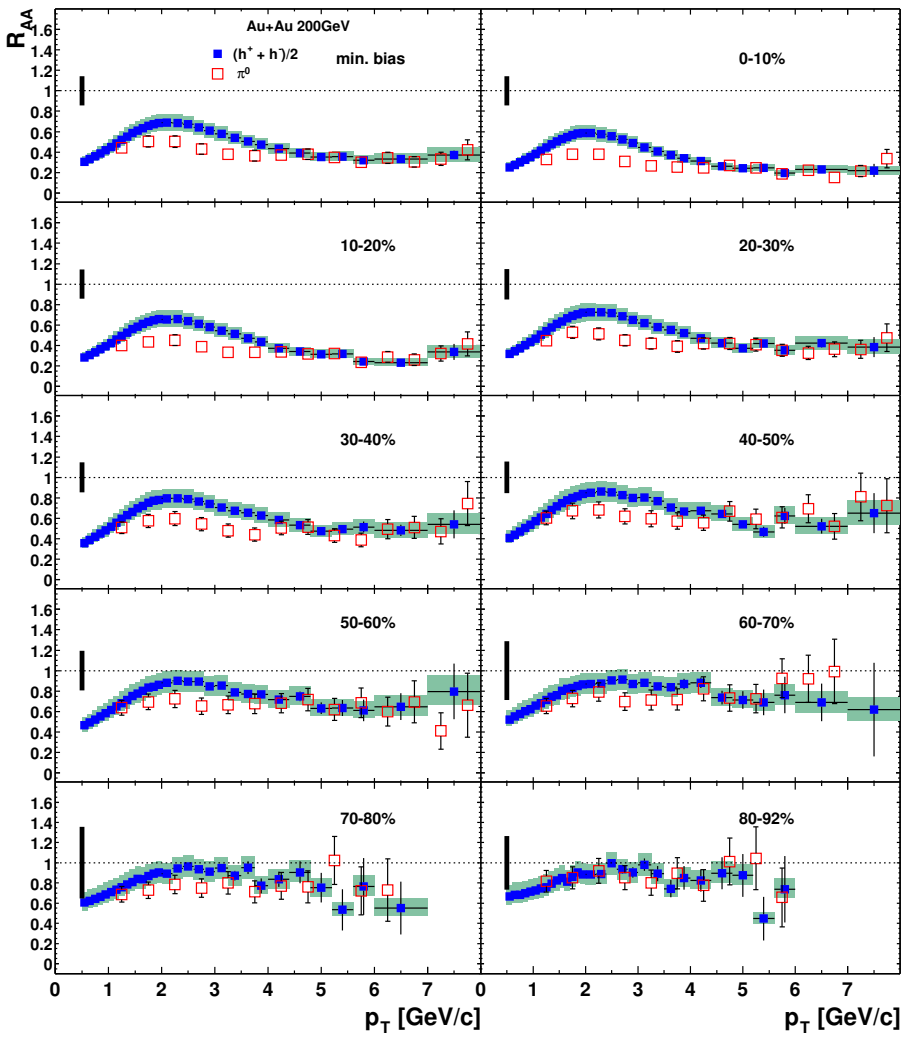

Figure 6.8: R_{AA} for $(h^+ + h^-)/2$ and π^0 as function of p_T for minimum bias and 9 centrality classes according to the "*Fine*" type of centrality classes defined in Table. 4.1.4. The error bars on the π^0 data points include statistical and systematical errors on the $Au-Au$ data and the $N-N$ reference. The error bars on $(h^+ + h^-)/2$ data points are statistical errors only. The normalization errors on the reference common for charged hadrons and π^0s are added in quadrature with the uncertainty on $\langle N_{coll} \rangle$ and are indicated by the black bar on the left side of each panel. This error ranges from 15% to 36% from central to peripheral collisions and can shift all points in the charged and neutral pion R_{AA} up and down together. The shaded band on charged R_{AA} includes the remaining systematic errors on the charged $N-N$ reference summed in quadrature with the systematic errors from the $Au-Au$ spectra. This error amounts to -12.5% – +18% at low p_T and changes to $\pm 12.5\%$ at $p_T = 4.5$ GeV/c and $\pm 18.5\%$ at $p_T = 8$ GeV/c.

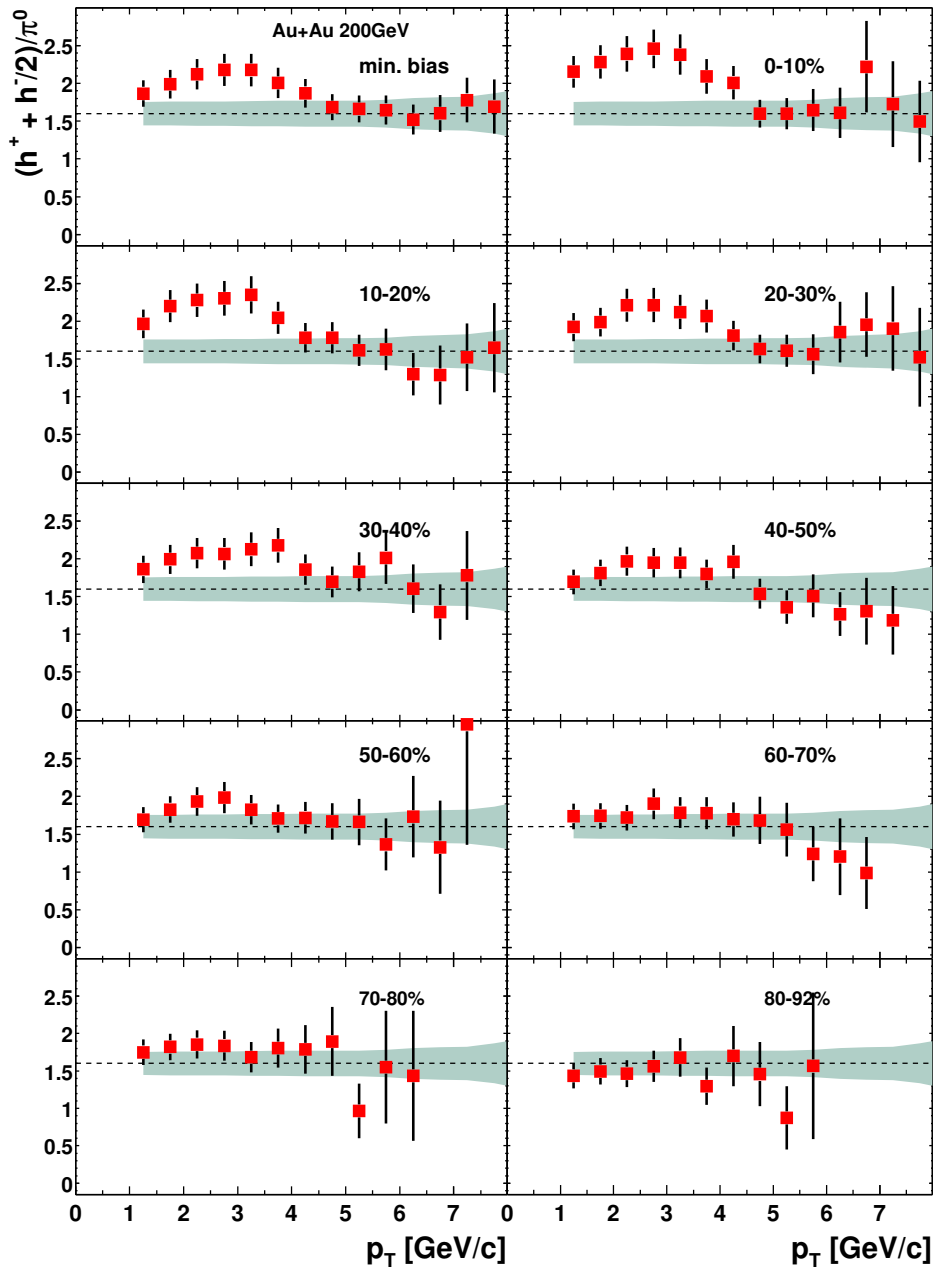

Figure 6.9: Charged hadron to π^0 ratios for minimum bias events and 9 centrality classes according to the "*Fine*" type of centrality classes defined in Table. 4.1.4. The error bars represent the quadratic sum of statistical and point-by-point systematic errors from $(h^+ + h^-)/2$ and π^0. The shaded band shows the percent normalization error (dominantly from $(h^+ + h^-)/2$ data) common to all centrality classes. The dashed line at 1.6 is the h/π ratio measured in $p-p$ [27] and e^+e^- [63] collisions.

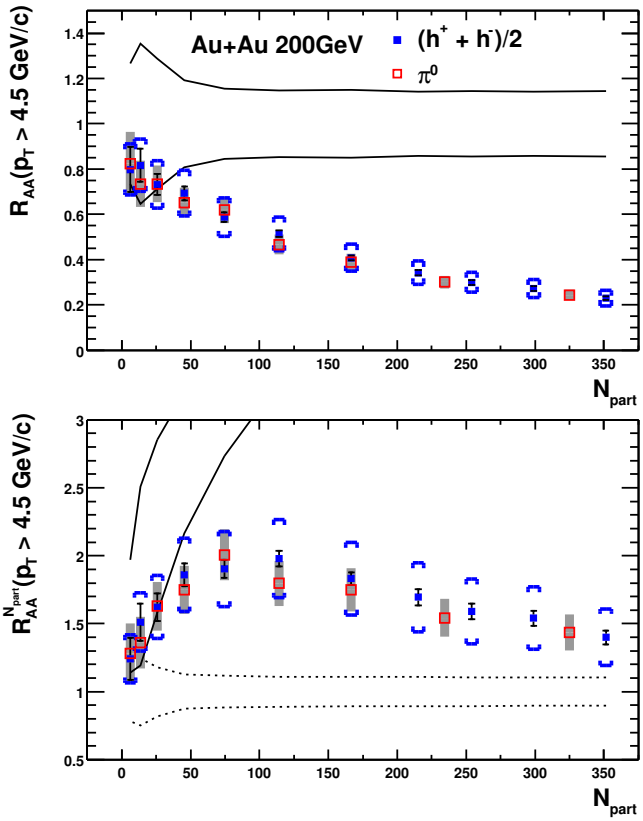

Figure 6.10: $Au-Au$ yield integrated for $p_T > 4.5$ GeV/c over the $N-N$ yield, normalized using either N_{coll} (R_{AA} in the top panel) or N_{part} ($R_{AA}^{N_{part}}$ in the bottom panel), plotted as function of $\langle N_{part}\rangle$. "*Fine*" and "*Coarse*" types of the centrality classes defined in Table. 4.1.4 are used for $(h^+ + h^-)/2$ and π^0, respectively. Following errors are shown in both figures: **i).** The bands denoted by solid (dashed) lines represent the binary collision (participant pair) scaling. The width of the bands represent the systematic errors due to the normalization errors common to $(h^+ + h^-)/2$ and π^0 added in quadrature with the uncertainty on $\langle N_{coll}\rangle$ ($\langle N_{part}\rangle$). These errors can move $(h^+ + h^-)/2$ and π^0 up and down together in centrality correlated way, and are the same as the black error bars discussed in Fig. 6.8. **ii).** The error bars for each $(h^+ + h^-)/2$ data point are statistical error. The p_T correlated systematic errors from $Au-Au$ and the rest of the systematic errors on the charged hadron $N-N$ reference are represented by the brackets, within which the charged hadron data points can move up or down relative to π^0. **iii).** Dark shaded error bands around each π^0 data point include both statistical and point-to-point systematic errors on $Au-Au$ and the π^0 $N-N$ reference.

6.3 Energy Dependence and x_T Scaling

The inclusive charged hadron and π^0 p_T spectra and h/π^0 ratios suggest that fragmentation of hard scattered partons is the dominant production mechanism of high p_T hadrons not only in $p-p$ but also in $Au-Au$ collisions. For $p-p$ collisions this fact was demonstrated on general principles well before the advent of QCD by the method of "x_T-scaling". This method does not depend on whether the initial projectiles are protons or Au ions, so it should be directly applicable to $Au-Au$ collisions. Since our data show a suppression of high-p_T particles in central $Au-Au$ collisions with respect to point-like scaling from $p-p$ and peripheral $Au-Au$ collisions, it is important to investigate whether the production dynamics of high-p_T particles in central (and peripheral) $Au-Au$ collisions are the same or different from those in $p-p$ collisions. We first review the x_T-scaling method in $p-p$ collisions and then apply it to the present $Au-Au$ data.

The idea of hard-scattering in $N-N$ collisions dates from the first indication of point-like structure inside the proton, in 1968, found in deep inelastic electron-proton scattering [114], i.e. scattering with large values of 4-momentum transfer squared, Q^2, and energy loss, ν. The discovery that the Deep Inelastic Scattering (DIS) structure function

$$F_2(Q^2,\nu) = F_2\left(\frac{Q^2}{\nu}\right) \tag{6.7}$$

"scales", or in other words, depends on the ratio

$$x = \frac{Q^2}{2M\nu} \tag{6.8}$$

independent of Q^2 as suggested by Bjorken [115], led to the concept of a proton being composed of point-like "partons". Since the partons of DIS are charged, and hence must scatter electromagnetically from each other in $p-p$ collisions, a general formula for the cross section of the single-particle inclusive reaction

$$p+p \rightarrow C+X \tag{6.9}$$

was derived [116] using the principle of factorization of the reaction into parton distribution functions for the protons, fragmentation functions to particle C for the scattered partons and a short-distance parton-parton hard scattering cross section (see Fig. 1.5).

The invariant cross section for the single-particle inclusive reaction (Eq. 6.9), where particle C has transverse momentum p_T near mid-rapidity, was given

by the general scaling form [117]:

$$E\frac{d^3\sigma}{dp^3} = \frac{1}{p_T^n} F\left(\frac{2p_T}{\sqrt{s}}\right) \quad \text{where} \quad x_T = 2p_T/\sqrt{s} \qquad . \tag{6.10}$$

The cross section has 2 factors: a function F which depends only on the ratio of momenta, and a dimensioned factor, p_T^{-n}, where n depends on the quantum exchanged in the hard-scattering. For QED or Vector Gluon exchange [116], $n = 4$. For the case of quark-meson scattering by the exchange of a quark [117], n=8. The discovery of high p_T pions in $p-p$ scattering at the CERN-ISR, in 1972 [118, 119, 120], at a rate much larger than predicted by electromagnetic scattering, but with the scaling form of Eq. 6.10, proved that the partons of DIS strongly interact with each other.

Inclusion of QCD [121] into the scaling form led to the x_T-scaling law (Eq. 6.10),

$$E\frac{d^3\sigma}{dp^3} = \frac{1}{\sqrt{s}^{\,n(x_T,\sqrt{s})}}\, G(x_T) \qquad , \tag{6.11}$$

where the "x_T-scaling power" $n(x_T, \sqrt{s})$ should equal 4 in lowest order (LO) calculations, analogous to the $1/q^4$ form of Rutherford Scattering in QED. The structure and fragmentation functions, which scale as the ratios of momenta are all in the $G(x_T)$ term. Due to higher order effects such as the running of the coupling constant, $\alpha_s(Q^2)$, the evolution of the structure and fragmentation functions, and the initial state k_T, measured values of $n(x_T, \sqrt{s})$ in $p-p$ collisions are in the range from 5 to 8.

The compilation of single particle inclusive transverse momentum spectra at mid-rapidity from $p-p$ and $p-\bar{p}$ collisions at c.m. energy $\sqrt{s}$ from 23 to 1800 GeV [27, 28, 110] is shown in Fig. 6.11a for $(h^+ + h^-)/2$, and in Fig. 6.12a for π^0 [122, 123, 124, 125, 29]. The spectra exhibit a characteristic shape: an exponential part at low $p_T \leq 1$ GeV/c which depends very little on $\sqrt{s}$ (soft physics), and a power-law tail for $p_T \geq 2$ GeV/c which depends very strongly on $\sqrt{s}$ (hard physics). The high p_T part of the spectra shows a characteristic scaling behavior indicative of fragmentation of jets produced by hard-scattering of the quark and gluon constituents of the proton as described by QCD [126, 127, 128].

The x_T-scaling of the single particle inclusive data is nicely illustrated by a plot of

$$\sqrt{s}^{\,n(x_T,\sqrt{s})} \times E\frac{d^3\sigma}{dp^3} = G(x_T) \qquad , \tag{6.12}$$

as a function of x_T, with $n(x_T, \sqrt{s}) = 6.3$. The $(h^+ + h^-)/2$ data (Fig. 6.11b) show an asymptotic power law with increasing x_T. Data at a given $\sqrt{s}$ fall

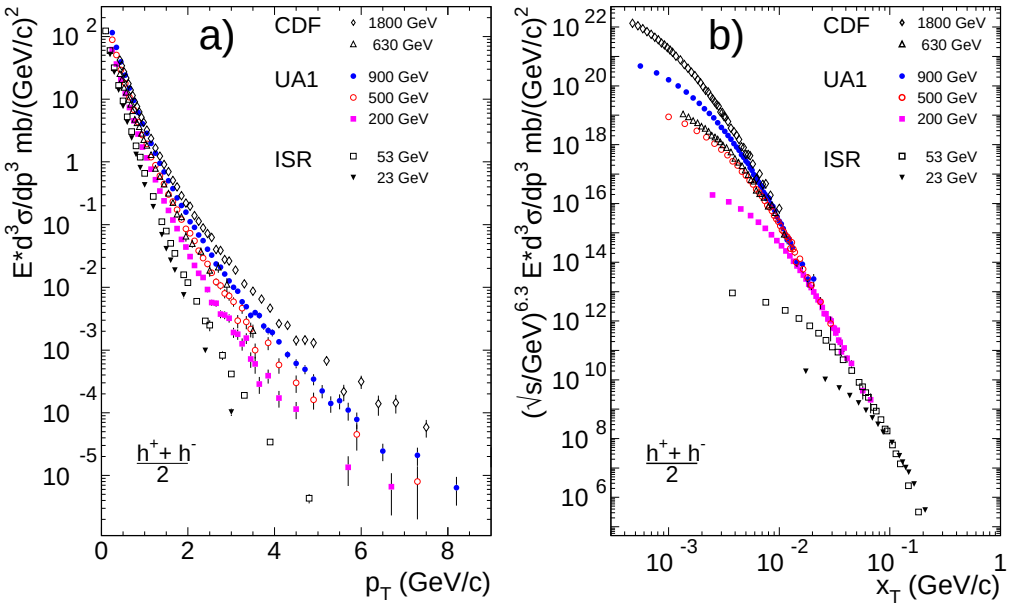

Figure 6.11: (a) CDF, UA1 and ISR transverse momentum dependence of the invariant cross section at seven center of mass energies from different experiments [27, 28, 110]. (b) The same data multiplied by $\sqrt{s}^{6.3}$, plotted as a function of $x_T = 2p_T/\sqrt{s}$.

below the asymptote at successively lower values of x_T with increasing $\sqrt{s}$, corresponding to the transition region from hard to soft physics in the p_T range of 1–2 GeV/c. The π^0 data (Fig. 6.12b) show a similar x_T-scaling but without the deviation at low x_T, since all available data are for p_T larger than 1–2 GeV/c. For $x_T \geq 0.3$, a value of $n = 5.1$ [122, 129] improves the scaling for the 3 lower c.m. energies, $\sqrt{s} = 38.7$, 52.7 and 62.4 GeV. It will be a challenge at RHIC to obtain data in this x_T range to see whether the value of $n \sim 5$ is the asymptotic limit for inclusive single particle production or whether n reaches the (LO) QCD value of 4. x_T-scaling has also been studied in jet production at $\sqrt{s} = 630$ and 1800 GeV [130], where $n = 4.45$ is observed in the jet x_T range 0.15–0.3.

In $Au - Au$ collisions, x_T-scaling should work just as well as in $p - p$ collisions and should yield the same value of $n(x_T, \sqrt{s})$ if the high p_T particles are the result of hard-scattering according to QCD. This is because the structure and fragmentation functions in $Au - Au$ collisions should scale, so that Eq. 6.11 applies, albeit with a different $G(x_T)$. Thus, if the suppression of high-p_T particles with respect to point-like scaling from $p - p$ collisions is due

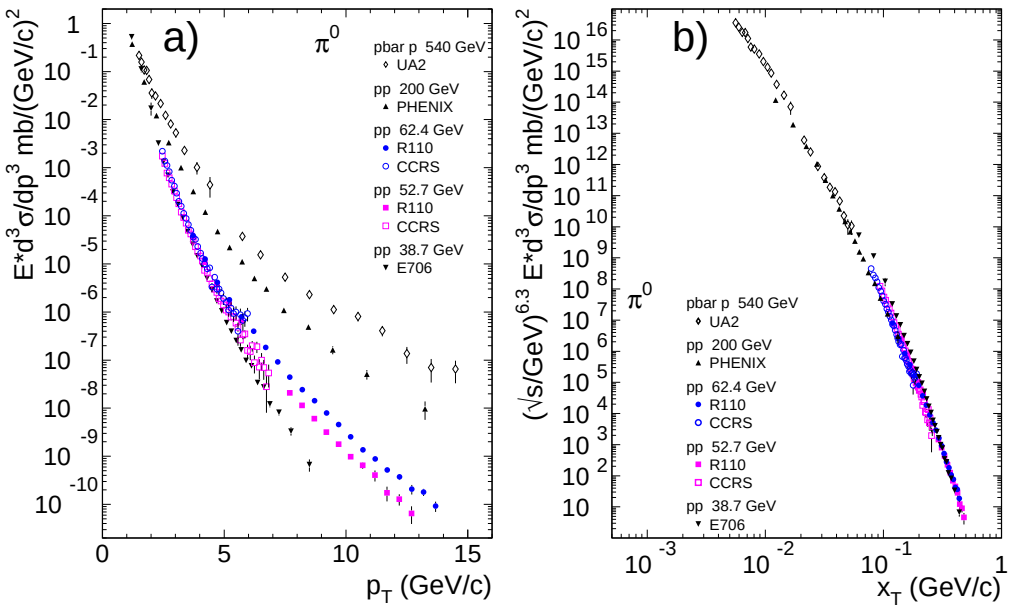

Figure 6.12: (a) Transverse momentum dependence of the invariant cross section for π^0 at five center-of-mass energies from different experiments [122, 123, 124, 125, 29]. (b) The same data multiplied by $\sqrt{s}^{6.3}$, plotted vs $x_T = 2p_T/\sqrt{s}$.

to shadowing of the structure functions [40] or gluon saturation [59], which are basically scaling effects [1], rather than due to a final state interaction with the dense medium, the cross sections (Eq. 6.11) at a given x_T (and centrality) should all exhibit the same suppression. The initial state shadowing may cause $G(x_T)$ to change with centrality, but $n(x_T, \sqrt{s})$ should remain constant. In the case of the interaction with the dense medium, x_T-scaling may or may not hold, depending on the details of the energy loss, for instance, whether or not the energy loss of the hard-scattered parton scales with its energy. It is also conceivable that the high p_T particles observed in $Au-Au$ collisions at RHIC have nothing to do with QCD hard-scattering [64, 111, 131]. In this case, striking differences from Eq. 6.11 and the systematics observed in $p-p$ collisions should be expected.

To test x_T-scaling in $Au-Au$ collisions, we plot the quantities defined

[1]There is a slight non scaling effect of the structure functions [40] since for fixed x_T, Q^2 changes by a factor of 2.4 between the $\sqrt{s_{NN}}$= 130 and 200 GeV.

by Eq. 6.12 in Fig. 6.13 for charged hadron and π^0 data from $\sqrt{s_{NN}} = 130$ GeV and 200 GeV for central (0-10%) and peripheral (60-80%) collisions. For the power n, we use the same value $n(x_T, \sqrt{s}) = 6.3$ that was used for the $p-p$ data shown in Fig. 6.11b and Fig. 6.12b. The data are consistent with x_T-scaling over the range $0.03 \leq x_T \leq 0.06$ for π^0 and $0.04 \leq x_T \leq 0.075$ for $(h^+ + h^-)/2$.

According to Eq. 6.11, the ratio of inclusive cross sections at fixed x_T equals $(200/130)^n$. Thus, the power $n(x_T, \sqrt{s})$ is related directly to the logarithm of the ratio of invariant hadron yield at fixed x_T as:

$$n(x_T) = \frac{log(yield(x_T, 130GeV)/yield(x_T, 200GeV))}{log(200/130)}. \qquad (6.13)$$

The power n's for both neutral pions and charged hadrons for central and peripheral collisions are shown in Fig. 6.14. While the π^0 data in central and peripheral collisions and charged hadron data in peripheral collisions seem to favor a similar power n, the charged hadron data from central collisions require a larger value of n.

For a more quantitative analysis, the $Au-Au$ data for a given centrality and hadron selection are fitted simultaneously for $\sqrt{s_{NN}} = 130$ and 200 GeV to the form,

$$\left(\frac{A}{\sqrt{s}}\right)^n (x_T)^{-m} \qquad , \qquad (6.14)$$

where we have approximated Eq. 6.11 by using a constant power $n(x_T, \sqrt{s})$ and a power-law, x_T^{-m}, for $G(x_T)$ over a limited range in x_T. The fit results and errors are quoted in Table. 6.2. The corresponding ratios of yields are presented by lines in Fig. 6.14, where the fit ranges ($0.03 \leq x_T \leq 0.06$ for π^0s and $0.04 \leq x_T \leq 0.074$ for charged hadrons) are indicated by the length of the line.

For peripheral collisions the fitted values for the power are $n = 6.33 \pm 0.54$ and $n = 6.12 \pm 0.49$, for π^0 and charged hadrons respectively, which are in quantitative agreement with the expectation from $p-p$ collisions. Approximate x_T-scaling in peripheral $Au-Au$ collisions with the same power as observed in $p-p$ collisions indicates that hard-scattering is the dominating production mechanism for high p_T particles. In central collisions, neutral pions also exhibit x_T-scaling with a similar power, $n = 6.41 \pm 0.55$. Thus, it seems that high-p_T π^0 production is consistent with hard-scattering for all centralities.

For charged hadrons, the power found for central collisions is $n = 7.53 \pm 0.44$. Most of the systematic errors are common and cancel between central and

Table 6.2: Results of the simultaneous fit to $\sqrt{s_{NN}} = 130$ and 200 GeV data using Eq. 6.14. The fit ranges are $0.03 \leq x_T \leq 0.06$ for π^0 and $0.04 \leq x_T \leq 0.074$ for charged hadron. Only statistical and point-to-point systematic errors on the data points are included in the fit, which gives the statistical error on n. The normalization errors and other p_T correlated systematic errors are not included in the fit but are directly translated into a systematic error on n.

Fitting results for π^0 over $0.03 < x_T < 0.06$		
parameters	0-10% centrality bin	60-80% centrality bin
A	0.973 ± 0.232	0.843 ± 0.3
m	8.48 ± 0.17	7.78 ± 0.22
n	$6.41 \pm 0.25(stat)$ $\pm 0.49(sys)$	$6.33 \pm 0.39(stat)$ $\pm 0.37(sys)$
Fitting results for $h^+ + h^-$ over $0.04 < x_T < 0.074$		
A	2.30 ± 0.44	0.62 ± 0.27
m	8.74 ± 0.28	8.40 ± 0.43
n	$7.53 \pm 0.18(stat)$ $\pm 0.40(sys)$	$6.12 \pm 0.33(stat)$ $\pm 0.36(sys)$

peripheral collisions, thus the difference of the two powers found for charged hadrons, $\Delta n = n_{cent} - n_{periph} = 1.41 \pm 0.43$ compared with that for neutral pion $\Delta n = 0.09 \pm 0.47$, is significant.

This difference is consistent with the large proton and anti-proton enhancement in central $Au - Au$ collisions for intermediate p_T seen at $\sqrt{s_{NN}} =$ 130 and 200 GeV, which appears to violate x_T-scaling. The x_T range $0.04 \leq x_T \leq 0.074$ corresponds to $4 < p_T < 7.4$ GeV/c at $\sqrt{s_{NN}} = 200$ GeV, but it corresponds to $2.6 < p_T < 4.8$ GeV/c at $\sqrt{s_{NN}} = 130$ GeV. If protons are enhanced at $2 < p_T < 4.5$ GeV/c in central collisions at both $\sqrt{s_{NN}} = 130$ GeV and 200 GeV, then n_{cent} will be larger than n_{periph} in the measured x_T range. Since the $\sqrt{s_{NN}} = 200$ GeV data indicate that the proton enhancement is limited to the medium p_T range, based on the equality of R_{AA} for charged hadrons and π^0 at $p_T > 4.5$ GeV/c (Fig. 6.8), this difference should go away at larger x_T .

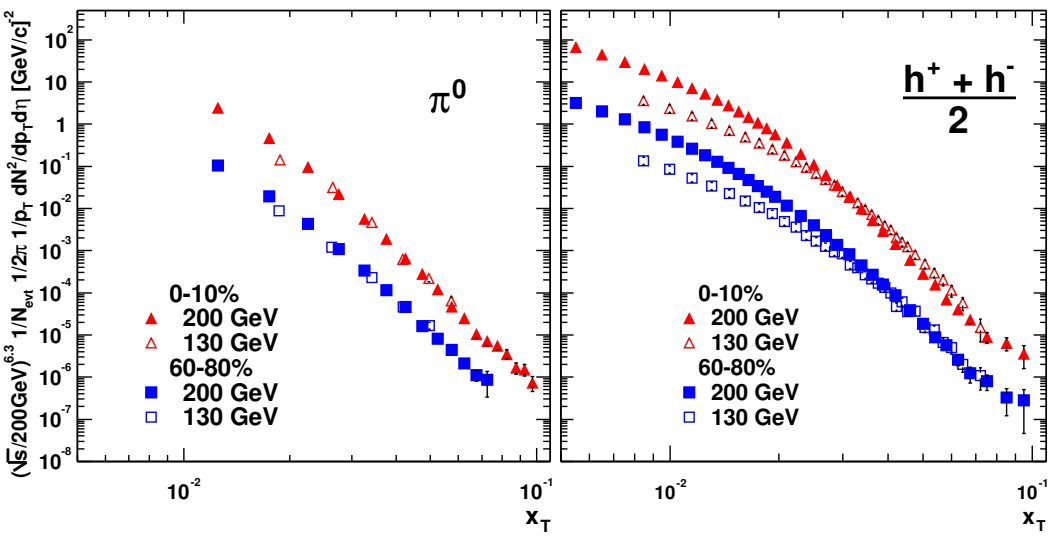

Figure 6.13: x_T scaled spectra for central collisions and peripheral collisions at $\sqrt{s_{NN}} = 130$ and 200 GeV. The left figure shows the π^0 x_T spectra, and the right figure shows the $(h^+ + h^-)/2$ x_T spectra. The central (0-10%) x_T spectra are represented by triangular symbols, and the peripheral (60-80%) x_T spectra are represented by square symbols. The open symbols represent x_T spectra from $\sqrt{s_{NN}} = 130$ GeV scaled by a factor of $(130/200)^{6.3}$. The solid symbols represent x_T spectra from $\sqrt{s_{NN}} = 200$ GeV. The error bars are statistical only.

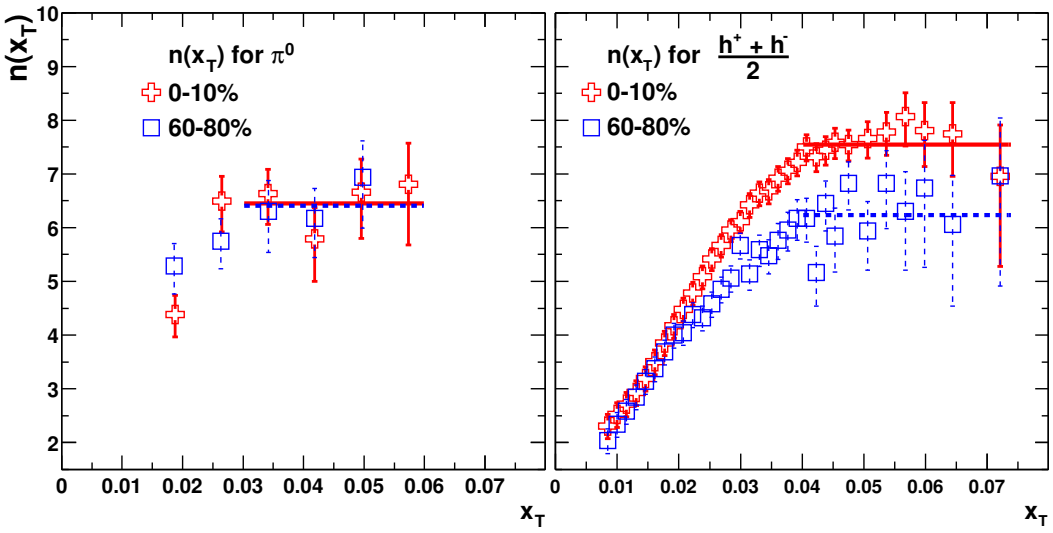

Figure 6.14: The x_T scaling power n (according to Eq. 6.13) plotted as function of x_T calculated for π^0 (top-left) and $(h^+ + h^-)/2$ (top-right) in central (0-10%) and peripheral (60-80%) collisions. The solid (and dashed) lines indicate a constant fit along with the fitting ranges to the central (and peripheral) $n(x_T)$ functions. The error bars at each data point include statistical and point-to-point systematic errors from $\sqrt{s_{NN}} = 130$ and 200 GeV. The scale errors on x_T spectra are 20.7% (15.9%) for π^0 x_T spectra ratio in central (peripheral) collisions, and 18.6% (15.7%) for $(h^+ + h^-)/2$ x_T spectra ratio in central (peripheral) collisions. These type of errors propagate into the systematic errors on x_T scaling power n listed in Table. 6.2.

6.4 Model Comparisons

The results on high p_T hadron production from $Au-Au$ collisions at $\sqrt{s_{NN}}$ = 130 and 200 GeV are intriguing. The observation of a factor of 4–5 suppression of hadron yields at $p_T >$ 4–5 GeV/c in central $Au-Au$ collisions, which is absent in high energy $p-p$, $p-A$ or low energy heavy-ion collisions, points to strong medium effects present in central $Au-Au$ collision. A variaty of theoretical models has been proposed in recent years to explain such a high p_T effect, and it is the focus of this section to compare those model calculations with the results presented in previous sections.

The dominating models for high p_T hadron suppression are based on the multiple scattering and induced gluon radiation energy loss of partons in a QGP phase. The predictions of R_{AA} at high p_T depends on the energy loss, $\Delta E = \int dx dE/dx$. In early studies, the modellings of radiative energy loss was very crude. The medium is assumed to be statistic and "thick", and interferences effects from successive radiation(the Laudau-Pomeranchuk-Migdal or LPM effect) was not included. The estimated dE/dx [132] varies widely from energy independent to $dE/dx \propto E$. The first predictions for the magnitude of the suppression was made based on the HIJING event generator as shown in Fig. 6.15 [133]. HIJING is a two component model, where high p_T hadron production is modelled by minijets and hard scattered jets with $p_T > p_0 = 2$ GeV/c computed through the PYTHIA code. The soft beam jet fragments are computed via a hybrid LUND and Dual Parton model algorithm. Jet quenching is implemented by a simplified gluon splitting algorithm to simulate induced gluon radiation. The jet energy loss in the plasma is assumed to be simply $dE/dx = 2$ GeV/fm. The middle panel of Fig. 6.15 shows that up to an order of magnitude suppression of charged hadrons was expected around $p_T \sim 5$ GeV/c.

Later developments of energy loss models take into account the finite size and expansion properties of the plasma. In addition, the basic formation time physics of the LPM effect are taken into account. The energy loss in these models are controlled by different, but related properties of the plasma in the initial state [134]: i) large initial gluon densities $dN^g/dy \sim 1000$, ii) large "transport coefficients" $\hat{q}^0 \sim 3.5$ GeV/fm^2, iii) high opacities $L/\lambda \sim$ 3-4, or iv) effective parton energy losses of the order of $dE/dx \sim 14$ GeV/fm. There are mainly two types of models for treating the radiation processes $q \rightarrow qg$ and $g \rightarrow gg$ due to multiple scattering. The first type includes various asymptotic approaches such as BDMCS/SW [23, 135], which are designed for applications to thick or macroscopic media at asymptotic jet energies. As shown in Fig. 6.16 [136], the phenomenological applications of the asymptotic

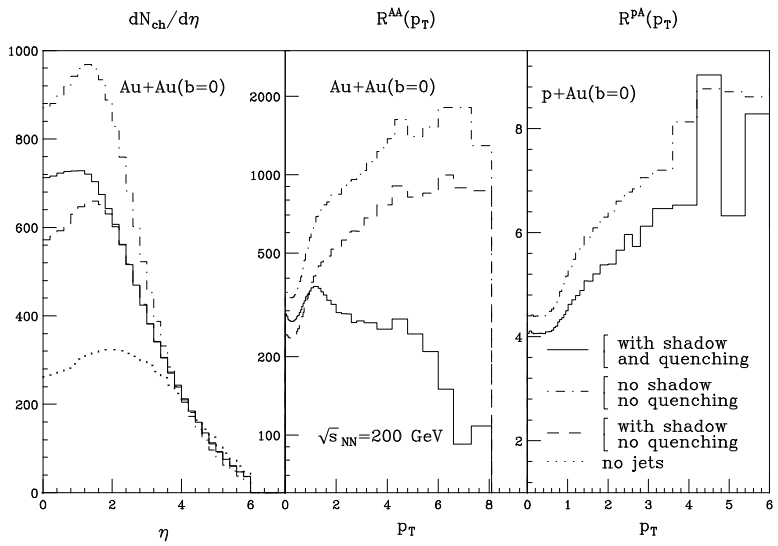

Figure 6.15: HIJING predictions[133] of the inclusive charged hadron spectra in central $Au - Au$ and $p + Au$ collisions at $\sqrt{s_{NN}} = 200$ GeV. The competing effects of minijet production (dash-dotted), gluon shadowing (dashed) (assuming that gluon shadowing is identical to that of quarks), and jet quenching (solid) with $dE/dx = 2$ GeV/fm are shown. $R^{AB}(p_T)$ is the ratio of the inclusive p_T spectrum of charged hadrons in $A - B$ collisions to that of $p - p$. In contrast to $Au - Au$, no significant quenching is expected in $p - A$ (or $d - Au$), since only the initial state shadowing effects (about $\sim$ 20%) and Cronin effects can modify the charged hadron spectrum at high p_T.

expressions tend to overpredict quenching at RHIC energy and leads to a too small R_{AA} for $p_T < 10$ GeV/c, which falls with decreasing p_T. The data do not support these trends, however, the BDMPS approach is only valid at asymptotic energy.

The second type of models includes the GLV [137] and WOGZ/WW [138, 139] approaches, which provide a systematic way to compute ΔE via an opacity or higher twist expansion in finite and expanding nuclear matter. In the GLV approach, multiple scattering in initial states (k_T broadening) and final state (elastic and radiation loss) are naturally included in the calculation. Fig. 6.17 [58] shows the main results for central $Au - Au$ reactions, which includes three important nuclear effects, i.e. the Cronin effect, shadowing effect and jet quenching. At SPS energy, although there is room for energy loss,

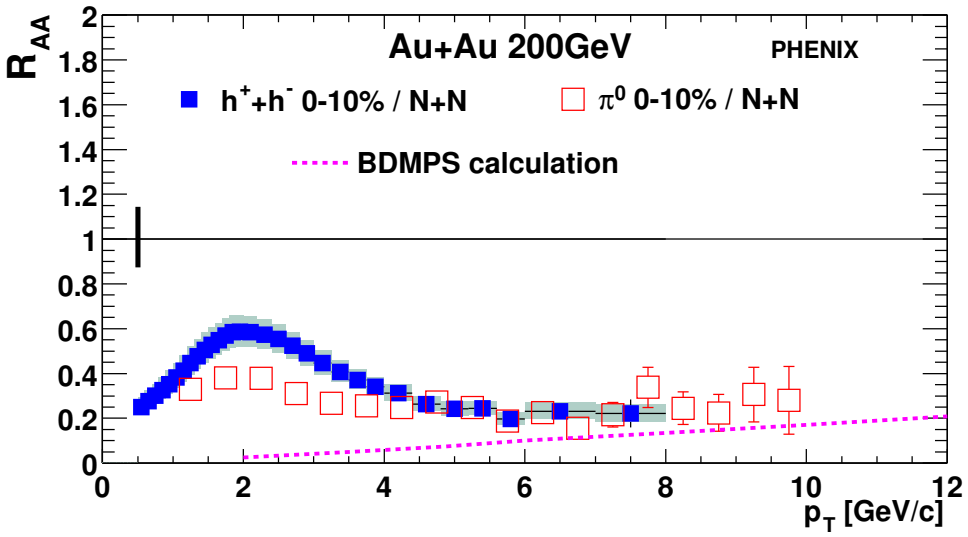

Figure 6.16: R_{AA} calculated from the BDMPS model [136] compared with PHENIX data.

R_{AA} is dominated by the Cronin effect. At RHIC energy, jet quenching dominates, but the inclusion of k_T broadening and shadowing effects reproduces the approximately constant suppression pattern.

The WOGZ/WW [138, 139, 142] approach generalizes the twist expansion of multiple parton scattering through a modified parton fragmentation function. In this approach, the quadratic dependence of the modification of the fragmentation functions and the effective parton energy loss on the nuclear size is caused both by the LPM interference and the specific form of gluon radiation spectra in QCD. The predicted nuclear modification of the fragmentation function for both the energy and the nuclear dependence, is found to agree very well with DIS in cold nuclear targets [142]. In heavy-ion collisions, the modified fragmentation function can be simplified as [143],

$$\widetilde{D}_{a\to h}(z) \approx \frac{1}{1-\Delta z} D_{a\to h}\left(\frac{z}{1-\Delta z}\right) \tag{6.15}$$

with Δz to account for the fractional parton energy loss. Shown in Fig. 6.18 are the calculated $R_{AA}(p_T)$ curves at RHIC energies [48]. Shadowing and k_T broadening are also taken into account. Below 4 GeV/c, the predicted R_{AA} agrees with π^0 data. At large p_T, however, the predicted R_{AA} using the energy-dependent energy loss obtained from cold nuclear matter gives a

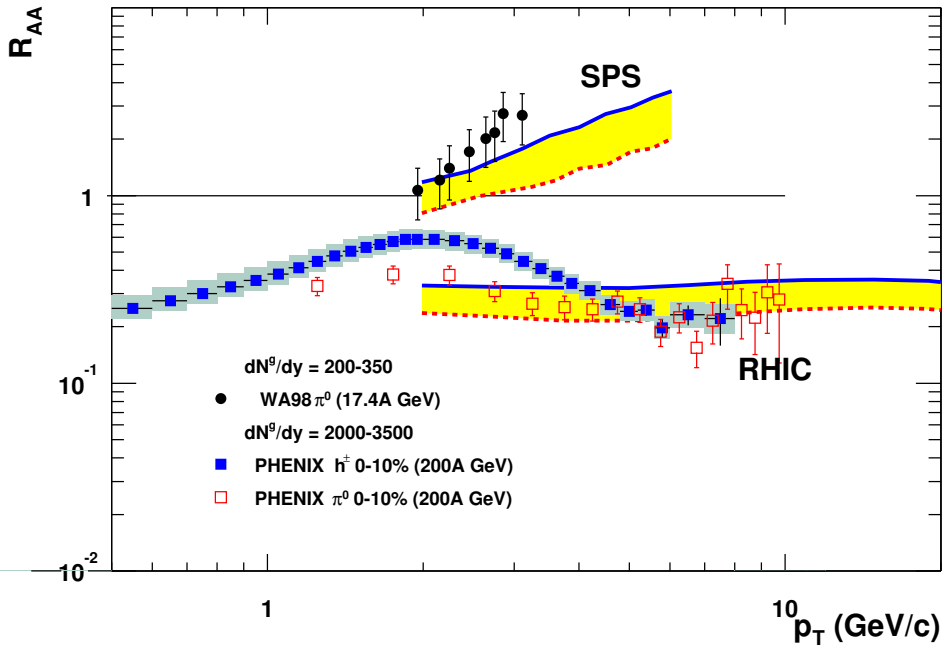

Figure 6.17: The calculated nuclear modification factor $R_{AA}(p_T)$ for neutral pions at $\sqrt{s_{NN}} = 17$ and 200 GeV from Ref.[58]. Solid (dashed) lines correspond to the smaller (larger) effective initial gluon rapidity densities at given $\sqrt{s}$ that drive parton energy loss. Data on π^0 production in central $Pb-Pb$ at $\sqrt{s_{NN}} = 17.4$ GeV from WA98[140] and on π^0 and charged hadrons in central $Au-Au$ at $\sqrt{s_{NN}} = 200$ GeV from PHENIX are shown.

suppression factor that increases with p_T in contradiction with the data at $\sqrt{s_{NN}} = 200$ GeV. This increase is similar to the results from the asymptotic BDMCS/SW [23, 135] approaches mentioned before. This discrepancy is removed by including in the model the detailed balance of stimulated gluon emission and thermal absorption in the calculation of energy loss [139]. Thermal absorption leads to a reduced energy loss for low p_T partons and at the same time increases the energy dependence. Effectively this leads to an energy independent suppression at $p_T < 10$ GeV/c.

In Fig. 6.19, we compare the calculated centrality dependence of the $R_{AA}^{N_{part}}$ at high p_T from BDMPS [113] and WOGZ/WW [145] with the PHENIX data integrated for $p_T > 4.5$ GeV/c. Both models reproduce the approximate N_{part} scaling behavior seen in the data. But both miss the details at peripheral

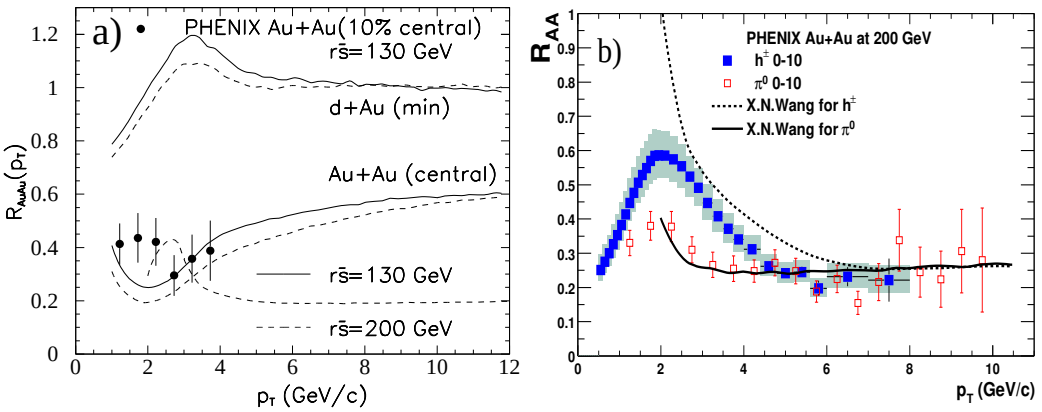

Figure 6.18: a) Calculated nuclear modification factor of π^0 p_T spectra for $d + Au$ and central $Au + Au$ collisions at $\sqrt{s} = 130$ (solid) and 200 GeV (dashed) as compared to PHENIX data. The lower dashed line [144] uses the energy loss including thermal absorption [139]. Figure from [48] b) The calculation for central $Au - Au$ collisions at $\sqrt{s_{NN}} = 200$ GeV from [145]including thermal absorption compared with charged hadron and neutral pion data from PHENIX.

collisions, namely the increase of $R_{AA}^{N_{part}}$ with centrality at $N_{part} < 50$. The solid line is our jet absorption model calculation (see Chapter. 6.7). This model can reproduce the centrality dependence of the data quite nicely.

In addition to the high p_T hadron suppression, jet quenching has also been proposed to account for the azimuthal anisotropy [146, 147, 57] and the disappearance of dijets observed in $Au - Au$ collisions at RHIC [57]. Quantitative studies indicate, however, that a more precise extraction of the parton energy loss from the hadron suppression in $A - A$ collisions requires a precise knowledge of the initial state before hard scattering occurs. The main initial state effects include the initial k_T broadening effect [148, 149, 150] and modifications of the nuclear structure function, in particular the shadowing effect (see Chapter. 1.2.2).

A very different interpretation of the suppression observed in central $Au - Au$ collisions is based on initial-state parton saturation effects [59]. The gluon density is expected to saturate for momenta below a scale Q_s^2, which is calculated to be $Q_s^2 = 2$ GeV^2 [151]. Below Q_s^2, particle production should be proportional to N_{part}. The saturation model has been rather successful in describing the charged particle multiplicity and its centrality, rapidity, and

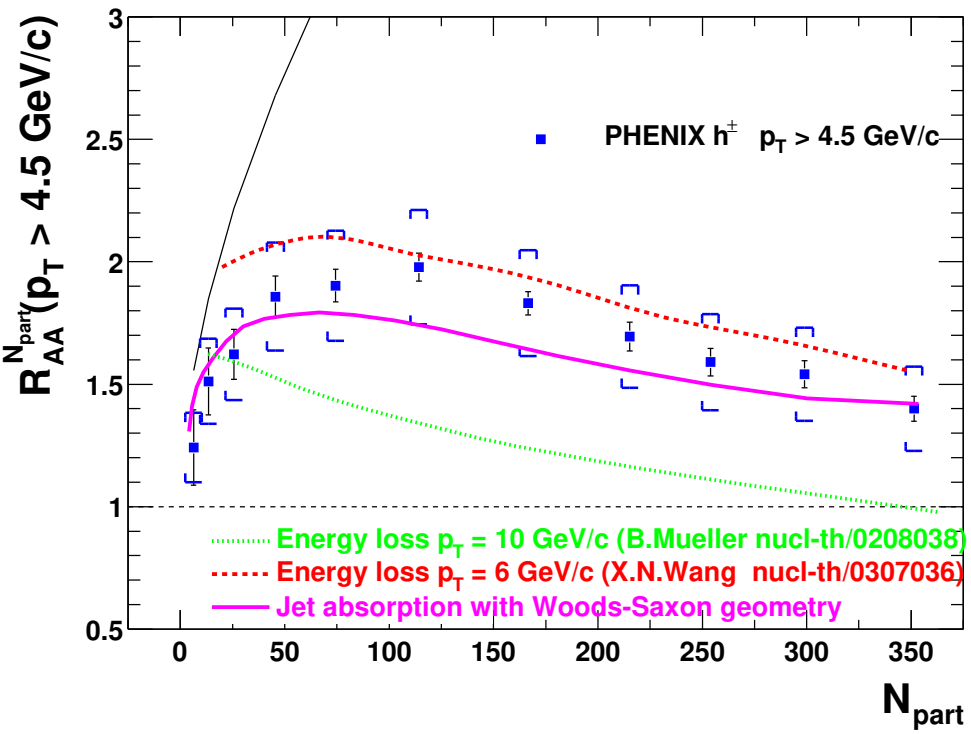

Figure 6.19: The calculated centrality dependence of high p_T charged hadron $R_{AA}^{N_{part}}$ for BDMPS [113] (dotted line), WOGZ/WW [145] (dashed line) and our jet absorption model (solid line) compared with the charged hadron data. The thin dashed line at 1 represents the participant scaling, and the thin solid line represents the collisions scaling.

$\sqrt{s_{NN}}$ dependence in $Au-Au$ collisions [13, 152]. Recently, it was proposed that gluon saturation phenomena alone may account for a significant part of the observed high p_T hadron suppression pattern [59]. It was argued that saturation not only affects the region around Q_s, but also affects region at much higher momenta, naively as large as Q_s^2/Λ_{QCD}. For central $Au-Au$ collisions, this new momentum scale is $\mathcal{O}$(5–10 GeV/c) at RHIC energies. The predicted $R_{AA}^{N_{part}}$ as function of centrality for several p_T bins is shown in Fig. 6.20 [59].

Whether the observed suppression is an initial or final state effect could not be judged from the $Au-Au$ data alone. The initial state effects can be isolated in $e-A, p-A$ or $d-A$ collisions, where no final state medium is present. Recent results from $d-Au$ collisions at $\sqrt{s_{NN}} = 200$ GeV thus provide a decisive test on whether the observed suppression is due to initial

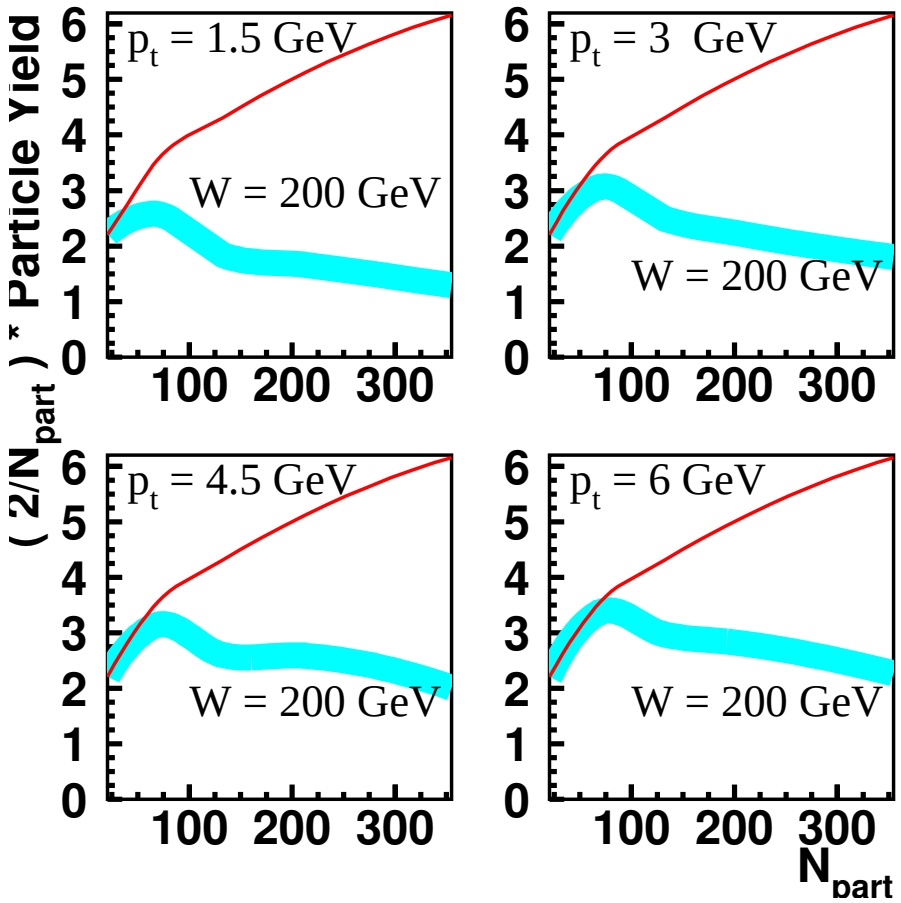

Figure 6.20: Saturation model calculation of the centrality dependence of hadron yields in $Au-Au$ collisions for different p_T at $\sqrt{s_{NN}}$ = 200 GeV. The band is the results from the calculation, and the thin line indicate the collision scaling.

state or final state effect. If the observed suppression pattern in $Au-Au$ is due to jet quenching in the final state, the Cronin effect is predicted to dominate over shadowing in the $x > 0.01$ range accessible at RHIC. Thus an 10-30% enhancement of the hadron yields relative to binary scaled $p-p$ is expected. If the strong suppression seen in $Au-Au$ collisions is due to gluon saturations, a 30% suppression of the hadron yields is expected at high p_T [59]. In the next section, we shall discuss the charged hadron results from $d-Au$ collisions, and their implications on $Au-Au$ results.

6.5 Comparison to Charged Hadron Production in $d-Au$ Collisions

For $d-Au$ collisions, the nuclear modification factor, which quantifies the nuclear medium effects on high p_T production, is defined similar to the $Au-Au$ case as,

$$R_{dAu}(p_T,\eta) = \left(\frac{1}{N_{evt}}\frac{d^2N^{d-Au}}{dp_T d\eta}\right) / \left(\frac{\langle N_{coll}\rangle}{\sigma_{inel}^{NN}}\frac{d^2\sigma^{N-N}}{dp_T d\eta}\right) \tag{6.16}$$

The inclusive charged hadron yield for minimum bias $d-Au$ collisions and the corresponding R_{dAu} as function of p_T are shown in Fig. 6.21. The $N-N$ reference used to calculate R_{dAu} is the same as the one used for $Au-Au$ collisions. It is scaled by $\langle N_{coll}\rangle$ and is shown in the left panel together with its systematic error band indicated by the dashed lines. In the right panel, R_{dAu} is compared with R_{AA} for 0-10% central $Au-Au$ collisions, together with the predictions from a saturation model for both data sets [59]. The uncertainties plotted in the right panel are i) error bars represent the quadrature sum of statistical errors and those systematic errors which vary point-to-point in p_T, ii) the bands represent the systematic errors on the absolute yield and those systematic errors that are correlated in p_T. All errors are taken from Table.A.4 and are presented as 1σ values as in the $Au-Au$ case.

The saturation model predictions are taken from Fig. 6.20, which gives $R_{AA}\sim 0.38$ at $p_T = 6$ GeV/c for the 0-10% most central $Au-Au$ collisions, and is shown by the light solid line. According to the same author, the R_{dAu} value can be simply calculated as the square root value of the R_{AA}, which gives $\sqrt{0.38} = 0.62$ for central collisions and is indicated by the dark solid line. The $d-Au$ data clearly indicate a lack of suppression of charged hadron production up to $p_T \sim 8$ GeV/c, contradicting the expectation from the saturation model. Instead, an enhancement of the inclusive charged hadron production is observed for $p_T > 2$ GeV/c. This enhancement is similar to what was observed in $p-A$ collisions at previous fixed-target experiments [33, 155] and is known as Cronin effect. Due to the rapid increase of hard-scattering cross section, Cronin effect usually decreases with increasing $\sqrt{s_{NN}}$, and the predicted values from various calculations at RHIC energy usually ranges from 1.1 to 1.4 [149, 150, 156, 38], depending on the implementation of initial multiple scattering and the assumptions on nuclear effects. Fig. 6.22 shows the comparison of R_{dAu} with the predictions from [150] and [156]. These calculations qualitatively describe the magnitude of R_{dAu}. However, the data are flat for $p_T > 2$ GeV/c, which is not predicted, but the differences between data and

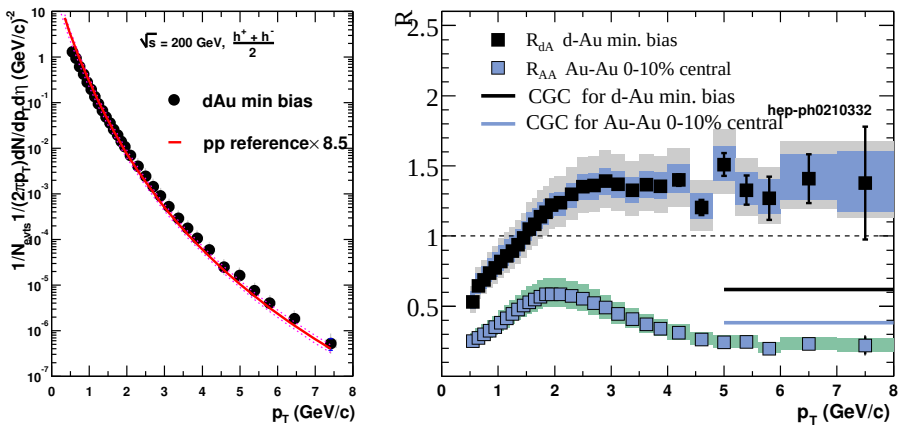

Figure 6.21: a) Inclusive charged hadron yield at mid-rapidity for minimum bias $d-Au$ events, scaled by $\langle N_{coll} \rangle$. b) Minimum bias R_{dA} compared with R_{AA} for the 10% most central $Au-Au$ collisions, together with the saturation model predictions (CGC) shown by the solid line. Figure taken from [153, 154].

predictions are within the 1σ systematic errors. It should be pointed out that the charged hadron spectrum includes baryons and antibaryons, which may have a different nuclear enhancement than mesons [33]. The predictions shown agree better with π^0 R_{dA}.[2]

The centrality dependence of $d-Au$ collisions provides additional valuable information about various initial state effects. If saturation effects dominate particle production at high p_T, then the charged hadron yields should be suppressed more in central collisions than in peripheral collisions. On the other hand, if the Cronin effect is responsible for the enhancement of R_{dAu} at $p_T > 2$ GeV/c, this enhancement should be strongest in central collision, where the Au nucleus on average is the thickest for incoming deuterons. Fig. 6.23 shows the PHENIX preliminary results on the centrality dependence of the R_{dAu} values side-by-side with the R_{AA} from $Au-Au$ collisions. Obviously, the centrality dependence of R_{dAu} is opposite to that of R_{AA}. This again indicates that the current saturation models can not explain the suppression of R_{AA} and the enhancement of R_{dAu} simultaneously. On the other hand, the increase of R_{dAu} towards more central collisions may indeed indicate that the initial state multiple scattering is responsible for the enhancement.

[2] A comparison of R_{dAu} values between charged hadrons and π^0 can be found in Ref. [153].

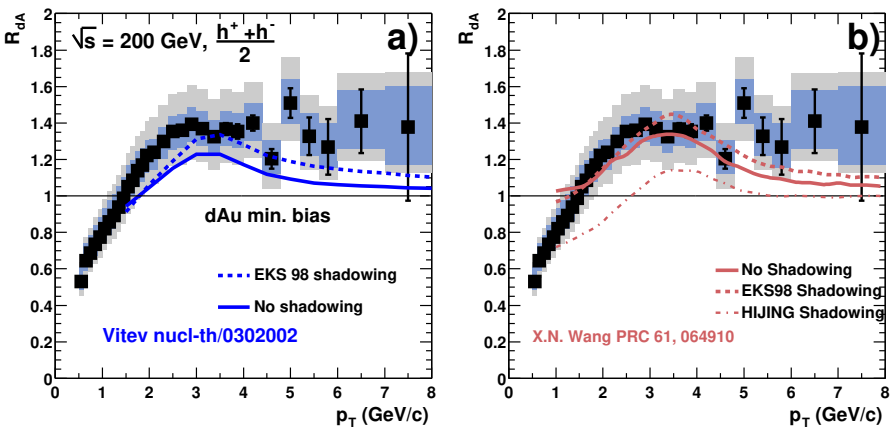

Figure 6.22: a) Comparison of minimum bias R_{dAu} with a prediction from [150]. b) Comparison with prediction from [156].

6.6 Cronin Effect in $Au - Au$ Collisions ?

In the discussion of the charged hadron R_{AA}, we have observed a characteristic p_T dependence of the R_{AA} in central $Au - Au$ collisions, namely a increase of R_{AA} up to 2 GeV/c, followed by a decrease to 4.5 GeV/c, then a flattening at a value around 0.23. The suppression of R_{AA}, as argued in the previous section, is due to final state jet quenching. Since energy loss occurs on the parton level, it should produce a species independent suppression. The domination of jet quenching in central $Au - Au$ collision can also obscure other competing initial state effects like the Cronin or shadowing effects, but does not imply that these effects are not present. On the contrary, the same initial state effects that exist in $d - Au$ collisions should also be present in central $Au - Au$ collisions and have similar magnitude. In particular, the k_T broadening due to multiple scattering in central $Au - Au$ collisions should at least be at the same magnitude as in $d - Au$ collision. Since the Cronin effect in central $d - Au$ collisions could result in an enhancement of up to 50% for charged hadrons(see Fig. 6.23), we should expect a similar enhancement in central $Au - Au$ collisions for charged hadrons but less enhancement for neutral pions. This can qualitatively explain the peak structure around 2 GeV/c in R_{AA} for both charged hadron and neutral pions.

The Cronin effect is known to be larger for baryons than for mesons [33]. Recently, an attempt has been made [112] to explain the large h/π ratio in $Au - Au$ as shown in Fig. 6.9. In these calculations, a particle mass dependent

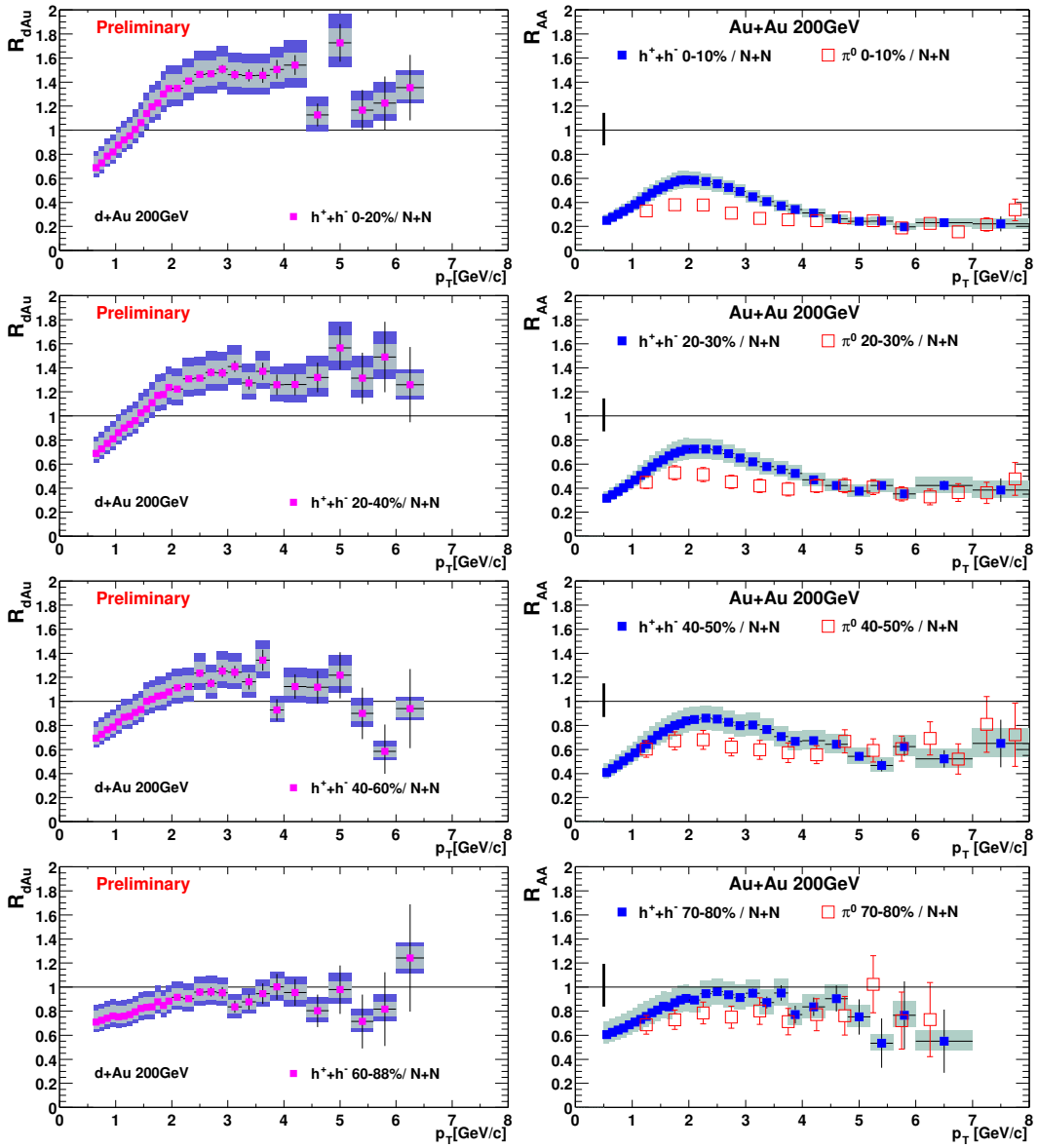

Figure 6.23: Comparison between R_{dAu} and R_{AA} for four centralities. The left column shows for $d-Au$, The right column shows $Au-Au$. From top to bottom, the centrality class goes from central to peripheral. The error bars on $d-Au$ are from Table.A.3 and Table.A.4. The $d-Au$ data points are provided by Sean Leckey.

k_T broadening is assumed. The proton, due to its larger mass, has on average a larger $\hat{s}$ (the energy involved in the partonic cross section) than that for pions. Larger $\hat{s}$ allows for a larger phase space for intrinsic k_T. Thus it leads to a larger Cronin effect for protons. This mass dependent Cronin effect can simultaneously describe the h/π ratio at intermediate p_T ($2 < p_T < 4.5$ GeV/c) for both $d-Au$ and $Au-Au$ collisions. The calculations for $Au-Au$ collisions are presented in Fig. 6.24 [3]. The calculation for R_{dA} is shown in Fig. 6.25.

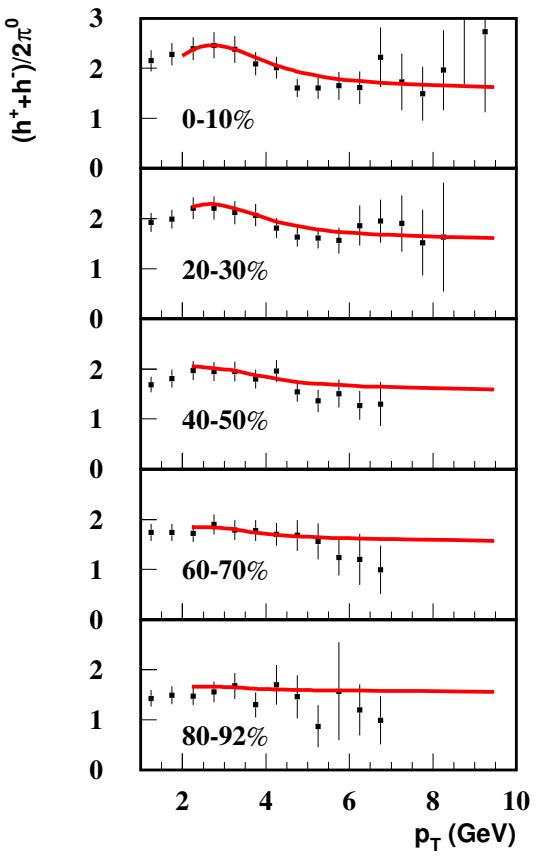

Figure 6.24: h/π ratios for different centralities in $Au-Au$ collision compared with the calculation from[112].

The Cronin effect is expected to decrease as $\sqrt{s}$ increases. The energy density increases from 130 to 200 GeV only by 10-15% [13]. The final state suppression effect could be similar. Fig. 6.26 compares the central-to-peripheral ratio, R_{cp}, between 130 and 200 GeV for charged hadrons and π^0. Most of the systematic errors cancel in this ratio. The error bars on the π^0 includes both

[3]This model can't describe the absolute value of R_{AA} since it is dominated by the jet energy loss.

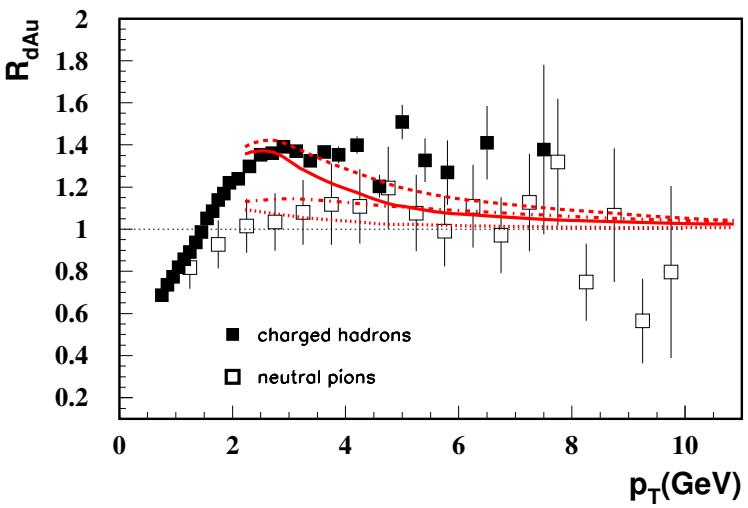

Figure 6.25: R_{dA} for charged hadrons (solid marker) and π^0 (open marker) in minimum bias collisions (from [153]). The lines are predictions from [112] for charged hadrons (solid line: without shadowing; dashed line: with EKS [40] shadowing) and π^0 (dotted line: without shadowing; dot-dashed line: with EKS shadowing).

statistical errors and systematic errors that don't cancel in the ratio. R_{cp} for the two energies agree with each other within errors. For charged hadrons, the remaining systematic errors on the differences of R_{cp} at the two energies is only 10%. We observe a $\sim$ 30% decrease of R_{cp} from 130 to 200 GeV, qualitatively consistent with the decrease of the Cronin effect. The differences between charged hadrons and π^0 could also indicate the relative importance of radial flow at 130 and 200 GeV [103]. The radial flow velocity is similar for the two energies [103]. However, the hard-scattering yield increases from 130 to 200 GeV by more than factor of 2 [4] in peripheral collisions, leading to a smaller R_{cp}. Of cause, it remains to be seen whether a more solid model calculation can explain the the p_T dependence of R_{cp} and its energy dependence at intermediate p_T for charged hadrons ($2 < p_T < 4.5$ GeV/c).

[4]This increase can simply be calculated assuming that the pQCD cross section follows the x_T-scaling with a power of 6.3, i.e. Eq. 6.12. The yields for the two c.m energies $\sqrt{s_1}$ and $\sqrt{s_2}$ are related to each other by:

$$\begin{aligned}\frac{\frac{Ed^3\sigma}{dp^3}^{\sqrt{s_1}}(p_T)}{\frac{Ed^3\sigma}{dp^3}^{\sqrt{s_2}}(p_T)} &= \frac{\frac{Ed^3\sigma}{dp^3}^{\sqrt{s_1}}(x_T)}{\frac{Ed^3\sigma}{dp^3}^{\sqrt{s_2}}(x_T)} \times \frac{\frac{Ed^3\sigma}{dp^3}^{\sqrt{s_2}}(x_T)}{\frac{Ed^3\sigma}{dp^3}^{\sqrt{s_2}}(\sqrt{s_1}x_T/\sqrt{s_2})} \\ &= \left(\frac{\sqrt{s_2}}{\sqrt{s_1}}\right)^{6.3} \times \frac{\frac{Ed^3\sigma}{dp^3}^{\sqrt{s_2}}(x_T)}{\frac{Ed^3\sigma}{dp^3}^{\sqrt{s_2}}(\sqrt{s_1}x_T/\sqrt{s_2})} \end{aligned} \quad (6.17)$$

This ratio at 5 GeV/c can be calculated from the parameterization given by Eq. 6.3 as,

$$\frac{\frac{Ed^3\sigma}{dp^3}^{200}}{\frac{Ed^3\sigma}{dp^3}^{130}} = \frac{130}{200}^{6.3} \times \left(\frac{(1.219 + 200/130 \times 5)}{(1.219 + 5)}\right)^{9.99} = 2.41$$

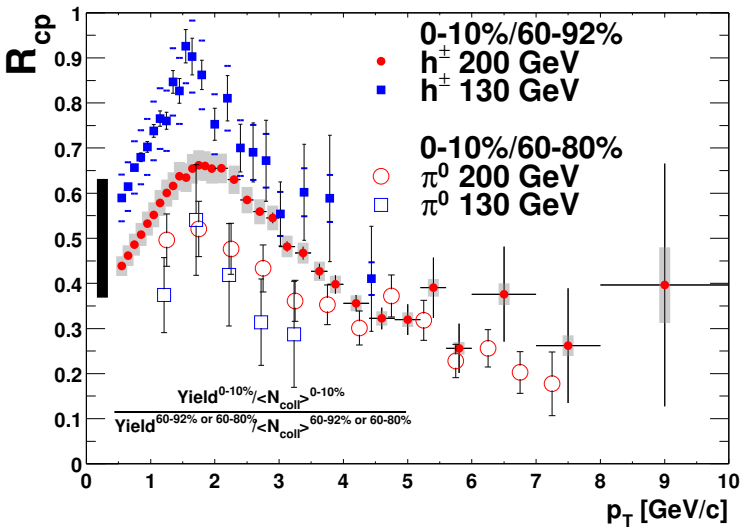

Figure 6.26: R_{cp} for $\sqrt{s_{NN}} = 130$ and 200 GeV $Au - Au$ collisions for charged hadrons (closed markers) and π^0 (open markers). The thick black bar is the error from N_{coll} and is common for all four sets of data points. For charged hadrons, the error on the 200 GeV data is the same as shown in Fig. 6.4. The error bars and the brackets on 130 GeV data are statistical errors and the systematic errors that do not cancel in the ratio, respectively. For π^0, the error bar includes both the statistical errors and errors that don't cancel in the ratio.

6.7 Collision Geometry and Jet Absorption

The results from $Au - Au$ collisions at RHIC reveal rich new information on high p_T phenomena. For the first time, particle production has been studied in many dimensions. In addition to the standard single spectra studied as function of p_T, centrality, particle species and $\sqrt{s}$, double differential spectra from anisotropic flow, and jet correlations also become available. The most striking observations are the apparent "jet quenching" in central collisions as discussed in Chapter. 6.2, and a suppression of the hadron back-to-back correlation strength by a factor of 5-10 [65], compared to expectations based on the underlying nucleon-nucleon collisions. The absence of these phenomena in $d - Au$ collisions suggests that the observed suppression in central $Au - Au$ collisions is indeed an effect of the dense medium created during the collisions, consistent with parton energy loss in dense medium [153, 157, 158, 159].

Both the suppression of the high p_T hardon yield and the back-to-back angular correlations show a characteristic centrality dependence, which seems to be independent of p_T for $p_T > 4.5$ GeV/c [54, 56]. Interestingly, in this p_T range, particle production seems consistent with jet fragmentation, despite the suppression. Specifically, experiments have observed:

1. An identical spectral shape compared to $p - p$ collisions within systematic errors.

2. A similar suppression for charged hadrons and π^0's from PHENIX (Fig. 6.8) and for charged hadron, Λ, and K^0_s from STAR [56].

3. An h/π^0 ratio consistent with values observed in $p - p$ collisions, indicating a similar particle composition in $p - p$ and $Au - Au$ at high p_T [61].

4. Strength, width, and charge composition of near angle correlation consistent with jet fragmentation [65].

5. PHENIX preliminary results shows a similar jet fragmentation transverse momentum j_T ($\sim$ 400 MeV/c) in $p - p$, $d - Au$, and $Au - Au$ collisions [160].

6. Scaling of the pion production cross section with x_T in $Au - Au$ from $\sqrt{s_{NN}}$=130 to 200 GeV similar to $p - p$ collisions.

The data suggest that produced jets are slowed down or absorbed in the medium and then fragment outside in vacuum.

The strong suppression implies a large initial gluon density [58, 57] and a large dE/dx [142]. The large radiative energy loss effectively thermalizes the initial state hard partons generated in the center of the collision zone and the remaining high p_T jets would come only from the surface. In this picture, since no jets from the center of the collision zone can escape (or if they survive, their energy is so much reduced that high p_T particle production is still dominated by surface emission), the jet quenching picture can be simplified as a simple jet absorption picture, in which a jet is absorbed with one single radiation process. Since the jet surviving probability depends on the amount of matter it traverses, the surface emission picture also naturally leads to a larger suppression of the away side jet and an anisotropy of high p_T particle emission with respect to the reaction plane.

In this section, we show that a simple model of jet absorption in an extremely opaque medium is consistent with the data. We demonstrate that the centrality dependence of the high p_T suppression of the yield and of the back-to-back correlation can be described naturally by jet absorption and the collision geometry. We also discuss the sensitivity of our results on the jet absorption pattern and different collision geometry assumptions.

6.7.1 The Model

In order to keep the model simple, we limit the discussion to the p_T range from 4.5 to 10 GeV/c. Based on the fact that the hadron suppression is independent of p_T in this region (see Chapter.6.2), we assume that the parton energy loss can be modelled as a p_T independent absorption of partons in dense matter. Furthermore, since hadron production in this p_T region seems to be consistent with vacuum jet fragmentation, we neglect the fragmentation step and assume that the suppression found for partons is identical to the one for jets and thus also to the one observed for hadrons, in accordance with parton-hadron duality.

The collision geometry is modelled by a Monte Carlo simulation of $Au - Au$ collisions based on the Glauber approach [15] similar to that discussed in Chapter.4.1.3. We use a Woods-Saxon density distribution for the Au nucleus, with radius $R = 6.38fm$ and diffusivity $a = 0.53fm$ [15]. In the simulation the collision impact parameter b is chosen randomly. For each $Au - Au$ collision we calculate the underlying number of nucleon-nucleon collisions (N_{coll}) and the number of participating nucleons (N_{part}), with the assumption that the nucleon-nucleon cross section is $\sigma_{NN}^{inel} = 42mb$.

Centrality classes are defined according to the fractional cross section, where we determine the fraction by cuts on the correlation between forward

going neutrons and the number of participants. This choice is similar to the one used by the PHENIX collaboration [54]. However, the results are insensitive to the specific cuts and consequently other methods give similar results [51, 161]. We tabulate the average number of participants, nucleon-nucleon collisions and impact parameter for different centrality selections in Table.6.3. For each centrality selection we determine the participant density $\rho_{part}(x, y)$ and the nucleon-nucleon collision density $\rho_{coll}(x, y)$ per unit area in the plane transverse to the beam direction. The result is shown in Fig. 6.27 for central and peripheral collisions. The peak values for each centrality class are also given in Table.6.3.

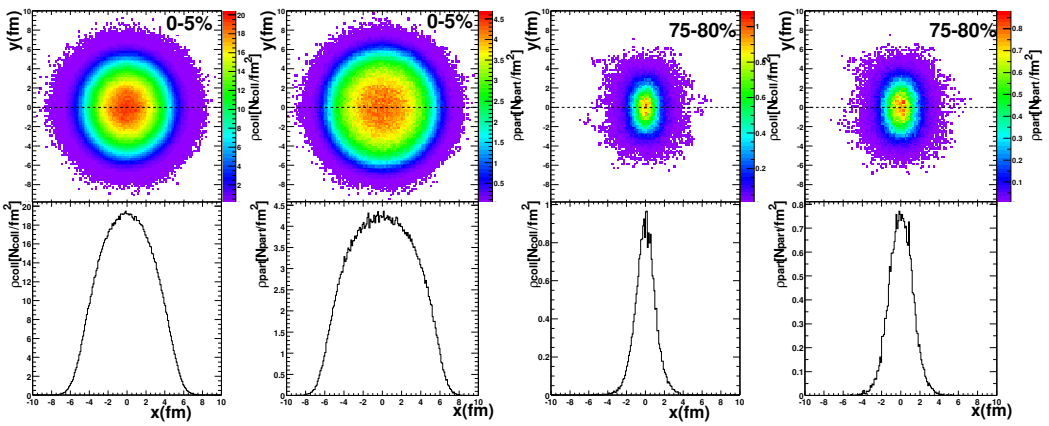

Figure 6.27: Collision density $\rho_{coll}(x, y)$ (left) and participant density $\rho_{part}(x, y)$ (right) in transverse plane for central (0-5%) and peripheral (75-80%) collisions.

In the following we assume that the matter density is proportional to the participant density. This is motivated by the recognition that the bulk particle production scales approximately with the number of participants [16, 13, 17, 161]. In a later section we study the dependence of our results on this assumption. To give the participant density a physical scale we relate it to the energy density using the Bjorken estimate [10]. For central collisions we approximate Eq. 1.1 as:

$$\epsilon_{bj} \propto \frac{N_{part}}{\tau_0 \pi r_0^2 \left(\frac{N_{part}}{2}\right)^{2/3}} \tag{6.18}$$

where $\tau_0 = 1fm/c$ is the typical formation time, $r_0 = 1.2fm$ is the nucleon radius, and N_{part} is the number of participating nucleons. For central collisions

Table 6.3: Glauber parameters calculated for a Woods-Saxon nuclear profile.

Centrality	$\langle N_{part}\rangle$	$\langle N_{coll}\rangle$	$\langle b\rangle$ (fm)	ρ_{part}^{max} fm^{-2}	ρ_{coll}^{max} fm^{-2}	ϵ_{bj}^{max} (GeV/fm^3)	$A(\epsilon_{bj}>1)$ (fm^2)
0-5%	353	1091	2.2	4.2	18.9	8.5	138
15-20%	215	537	6.2	3.8	15.0	7.6	94.7
30-35%	125	250	8.5	3.1	10.3	6.3	64.7
45-50%	66.7	103	10.2	2.4	6.2	4.9	41.6
60-65%	30.2	35	11.7	1.5	2.7	3.1	23.2
75-80%	11.1	9.7	13	0.76	0.9	1.5	6.9
90-95%	4.1	2.8	14.5	0.3	0.23	0.61	0

the experimentally observed value of ϵ_{bj} is ~ 5 GeV/fm^3 [12]. With approximately 350 participants the scale factor to convert participant density to ϵ_{bj} is 2 GeV/fm. The peak values for ϵ_{bj} are given in Table.6.3.

Binary scaling of hard scattering assumes that the incoming parton distribution in $Au-Au$ collisions is a superposition of the individual nucleon parton distribution functions. According to the factorization theorem the probability for a hard scattering process in $Au-Au$ is then proportional to ρ_{coll}. Therefore, we generate back-to-back parton pairs with isotropic azimuthal angular distribution in the transverse plane with a distribution following $\rho_{coll}(x,y)$. These partons are then propagated through the nuclear medium with density $\propto \rho_{part}(x,y)$. The probability with which a parton produced at (x,y) penetrates the matter along in direction (n_x,n_y) is calculated as

$$f = exp(-\kappa I) \qquad , \tag{6.19}$$

where κ is the absorption strength, which is the only free parameter in the model, and I is the matter integral along the path of the parton. For I we choose:

$$I = \int_0^\infty dll\frac{l_0}{l+l_0}\rho(x+l\times n_x, y+l\times n_y) \tag{6.20}$$

This parameterization corresponds to a quadratic dependence of the absorption ($\propto \int ldl$) in a longitudinally expanding medium ($\frac{l_0}{l+l_0}$). Here we assume that partons move with the speed of light and that they sense the dense matter after a formation time of 0.2 fm/c; this results in $l_0 = 0.2\ fm$. However, the results presented in this work do not depend strongly on the choice of l_0.

We fix the absorption strength κ for central collisions to reproduce the observed hadron suppression of 4–5 for $p_T > 5$ GeV/c reported by PHENIX

(see Fig. 6.10) and STAR [56]. In the following we use κ=0.6, which gives a suppression factor of 4.35 as measured for the 0-5% most central events by PHENIX (see Fig. 6.10). The κ value corresponds to an absorption length of $\lambda \sim 3.4\ fm$. For central collisions Fig. 6.28 shows the (x, y) position of partons that escape the medium. As expected partons emitted in the center of the overlap region have to traverse more matter and thus suffer larger absorption than those generated near the surface. Therefore, a short absorption length naturally leads to approximate surface emission of jets and thus of high p_T hadrons.

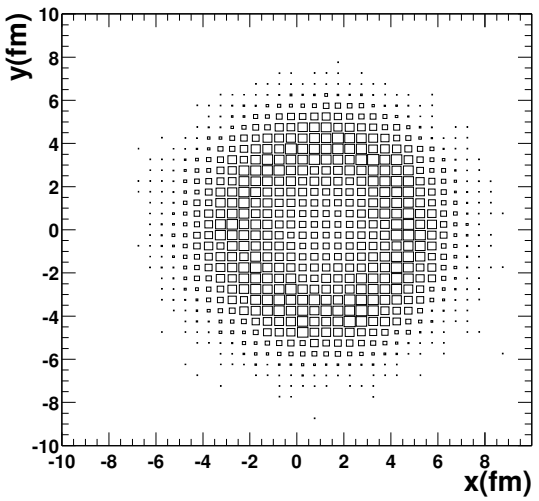

Figure 6.28: Origination point distribution in the transverse plane for jets that escape from the overlap region.

6.7.2 Centrality Dependence Compared to Data

Once κ is determined, the survival rate of jets, the probability to find back-to-back jets, and also the azimuthal anisotropy in jet emission with respect to the reaction plane is fixed for any centrality selection. In Fig. 6.29 we compare the results of our model calculation with three compilations of experimental data:

1. The ratio of the observed hadron yield per participant pair relative to the expected yield from the underlying nucleon-nucleon collisions as function of centrality. Charged hadron and π^0 data from PHENIX (Fig. 6.10) and charged hadron data from STAR [56] are plotted on the top panels (a) and (b) of Fig. 6.29. The p_T ranges are chosen to be above 4.5 GeV/c for PHENIX and 6 GeV/c for STAR.

2. The back-to-back correlation strength can be defined as: [57]

$$D_{AA}(p_T^{trig}) = \int_{p_0}^{p_T^{trig}} dp_T \int^{|\phi_1-\phi_2|>\phi_0} d\phi \frac{d\sigma_{AA}^{h_1h_2}/d^2p_T^{trig}dp_Td\phi}{d\sigma_{AA}^{h_1}/d^2p_T^{trig}} \qquad (6.21)$$

   for an associated hadron h_2 with p_T in the back-side direction of a hadron h_1 with p_T^{trig}. The bottom left panel (c) gives the strength of back-to-back angular correlation, D_{AA}, measured for charged particles with $4 < p_T^{trig} < 6$ GeV/c and associated hadrons with $p_T > p_0 = 2$ GeV/c and $|\phi_1 - \phi_2| > \phi_0 = 2.24$ as function of centrality. The correlation is normalized to the expectation form $p-p$ collisions corrected for combinatorial random background and the azimuthal anisotropy of bulk particle production [65].

3. The azimuthal anisotropy of charged particles emission can be quantified by v_2, the second coefficient of a Fourier decomposition of the $dN/d\phi$ distribution, is shown in the bottom right panel (d). The PHENIX data are measured for $4 < p_T < 5$ GeV/c with respect to the reaction plane [68]. The v_2 values from STAR data were determined from 2 particle cumulant [163] for $4 < p_T < 5$ GeV/c and 4 particle cumulants for $5 < p_T < 7$ GeV/c [162].

The results of our model calculation are shown as thick solid lines on all panels. Once the absorption strength is normalized to the most central collisions, the centrality dependence of the normalized yield is well reproduced. For peripheral collision the normalized yield increases as expected from scaling with the number of nucleon-nucleon collisions (thin line). Only a small fraction of the partons is absorbed since the matter density and volume are small. As the centrality increases both matter density and volume increase. For collisions with more than 100 participants, the absorption overwhelms the increase due to point like scaling and the normalized yield decreases with centrality.

The jet absorption model reproduces the magnitude and centrality dependence of the back-to-back correlations. The calculated suppression is negligible for peripheral collisions, increases continuously and reaches a suppression factor of 7 for the most central bin, consistent with the data. Interestingly, the data suggest that the suppression of back-to-back correlations is almost a factor of 2 stronger than that for the single inclusive hadron yield[5]. In the jet absorption model, partons are produced back-to-back in the transverse plane.

[5]In the 0-5% centrality bin, STAR data show a factor of 3.3 suppression of the charged hadron yield, while the back-to-back suppression factor is 7.

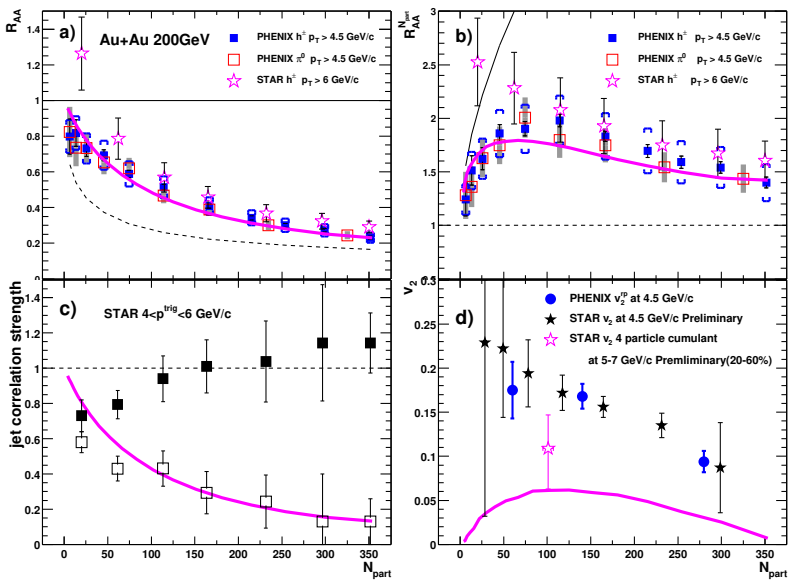

Figure 6.29: Centrality dependence of single hadron suppression, back-to-back suppression, and v_2 at high p_T. In all four panels, the thick solid line indicates the prediction from calculations based on Eqs. 6.19-6.20. a,b) R_{AA} (left) and $R_{AA}^{N_{part}}$ (right) for charged hadron and π^0 from PHENIX (Fig. 6.10) and charged hadrons from STAR [56]. The thin solid line indicates the N_{coll} scaling, and the dashed line indicates the N_{part} scaling limit. c) suppression of the charged hadron back-to-back correlation measured by STAR [65]. d) v_2 measured by PHENIX [68] using the BBC reaction-plane method, v_2 measured by the 2 particle cumulant in $4 < p_T < 5$ GeV/c [163] and the 4 particle cumulant in $5 < p_T < 7$ GeV/c [162] by STAR.

But due to the strong absorption in central events, in most cases, only one parton survives. This naturally leads to a stronger suppression of the back-to-back correlation. It should be noted that in our model, by construction, the near angle jet strength is always 1.

Due to the asymmetry of the overlap region of the two nuclei, the average amount of matter traversed by a parton depends on its azimuthal direction with respect to the reaction plane. Therefore, the average integral I depends on the azimuthal angle, which leads to an azimuthal asymmetry in jet production [147]. This anisotropy is small for peripheral and central collisions, and reaches a maximum for mid-central collisions with ~ 100 participants. Though our calculation reproduces the centrality dependence of v_2, the magnitude is

smaller than measured values from reaction plane or 2 particle cumulant methods, but is within 1σ error from 4 particle cumulant result. Larger values of v_2 could be obtained with larger absorption parameter κ. In the absence of absorption, there is no azimuthal anisotropy, while increasing absorption increases v_2. In Woods-Saxon nuclear profile, v_2 reaches maximum at certain κ, but then decrease to 0 as $\kappa \to \infty$ because the only surviving jets come from the "halo" of the overlap, which is azimuthally symmetric. As we demonstrate in Chapter. 6.7.3, the calculated v_2 values are also very sensitive to the actual nuclear profile used. The Wood-Saxon gives the minimum v_2.

6.7.3 Discussions

Dependence on Absorption Pattern

Parton energy loss is the most popular model for high p_T suppression, but it was argued that final state hadronic interaction [131] could be responsible for suppression seen at RHIC, in this case, the energy loss will be proportional to l instead to l^2. We repeated the same calculation for two additional types of absorption patterns,

$$\begin{aligned} I_2 &= \int_0^\infty dl \frac{l_0}{l+l_0} \rho(x + l \times n_x, y + l \times n_y) \\ I_3 &= \int_0^\infty dl l \rho(x + l \times n_x, y + l \times n_y) \end{aligned} \tag{6.22}$$

I_2 assumes a longitudinal expanding source and absorption $\propto l$; I_3 assumes a static source and absorption $\propto l^2$. It is also worth pointing out that I calculated from Eq. refeq:2 may also be interpreted as absorption proportional to the path length in a static medium, and we will denote it as I_1.

The results are compared in Fig. 6.30. The centrality dependence of the normalized yield is very similar among the three different absorption patterns. The differences in the D_{AA} in most central collisions and the v_2 values in all centralities are quite different between different absorption patterns. Due to the quick drop of the matter density towards peripheral collisions, the pure expansion scenario (I_2) tends to localize the absorption in the region $\approx l_0$ from the jet creation point. In this case, the suppression is dominated by the initial matter profile (t l_0) and is insensitive to the later evolution of the system. This naturally leads to a similar suppression for the high p_T hadron yield and the back-to-back correlation. The surviving jets also become more isotropic resulting in a much smaller v_2.

On the other hand, the absorption in a static medium with quadrat path length dependence (I_3) has a stronger dependence on the jet path. The absorption happens along the full trajectory of the jet inside the medium. Thus both the suppression and v_2 have a stronger dependence on the global property of the overlap region. In particular, one observes a stronger centrality dependence of R_{AA}, reduced back-to-back correlation, and enhanced anisotropy. The resulting magnitude of v_2 agrees with the 4-particle cumulant.

It is not surprising that the predictions for the more realistic absorption I_1 are between I_2 and I_3. In our approach, the suppression of the single particle yield is not sensitive to the absorption pattern used, while the suppression of the back-to-back correlation in central collisions and the v_2 values vary by almost a factor of 2. This indicates that the back-to-back correlation central collisions and v_2 are more sensitive to the collision geometry.

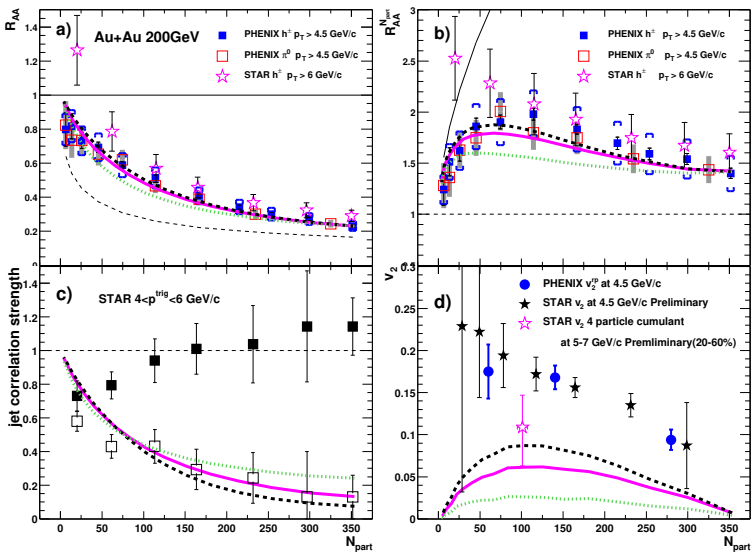

Figure 6.30: Calculation of R_{AA} (a) $R_{AA}^{N_{part}}$ (b), D_{AA} (c), and v_2 (d) using a Woods-Saxon nuclear profile for I_1 (solid line), I_2 (dashed line), and I_3 (dotted line) types of jet absorption.

Dependence on Density Profile

We have assumed $\epsilon \propto \rho_{part}$ in previous calculations. However, data indicates that both E_T and the particle multiplicity [166, 13, 165] scale faster

than N_{part}. In two component models, this was attributed to minijet [167] production. In order to test the sensitivity of our model to the initial energy density profile, we repeated the calculation from Chapter 6.7.3, assuming that the energy density is proportional to the collision density $\rho_{coll}(x, y)$. The results of the calculation are presented in Fig. 6.31. There is little sensitivity between different absorption patterns. One also notices that the centrality dependence and magnitude of v_2 are similar to Fig. 6.30, indicating that the two density profiles produce an almost identical anisotropy. However, the suppression of R_{AA} (or $R_{AA}^{N_{part}}$) and D_{AA} is significantly reduced, especially around $N_{part} \sim 50 - 100$. The reason is the following: As shown in Fig. 6.27, the average density $\langle\rho_{coll}(x, y)\rangle$ has a much stronger centrality dependence than $\langle\rho_{part}(x, y)\rangle$. $\langle\rho_{coll}(x, y)\rangle$ changes by factor of 20 from peripheral to central collisions, while $\langle\rho_{part}(x, y)\rangle$ only changes by factor of 5. Since the absorption strength κ is fixed for the most central collisions, and subsequently applied for all other centrality bins, a larger decrease of $\langle\rho_{coll}(x, y)\rangle$ leads to a reduced suppression for peripheral collisions.

The second difference between the two matter densities is shown in Fig. 6.32. The ρ_{coll} profile gives a more pronounced jet emission surface than that for ρ_{part} (compare with Fig. 6.28). This is due to the fact that the $\rho_{coll}(x, y)$ profile has a larger variation, thus there is more matter on the surface volume than for $\rho_{part}(x, y)$.

Dependence on Nucleus Profile

In heavy-ion collisions, often simplified nuclear distributions is used for nuclei. In addition to the Woods-Saxon distribution, some models assume hard-sphere [57] or cylindrical nuclear distributions [59, 164, 113] to simplify the calculation. However, it should be pointed out that the physics predictions are sensitive to the actual nucleus profile one uses. An example is v_2, where $v_2^{cylindrical} > v_2^{sphere} > v_2^{woods-saxon}$ [147].

Fig. 6.33 shows the calculations for a hard-sphere nuclear distribution in the top panel and a cylindrical nuclear distribution in the bottom panel. In both cases, all three absorption scenarios miss the centrality dependence trend for R_{AA}. The calculated suppression from the spherical geometry shows a better agreement with the data than from cylindrical geometry, but both predict a suppression that sets in at rather peripheral collisions, in contradiction with the data.

On the other hand, both cylindrical and spherical profiles are able to reproduce v_2 in reasonable agreement with the data from the 4-particle cumulant. Similar calculations have been done before in Ref [168] for a hard

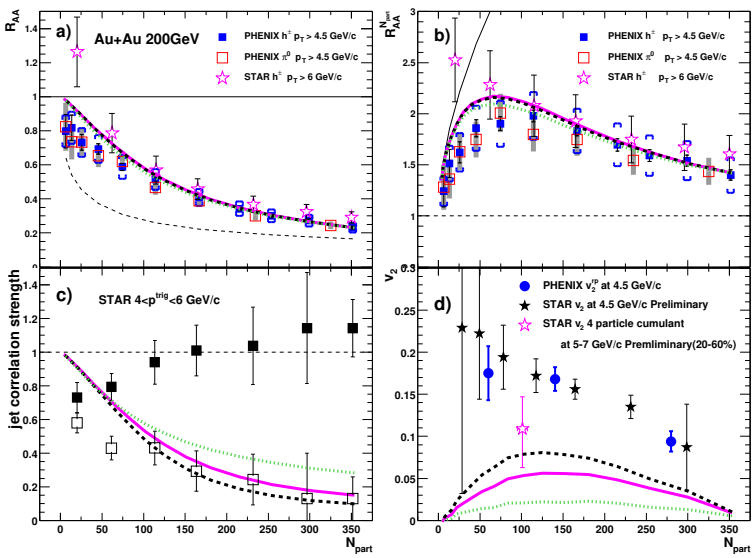

Figure 6.31: Calculation of R_{AA} (a), $R_{AA}^{N_{part}}$ (b), jet correlation (c), and v_2 (d) assuming $\epsilon \sim \rho_{coll}$. The three curves are for I_1 (solid line), I_2 (dashed line), and I_3 (dotted line) types of jet absorption, respectively.

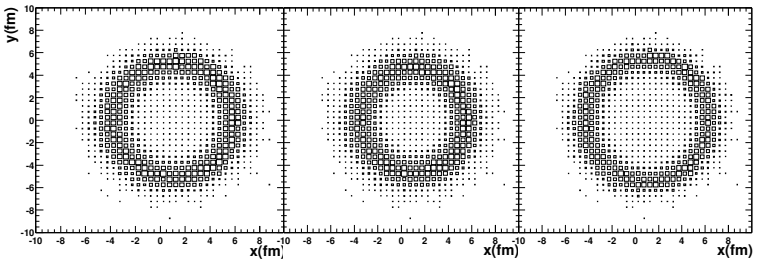

Figure 6.32: Origination point distributions in the transverse plane for jets that escape from the overlap region assuming a ρ_{coll} density profile. The three panels are for I_1 (left), I_2 (middle), and I_3 (right), respectively.

sphere with a ρ_{coll} density profile. The reason is that while the Woods-Saxon profile has a very diffuse surface, both cylindrical and hard-sphere geometry have sharp surfaces. Their surfaces have an asymptotically large eccentricity, which would lead to a large finite v_2 [170].

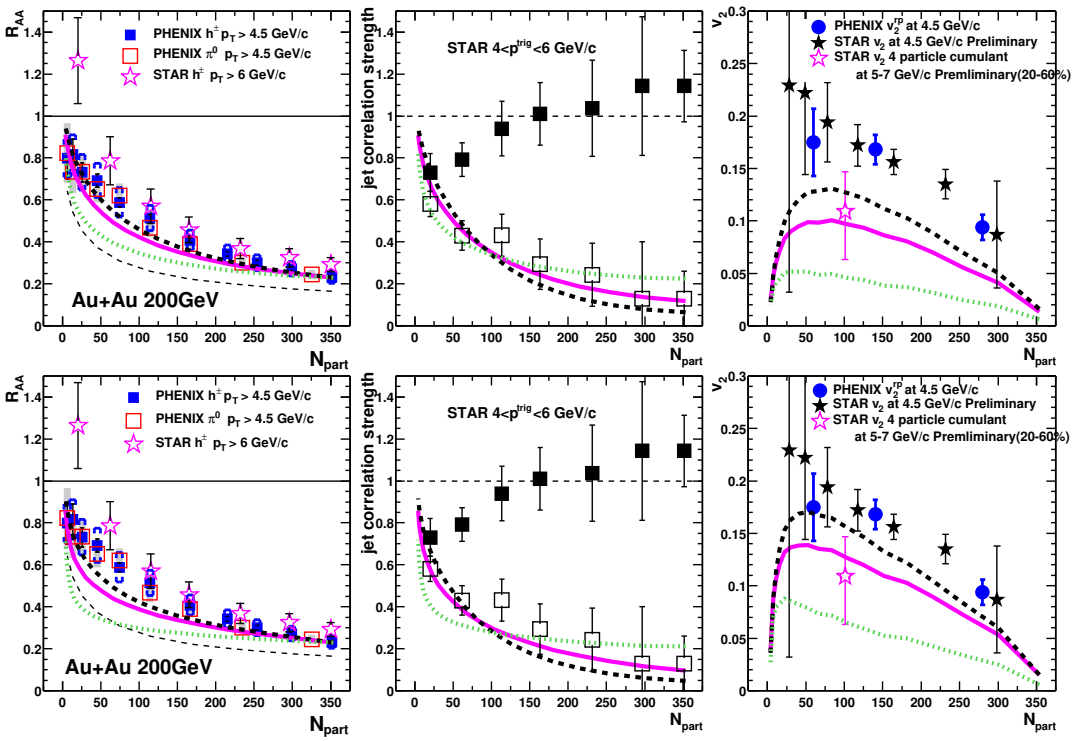

Figure 6.33: Calculation of $R_{AA}^{N_{part}}$, jet correlation, and v_2 for a hard-sphere nuclear profile (top panels) and a cylindrical nuclear profile (bottom panels) using the I_1 (solid line), I_2 (dashed line), and I_3 (dotted line) form of jet absorption.

Chapter 7

Summary and Outlook

We have presented a systematic study of the p_T and centrality dependence of charged hadron production for $|\eta|$ <0.18 at $\sqrt{s_{NN}}$ = 200 GeV. The yields per nucleon-nucleon collision in central $Au-Au$ collisions are significantly suppressed compared to peripheral and nucleon-nucleon collisions. The suppression is approximately independent of p_T above 4.5 GeV/c for all centrality classes, suggesting a similar spectral shape for $Au-Au$ and $p-p$ collisions. For $p_T > 4.5$ GeV/c, charged hadron and neutral pion production are suppressed by a similar factor. The ratio h/π^0 is ~ 1.6 for all centralities, similar to the h/π value measured in $p-p$ and e^+e^- collisions. The similar spectral shape and particle composition at high p_T are consistent with jet fragmentation as the dominating mechanism of particle production in $Au-Au$ collisions for $p_T >$ 4–5 GeV/c. For both charged hadrons and neutral pions, the suppression sets in gradually from peripheral to central collisions, consistent with the expectation of partonic energy loss and surface emission of high p_T hadrons. x_T-scaled hadron yields are compared between $\sqrt{s_{NN}}$ = 130 GeV and $\sqrt{s_{NN}}$ = 200 GeV $Au-Au$ collisions. We find that the x_T scaling power n calculated for neutral pions in central and peripheral collisions and charged hadron in peripheral collisions is 6.3 ± 0.6, similar to $p-p$ collisions. This again points towards similar production dynamics, i.e. hard-scattering processes as described by QCD. However, n is 7.5 ± 0.5 for charged hadrons in central collisions, indicating a strong non-scaling modification of the particle composition of charged hadron spectra compared to that of $p-p$ at intermediate p_T, i.e. 2–4.5 GeV/c. This is consistent with the large h/π^0 ratio observed over the same p_T range in central collisions.

The suppression pattern observed in $Au-Au$ collisions are then compared with results from $d-Au$. An enhancement in $d-Au$ collisions is observed. The enhancement sets in at intermediate centrality and increases towards more central collisions, reaching a 50% enhancement around 2 GeV/c

relative to the N_{coll} scaled yield in $p-p$ collisions, and is consistent with the initial state Cronin effect. This enhancement indicates that the suppression in central $Au-Au$ collisions is not a final state effect, nor does it arise from nuclear shadowing. A similar amount of Cronin enhancement should also be expected in central $Au-Au$ collisions, though it may be overwhelmed by the large suppression from jet energy loss.

We also discussed the interpretation of the characteristic centrality dependence of the suppression of hadron yield, suppression of back-to-back correlation, and the anisotropic flow (v_2) based on collision geometry and jet absorption. Our model quantitatively describes the centrality dependence of the suppression of hadron yields and back-to-back correlation. This may indicate that in central collisions the initial hard scattered partons may be completely thermalized in the medium and the surviving jets come from the surface. Inclusive hadron suppression is not very sensitive to the absorption pattern while the back-to-back correlations are sensitive to the detailed modelling of the absorption, indicating that the experimentally measured centrality dependence of back-to-back correlations can be used to constrain different energy loss assumptions. On the other hand, the calculated v_2 qualitatively describes the experimentally measured centrality dependence, but the predicted magnitude is smaller than the measured v_2 for a Woods-Saxon nuclear profile. However, for either hard-sphere or cylindrical nuclear profiles, the predicted v_2 values are closer to or even exceed the experimentally measured v_2 from the 4-particle cumulant method. This indicates that the initially formed dense matter might be different from the Woods-Saxon profile. Thus the experimentally measured v_2, after carefully removing the non-geometric effect, can help to understand the shape and evolution of the dense matter created in the $Au-Au$ collisions.

Since the suppression of high p_T hadrons due to final state medium modification has been firmly established from the first three year's of RHIC running, it is important to ask what the future of the heavy-ion high p_T physics is at RHIC? In author's personal opinion, there are several important next tasks:

- An energy scan is required. From SPS ($\sqrt{s_{NN}}$ = 17 GeV) to RHIC ($\sqrt{s_{NN}}$ = 200 GeV), the energy density only increases by 50%. However, high p_T hadron production changes from a factor of 4 enhancement at SPS to a factor of 4-5 suppression at RHIC. Does the SPS result imply no suppression or is the suppression totally overwhelmed by the Cronin effect? Is the dense matter produced at SPS has a similar opacity as that created at RHIC? Future RHIC $Au-Au$ runs at a set of various energy points with sufficient statistics can help the experiments to map out the

detailed energy dependence of the suppression pattern, and allows the extrapolation of the suppression pattern to lower $\sqrt{s_{NN}}$.

Fig. 7.1 shows the jet absorption model prediction of the $\sqrt{s_{NN}}$ dependence of R_{AA} for high p_T hadron production in most central collisions. In this calculation, the absorption strength is fixed by R_{AA} at $\sqrt{s_{NN}} = 200$ GeV. The measured dE_T/dy values (left panel) have been used to calculate the energy density profiles at different $\sqrt{s_{NN}}$, which in turn give the R_{AA} as different $\sqrt{s_{NN}}$. The jet absorption model predicts a rather smooth $\sqrt{s_{NN}}$ dependence. Even at SPS energy, the jet still has a factor of 3 suppression [1]

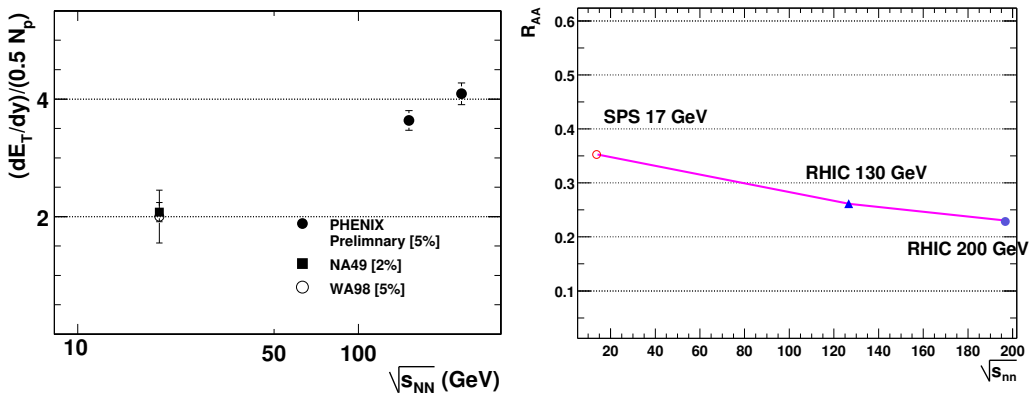

Figure 7.1: a) $dE_T/dy|_{y=0}$ per pair of participants vs. $\sqrt{s_{NN}}$ for the most central collisions (the N_{part} are almost identical for all energies). Figure taken from [13]. b) The calculated R_{AA} as function of $\sqrt{s_{NN}}$ using the Woods-Saxon nuclear profile for the I_1 type of absorption (see Eq. 6.20).

- Inclusive hadron spectra should be measured out to the highest p_T, preferably $p_T \gtrsim 20$ GeV/c, at which p_T the jets are so penetrating that R_{AA} should come back to 1. The PHENIX Level-1 and Level-2 high p_T hadron triggers using EMCal and RICH can help to extend the p_T range and achieve this goal in RUN-4.

- More detailed study of the medium modifications is needed. In particular, measurements of the back-to-back correlations and v_2 for identified

[1] We assume a constant absorption strength. However, the absorption strength could decrease towards smaller $\sqrt{s_{NN}}$, which will lead to a smaller suppression.

hadrons and R_{AA} for baryons out to ≈ 10 GeV/c are missing. This can help to understand the origin of high p_T hadrons and the flavor dependence of the medium modification. This goal can also be achieved in RUN-4 due to the significantly increased statistics and the various high p_T Level-1 and Level-2 triggers.

Bibliography

[1] Gross, D. J. and F. Wilczek, Phys. Rev. Lett. **30**, 1343 (1973).

[2] Cheuk-Yin Wong "Introduction to High-Energy Heavy-Ion Collisions", World Scientific.

[3] F. Karsch, Phys. Lett. **B478**, 447 (2000).

[4] F. Karsch, Lect. Notes. Phys. **583**, 209 (2002).

[5] F. Karsch, E. Laermann and A. Peikert, Nucl. Phys. **B605**, 579 (2001).

[6] S.A. Bass, M. Gyulassy, H. Stoecker, W. Greiner, J. Phys **G25**, R1 (1999).

[7] P.F. Kolb, nucl-th/0304036.

[8] R. Stock, Nucl. Phys. **A661**, 282c (1999); T. Alber, *et al.*, Phys. Lett. **B366**, 56 (1996); L. Kluberg, Nucl. Phys. **A661**, 300c (1999); L. Ramello *et al.*, Nucl. Phys. **A638**, 261 (1998).

[9] X.N. Wang, Phys. Repts. **280**, 287 (1997).

[10] J.D. Bjorken, Phys. Rev. **D27**, 140 (1983).

[11] T. Alber *et al.*, [NA49 Collaboration], Phys. Rev. Lett. **75**, 3814 (1995).

[12] K. Adcox *et al.*, [PHENIX Collaboration], Phys. Rev. Lett. **87**, 052301 (2001).

[13] A. Bazilevsky *et al.*, [PHENIX Collaboration], Nucl. Phys. **A715**, 486 (2003).

[14] C.W. deJager, H. deVries, and C. deVries, Atomic Data and Nuclear Data Tables **14**, 485 (1974).

[15] R.J. Glauber and G. Matthiae, Nucl. Phys. **B21**, 135 (1970).

[16] P.D. Jones *et al.*, [The NA49 Collaboration], Nucl. Phys. **A610**, 189c (1996); T. Peitzmann *et al.*, [The WA98 Collaboration], Nucl. Phys. **A610**, 200c (1996); R. Albrecht *et al.*, [The WA80 Collaboration], Phys. Rev. **C44**, 2736 (1998).

[17] A. Bialas, A. Bleszynski, and W. Czyz, Nucl. Phys. **B111**, 461 (1976).

[18] X.N. Wang and M. Gyulassy, Phys. Rev. **D44**, 3501 (1991).

[19] K.J. Eskola, K. Kajantie, and K. Tuominen, Phys. Lett. **B497**, 39 (2001) [hep-ph/0009246].

[20] D. Kharzeev and E. Levin, Phys. Lett. **B523**, 79 (2001) [nucl-th/0108006].

[21] X.N. Wang and M. Gyulassy, Phys. Rev. Lett. **68**, 1480 (1992);

[22] M. Gyulassy and M. Plümer, Phys. Lett. **B243**, 432 (1990); R. Baier *et al.*, Phys. Lett. **B345**, 277 (1995).

[23] R. Baier, D. Schiff, and B.G. Zakharov, Ann. Rev. Nucl. Part. Sci. **50**, 37 (2000).

[24] R. Baier, Y.L. Dokshitzer, A.H. Mueller, and D. Schiff, J. High Energy Phys. **9**, 33 (2001).

[25] J.C. Collions *et al.*, in Perturbative Quantum Chromodynamics, ed. A.H. Mueller, AdV. Ser. Direct. High Energy Phys. **5** 1 (1988).

[26] W.M. Geist, *et al.*, Phys. Repts. **197**, 263 (1990).

[27] B. Alper *et al.*, Nucl. Phys. **B100**, 237 (1975).

[28] F. Abe *et al.*, Phys. Rev. Lett. **61**, 1819 (1988).

[29] S.S. Adler *et al.*, [PHENIX Collaboration], `hep-ex/0304038`, submitted to Phys. Rev. Lett.

[30] F. Aversa *et al.*, Nucl. Phys. **B327**, 105 (1989); B. Jäger *et al.*, Phys. Rev. **D67**, 054005 (2003); D. de Florian, Phys. Rev. **D67**, 054004 (2003).

[31] B.A. Kniehl *et al.*, Nucl. Phys. **B597**, 337 (2001).

[32] S. Kretzer, Phys. Rev. **D62**, 054001 (2000).

[33] D. Antreasyan *et al.*, Phys. Rev. **D19**, 764 (1979).

[34] G. Piller and W. Weise, Phys. Repts. **330**, 1 (2000).

[35] M. Arneodo, *et al.*, [NMC Collaboration], Nucl. Phys. **B481**, 23 (1996).

[36] L.V. Gribov, E.M. Levin, and M.G. Ryskin, Phys. Repts. **100**, 1 (1983); A.H. Mueller and J. Qiu, Nucl. Phys. **B268**, 427 (1986).

[37] L. McLerran and R. Venugopalan, Phys. Rev. **D49**, 2233,3352 (1994); L. McLerran and R. Venugopalan, Phys. Rev. **D59**, 094002 (1999); Yu.V. Kovchegov, Phys. Rev. **D54**, 5463 (1996),Phys. Rev. **D60**, 034008 (1999); E. Iancu, A. Leonidov and L. McLerran, hep-ph/0011241.

[38] A. Accardi, hep-ph/0212148.

[39] J. Ashman *et al.*, [European Muon Collaboration], Phys. Lett. **B202**, 603 (1988).

[40] K.J. Eskola, V.J. Kolhinen, and P.V. Ruuskanen, Nucl. Phys. **B535**, 351 (1998); K.J. Eskola, V.J. Kolhinen, and C.A. Salgado, Eur. Phys. J. **C9**, 61 (1999).

[41] NMC, M. Arneodo *et al.*, Nucl. Phys. **B441**, 12 (1995).

[42] A.H. Muller and J.W. Qiu, Nucl. Phys. **B268**, 427 (1986).

[43] L.D. McLerran and R. Venugopalan, Phys. Rev. **D49**, 3352 (1994), Phys. Rev. **D50**, 2225 (1994).

[44] D. Kharzeev and E. Levin, Phys. Lett. **B523**, 79 (2001), [nucl-th/0108006].

[45] J. Huth *et al.*, in Proceedings of the DPF 1990 Summer Study on High Energy Physics, Snowmass, Colorado, ed. E. L. Berger, World Scientific, 134 (1992).

[46] W. Bartel *et al.*, JADE Collaboration, Z. Phys. **C33**, 23 (1986).

[47] S. Catani, Yu.L. Dokshitzer, M.H. Seymour, and B.R. Webber, Nucl. Phys. **B406**, 187 (1993).

[48] M. Gyulassy, I. Vitev, X.N. Wang, and B.W. Zhang nucl-th/0302077.

[49] M.H. Thoma and M. Gyulassy, Nucl. Phys. **B351**, 491 (1991);M.H. Thoma, Phys. Rev. **D49**, 451 (1994).

[50] K. Adcox *et al.*, [PHENIX Collaboration], Phys. Rev. Lett. **88**, 022301 (2002).

[51] C. Adler *et al.*, [STAR Collaboration], Phys. Rev. Lett. **89**, 202301 (2002).

[52] K. Adcox *et al.*, [PHENIX Collaboration], Phys. Lett. **B561**, 82 (2003).

[53] B.B. Back *et al.*, [PHOBOS Collaboration], `nucl-ex/0302015`, submitted to Phys. Lett. **B**.

[54] S.S Adler *et al.*, [PHENIX Collaboration], `nucl-ex/0304022`.

[55] S.S Adler *et al.*, [PHENIX Collaboration], `nucl-ex/0308006`.

[56] J. Adams *et al.*, [STAR Collaboration], `nucl-ex/0305015`.

[57] X.N. Wang, nucl-th/0305010.

[58] I. Vitev and M. Gyulassy, Phys. Rev. Lett. **89**, 252301 (2002).

[59] D. Kharzeev, E. Levin, and L. McLerran, Phys. Lett. **B561**, 93 (2003), and references therein.

[60] K. Adcox *et al.*, [PHENIX Collaboration], Phys. Rev. Lett. **88**, 242301 (2002).

[61] S.S Adler *et al.*, [PHENIX Collaboration], `nucl-ex/0305036`.

[62] J. Adams *et al.*, [STAR Collaboration], `nucl-ex/0306007`.

[63] P. Abreu *et al.*, Eur. Phys. J. **C17**, 207 (2000); O. Klapp, Doctoral Thesis, *Eine umfassende Studie der Eigenschaften von Quark and Gluon Jets*, University Wuppertal 1999.

[64] R.C. Hwa and C.B. Yang, Phys. Rev. **C67**, 034902 (2003); R.J. Fries, B. Muller, C. Nonaka, and S.A. Bass, `nucl-th/0301087`, to appear in Phys. Rev. Lett. ; V.Greco, C.M. Ko, and P. Levai, nucl-th/0301093, to appear in Phys. Rev. Lett. ; V. Greco, C.M. Ko, and P. Levai, `nucl-th/0305024`; R.J. Fries, B Müller, C. Nonaka, and S.A. Bass, `nucl-th/0306027`.

[65] C. Adler *et al.*, [STAR Collaboration], Phys. Rev. Lett. **90**, 082302 (2002).

[66] K.H. Ackermann, *et al.*, STAR Collaboration, Phys. Rev. Lett. **86**, 402 (2001);K. Adcox *et al.*, Phys. Rev. Lett. **89**, 212301 (2002).

[67] C. Adler, *et al.*, Phys. Rev. **C66**, 034904 (2002).

[68] S.S Adler *et al.*, [PHENIX Collaboration], `nucl-ex/0305013`.

[69] PHENIX Conceptional Design Report. Unpublished.

[70] M. Chiu *et al.*, Phys. Rev. Lett. **89**, 012302 (2002).

[71] C. Adler *et al.*, Nucl. Instrum. Methods**470**, 488 (2001).

[72] S.N. White, Nucl. Instrum. Methods**409**, 618 (1998).

[73] Tomoaki Nakamura, talk given in PHENIX RUN-2 focus seminar for BBC.

[74] H. Akikawa *et al.*, [PHENIX Collaboration] Nucl. Instrum. Methods**499**, 537 (2003).

[75] K. Adcox *et al.*, Nucl. Instrum. Methods **A499**, 469 (2003).

[76] A. Milov, Ph.D thesis, Weizmann Institute, Rohovot Israel, May 2002.

[77] A. Oskarsson, talk given in PHENIX RUN-2 focus seminar for PC.

[78] M. Aizawa *et al.*, Nucl. Instrum. Methods **A499**, 508 (2003).

[79] Takao Sakaguchi, talk given in PHENIX RUN-2 focus seminar for RICH.

[80] F. Messer and J. Jia, PHENIX internal analysis note 127.

[81] Tassilo Christ, Master Thesis, StonyBrook 2001.

[82] S. Butsyk talk given in PHENIX RUN-2 focus seminar for DC.

[83] Developed by Sergy Butsyk.

[84] Jane Burward-Hoy, Ph.D thesis, SUNY at Stony Brook, Dec. 2001.

[85] K. Adcox *et al.*, Nucl. Instrum. Methods **A499**, 489 (2003); J.T. Mitchell *et al.*, Nucl. Instrum. Methods **A482**, 491 (2002).

[86] Track Model is developed by Jane Burward-Hoy and Stephen Johnson.

[87] R. Averbeck,*et al.*, PHENIX internal analysis note 37.

[88] The DC internal alignments are performed by Sergy Butsyk and Tom Hemmick.

[89] J. Burward-Hoy,*et al.*, PHENIX internal analysis note 172.

[90] T. Chujo,*et al.*, PHENIX internal analysis note 187.

[91] Vlad Pantuev's study on Ecore effiency.

[92] T. Hachiya, *et al.*, PHENIX internal analysis note 107.

[93] J.L. Nagle, *et al.*, PHENIX internal analysis note 113.

[94] NA 49 Collaboration. Eur. Phys. J. **C2**, 383 (1998).

[95] M. Chiu, *et al.*, PHENIX internal analysis note 014.

[96] K. Reygers, PHENIX Glauber Simulation Software.

[97] S. Kelly, *et al.*, PHENIX internal analysis note 033.

[98] K. Reygers, *et al.*, PHENIX internal analysis note 169.

[99] Developted by Yasuyuki Akiba and Federica Messor.

[100] GEANT 3.2.1, CERN program library.

[101] Yung-Su Tsai, Rev. Mod. Phys. **46**, 815 (1974).

[102] J. Jia, *et al.*, PHENIX internal analysis note 177 It contains more details on the background subtraction.

[103] PHENIX Collaboration, S.S. Adler *et al.*, nucl-ex/0307022.

[104] K. Adcox *et al.*, [PHENIX Collaboration], Phys. Rev. Lett. **89**, 092302 (2002).

[105] C. Adler *et al.*, [STAR Collaboration], `nucl-ex/0206008`.

[106] C. Adler *et al.*, [STAR Collaboration], Phys. Rev. Lett. **89**, 092301 (2002).

[107] S. Bazilevsky, *et al.*, PHENIX internal analysis note 175, 176 and 178.

[108] S. Bazilevsky, PHENIX internal analysis note 143 and 176.

[109] T. Alexopoulos *et al.*, Phys. Rev. **D48**, 984 (1993).

[110] C. Albajar *et al.*, Nucl. Phys. **B335**, 261 (1990).

[111] I. Vitev and M. Gyulassy, Phys. Rev. **C65**, 041902(R) (2002).

[112] Xiaofei Zhang and George Fai, hep-ph/0306227.

[113] B. Müller, Phys. Rev. **C67**, 061901 (2003) or [nucl-th/0208038].

[114] M. Breidenbach *et al.*, Phys. Rev. Lett. **23**, 935 (1969); See also W.K.H. Panofsky, in *Proceedings of the Fourteenth International Conference On High Energy Physics*, Vienna, Austria, 1968 (CERN Scientific Information Service, Geneva, Switzerland, 1968), p. 23.

[115] J.D. Bjorken, Phys. Rev. **D179**, 1547 (1969).

[116] S.M. Berman, J.D. Bjorken, and J.B. Kogut, Phys. Rev. **D4**, 3388 (1971).

[117] R. Blankenbecler, S.J. Brodsky, and J.F. Gunion, Phys. Lett. **B42**, 461 (1972).

[118] F.W. Büsser *et al.*, Phys. Lett. **B46**, 471 (1973), see also *Proc. 16th Int. Conf. HEP*, edited by J.D. Jackson and A. Roberts, (NAL, Batavia, IL, 1972) Vol. 3, p. 317.

[119] M. Banner *et al.*, Phys. Lett. **B44**, 537 (1973).

[120] B. Alper *et al.*, Phys. Lett. **B44**, 521 (1973).

[121] R.F. Cahalan, K.A. Geer, J. Kogut, and L. Susskind, Phys. Rev. **D11**, 1199 (1975).

[122] A.L.S. Angelis *et al.*, Phys. Lett. **B79**, 505 (1978). See also, A.G. Clark *et al.*, Phys. Lett. **B74**, 267 (1978).

[123] F.W.Büsser *et al.*, Nucl. Phys. **B106**, 1 (1976).

[124] M. Banner *et al.*, Phys. Lett. **B115**, 59 (1982); M. Banner *et al.*, Z. Phys. **C27**, 329 (1985).

[125] L. Apanasevich *et al.*, hep-ex/0204031.

[126] L. DiLella, Ann. Rev. Nucl. Part. Sci. **35**, 107 (1985).

[127] P. Darriulat, Ann. Rev. Nucl. Part. Sci. **30**, 159 (1980).

[128] J.F. Owens, Rev. Mod. Phys. **59**, 465 (1987).

[129] C. Kourkoumelis *et al.*, Phys. Lett. **B84**, 271 (1979).

[130] J. Huston, *Proc. 29th Int. Conf. HRP (ICHEP 98)*, Vancouver, Canada, 1998 (World Scientific Singapore, 1999), `hep-ph/9901352`.

[131] K. Gallmeister, C. Greiner, and Z. Xu, `nucl-th/0202051`; K. Gallmeister, C. Greiner and Z. Xu, Phys. Rev. **C67**, 244905 (2003).

[132] M.G. Ryskin, Sov. J. Nucl. Phys. **52**, 139 (1990); S. Gavin and J. Milana, Phys. Rev. Lett. **68**, 1834 (1992);A.H. Sorensen, Z. Phys. **C53**, 595 (1992); S.J. Brodsky and P. Hoyer, Phys. Lett. **B298**, 165 (1993).

[133] X.N. Wang and M. Gyulassy, Phys. Rev. Lett. **68**, 1480 (1992).

[134] D. d'Enterria, nucl-ex/0306001.

[135] U.A. Widdemann, hep-ph/0302184, hep-ph/0302194.

[136] F. Arleo, J. High Energy Phys. **211**, 044 (2002).

[137] M. Gyulassy, P. Levai, and I. Vitev, Nucl. Phys. **B594**, 371 (2001); M. Gyulassy, P. Levai, and I. Vitev, Phys. Rev. Lett. **85**, 5535 (2000).

[138] X.N. Wang and X.F. Guo, Nucl. Phys. **A696**, 788 (2001);X.F. Guo and X.N. Wang, Phys. Rev. Lett. **85**, 3591 (2000).

[139] E. Wang and X.N. Wang, Phys. Rev. Lett. **87**, 142301 (2001).

[140] M.M. Aggarwal *et al.* [WA98 Collaboration], Phys. Rev. Lett. **81**, 4087 (1998).[Erratum-ibid. **84**, 578 (1998)].

[141] G.J. Kunde [STAR Collaboration], arXiv:nucl-ex/0211018.

[142] E. Wang and X.N. Wang, Phys. Rev. Lett. **89**, 162301 (2002).

[143] X.N. Wang, Z. Huang, and I. Sarcevic, Phys. Rev. Lett. **77**, 231 (1996);X.N. Wang and Z. Huang, Phys. Rev. **C55**, 3047 (1997).

[144] X.N. Wang, hep-ph/0301196.

[145] X.N. Wang, nucl-th/0307036.

[146] X.N. Wang, Phys. Rev. **C63**, 054902 (2001).

[147] M. Gyulassy, I. Vitev, and X.N. Wang, Phys. Rev. Lett. **86**, 2537 (2001).

[148] Y. Zhang *et al.*, Phys. Rev. **C65**, 034903 (2002)[hep-ph/0109233]

[149] B.Z. Kopeliovich *et al.*, Phys. Rev. Lett. **88**, 232303 (2002) [hep-ph/0201010]

[150] I. Vitev and M. Gyulassy, Phys. Rev. Lett. **89**, 252301 (2002)[hep-ph/0209161].

[151] D. Kharzeev and M. Nardi, Phys. Lett. **B507**, 121 (2001).

[152] D. Kharzeev Nucl. Phys. **A715**, 35 (2003).

[153] S.S Adler *et al.*, [PHENIX Collaboration], `nucl-ex/0306021`.

[154] J. Jia, *et al.*, PHENIX internal analysis note 202.

[155] P.B. Straub et al., Phys. Rev. Lett. **68**, 452 (1992).

[156] X.N. Wang, Phys. Rev. **C61**, 064910 (2000).

[157] J. Adams *et al.*, [STAR Collaboration], `nucl-ex/0306024`.

[158] B.B. Back *et al.*, [PHOBOS Collaboration], `nucl-ex/0306025`.

[159] I. Arsene, *et al.*, [BRAHMS Collaboration], `nucl-ex/0307003`.

[160] Talk given in CIPANP2003 conference.

[161] D. Kharzeev and M. Nardi , Phys. Lett. **B507**, 121 (2001) nucl-th/0012025.

[162] R. Snellings, Proceedings for 19th Winter Nuclear Dynamics Workshop, nucl-ex/0305001.

[163] A. Tang, Talk in Transverse Dynamic Workshop, March 2003, BNL.

[164] Y.V. Kovchegov and K.L. Tuchin, Nucl. Phys. **A708**, 413 (2002).

[165] B.B. Back *et al.*, [PHOBOS Collaboration],Phys. Rev. **C67**, 021901R (2003).

[166] K. Adcox *et al.*, [PHENIX Collaboration], Phys. Rev. Lett. **86**, 3500 (2001).

[167] S. Li, X.N. Wang Phys. Lett. **B527**, 85 (2002).

[168] E.V. Shuryak Phys. Rev. **C**66 027902 (2002), nucl-th/0112042.

[169] J.Y. Ollitrault, Phys. Rev. **D46**, 229 (1992).

[170] S.A. Voloshin, Nucl. Phys. **A715**, 379 (2003).

[171] A. Drees, J. Jia and F. Messer, PHENIX internal analysis note 071 and 114;

[172] A. Milov, *et al.*, PHENIX internal analysis note 201.

[173] A. Drees, *et al.*, PHENIX internal analysis note 210.

[174] Kensuke Okada, analysis note under preparation.

[175] P.E. Hodgson. Nuclear Reactions and Nuclear Structure. Clarendon Press, Oxford, 1971.

[176] M. Lacombe *et al.*, Phys. Lett. **B101**, 139 (1981).

[177] K. Homma, PHENIX internal analysis note 211.

[178] D. Morrison, PHENIX internal analysis note 165.

Appendix A

Charged Hadron Analysis for 130 GeV $Au-Au$ and 200 GeV $d-Au$ Collisions

There are four independent charged hadron analysis in PHENIX. They are:

- RUN-1: Charged Hadrons in $Au-Au$ collisions at $\sqrt{s_{NN}} = 130$ GeV [171]
- RUN-2: Charged Hadrons in $Au-Au$ collisions at $\sqrt{s_{NN}} = 200$ GeV
- RUN-3: Charged Hadrons in $d-Au$ collisions at $\sqrt{s_{NN}} = 200$ GeV [154, 172, 173]
- RUN-2: Charged Hadrons in $p-p$ collisions at $\sqrt{s_{NN}}$ =200 GeV [174]

In Chapter.6, we compare the charged hadron results from the second analysis with selected results from the first and third analysis. For completeness, in this appendix, we discuss briefly the first and third analysis, focusing on the differences from the second analysis, which we have discussed in Chapters.3–5.

So far, the first three analysis have been published [50, 52, 55, 103]. All four analysis uses similar techniques. However, there are differences in terms of the centrality selection, available statistics, the tracking detectors involved, and the detector performances. These differences lead to different strategies for data analysis and efficiency correction. The main features for three analysis are listed in Table.A.1.

Table A.1: The comparison between different charged hadron analysis.

	$Au-Au$ at 130 GeV	$Au-Au$ at 200 GeV	$d-Au$ at 200 GeV
Tracking detectors	East arm DC, PC1, PC3	West arm DC, PC1, PC2, PC3	Both arms DC, PC1, PC3
Statistics	1.67 M	27.2M	11.9M
Momentum resolution $\delta p/p$	$0.6 \oplus 3.6\%p$	$0.7 \oplus 1\%p$	$0.7 \oplus 1.1\%p$
p_T range	0.2-5 GeV/c	0.5-10 GeV/c	0.5-8 GeV/c
Trigger efficiency	$91 \pm 1\%$	$92.2 \pm 1\%$	$88 \pm 1\%$
DC active area	$\sim 50\%$	$\sim 80\%$	$\sim 90\%$
Cuts	$\lvert z_{vtx}\rvert < 30cm$ all quality tracks	$\lvert z_{vtx}\rvert < 30cm$ $\lvert z_{DC}\rvert < 40cm$ high quality tracks	$\lvert z_{vtx}\rvert < 20cm$ $\lvert z_{DC}\rvert < 40cm$ high quality tracks
Matching	2σ at PC3	2σ at PC2,PC3	2.5σ at PC3
Random background	Yes	No	No
Background subtraction	No	Yes	Yes

A.1 Charged Hadron Analysis in $Au-Au$ Collisions at $\sqrt{s_{NN}} = 130$ GeV

The main differences between the 130 and 200 GeV analysis come from the differences in the detector systems involved. Because the PC2 and PC3 in the west arm are missing in RUN-1 (see Fig. 2.2a), the 130 GeV $Au-Au$ analysis uses DC, PC1, PC3 in the east arm for track reconstruction and background rejection. Due to the limited statistics, the 130 GeV results focus on the hadron suppression in the intermediate p_T region 2-4 GeV/c, and discuss in detail the centrality dependence of the yield and the spectral shape [50, 52].

One of the main differences between RUN-1 and RUN-2 is the DC momentum resolution. The RUN-1 resolution is a factor 3 worse than RUN-2 because i) the DC internal wire alignments were not performed, ii) low quality tracks, where tracks have hits only in one of the two X wire nets, were used[1]. Those tracks have much worse momentum resolution. Due to the momentum smearing effect, this poor momentum resolution leads to a momentum dependent correction (decreasing as function of p_T) as shown in Fig. A.1. The poor DC alignment and the use of low quality tracks also lead to a large matching width to outer detectors. The matching widths for RUN1 and RUN-2 have

[1]In RUN-1, the DC has more than 50% inactive area. A large fraction of the tracks are low quality. In RUN-2 and RUN-3, the inactive area is less than 20%, and $> 90\%$ tracks are high quality tracks, so the low quality tracks are not used.

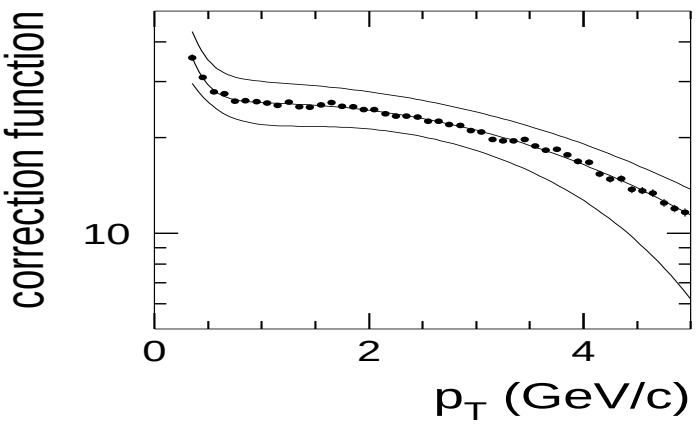

Figure A.1: Correction function for the RUN-1 charged hadron analysis [52], the decrease at high p_T is a result of poor momentum resolution.

been compared in Table. 3.4. The matching window for PC3 in RUN-1 is almost 50% as wider as in RUN-2 [2].

The background sources at high p_T are also different. Due to limited statistics, RUN-1 charged hadron spectra only go out to 5 GeV/c. In cental collisions, although the conversion and decay background is already significant around 4-5 GeV/c, the dominating background after 2σ matching cuts comes from randomly associated background. Since the PC3 matching window is 50% larger than in RUN-2, the random background is also larger than the estimate in Fig. 4.11 for RUN-2. This random background is shown in Fig. A.2 for minimum bias collisions.

Finally, the occupancy efficiency correction is also different from that in RUN-2. This efficiency was evaluated separately for high quality and low quality tracks. Since low quality tracks have only half of the hits compared to high quality tracks, they are much easier to get destroyed in central events. The occupancy efficiency for these two sets of tracks are shown in Fig. A.3. The final occupancy efficiency is the weighted sum of these two efficiencies.

The p_T dependent systematic errors on the charged hadron spectra is summarized in Table. A.2. [52]. Here δ_{track} includes the uncertainties of the

[2]In RUN-1, this feature is used to calculate the difference of the momentum resolution for high quality and low quality tracks. (see [87])

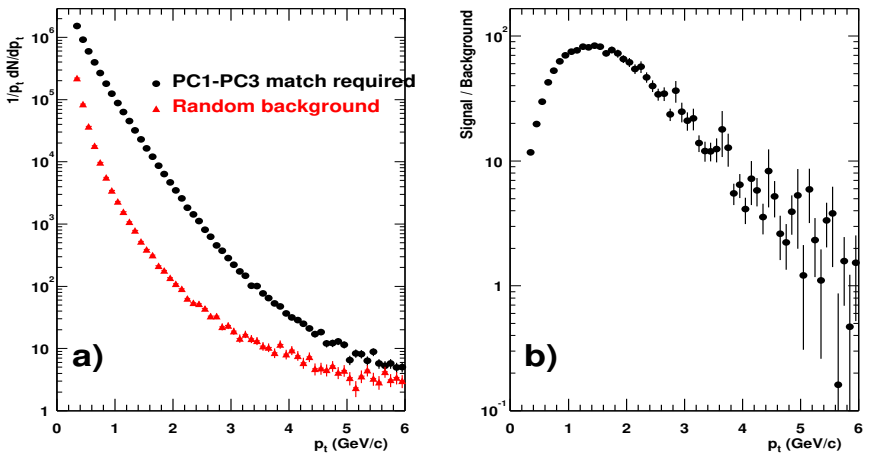

Figure A.2: a) The random association background. b) The signal/background ratio.

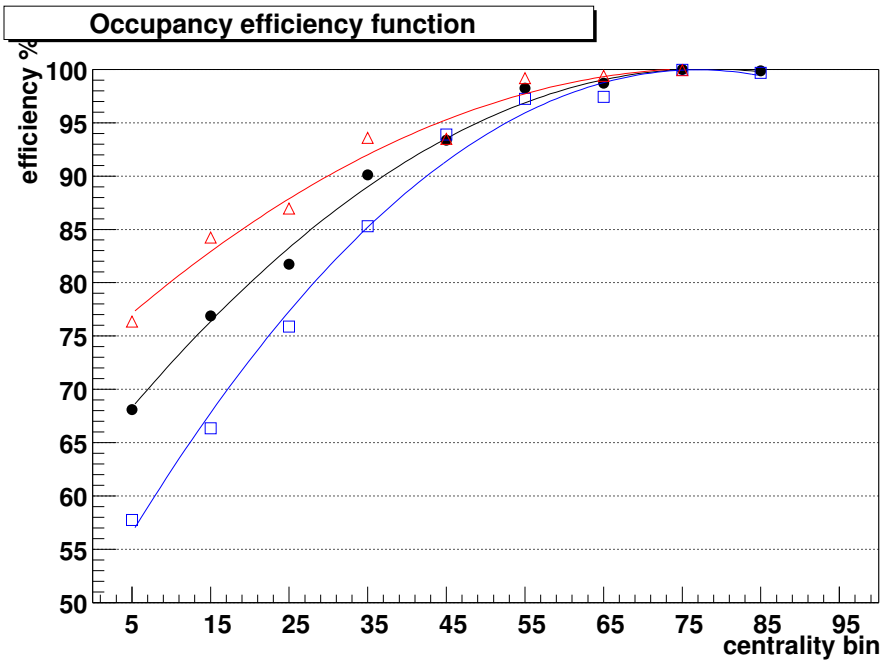

Figure A.3: Occupancy correction. Triangles are for high quality tracks, boxes are for low quality tracks, and circles represent the average efficiency.

Table A.2: Upper bounds of the systematic error on the p_T dependent single particle correction function. This error table is taken from [52].

p_T (GeV/c)	δ_{track} (%)	δ_{decay} (%)	δ_{reso} (%)	δ_{bgr} (%)	total
1	±13.5	+ 10	± 0	0	-13.5 +16.4
2	±13.5	+ 5	± 1	0	-13.7 +14.4
3	±13.5	+ 2.5	± 4	-1.6	-14.2 +14.2
4	±13.5	+ 1.25	± 9	-11.5	-20 +16
5	±13.5	+ 0.6	± 15	-40	-45 +20

acceptance, inactive area, track matching cuts, and the track reconstruction efficiency. The δ_{decay} term accounts for the uncertainty of the decay correction. The effect of the momentum resolution contributes with δ_{reso} to the systematic error. Uncertainties due to potentially un-subtracted background are quantified by δ_{bgr}. The total systematic error given in the last column is calculated as quadrature sum of the individual contributions. It is calculated separately for positive and negative errors.

A.2 Charged Hadron Analysis in $d-Au$ Collisions at $\sqrt{s_{NN}} = 200$ GeV

The detector performance during the RUN-3 $d-Au$ run is slightly better than in RUN-2. There are less inactive areas in the DC (about 10%), and the DC momentum resolution remains essentially the same. The main differences in the analysis come from the difference in the colliding species. $d-Au$ collisions on average have much less (factor of 13) tracks in the central arms. So no occupancy correction is needed. In fact, since the random background is negligible, only the PC3 matching is used to include statistics from the east arm. The minimum bias trigger efficiency in $d-Au$ collisions is lower due to the reduced multiplicity in the BBC. The accuracy with which one can determine the N_{coll}, N_{part} and impact parameter b is worse because the event-by-event fluctuations are much larger than in $Au-Au$ collisions.

In the following, we will discuss the two main differences between $d-Au$ and $Au-Au$ analysis, i.e. centrality selection and matching cuts.

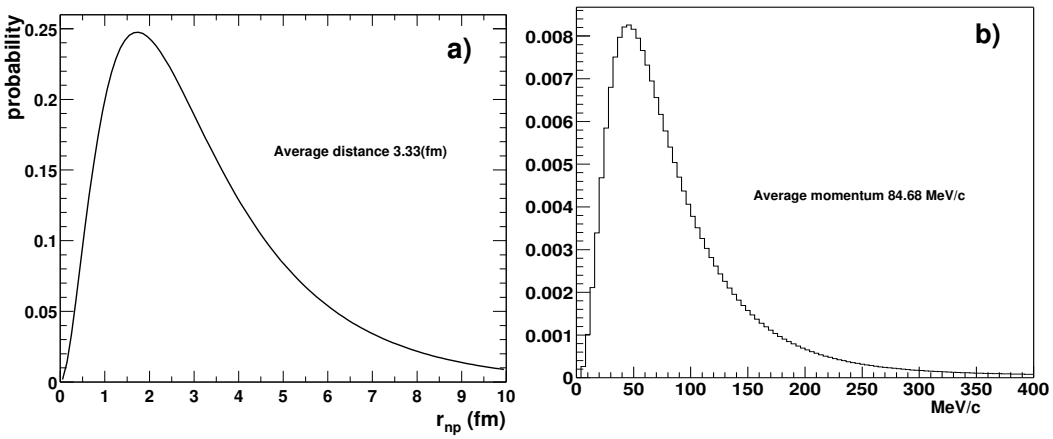

Figure A.4: a) Distance distribution between the neutron and the proton inside a deuteron. b) The momentum distribution of the nucleons inside a deuteron [176].

A.2.1 Centrality Selection

A deuteron is a loosely bound system of one neutron and one proton. It's binding energy is only 2.24 MeV, thus the size of the deuteron is large. From the wave function from Hulthèn [175], one obtains the following probability distribution for r_{np}

$$P_d(r_{pn}) = \frac{2\alpha\beta(\alpha+\beta)}{(\alpha-\beta)^2}(e^{-2\alpha r_{pn}} + e^{-2\beta r_{pn}} - 2e^{-(\alpha+\beta)r_{pn}}). \qquad \text{(A.1)}$$

with $\alpha = 0.228 fm^{-1}$ and $\beta = 1.18 fm^{-1}$, where r_{np} is the distance between the proton and the neutron. The distance distribution r_{np} and the momentum distribution of nucleons inside the deuteron is shown in Fig. A.4.

Based on a similar procedure as discussed in Chapter.4.1, the BBC trigger efficiency for events with $|z_{vtx}| < 20cm$ is found to be 88%±1%. This efficiency is lower than that in $Au - Au$ collisions due to a smaller dN/dy in the BBC acceptance in $d - Au$ collisions.

The centrality selection techniques [172, 177] are different from those used for $Au - Au$ collisions. Only the south BBC (BBCS)(Au ions go towards south) is used to define the centrality selection. The same Glauber code as for Au is used to determine the number of participants in the gold nucleus. The following assumptions are made about the BBCS response [173]:

- The number of hits in the BBCS (N_{hits}^{BBCS}) follows a Negative Binomial Distribution (NBD) given by the formula,

$$P(n,\mu,k) = \frac{\Gamma(n+k)}{\Gamma(k)n!}\frac{(\mu/k)^n}{(1+\mu/k)^{n+k}}. \quad \text{(A.2)}$$

  where μ is N_{hits}^{BBCS} for one participant, k is related to the width of the distribution by $(\sigma/\mu)^2 = 1/k + 1/\mu$.

- The observed N_{hits}^{BBCS} is proportional to the number of participants in the Au ion, $\mu \propto N_{part}^{Au}$.

Since both N_{part}^{Au} and the BBC multiplicity are small, the NBD distribution is necessary in order to taken into account the event-by-event fluctuation. The centrality classes are defined by slicing the N_{hits}^{BBCS} distribution into bins containing equal number of events. Each bin is then assigned a percentage range within [0-88%], where 88% is the overall BBC trigger efficiency. These bins are then grouped to form larger centrality bins. Fig. A.5 shows the BBCS multiplicity distribution for the 4 centrality classes used in the $d-Au$ analysis [3].

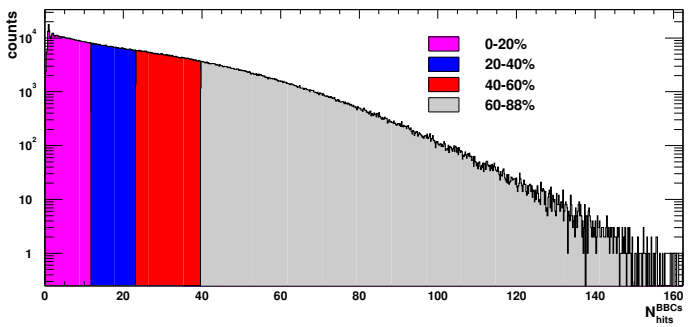

Figure A.5: The four centrality classes used in the $d-Au$ analysis.

For each centrality class, the corresponding N_{part}^{Au} and N_{coll} are determined from the Glauber simulation. The procedure is the following: i) For a collision with a given impact parameter, N_{part}^{Au} and N_{coll} are calculated in the Glauber model. The corresponding number of BBC hits is calculated according to a NBD distribution with parameters $\mu \times N_{part}^{Au}$ and $k \times N_{part}^{Au}$. ii) The simulated BBCS hit distribution is then fitted to the data to obtain the coefficients μ

[3]Note that there are the so called "tagged-neutron" events, where only the proton from the deuteron participates in the collisions, while the spectator neutron proceeds and is detected by the North ZDC. The analysis procedure for this sample of events is similar to minimum bias events. More details can be found in Ref. [172].

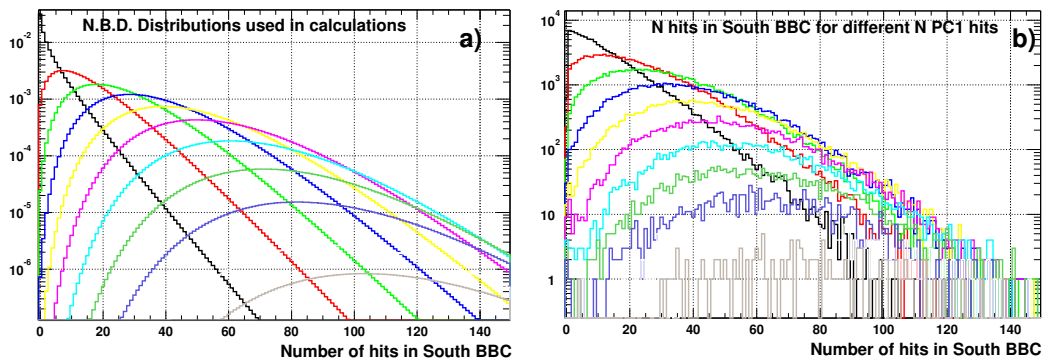

Figure A.6: a) NBD distribution for BBCS hits from simulation. b) The BBCS hits distribution from real data, different curves represents events with different number of PC1 hits from real data. [173].

and k. iii) Combined with the Glauber model, these μ and k values are then used to determine $\langle N_{part} \rangle$ and $\langle N_{coll} \rangle$.

An example of the NBD distribution from simulation and the number of hits in BBCS from data for different number of PC1 hits is shown in Fig. A.6. PC1 is used as a simple way to select centrality for real data. The measured distribution is broader than the simulated distribution due to additional fluctuations from the PC1, but the general trend agrees very well.

The simulated NBD distributions are then fitted to the data. Fig A.7 shows the fit to the BBCS hits distribution for minimum bias collisions. The general agreement is good. However, the simulated NBD distribution is above the data for a small BBCS signal. This difference indicates an inefficiency of the BBCS for events with small multiplicities.

Figure A.7: Results of NBD fits to BBCS charges for minimum bias data. Figure from [173].

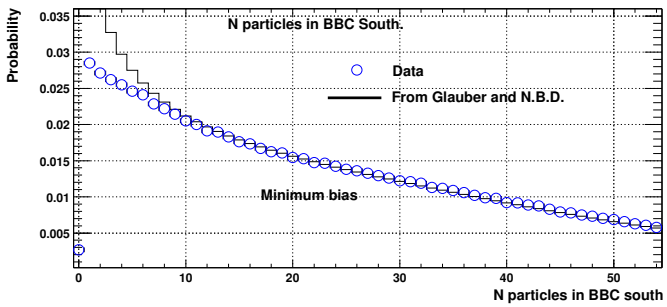

By dividing the data by the simulated N_{hits}^{BBCS} distribution, we obtained the BBC efficiency as function of N_{hits}^{BBCS}. This is shown in Fig. A.8a. Since for

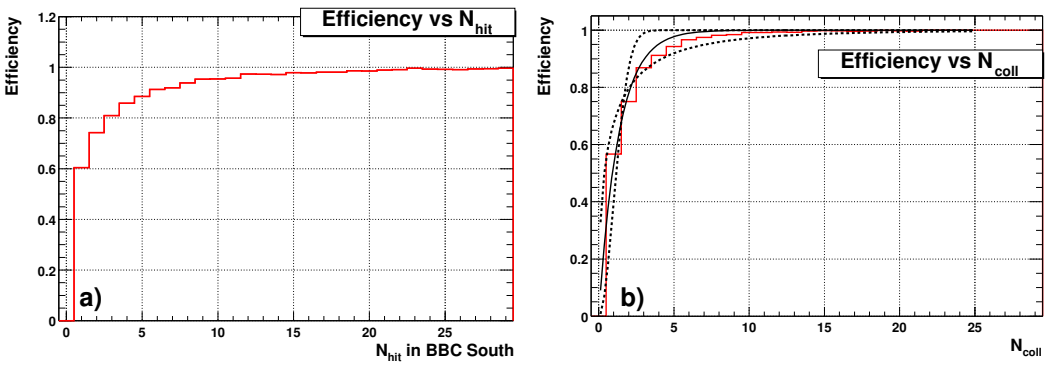

Figure A.8: a) Minimum bias trigger efficiency given by measured over calculated N_{hits}^{BBCS} distribution. b) Efficiency as a function of N_{coll}. Figure from [173].

each N_{hits}^{BBCS} value, we have a number for N_{coll} from the Glauber simulation, the efficiency can also be plotted as function of N_{coll}. This is shown in Fig. A.8b. For $N_{coll} = 1$, the efficiency is equal to 57% which is close to 52% measured in $p-p$ collisions [29, 174]. This efficiency distribution results into an 88.5% efficiency for minimum bias spectra with $\langle N_{coll} \rangle = 8.4$, consistent with the efficiency value obtained in [177].

The NBD distributions as function of N_{coll} for the centrality classes defined in Fig. A.5 are then plotted in Fig. A.9. The final values for all centrality classes used in the $d-Au$ analysis are summarized in Table A.3. The systematic error quoted comes from i) vertex dependence of the BBCS trigger efficiency, ii) dependence on nucleon cross section, σ_{nn}, iii) centrality dependence of the BBCS trigger efficiency, iv) model assumptions and NBD fits, and v) variation of Woods-Saxon parameters [172, 173]. Many of these systematic checks are similar to those discussed in Chapter.4.1.3. The results of the systematic variations are shown in Fig. A.10. The solid line shows the sum of all different types of variations.

Finally, the Glauber model also determines the total cross section in $d-Au$ collisions to be [178]

$$\sigma_{dAu}^{total} = 2.25 \pm 0.1b \tag{A.3}$$

assuming an $N-N$ cross section of $\sigma_{nn} = 42mb$.

In peripheral $d-Au$ collisions, events with the same N_{coll} can have very different multiplicity. This event-by-event fluctuation of the number of charged

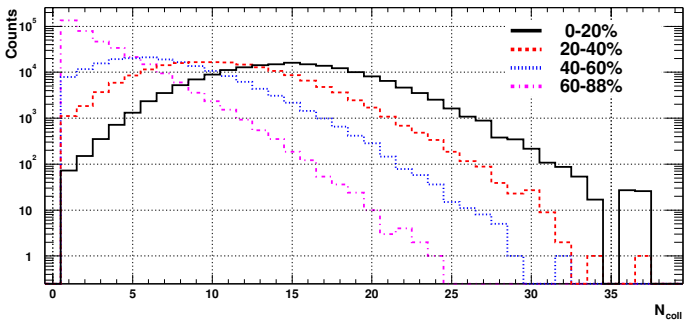

Figure A.9: N_{coll} distributions for different centrality classes.[173]

Table A.3: $\langle N_{coll} \rangle$ and it errors and BBC trigger bias (see following discussion) for minimum bias collisions and the four centrality classes shown in Fig. A.5.[173]

centrality	$\langle N_{coll} \rangle$	Ratio to most peripheral class	Bias correction
0-88	8.5 ± 0.4	-	> 0.99
0-20	15 ± 1	4.6 ± 0.5	> 0.99
20-40	10.4 ± 1.7	3.2 ± 0.2	> 0.99
40-60	6.9 ± 0.6	2.1 ± 0.1	0.974 ± 0.01
60-88	3.2 ± 0.3	1.0	0.885 ± 0.04

tracks in the BBC acceptance leads to a trigger bias, where events with the same N_{coll} but larger multiplicity have a higher probability to be triggered by the BBCS.

This bias effect was first studied in $p-p$ collisions using high p_T π^0 triggers (ERT trigger) [108]. It triggers on the events with high p_T photons from $\pi^0 \rightarrow \gamma\gamma$ decays independent of the BBC trigger decision. It was found that the BBC triggers on $\epsilon_{trig}^{BBC} \approx 50\%$ of the inelastic collisions, but these collisions include a higher fraction ($\epsilon_{\pi^0}^{BBC} \approx 75\%$) of the events for which a π^0 is detected by the ERT trigger. $\epsilon_{\pi^0}^{BBC}$ was found to be constant at $p_T > 1.5$ GeV/c, and slightly decreases towards lower p_T. A similar study was performed later for charged hadrons [174]. The efficiency of the BBC trigger for charged hadrons ($\epsilon_{h^\pm}^{BBC}$) was found to be almost identical to that for π^0's. Fig. A.11 shows the efficiency of the BBC trigger for π^0 (left) and $h^+ + h^-$ (right) in the central arms.

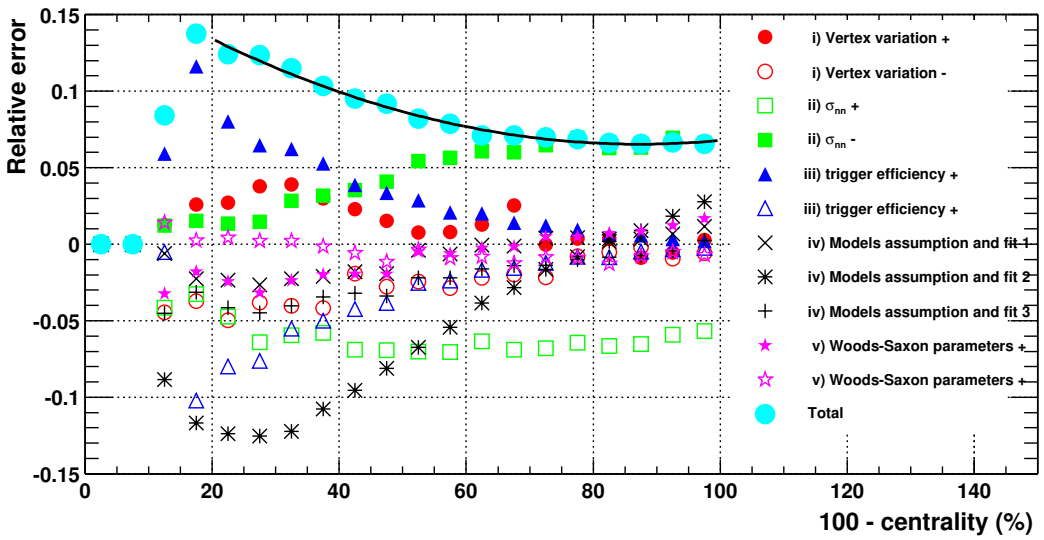

Figure A.10: Relative errors introduced by different systematic errors as function of centrality for most peripheral (left panel) and for most central (right panel) collisions.[173]

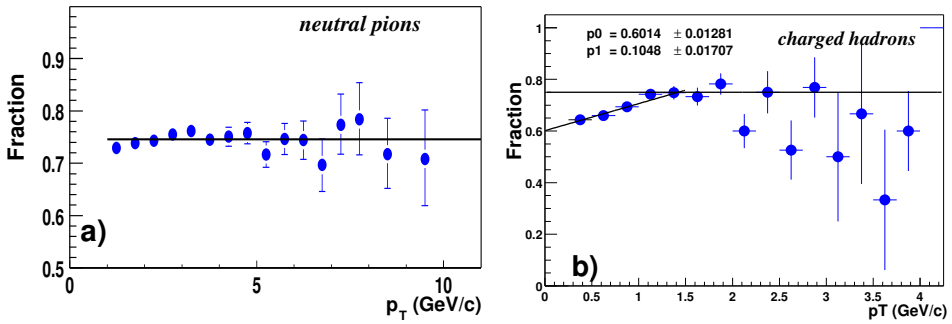

Figure A.11: Efficiency of the BBC trigger for π^0 (left) [29] and charged hadrons (right) [174].

The correction factor for the $p-p$ case, where $N_{coll}=1$, is simply,

$$c_1 = \frac{\epsilon^{BBC}_{trig}}{\epsilon^{BBC}_{h^{\pm}}} = \frac{0.5}{0.75} = 0.667. \tag{A.4}$$

For the case where $N_{coll} = n$, the BBC trigger efficiency can be calculated

according to simple binomial statistics. The efficiency of the BBC trigger for inelastic collisions is $1-(1-\epsilon_{trig}^{BBC})^n$, and the efficiency for charged hadrons is $1-(1-\epsilon_{h^\pm}^{BBC})(1-\epsilon_{trig}^{BBC})^n$. The correction factor then is,

$$c_n = \frac{1-(1-\epsilon_{trig}^{BBC})^n}{1-(1-\epsilon_{h^\pm}^{BBC})(1-\epsilon_{trig}^{BBC})^n} \quad . \tag{A.5}$$

The final correction for a given centrality class is calculated as the weighted average from the N_{coll} distribution in Fig. A.9, with the weight given by Eq. A.5. The calculated correction values for all centrality classes are shown in the last column of Table.A.3.

A.2.2 Matching Cuts and Background

Although only the PC3 matching cut is used in the$d-Au$ charged hadron analysis, the background subtraction method is still robust. Fig. A.12 shows the background subtraction in $5 < p_T < 6$ GeV/c for negative particles. The left (right) panel shows the subtraction for $N_{PMT} \geq 0$ ($N_{PMT} < 0$) tracks, respectively. The black line represents the original distribution, the red line represents the estimated background, and the blue line represents the signal distribution. The estimated R_e and R_{decay} values are,

$$\begin{aligned} R_e &= \frac{N_R(N_{PMT} \geq 5)}{N_R(N_{PMT} \geq 0)} = 0.45 \pm 0.05 \\ R_{decay} &= \frac{N_{NR}(D_{r\text{-}\phi}^{PC3} < 2.5\sigma)}{N_{NR}(4\sigma < D_{r\text{-}\phi}^{PC3} < 10\sigma)} = 0.62 \pm 0.09 \end{aligned} \tag{A.6}$$

R_e should not depend on the matching window used, since it is a property of the RICH and its radiator gas. So its value is similar to that determined for $Au-Au$. For R_{decay}, the amount of decay background inside and outside the signal window depends on the matching cut. Since a 2.5 σ matching cut is used in $d-Au$, which is wider than the cut used in $Au-Au$ (2 σ), R_{decay} is larger in $d-Au$ than in $Au-Au$ as expected.

A.2.3 Systematic Errors on Inclusive Spectra

In addition to the systematic errors on the BBC trigger from Table. A.3, we also need to estimate the systematic errors for tracking. The procedure for this type of error estimation is almost identical to that used for the charge

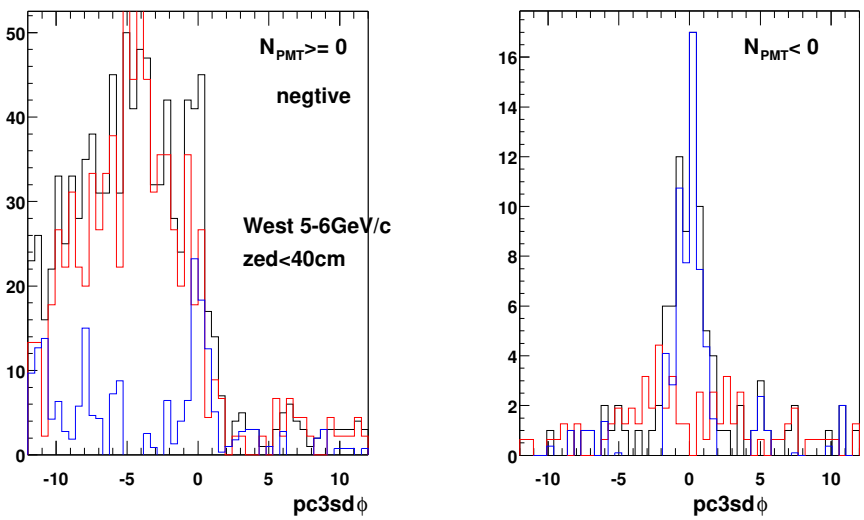

Figure A.12: The background subtraction for $d-Au$ minimum bias events for a sample p_T range of $5 < p_T < 6$ GeV/c. a) conversion background subtraction for $N_{PMT} \geq 0$ tracks, b) decay background subtraction for $N_{PMT} < 0$ tracks.[154]

hadron analysis at $\sqrt{s_{NN}} = 200$ GeV $Au-Au$ as discussed in Chapter.5. We simply quote the values in the Table A.4[4].

Table A.4: Lists of all systematics uncertainties for charged hadron spectra in $d-Au$ collisions. All errors have been estimated as full extent errors. The total errors are the quadrature sum of all errors sources. To derive 1σ errors, all values should be divided by 1.73.

p_T (GeV/c)	p_T independent	< 4	4	5	6	7
PC3 Match	Yes	4%	4%	4%	4%	4%
Acceptance	Yes	5%	5%	5%	5%	5%
MC correction	No	6.7%	6.2%	6.2%	6.2%	6.2%
Momentum resolution	No	$<<1$%	$<<1$%	<1%	1%	2%
Momentum scale	No	<5.5%	5.5%	5.8%	6.0%	6.3%
Background Subtraction	No	<1%	1%	3%	6.5%	14%
π over subtraction	No	$<<1$%	$<<1$%	$<<1$%	3%	8%

[4]The details can be found in Ref. [154].

Appendix B

Definition of Glauber Variables

- **Thickness function T_A**

  The nuclear density profile for a nucleus A in the plane perpendicular to the beam axis z,

  $$T_A(\vec{s}) = \int dz \rho_A(z, \vec{s}) \quad , \tag{B.1}$$

  is called the thickness function for nucleus A, where $\vec{s}$ is a 2-d vector from the center of the nucleus.

- **Nuclear overlap integral T_{AB}**

  For an interaction of nucleus A with nucleus B at an impact parameter $\vec{b}$, the nuclear overlap integral $T_{AB}(\vec{b})$ is defined as

  $$T_{AB}(\vec{b}) = \int d^2s T_A(\vec{s}) T_B(\vec{b} - \vec{s}) \quad , \tag{B.2}$$

  where $d^2s = 2\pi s ds$ is the 2-dimensional area element.

- **Cross section**

  The total (geometrical) cross section for the interaction of nucleus A with nucleus B is:

  $$\int d^2b = \sigma_{int}^{AB} = \pi(R_A + R_B)^2 \quad . \tag{B.3}$$

  The inclusive hard cross section is related to the $N - N$ hard cross section via,

  $$\sigma_{AB}^{hard} = AB\sigma_{NN}^{hard}. \tag{B.4}$$

- **Number of binary collisions** N_{coll}

  The meaning of Eq. B.2 can be understood by considering a nucleon in A at $(z_A, \vec{s})$ and calculating the chance of a collision (equivalent to the expected number of collisions) with the nucleons from B at the same 2-d position ($\vec{b} - \vec{s}$ in coordinates from the center of B)

$$N_{coll}(\vec{s}, \vec{b}) = \sigma_{NN}^{inel} \times \int dz_B \, \rho_B(z_B, \vec{b} - \vec{s}) = \sigma_{NN}^{inel} \times T_B(\vec{b} - \vec{s}) \quad , \quad \text{(B.5)}$$

  where σ_{NN}^{inel} is the total inelastic cross section in $N - N$ collisions.

  Integrating over all the nucleons in A yields:

$$\begin{aligned} N_{coll}(\vec{b}) &= \sigma_{NN}^{inel} \times \int d^2s T_A(\vec{s}) T_B(\vec{b} - \vec{s}) \\ &= \sigma_{NN}^{inel} \times T_{AB}(\vec{b}) \quad . \end{aligned} \quad \text{(B.6)}$$

- **Eccentricity** Ecc

  The overlap region of the nucleus A and B for $b > 0$ has an almond shape. The eccentricity describes the deviation of that shape from spherical

$$Ecc = \frac{\langle s_y \rangle^2 - \langle s_x \rangle^2}{\langle s_y \rangle^2 + \langle s_x \rangle^2} \quad \text{(B.7)}$$

  The average is performed only in the overlap region. e.g.

  $\langle s_y \rangle^2 = \int^{T_A(\vec{s}) T_B(\vec{b} - \vec{s}) > 0} d^2s \; s_y^2 \; (T_A(\vec{s}) + T_B(\vec{b} - \vec{s}))$

- **Number of participant** N_{part}

  The number of participating nucleons refers to the number of nucleons in the overlap region

$$N_{part} = \int^{T_A(\vec{s}) T_B(\vec{b} - \vec{s}) > 0} d^2s \; (T_A(\vec{s}) + T_B(\vec{b} - \vec{s})) \quad \text{(B.8)}$$